Head Office: Università degli Studi di Padova

Department of Geosciences

Ph.D. COURSE IN EARTH SCIENCES

SERIES XXX

DEPTH OF FORMATION OF SUPER-DEEP DIAMONDS

Thesis written with the financial contribution of Fondazione Cassa di Risparmio di Padova e Rovigo and project INDIMEDEA, funded by the ERC Starting Grant 2012 to Fabrizio Nestola (N° 307322).

Coordinator: Ch.mo Prof. Fabrizio Nestola
Supervisor: Ch.mo Prof. Fabrizio Nestola
Co-Supervisor: Ch.mo Prof. Jeffrey W. Harris

Ph.D. student: Chiara Anzolini

Thesis submitted in fulfilment of the requirements for the degree of Doctor of Philosophy at the University of Padova, Department of Geosciences, on October 31st, 2017.

Supervisor: Prof. Fabrizio Nestola
Department of Geosciences
University of Padova
Padova, Italy

Co-supervisor: Prof. Jeffrey W. Harris
School of Geographical and Earth Sciences
University of Glasgow
Glasgow, United Kingdom

Reviewer: Prof. Ben Harte
School of Geosciences
The University of Edinburgh
Edinburgh, United Kingdom

Reviewer: Dr. Hélène Bureau
Institut de Minéralogie, de Physique des Matériaux et de Cosmochimie
Université Pierre et Marie Curie
Paris, France

Declaration:

Hereby I declare that the work presented in this thesis is, except where otherwise acknowledged, my original investigation and achievement, and has not been previously submitted for a degree at this, or any other university or institute of learning.

Padova, 31st October 2017

Signature

Chiara Anzolini

Abstract

Diamonds, and the mineral inclusions they trap during growth, are pristine samples from the mantle that reveal processes in the deep Earth, provided the depth of formation of an inclusion-diamond pair being known. The majority of diamonds are lithospheric, while the depth of origin of super-deep diamonds (SDDs), which represent only 6% of the total, is uncertain. SDDs are considered to be sub-lithospheric, with formation from 300 to 800 km depth, on the basis of the inclusions trapped within them, which are believed to be the products of retrograde transformation from lower-mantle or transition-zone precursors.

This Ph.D. project aims to obtain the real depth of formation of SDDs by studying the most common mineral phases enclosed within them by non-destructive methods. We have studied about 40 diamonds with such inclusion phases as $CaSiO_3$-walstromite or ferropericlase using in-house single-crystal X-ray diffraction and micro-Raman spectroscopy as well as field emission gun-scanning electron microscopy, synchrotron X-ray tomographic microscopy and synchrotron Mössbauer source at outside Institutions. In addition, laser-heating diamond-anvil cell experiments were performed on a synthetic Ti-free jeffbenite to determine if the absence of Ti extends the stability field of such mineral compared to previous studies. Finally, elastic geobarometry has been completed both on ferropericlase and $CaSiO_3$-walstromite, in this last case together with thermodynamic and first-principles calculations.

One of our principal results suggests that $CaSiO_3$-walstromite may be considered a sub-lithospheric mineral, but retrograde transformation from a $CaSiO_3$-perovskite precursor is only possible if the diamond around the inclusion expands in volume by ~30%. Moreover, high-pressure and high-temperature experiments indicate that Ti-free jeffbenite could be directly incorporated into diamond in the transition zone or uppermost lower mantle and therefore this mineral may represent a high-pressure marker to detect SDDs. Finally, the observation of magnesioferrite exsolutions within ferropericlase, combined with elastic geobarometry results, strengthen the hypothesis that single ferropericlase inclusions might not be reliable markers for a diamond lower-mantle provenance.

Riassunto

I diamanti e le inclusioni minerali da essi intrappolate durante l'accrescimento sono campioni inalterati provenienti dal mantello terreste che possono fornire importanti informazioni sull'interno della Terra, a patto di conoscerne la reale profondità di formazione. La maggior parte dei diamanti sono litosferici, mentre la profondità di formazione dei diamanti super-profondi (DSS), che rappresentano solo il 6% del totale, è ancora incerta. Le inclusioni in essi contenute sono ritenute essere i prodotti di trasformazione retrograda da precursori stabili nel mantello inferiore o nella zona di transizione e, sulla base di ciò, si pensa che i DSS si formino in condizioni sub-litosferiche, tra 300 e 800 km di profondità.

L'obiettivo di questa tesi è ottenere la reale profondità di formazione dei DSS tramite lo studio non distruttivo delle più comuni inclusioni in essi racchiuse. Abbiamo studiato circa 40 diamanti contenenti $CaSiO_3$-walstromite o ferropericlasio utilizzando la diffrazione a raggi X a cristallo singolo, la spettroscopia micro-Raman, la microscopia elettronica a scansione con sorgente ad emissione di campo, la tomografia a raggi X in luce di sincrotrone e la spettroscopia Mössbauer in luce di sincrotrone. In più, sono stati eseguiti degli esperimenti in cella a incudine di diamante mediante riscaldamento laser sulla jeffbenite sintetica allo scopo di verificare se l'assenza di Ti estende il suo campo di stabilità rispetto a studi precedenti. Infine, la geobarometria elastica è stata applicata sia sul ferropericlasio che sulla $CaSiO_3$-walstromite, in quest'ultimo caso combinata con calcoli termodinamici e ab initio.

Uno dei principali risultati suggerisce che la $CaSiO_3$-walstromite sia sub-litosferica, ma che una trasformazione retrograda dalla $CaSiO_3$-perovskite sia possibile solo se il diamante si espande del ~30%. Inoltre, gli esperimenti in alta pressione e temperatura indicano che la jeffbenite povera di Ti sia stabile nella zona di transizione o all'inizio del mantello inferiore, pertanto può essere considerata una fase indicatrice per i DSS. Infine, la presenza di essoluzioni di magnesioferrite nelle inclusioni di ferropericlasio, insieme coi risultati della geobarometria elastica, suggeriscono che tali inclusioni non possano, da sole, rappresentare un'origine dei diamanti nel mantello inferiore.

Acknowledgments

First of all, I wish to thank my supervisor, Prof. Fabrizio Nestola, who not only gave me the opportunity to do this Ph.D., but always supported me with enthusiasm and unwavering optimism.

Secondly, I thank my co-supervisor, Prof. Jeffrey W. Harris, who generously provided me with tea and samples and said: *"That thou art Chiara, and upon these stones you will build your Thesis"*.

I am grateful to all my co-authors and to people who somehow contributed to the research presented here. Above all I am deeply indebted to Dr. Ross J. Angel and Dr. Matteo Alvaro for their priceless help and numerous suggestions throughout these years.

Thank you also to all the INDIMEDEA group, split between Padova and Pavia, in particular to Paolo, Sula, Mauro, Mattia, Greta and Daria.

Special thanks to Prof. Michael J. Walter, who supervised me during my stay at the University of Bristol, and to James, Olly and Marzena, for their precious help and endless patience in the lab.

During these three years I have had the immense pleasure to meet many new friends in Padova and in the rest of the world. Together we spent unforgettable moments and certainly, without you, this path would not have been so exciting. Thank you!

Now that I came to the very end of my career as a student, I want to sincerely thank all the teachers I have had in my life, because the contribution of each of them has brought me where I am.

Lastly, infinite thanks to mum and dad, for their continuous support and for always being with me.

Preface

The Thesis starts with an introduction chapter, which provides an overview of the current state of knowledge on super-deep diamonds and their occurrence, with emphasis on issues addressed in this work, and outlines the specific focuses and aims of the Thesis as a whole.

The introduction is followed by a chapter which summarizes materials and methods adopted throughout the research. However, for a comprehensive knowledge of the techniques, I forward the reader to the single manuscripts which are part of the Thesis.

The body of the text is constituted by one manuscript which has been published in a peer-reviewed journal (*Anzolini et al., 2016, Depth of formation of* $CaSiO_3$*-walstromite included in super-deep diamonds. Lithos, 265, 138-147*), a second manuscript published in a peer-reviewed journal (*Anzolini et al., 2018, Depth of formation of super-deep diamonds: Raman barometry of* $CaSiO_3$*-walstromite inclusions. American Mineralogist, 103(1), 69-74*), a third manuscript which has to be submitted (*Anzolini et al., New stability field of jeffbenite (ex-"TAPP"): possible marker for diamonds super-deep origin*) and a fourth manuscript which is in preparation (*Anzolini et al., Depth of formation of ferropericlase included in super-deep diamonds*).

The Thesis ends with a summary of the results reported in the work and some concluding remarks in the light of the entire Ph.D. project.

Each manuscript is self-contained and has its own references; references for chapters 1, 2 and 7 are reported altogether at the end.

The appendixes report material not published in support of the manuscripts, and other related publications in which I have contributed as a co-author.

Padova, 31st October 2017

Signature

Chiara Anzolini

Table of contents

List of figures

List of tables

1 Introduction

1.1 Geological importance of diamond

"Diamonds are a girl's best friend", they say.

I would rather say *"Diamonds are a geologist's best friend".*

The word "diamond" comes from the Greek "adamas", meaning unconquerable, which was quite a good intuition for ancient Greeks. Aside from being the hardest known material on Earth, having clear aesthetic and commercial value, it is also used for several industrial and technological applications. Despite its strength and value, which have been acknowledged and exploited since ancient times, only in the last half decade has this material undergone serious detailed scientific investigations. It soon became clear to the scientific community the invaluable role that diamond plays in our understanding of the Earth and, by extrapolation, in our comprehension of planetary states in general.

Diamond is in fact the paramount phase mineral to understand the evolution and the physico-chemical conditions of the Earth's mantle mainly because: (i) it is the stable phase through which carbon is stored in the deep mantle for long periods of geological time; (ii) it contains and preserves different types of crystalline and fluid inclusions; (iii) it is the only material able to sample depths within our Earth ranging from 120 km to, eventually, 800 km. Even if other mantle materials, like mantle xenolith and exposed mantle rocks, are directly observable, the deeper into the earth we want to sample, the more we have to rely upon diamond to provide material for study. Indeed, diamond's unique indestructibility places it as, arguably, the only means by which deep earth material, particularly from the transition zone and lower mantle, can be supplied to science for study.

1.2 Diamond and its occurrence

Diamond, the high-pressure polymorph of carbon, has a simple but elegant crystal structure (Figure 1.1), in which each carbon atom is bonded to four other atoms in a tetrahedral arrangement, which yields a strong rigid framework. Combining this structural arrangement, which coincides with the hybrid *sp3* orbitals of carbon, with the unmatched strength of the C–C bond, explains most of diamond's properties (Harlow and Davies, 2005).

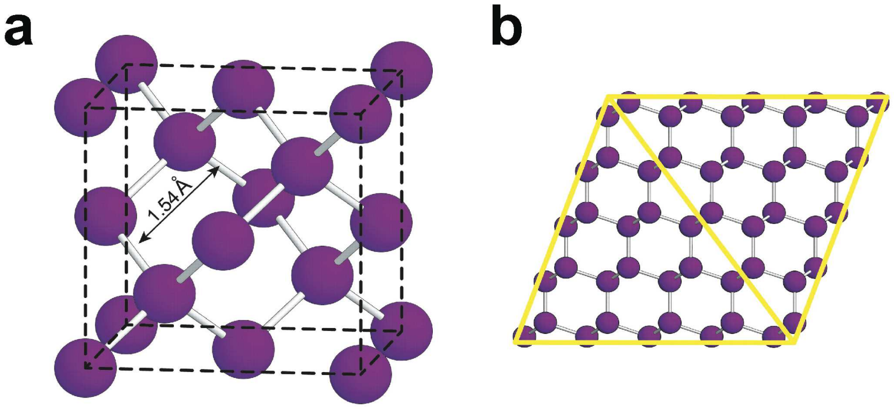

Figure 1.1: Ball and stick models of the diamond structure showing a) the unit cell with the C–C distance indicated and b) a projection with the boundaries of an octahedron, the archetypal "diamond" shape (modified from Harlow and Davies, 2005).

The rigid uniform covalent bonding gives rise to such properties as great hardness, incompressibility, thermal conductivity, electrical insulation and optical transparency. Their extreme strength and refractory nature not only permit diamonds to survive exhumation to the Earth's surface and any subsequent weathering, but also acts as a shield to protect the mineral inclusions they carry. In addition, diamonds optical transparency allows the application of in situ techniques, such as single-crystal X-ray diffraction and micro-Raman spectroscopy, to become powerful tools to investigate diamond non-destructively, thus preserving specific information on host-inclusion relationships.

Diamond occurs in a variety of forms, monocrystalline, polycrystalline, and coated diamonds being the three main groups usually considered for geological purposes. Each of these types represents different environment of growth that are mainly controlled by supersaturation and resorption phenomena (Shirey et al., 2013).

Diamond forms mostly in the Earth's upper mantle in two environments. The principal environment is peridotitic, where the associated mineralogy is commonly olivine, enstatite, pyrope garnet and chrome diopside. With the second environment referred to as eclogitic, almandine garnet and omphacitic clinopyroxene are principally involved.

Diamonds are carried as xenocrysts to the Earth's surface in three rare types of magma: kimberlite, lamproite and lamprophyre (Gurney et al., 2010). Among these, kimberlites are the most important hosts for diamonds and are usually associated with stable Archean continental nuclei called cratons (Figure 1.2). When these old, seismically stable and thick (i.e. 250–300 km) block formed, they were relatively cold compared to adjacent crustal zones. For stability, they have a keel and it is in this keel area that diamonds can form, because the cratonic geotherms are perturbed downwards allowing diamond formation at a relatively shallow level (see § 1.3).

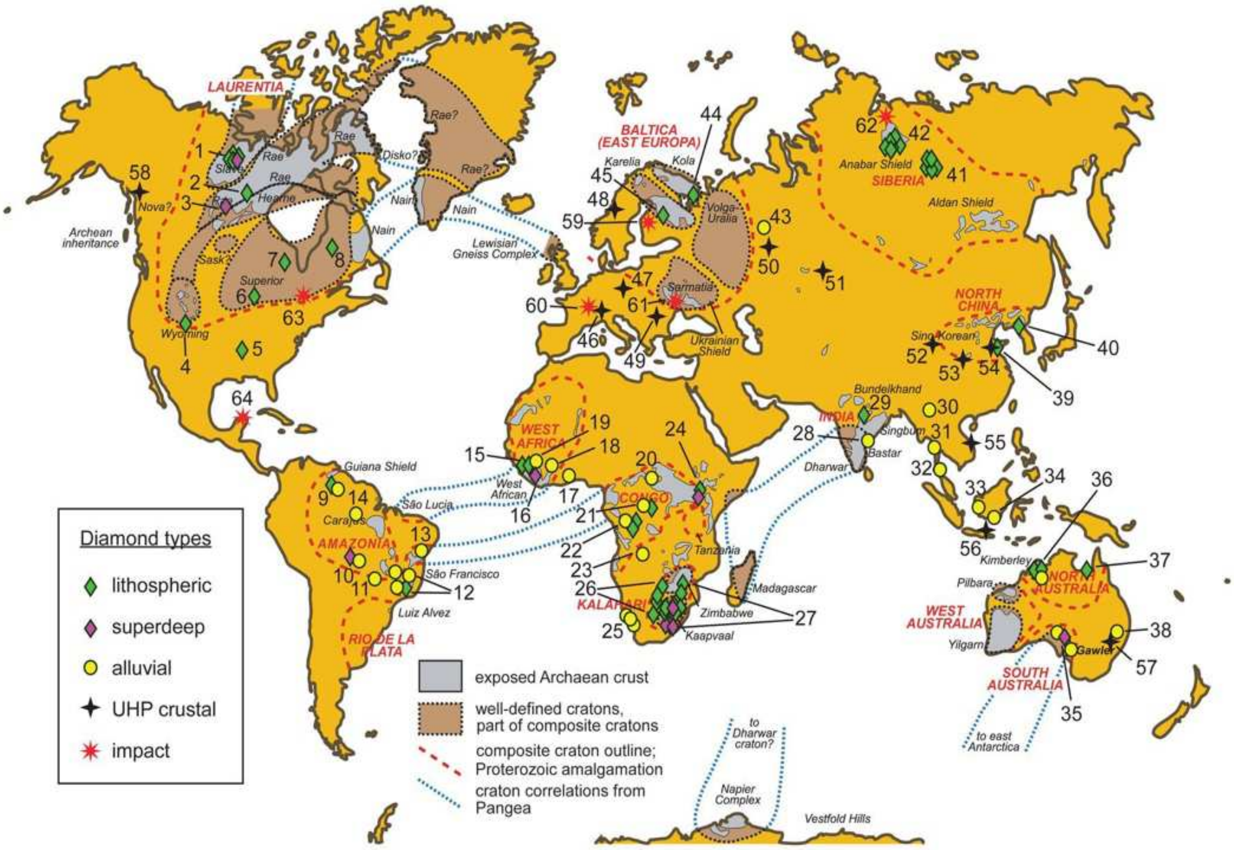

Figure 1.2: Diamond localities of the world in relation to Archean cratons and classified on the basis of their origin (from Shirey et al., 2013).

1.3 Lithospheric VS Super-deep diamonds

Apart from the two principal growth environments, diamonds can further be subdivided by depth of formation into lithospheric and sub-lithospheric or "super- deep". The basis for this division is largely based on the type of mineral inclusion contained within the diamond. Thus, in terms of relative abundance within the global diamond population, 94% are represented by lithospheric diamonds and only 6% by super-deep diamonds (Figure 1.3, Stachel and Harris, 2008).

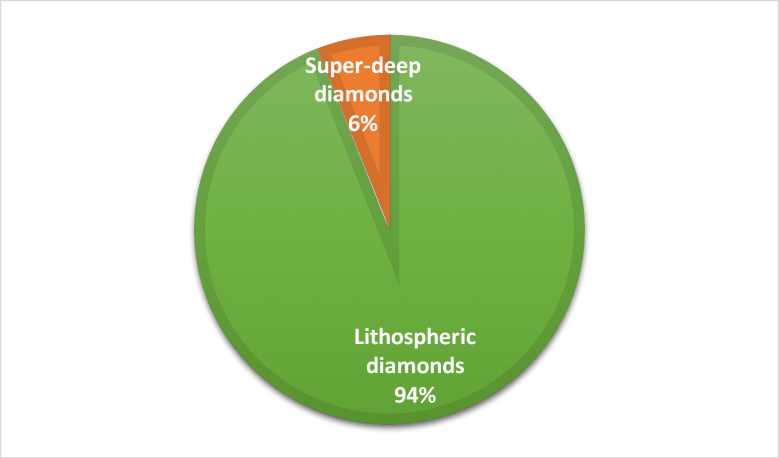

Figure 1.3: The relative abundance of diamond source regions in the Earth's mantle (after Stachel and Harris, 2008).

If you consider that diamonds as a whole are rare, the amount even in the most diamondiferous of diamonds primary occurrences usually being at the part-per-billion (ppb) level, that super-deep diamonds are only a small subset of them and that inclusion-bearing diamonds amount only to about a maximum of 4% of a population, then you can imagine how tricky it is to study super-deep diamonds. Therefore, the information available about them is very limited.

It is now established that lithospheric diamonds form in subcratonic lithospheric mantle, where heat loss due to conduction and radioactive decay make cratonic roots significantly cooler than surrounding convecting mantle. As a consequence of relaxed geotherms, the graphite-diamond transition is raised to shallower depth within subcratonic lithosphere, creating a diamond stable window where cratonic roots extend down into the diamond stability field (Stachel and Harris, 2008), which means between 120 and 250 km depth (Figure 1.4).

On the other hand, a big debate exists about the real depth of origin of the so-called super-deep diamonds. Over the last thirty years, numerous observations have suggested that among the dominant diamond population are samples derived from deeper parts of the mantle. Since they are found in the same deposits as lithospheric diamonds, it is suggested they were brought up by the same kimberlitic volcanism and, thus, they must be carried into the depth of kimberlite generation by upwelling convection in mantle plumes. Some super-deep diamonds are interpreted to crystallize as slab-derived carbonatites interacting with peridotitic mantle (Thomson et al., 2016) between 300 and at least 800 km depth (Figure 1.4; Stachel and Harris, 2005; Harte, 2010), this because some of the inclusions entrapped within them are considered to be the products of retrograde transformation from lower-mantle or transition-zone precursors. However, in many cases undisputed evidence of these purported high-pressure precursors as inclusions in diamonds is lacking, and, consequently, their real depth of origin has been proven only in a few cases (e.g. Brenker et al., 2002; Pearson et al., 2014; Smith et al., 2016). This lack in our knowledge arises mostly from the extreme rarity of such stones, which makes a statistically robust study on them challenging.

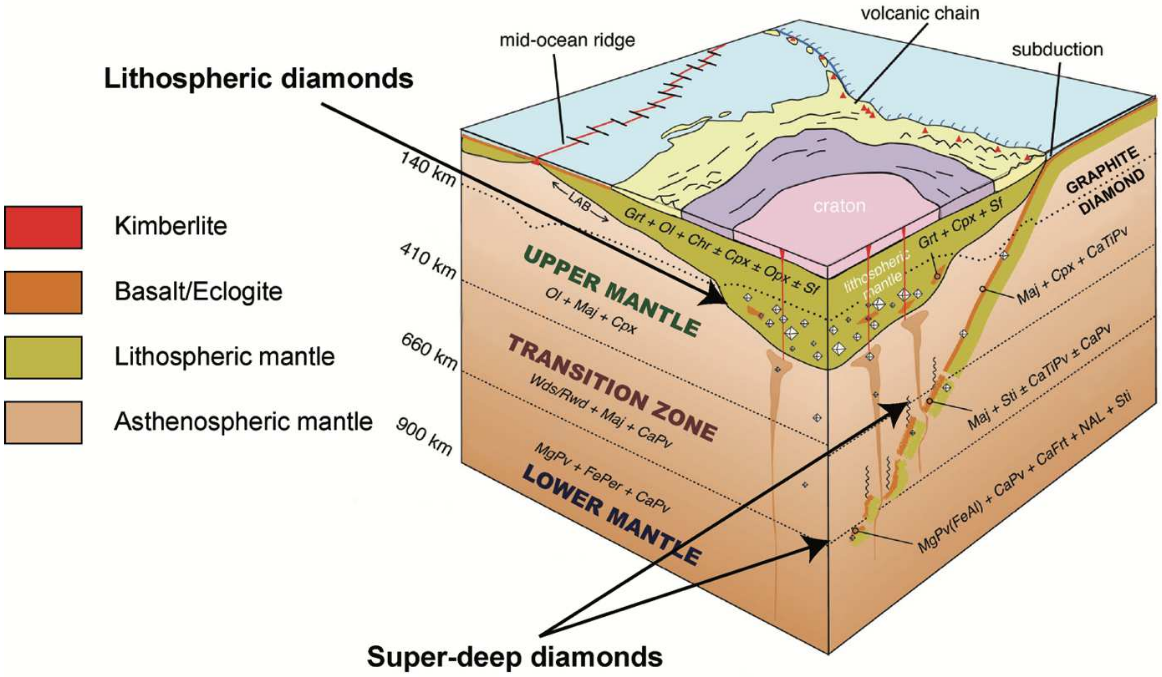

Figure 1.4: Block diagram showing the basic relationship between a continental craton, its lithospheric mantle keel and diamond stable regions in the keel, and the asthenospheric mantle. The upper mantle extends to 410 km, the transition zone is taken between the major seismic discontinuities at 410 km and 660 km depth, the lower mantle starts at 660 km (modified from Shirey et al., 2013).

Lithospheric diamonds are known for their regular morphology, higher nitrogen content and minor evidence of plastic deformation. Conversely, super-deep diamonds often show very distinctive features: they usually exhibit irregular crystal shape, pervasive fracturing, low nitrogen content and strong evidence of plastic deformation, which suggest a long and complex journey from the interior to the surface of our planet. (Figure 1.5; Nestola, 2017). However, the most reliable difference that allows us to distinguish between the two diamond categories is the type of mineral inclusions found within them. Lithospheric diamonds contain phases stable in the shallower part of the upper mantle (down to ~250 km); the most abundant ones are olivine, eclogitic and peridotitic garnet, omphacite, diopside, enstatite, sulfides, and minor amounts of coesite and kyanite. Super-deep diamonds contain significantly different types of inclusions, with the most abundant ones being ferropericlase, $CaSiO_3$-walstromite, jeffbenite (former TAPP phase) and majoritic garnet.

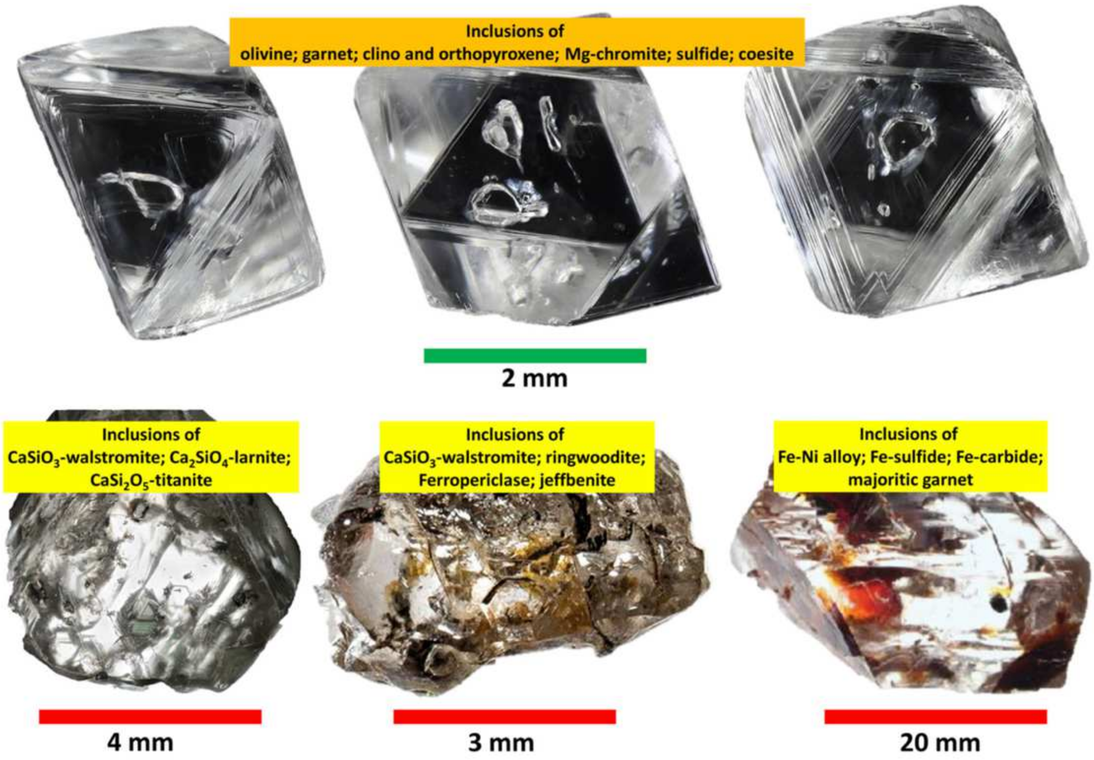

Figure 1.5: Lithospheric diamonds (top) and super-deep diamonds (bottom). Figures were modified after: Pearson et al., 2014; Nestola et al., 2014; Novella et al., 2015; Anzolini et al., 2016; Smith et al., 2016.

1.4 Typical phases found in super-deep diamonds

1.4.1 Ferropericlase

Ferropericlase [(Mg,Fe)O] is likely the most abundant phase found in super-deep diamonds, where it occurs as euhedral brown/black grains, and the second, in terms of volume, in the lower mantle (Figure 1.6). Since the coexistence of ferropericlase and low-Ni enstatite in a diamond was first reported (Harte and Harris, 1994; Harte et al., 1999; Stachel et al., 2000; McCammon, 2001), this couple of minerals have been considered proof of lower-mantle origin. This origin is based on two facts that apply only to this particular mineral pair, and, not surprisingly, in view of the low overall percentage of super-deep diamonds, such a pair is seldom found in one diamond: 1) the two minerals would recombine to form olivine at shallower depths; 2) an enstatite enriched in Al and depleted in Ni is considered to be the decompression product of bridgmanite (see § 1.4.3; Stachel et al., 2000). The situation is different, however, if only ferropericlase is found as an inclusion because it is stable within the entire range of pressure and temperature conditions from lower mantle to the Earth's surface (Brey et al., 2004) and it can form not only by decomposition of ringwoodite, but also by decarbonation (Brenker et al., 2007). Two main arguments are reported against its lower-mantle origin: (1) the number of ferropericlase inclusions found in super-deep diamonds does not match at all the expected volume fraction typical of lower mantle (Irifune, 1994; Fei and Bertka, 1999; Wood, 2000); (2) ferropericlase inclusions in diamond show a very strong chemical variability, from $Mg_{0.90}Fe_{0.10}O$ (typical composition expected for ferropericlase stable in the lower mantle) to $Mg_{0.36}$–$Fe_{0.64}O$ (Kaminsky, 2012), which mineralogically must be defined Mg-rich wüstite. In particular, ferropericlase from Canada, South Australia and South Africa has #Mg = 0.80–0.90, that is close to the theoretical value. Ferropericlase from Guinea, along with similar Mg values, also has lower Mg values of 0.75. Moreover, iron-rich ferropericlase from Brazil, reaching #Mg = 0.38, comprises almost a half of all grains in this region (Kaminsky, 2012). Such great deviations have been related to the hypothetical decomposition of bridgmanite, to form iron-rich ferropericlase and SiO_2 (Fei et al., 1996; Harte et al., 1999); however, this suggestion only replaces one discrepancy with another: how, in the lower mantle with #Mg = 0.80–0.95 can exist a highly Fe-rich bridgmanite (Kaminsky, 2012). Moreover, the ferric iron proportion ($Fe^{3+}/\Sigma Fe$) in ferropericlase is low; only 0–7% of the total iron content (McCammon et al., 1997). In order to solve both discrepancies, Liu (2002) proposed a model of decarbonation of ferromagnesite, having variable Fe content, with the formation of ferropericlase with a variable Mg index. Wirth et al. (2014) reported a Fe-rich ferropericlase with high ferric iron content and, on the basis of this, suggested it comes from very deep in the mantle.

1.4.2 $CaSiO_3$-walstromite

Walstromite-structured $CaSiO_3$ is the most important Ca-bearing phase contained in super-deep diamonds and it is believed to be the retrograde transformation product of $CaSiO_3$-perovskite. On an experimental basis, $CaSiO_3$-perovskite is considered to be the third most abundant mineral in the lower mantle, with a 5–10 wt% abundance in the pyrolite model (Figure 1.6, Akaogi, 2007; Irifune et al., 2010) and even higher if associated with subducted mid-oceanic ridge basalt, with values between 21–29% (Hirose et al., 1999; Funamori et al., 2000; Perrillat et al., 2006). $CaSiO_3$-walstromite occurs as small, colourless or milky-white grains and usually associates with enstatite, ferropericlase and coesite, as well as with $CaTiO_3$-perovskite, jeffbenite, majorite, olivine, and native Ni (Kaminsky, 2012; Zedgenizov et al., 2016). In some Guinean and Brazilian diamonds samples (Stachel et al., 2000; Hayman et al., 2005; Anzolini et al., 2016; Burnham et al., 2016; Zedgenizov et al., 2016) $CaSiO_3$-walstromite was associated with larnite β-Ca_2SiO_4 + $CaSi_2O_5$-titanite. On the basis of the $CaSiO_3$ phase diagram (Figure 3.4, Gasparik et al., 1994) this inclusions association is believed to be formed at ~9.5–11.5 GPa and 1500 K.

1.4.3 Low-Ni Enstatite

Enstatite ($MgSiO_3$) with its' characteristic low-Ni and high-Al content is believed to be the back-transformation product of bridgmanite ($MgSiO_3$) (Harte et al., 1999; Stachel et al., 2000), which is the most abundant mineral in the lower mantle (Figure 1.6, Tschauner et al., 2014) and was previously known as Mg-silicate perovskite. Bridgmanite is formed as a result of the dissociation of ringwoodite [$(Mg,Fe)_2SiO_4$] into ferropericlase and bridgmanite and is responsible for the major 660 km seismic discontinuity within the mantle. Within diamonds, the low-Ni enstatite inclusions occur as colourless associated with ferropericlase, $CaSiO_3$-perovskite and jeffbenite, chrome spinel, native nickel and sulphide (Kaminsky, 2012).

1.4.4 Majoritic garnet

Majoritic garnet [$Mg_3(Mg,Fe,Al,Si)_2Si_3O_{12}$] (in which there is an excess of Si in octahedral coordination) is the major mineral of the transition zone (Figure 1.6) and occurs as dark red inclusions. In majorite grains from diamonds at the Monastery and Jagersfontein pipes, South Africa, the silica excess is as high as $X_{Si} = 3.2–3.6$ (Moore and Gurney, 1985; Chinn et al., 1998; Tappert et al., 2005). Some experiments demonstrated that it is stable under pressures of up to 28 GPa (Irifune and Ringwood, 1993), and its association with perovskite ($CaTiO_3$) and ilmenite (Wilding et al., 1991; Kaminsky et al., 2001) in diamonds from the Juina placers in Brazil suggests it is stable in the uppermost part of the lower mantle. It is commonly found as retrogressed jeffbenite and/or Na-Ca-Mg-Fe-Al-pyroxene (Harte and Hudson, 2013).

1.4.5 Jeffbenite

Jeffbenite (ideally $Mg_3Al_2Si_3O_{12}$) is a new tetragonal phase with garnet-like stoichiometry (Nestola et al., 2016) previously referred to as TAPP (Tetragonal Almandine-Pyrope Phase) (Harte and Harris, 1994; Harris et al., 1997). which was discovered as small inclusions of 30–100 µm in diameter in diamonds from the São Luiz placer deposits in the Juina area, Brazil. The mineral has only been found as a cubo-octahedral or elongate-tabular shaped, apple-green inclusion in super-deep diamonds. Nevertheless, whether jeffbenite forms as a primary phase in the transition zone or in the lower mantle, or is the product of retrogression from high-pressure mantle phases is still controversial. On the basis of the experimentally determined stability field by Armstrong and Walter in 2012, at present two possibilities are proposed for its formation: 1) entrapment as a primary mineral by diamond in the upper mantle at pressures up to 13 GPa (Armstrong and Walter, 2012); 2) retrograde formation from a bridgmanite or a majoritic garnet below 13 GPa (Brenker et al., 2002; Armstrong and Walter, 2012; Harte and Hudson, 2013). However, these results were obtained on a Ti-rich jeffbenite (jfb), which is usually found as part of composite inclusions, and not on a Ti-free jfb, which occurs as single-phase inclusions in diamonds.

1.4.6 Silica (SiO_2)

Quartz, the stable form of SiO_2 at ambient conditions, is expected to transform first to coesite and then to stishovite at high pressures. Stishovite should be stable together with ferropericlase in the lower mantle at elevated iron contents (Figure 1.6); otherwise the two phases would combine to form bridgmanite. Harte et al. (1999) constrained the magnesium-iron ratio for this reaction using the compositions of inclusions in diamonds from Juina and found that stishovite coexists with ferropericlase and bridgmanite at Mg-numbers as high as 70 for the former and 86 for the latter. Compared with high-pressure experiments, these ferropericlase and bridgmanite Mg-numbers are relatively high. The other four occurrences of stishovite together with ferropericlase in diamonds worldwide all reflect even more magnesian compositions and, therefore, should not exist in equilibrium. Disequilibrium seems

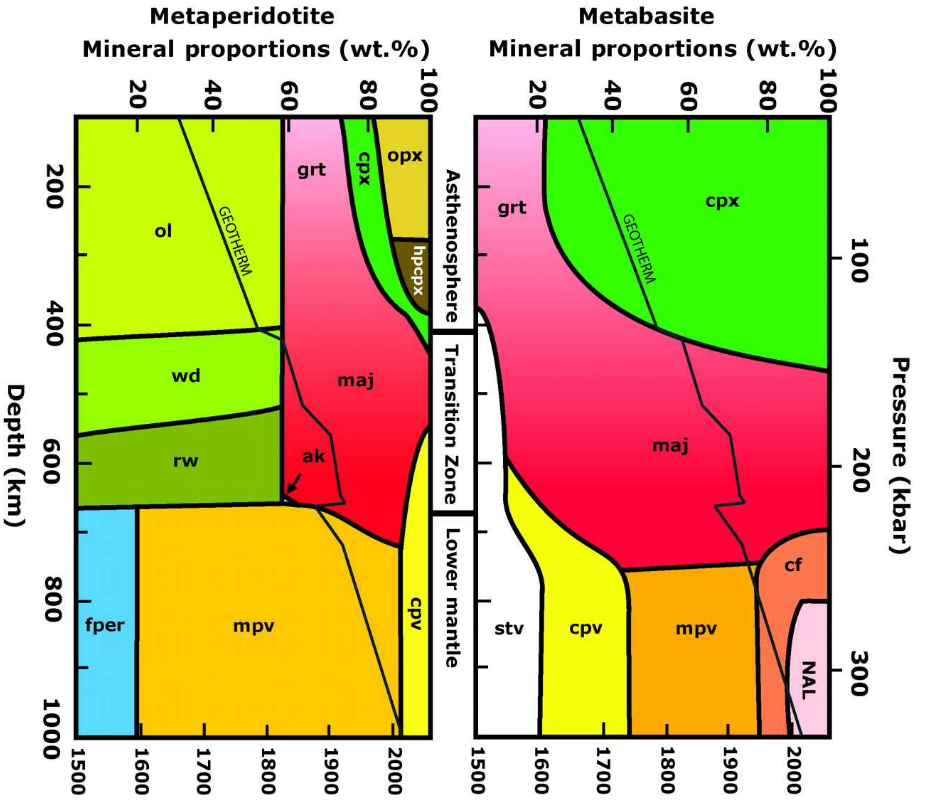

Figure 1.6: Mineral proportions present in average metaperidotite and metabasite bulk compositions as a function of depth ranging from 100–1000 km (from Harte, 2010).

the most straightforward explanation, but considering the relative “abundance” of these samples, some doubts are justified. Silica occurs as colourless inclusions chemically almost pure with a minor amount of Al, which is characteristic for stishovite formed under an elevated pressure (Ono, 1999; Sano et al., 2004).

1.5 Aim of the work

This Ph.D. project aims to obtain the depth of formation of super-deep diamonds by studying the most common mineral phases enclosed within them by non-destructive methods. A non-destructive in situ investigation of an inclusion in diamond has a strategical importance because: (a) some mineral inclusions under pressure, once extracted, would invert to lower-pressure phases; (b) the internal pressure on the inclusion can provide information about the formation pressure of the diamond (Izraeli et al., 1999; Sobolev et al., 2000; Nestola et al., 2011); (c) the morphology and orientation relationships of the inclusion with the host diamond can provide indications about its protogenetic vs. syngenetic and/or epigenetic nature (Nestola et al., 2014); (d) preservation of the diamond surface growth features can provide indications of oxidation processes (Fedortchouk et al., 2011) and (e) last but not least, it is not always allowed to break the stones!

We have studied about 40 diamonds containing $CaSiO_3$-walstromite or ferropericlase using in-house single-crystal X-ray diffraction and micro-Raman spectroscopy as well as field emission gun-scanning electron microscopy and both synchrotron X-ray tomographic microscopy and synchrotron Mössbauer source at outside Institutions. In addition, laser-heating diamond-anvil cell experiments were performed on a synthetic Ti-free jeffbenite to determine if the absence of Ti extends the stability field of such mineral compared to previous studies. Finally, elastic geobarometry, which provides the depth of formation of a diamond-inclusion pair, has been completed both on ferropericlase and $CaSiO_3$-walstromite, in this last case combined with thermodynamic and first-principles calculations.

In the next chapter I will give an overview of the material and methods used in this work. However, for a more detailed description of both the samples and the techniques adopted, I forward the reader to the single manuscripts which are part of the Thesis.

2 Material and methods

2.1 Geological setting

The super-deep diamonds which form the main part of this Thesis come from the São Luiz placer deposits in the Juina area of Mato Grosso State, Brazil.

The Juina Kimberlite Field is located in the Proterozoic Rio Negro-Juruena Province, formed during 1.8–1.55 Ga accretion onto the Palaeoproterozoic and Archaean terrains at the south-western edge of the Amazon Craton (Tassinari and Macambira, 1999). The Juina kimberlites are one of many NW–SE (125°) trending expressions of alkaline magmatism present in Brazil previously associated with the passage of the Trindade plume beneath the South American lithosphere (Gibson et al., 1995) during the Cretaceous period and have eruption ages of 92–95 Ma (Heaman et al., 1998). However, a newly reported study by Guarino et al. (2013) suggests that the location of this alkaline magmatism is outside the region of plume influence, and kimberlites appear to have no link with the Trindade plume. These authors suggest that the kimberlites may have been emplaced along pre-existing weaknesses in the South American lithosphere that were exploited during the formation of sedimentary basins associated with the opening of the Atlantic Ocean, a proposal considered by Riccomini et al., (2005). In total, 51 kimberlites are known to date in the Juina area, including 47 pipes and 4 dykes, with an average pipe size of approximately five hectares, but they vary between 0.10 ha and 60 ha (Andreazza et al., 2008). All diamond production has been from recent alluvial and coalluvial deposits.

Figure 2.1 shows that the São Luiz alluvial diamond deposit lies centrally within the Juina Province. The principal deposit is located within channels, palaeo-channels, flats and terraces of the Rio Cinta Larga, a tributory of the Rio Aripuanã. A number of secondary deposits lie in the Rio Cinta Larga catchment area, namely the Rio Vinte e Um, Rio Mutum, Igarapé Porcão, Rio Juininha and Rio Juina-Mirim.

During the mid-1980's, diamonds were recovered by a subsidiary of the DeBeers Group of Companies from the São Liuz valley. The inclusion content of these diamonds showed them to contain relatively high levels of ferropericlase, enstatite, $CaSiO_3$-walstromite, and other minerals considered to be of lower-mantle origin. These identifications lead to systematic studies of these diamonds (Wilding et al., 1991; Harte and Harris, 1994; Harris et al., 1997; Harte et al., 1999; Hutchison et al., 2001). In addition, subsequent reviews on the importance of the inclusion content were published, notably Harte et al. (1999), Harte (2010) and Harte and Hudson (2013).

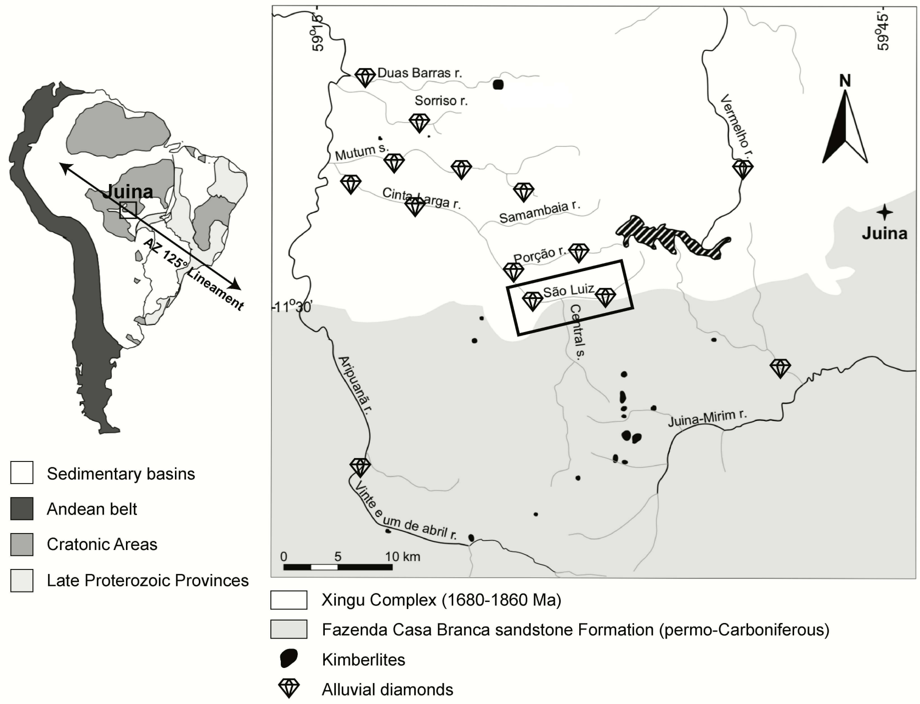

Figure 2.1: Geological map showing the location of the Juina region in south-west Brazil with the location of the São Luiz river, and other alluvial diamonds deposits, in the enlarged panel (modified after Araujo et al., 2013).

2.2 Samples

The 38 diamonds from São Luiz, Juina, Brazil and involved in the present study (Figure 2.2 and Figure 2.3) were donated by the Diamond Trading Company (a member of the DeBeers Group of Companies) to JWH. Throughout this work, these samples are referred to by numbers prefixed by SL_FFM_ and AZ and suffixed by the inclusion number. The stones are 2–8 mm in size and colourless to brown. Recognized shapes include octahedra, dodecahedra and octahedra-dodecahedra transition forms, macles, (twinned diamonds) and flattish irregular stones. Most of the diamonds are broken and heavily resorbed. Several samples show signs of plastic deformation and sometimes exhibit internal fractures at the diamond-inclusion interfaces.

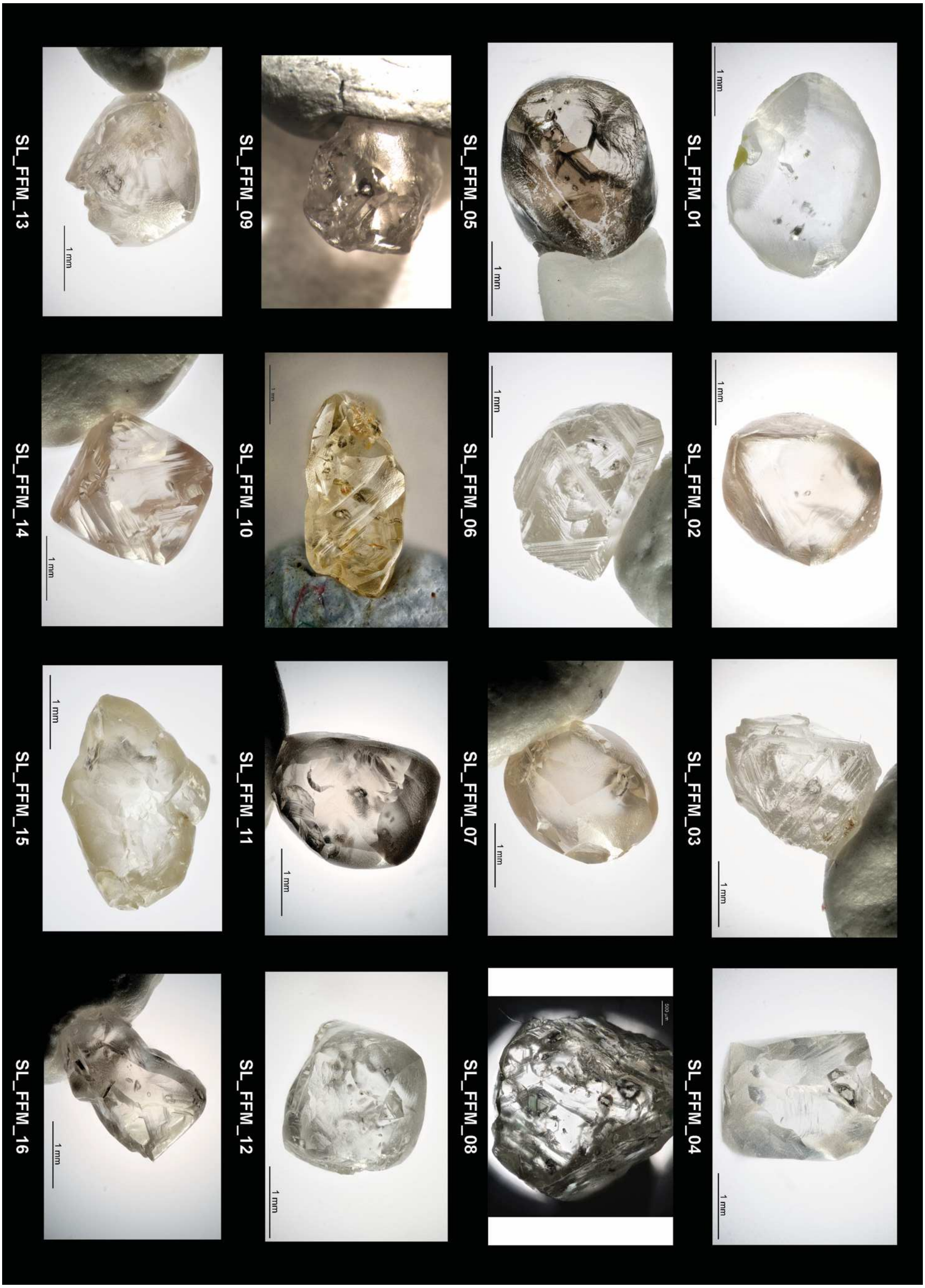

Figure 2.2: The first suite of diamonds, labelled SL_ FFM, studied in this work.

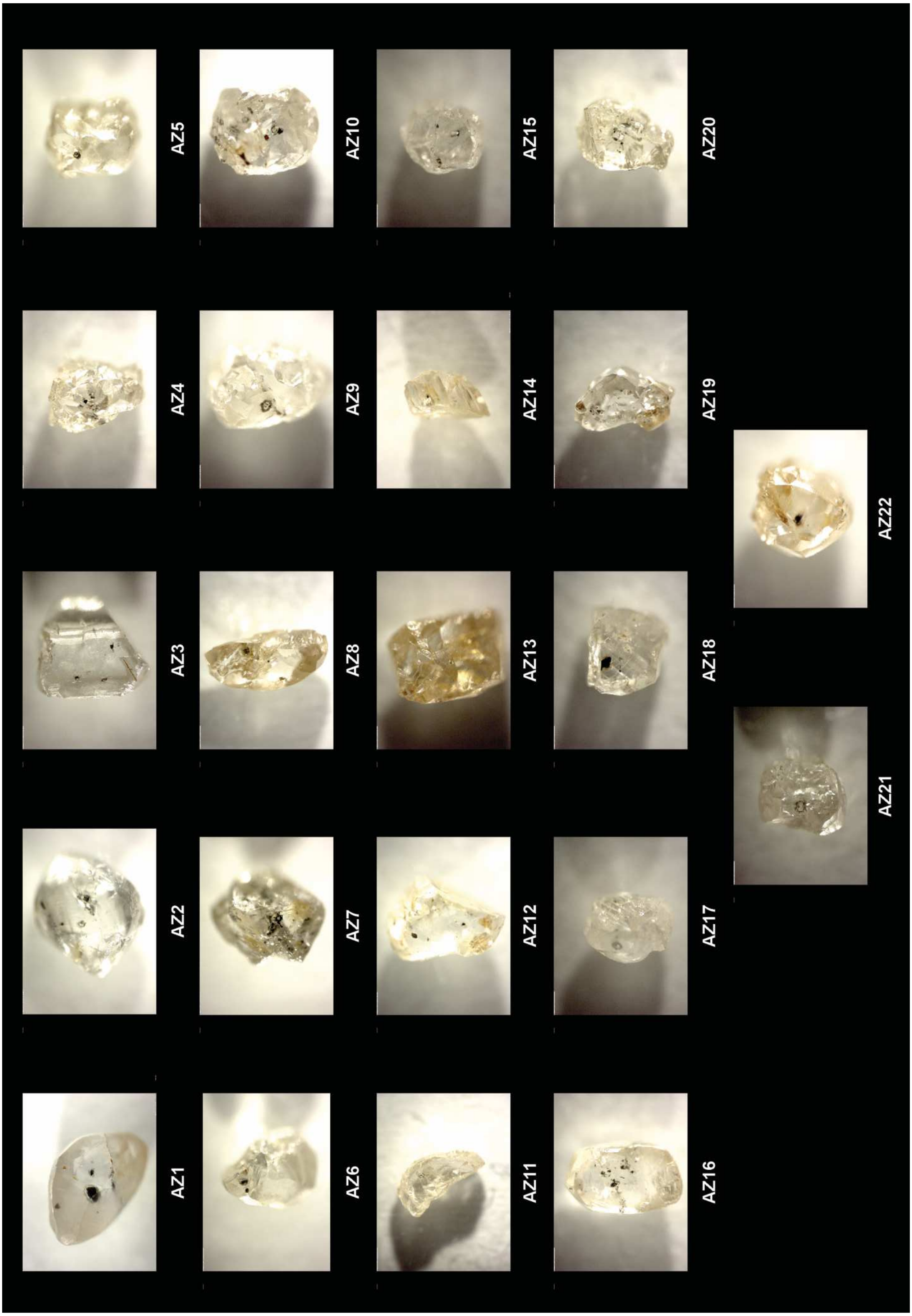

Figure 2.3: The second suite of diamonds, labelled AZ, studied in this work.

2.3 In-house facilities

2.3.1 Single-crystal X-ray diffraction (Department of Geosciences, University of Padova)

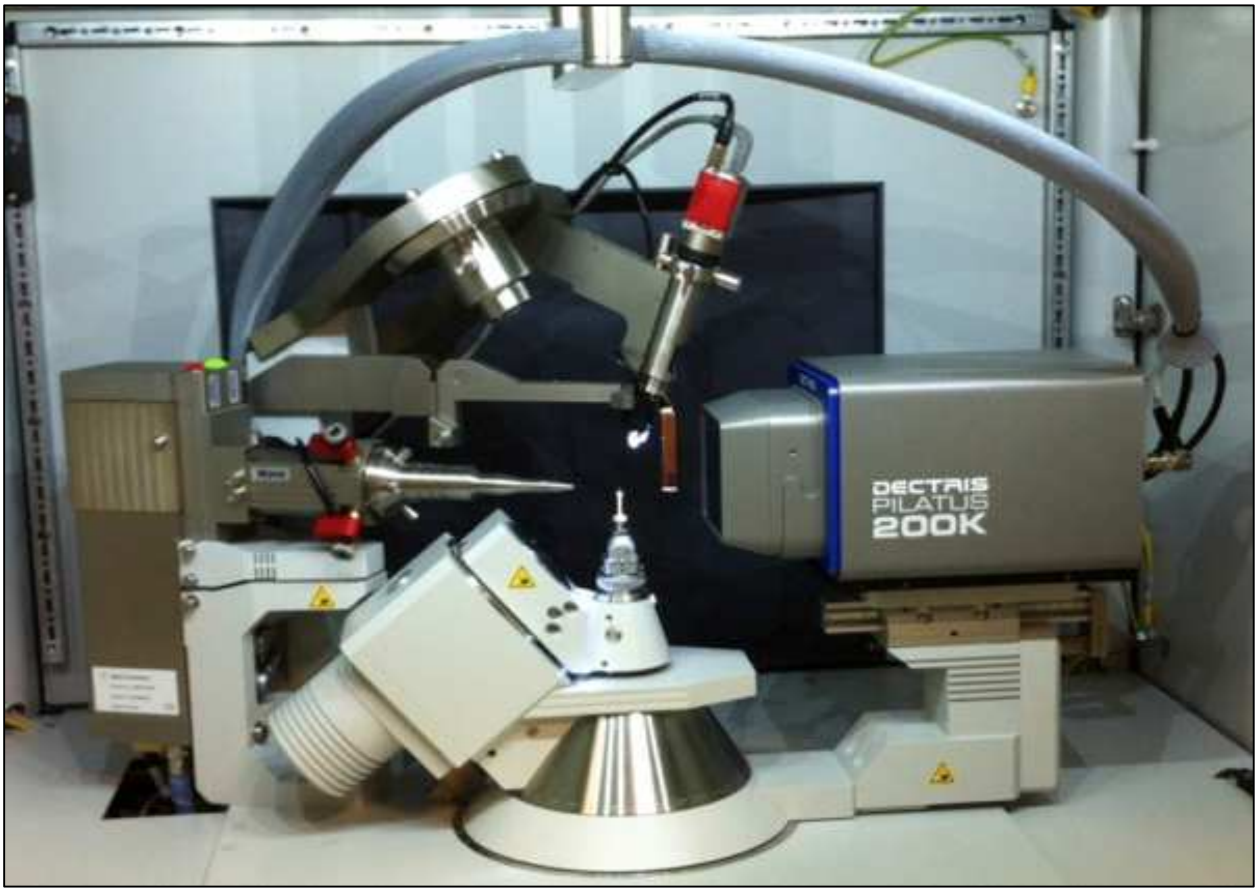

Figure 2.4: Rigaku Oxford Diffraction SuperNova diffractometer equipped with a Pilatus 200 K detector by Dectris (Department of Geosciences, University of Padova).

Single-crystal X-ray diffraction was performed on samples SL_FFM_08 and AZ1 to AZ22 to obtain the inclusions cell parameters. From these it is possible to determine the residual pressure retained by the inclusions, which in turn is necessary for the “elastic geobarometry” method to be applied (see § 2.6).

X-ray data were collected using a Rigaku Oxford Diffraction *SuperNova* single-crystal diffractometer, equipped with a Dectris *Pilatus* 200 K area detector and with a *Mova* X-ray microsource (Figure 2.4). A monochromatized Mo*K*a radiation ($\lambda = 0.71073$ Å), working at 50 kV and 0.8 mA, was used to minimize the absorption effects due to the large size of the host diamond. The sample-to-detector distance was 68 mm. Data reduction was performed using the CrysAlisPro software (Rigaku Oxford Diffraction) using frame scaling based on maximizing the agreement between intensities of symmetry-equivalent reflections.

2.3.2 Micro-Raman spectroscopy (Department of Geosciences, University of Padova)

Figure 2.5: Thermo Scientific^{TM} DXR Raman Microscope (Department of Geosciences, University of Padova).

Raman spectroscopy provides direct insight into the vibrational behaviour of ions or groups of ions bonded together, allowing a quick identification of phases, even if they are still contained within their diamond hosts. Raman spectra were collected on samples SL_FFM_01 to SL_FFM_16.

Unless otherwise specified, Raman measurements were carried out with a Thermo Scientific^{TM} DXR Raman Microscope using a 532 nm laser (Figure 2.5). The analyses were performed using a 50× objective with ~2.5 cm^{-1} spectral resolution and 1.1 μm spatial resolution at 10 mW of power. Spectra were recorded in the frequency range extending from 100 to 3500 cm^{-1}. To maximize the signal-to-noise ratio, each spectrum was collected four times using an exposure time of 30 s, and then merged together at the end of the acquisition. Spectral fitting was carried out using the Thermo Scientific^{TM} OMNIC^{TM} Spectra Software. The instrument was calibrated by using the calibration tool provided by Thermo Scientific^{TM}.

2.4 External facilities

2.4.1 Laser-heating diamond-anvil cell (School of Earth Sciences, University of Bristol)

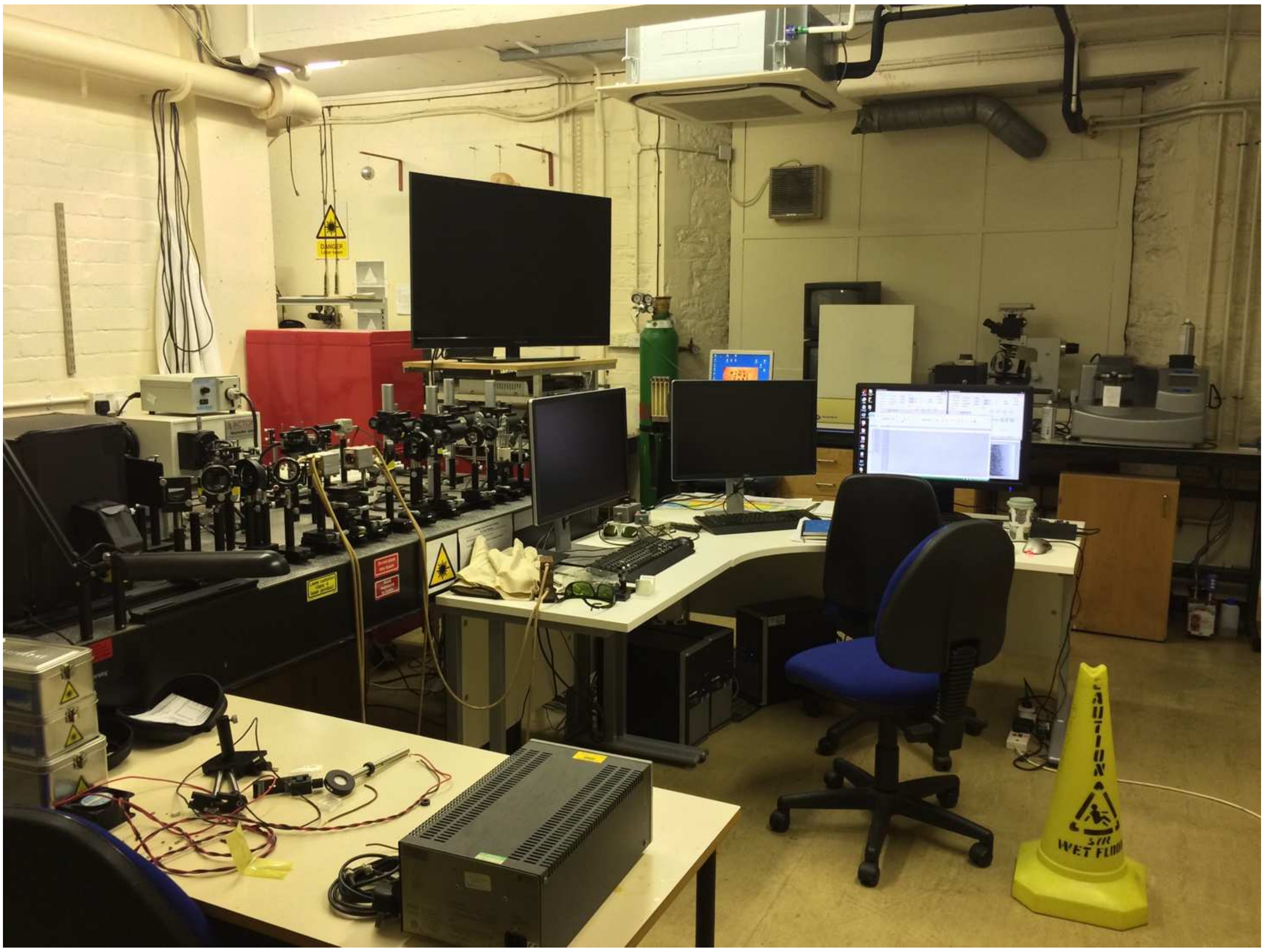

Figure 2.6: Double-sided laser-heating setup (School of Earth Sciences, University of Bristol).

Laser-heating diamond-anvil cell experiments were carried out on synthetic Ti-free jeffbenite to determine its stability field.

Double-sided laser heating (Figure 2.6), where 100 W fiber lasers produced heated spots that were 20-30 µm in diameter, was performed in symmetric diamond-anvil cells with culet sizes of 250 µm. Re gaskets were pre-indented to a thickness of ~50 µm. In the first set of experiments the glass sample discs were loaded in between SiO_2 insulators into 90 µm diameter laser-drilled sample chambers. In a second set of experiment, the powdered-glass starting material (mixed with 10 wt% Pt black as a laser absorber) was loaded into four 30 µm chambers laser-drilled in the indentation; no insulating material was used. In both cases the pressure was measured from the Raman shift of the singlet peak of the diamond culet.

2.4.2 High-pressure micro-Raman spectroscopy (Department of Sciences, University of Roma Tre)

Figure 2.7: Horiba LabRam HR micro-Raman spectrometer (Department of Sciences, University of Roma Tre).

High-pressure Raman investigations were carried out on a synthetic $CaSiO_3$-walstromite crystal to analyse its behaviour with increasing pressure. Thus, we obtained a calibration system to determine the residual pressure of a $CaSiO_3$-walstromite inclusion without breaking the diamond.

The Raman spectra were collected with a Horiba LabRam HR micro-Raman spectrometer (Figure 2.7) equipped with a green solid state laser (532 nm) focused through a 20× LWD objective. The spatial resolution of the sample surface was ~1 μm and the spectral resolution was 0.3 cm^{-1}. For the ruby, optical filters were employed in order to achieve ~1 mW at the sample surface; the Raman system was set with 1800 T grating, exposure time 1 s (3 times), confocal hole of 300 μm and slit of 200 μm. For the $CaSiO_3$-walstromite, optical filters were employed in order to achieve ~50 mW at the sample surface; the Raman system was set with 1800 T grating, exposure time 60 s (3 times), confocal hole of 100 μm and slit of 100 μm. For the high-pressure measurements a ETH DAC with 600 μm size culets was loaded with the crystal of $CaSiO_3$-walstromite, a piece of ruby as internal pressure standard and a 4:1 mixture of methanol:ethanol as pressure-transmitting medium. The calibration was done using the main Raman line (520.5 cm^{-1}) of a silicon standard.

2.4.3 Field Emission Gun – Scanning Electron Microscopy (Department of Physics and Astronomy, University of Padova)

Figure 2.8: Zeiss SIGMA HD Field Emission Gun-Scanning Electron Microscope (Department of Physics and Astronomy, University of Padova).

Two ferropericlase inclusions, extracted from diamond AZ1, were polished in a three-steps process and then carbon coated to be suitable for scanning electron microscopy and energy dispersive X-ray analyses.

Field Emission Gun–Scanning Electron Microscopy measurements were carried out using a *Zeiss* SIGMA HD FEG-SEM microscope (Figure 2.8) operating at 20 kV, with a spot-size of ~1 nm. Imaging was performed using an InLens secondary electron detector. Compositional analysis was performed using an energy dispersive X-ray spectrometer (EDX by Oxford Instruments). The spatial resolution in microanalysis was of ~1 μm.

2.5 Synchrotron facilities

2.5.1 Synchrotron X-ray Tomographic Microscopy (Swiss Light Source, TOmographic Microscopy and Coherent rAdiology experimenTs beamline, Paul Scherrer Institute, Switzerland)

Figure 2.9: Swiss Light Source TOMCAT (Paul Scherrer Institute, Villigen, Switzerland).

Micro-tomography experiments were performed on samples AZ1 to AZ22 in order to (i) check for the presence of mineral inclusions, tentatively detected by optical examination, (ii) determine the position and crystal size of the inclusions with a spatial resolution of a few micrometres, and (iii) detect the presence of fractures.

Measurements were performed at 60 KeV in order to reduce the X-ray absorption effects from the diamonds. The technique is based on the acquisition of a very large number of X-ray radiographs from different angular positions around a vertical rotation axis, followed by the application of a mathematical algorithm for the reconstruction of cross-sectional slices. Such slices can be stacked together to obtain a digital 3-D model of the investigated object.

2.5.2 Synchrotron Mössbauer Source (Nuclear Resonance beamline ID18, European Synchrotron Radiation Facility, Grenoble, France)

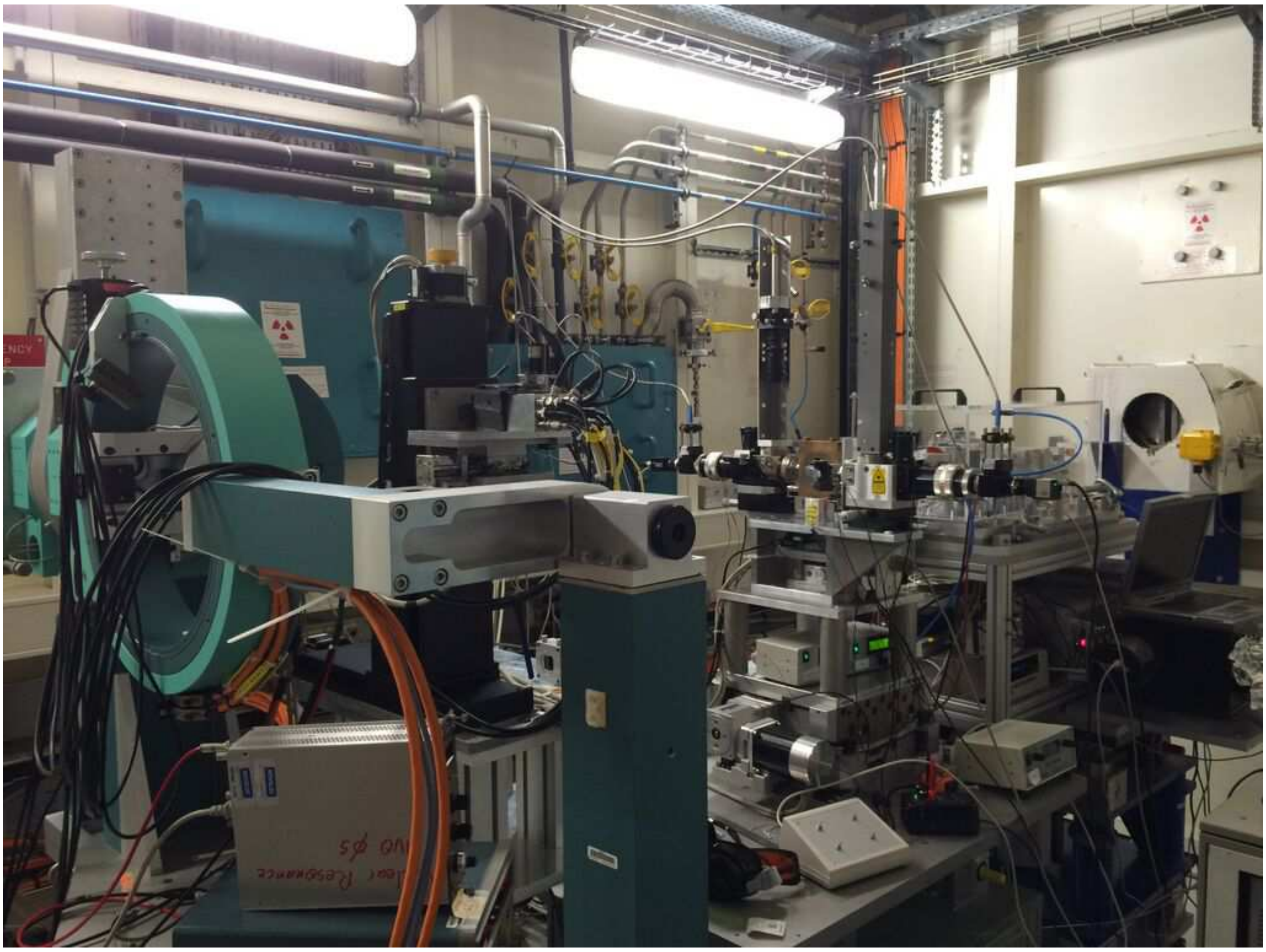

Figure 2.10: Synchrotron Mössbauer Source (European Synchrotron Radiation Facility, Grenoble, France).

Mössbauer spectroscopy provides information about the electronic, magnetic, and structural properties of specific elements within a material. Synchrotron Mössbauer Source analyses were carried out on 5 single-crystal inclusions of ferropericlase still kept inside 5 different diamonds (AZ1, AZ2, AZ7, AZ12 and AZ15), with the goal to determine in situ the $Fe^{3+}/\sum Fe$ ratios.

The narrow (~6 neV) energy component of X-rays at the Mössbauer energy of 14.4 keV was extracted from a wide spectrum of synchrotron radiation using a $^{57}FeBO_3$ single-crystal monochromator and focused to a beam width of size of 10×15 μm^2 using Kirkpatrick-Baez mirrors. Each SMS spectrum took approximately 2 h to collect. The velocity scales of all Mössbauer spectra were calibrated relative to 25 mm thick α-Fe foil, and all spectra were fitted using the software package MossA.

2.5.3 Synchrotron powder X-ray diffraction (Beamline I15, Diamond Light Source, Rutherford Appleton Laboratory, United Kingdom)

Figure 2.11: Synchrotron X-ray powder diffractometer (Diamond Light Source, Rutherford Appleton Laboratory, United Kingdom).

The pressure-temperature quenched run products obtained from laser-heating diamond-anvil cell experiments were analysed by synchrotron powder X-ray diffraction (Figure 2.11).

The monochromatic X-ray beam had a diameter of ~6 μm and a wavelength of 0.4133 Å. The acquisition time was typically 10 s and the sample to detector distance was calibrated using a CeO_2 standard. Diffraction patterns were preliminarily integrated into 1-D spectra using the program Dioptas (Prescher and Prakapenka, 2015) and then fitted and indexed with the software HighScore Plus (PANalytical).

2.6 Elastic Geobarometry

Diamonds are, as mentioned earlier, the only direct samples we have from the deep Earth. Up to now the principal method to determine the depth of diamond formation (and their formation temperature also) has been through the partitioning, mostly of Fe and Mg, between coexisting mineral inclusions within the diamonds (Stachel and Harris, 2008).

Apart from some early work (see below), a new approach in the last decade to evaluate the depth of diamond formation has been through what is called the "elastic method". In this method the formation conditions of a diamond-inclusion pair can be determined by knowing the residual pressure of an inclusion trapped within the diamond, as measured at ambient conditions, and the equations of state of the mineral inclusion and the diamond host (Angel et al., 2014a,b; Angel et al., 2015a,b). The two advantages of the "elastic method" are that can be applied to any diamond-inclusion pair, provided that the equation of state of both phases are known and reliable, and the method is a non-destructive alternative to chemical geobarometry. The method however does rely upon several assumptions: (i) for the calculations, the inclusion is regarded as being spherical (Eshelby, 1957, 1959; Mazzucchelli et al., 2016), (ii) both the host and inclusion are elastically isotropic and homogeneous (Angel et al., 2014b), (iii) at the moment of formation the inclusion perfectly fits in the diamond and (iv) any subsequent deformation of both the host or the inclusion is elastic, there being no plastic or brittle deformation.

The basic concept behind this approach is that at the time of entrapment the inclusion and its cavity in the host would have had the same P, T and V (Howell et al., 2010; 2012). Once encapsulated the contrasting thermoelastic behaviour of diamond and inclusion means that the inclusion would expand at a great rate relative to that of the hole in the diamond during ascend, regardless of the pressure-temperature-time path taken during the exhumation. As a consequence, the inclusion is placed under an increased pressure by the surrounding diamond and, in consequence, shows a pressure greater than the ambient pressure. This so-called P_{inc} can be determined starting from measurements performed with different techniques such as single-crystal X-ray diffraction (Harris et al., 1970; Nestola et al., 2011), micro-Raman spectroscopy (Izraeli et al., 1999; Nasdala et al., 2003; Barron et al., 2008; Cayzer et al., 2008) and strain birefringence analysis (Howell et al., 2010).

2.6.1 The concept of an isomeke

When a diamond-inclusion pair is studied, both are at ambient temperature (T_{room}), but only diamond is at ambient pressure, the inclusion usually being under a uniform small pressure called P_{inc} (see above). If we recompress the system, a point will be reached when the diamond hole and the inclusion become equal. This point represents the pressure under which, at ambient temperature, the inclusion fits perfectly with its cavity and is one of the points that constitute a curve called an isomeke.

The isomeke is defined as a line in P-T space that represents conditions under which, in this case, diamond hole and inclusion phase have the same real volumes. It therefore represents the possible entrapment pressure P_{e} at a particular temperature. At ambient temperature (T_{room}) the corresponding pressure of the isomeke line is called P_{foot} (see Figure 2.12). This pressure is determined solely by both the final inclusion pressure at ambient conditions (P_{inc}) and the isothermal equation of state of the diamond and the inclusion. However, both P_{foot} and T_{room} are not realistic parameters because (*i*) diamonds do not grow at 297 K in nature (which is part of the definition of P_{foot}) and (*ii*) P_{foot} lies, for most inclusions, outside the diamond stability field.

For these reasons, the path of the isomeke at different pressure and temperature conditions need to be calculated. Being defined as the line along which the volumes of the two phases remain equal, the isomeke's slope is given by $\left(\frac{\partial P}{\partial T}\right)_{isomeke} = \frac{\Delta\alpha}{\Delta\beta}$, where Δa is the difference between the volume thermal expansion coefficients of the diamond and the inclusion and $\Delta\beta$ is the difference in their volume compressibilities. The path of the isomeke in P-T space can therefore be calculated away from the point at P_{foot}, T_{room}, by using the equation of state parameters of the two phases. If we assume the absence of plastic relaxation, which could decrease the pressure of the inclusion, and adopt accurate and precise equation of state parameters, the calculated isomeke line will pass into the stability field of diamond, where it will then represent the possible *P-T* conditions for the growth of the diamond (Figure 2.12).

2.6.2 The role of elastic relaxation

When one mineral is included inside another of very differing properties, in this case a relatively stiff diamond and a more pliant inclusion, the likelihood is that there is a difference in radial stress at the host/inclusion wall that will force the wall outwards. This expansion leads to compression of the host and a relaxation of the initial pressure inside the inclusion. The resulting expansion of the inclusion can continue until the radial stress in the inclusion matches that in the host adjacent to the inclusion (Angel et al., 2014b).

The final observed inclusion pressure is therefore comprised of two parts: $P_{inc} = P_i + \Delta P_{relax}$. Since the initial pressure P_i can be calculated from the equation of state of the two phases, the problem of estimating entrapment conditions from observed inclusion pressures lies in the calculation of the change in pressure upon relaxation. Previous estimates of this relaxation have relied on the assumption of linear elasticity theory, but more recently, Angel et al. (2014b) proposed a new formulation of the problem that avoids this assumption and allows the calculation of ΔP_{relax} only from the volume change and the equation of state of the inclusion.

In the present Thesis, this procedure is implemented through the EosFit7c package (Angel et al., 2014a; 2017), which determines the entrapment pressure and temperature conditions of any diamond-inclusion pair studied.

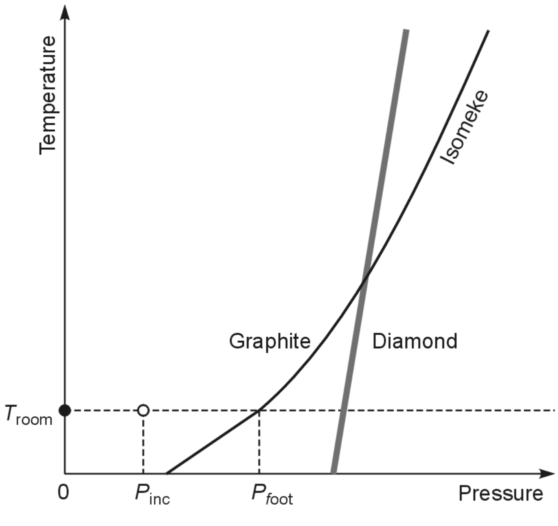

Figure 2.12 The concept of isomeke. At ambient conditions the inclusion is under a pressure P_{inc}, even though the host is subject to ambient pressure (essentially $P = 0$). Isothermal compression of the host-inclusion pair leads to them having the same volumes at P_{foot}, which lies on the isomeke. The isomeke is calculated from the EoS parameters of the two phases, and represents the line of possible entrapment conditions for this specific inclusion in its diamond host. At higher temperatures the isomeke passes in to the diamond stability field and represents possible P, T conditions for entrapment of the inclusion by the diamond host (from Angel et al., 2015a).

3 Depth of formation of $CaSiO_3$-walstromite included in super-deep diamonds

C. Anzolini[1], R. J. Angel[1], M. Merlini[2], M. Derzsi[1,3], K. Tokár[4], S. Milani[1], M. Y. Krebs[5], F. E. Brenker[6], F. Nestola[1] and J. W. Harris[7]

[1]Department of Geosciences, University of Padova, Via G. Gradenigo 6, 35131 Padova, Italy

[2]Department of Earth Sciences, University of Milano, Via Botticelli 23, 20133 Milano, Italy

[3]Centre for New Technologies, University of Warsaw, Żwirki i Wigury 93, 02089 Warsaw, Poland

[4]Institute of Physics, CCMS, Slovak Academy of Sciences, Dúbravská cesta 9, 84511 Bratislava, Slovakia

[5]Earth and Atmospheric Sciences, University of Alberta, AB T6G2E3 Edmonton, Canada

[6]Geoscience Institute – Mineralogy, Goethe University, Altenhöferallee 1, 60438 Frankfurt am Main, Germany

[7]School of Geographical and Earth Sciences, University of Glasgow, G12 8QQ Glasgow, United Kingdom

The paper has been published in *Lithos* Vol. 265, pp. 138–147, 2016.

The layout has been revised.

Abstract

"Super-deep" diamonds are thought to crystallize between 300 and 800 km depth because some of the inclusions trapped within them are considered to be the products of retrograde transformation from lower mantle or transition zone precursors. In particular, single inclusion $CaSiO_3$-walstromite is believed to derive from $CaSiO_3$-perovskite, although its real depth of origin has never been proven. Our aim is therefore to determine for the first time the pressure of formation of the diamond-$CaSiO_3$-walstromite pair by "single-inclusion elastic barometry" and to determine whether $CaSiO_3$-walstromite derives from $CaSiO_3$-perovskite or not.

We investigated several single phases and assemblages of Ca-silicate inclusions still trapped in a diamond coming from Juina (Brazil) by in-situ analyses (single-crystal X-ray diffraction and micro-Raman spectroscopy) and we obtained a minimum entrapment pressure of ~5.7 GPa (~180 km) at 1500 K. However, the observed coexistence of $CaSiO_3$-walstromite, larnite (β-Ca_2SiO_4) and $CaSi_2O_5$-titanite in one multiphase inclusion within the same diamond indicates that the sample investigated is sub-lithospheric with entrapment pressure between ~9.5 and ~11.5 GPa at 1500 K, based on experimentally-determined phase equilibria. In addition, thermodynamic calculations suggested that, within a diamond, single inclusions of $CaSiO_3$-walstromite cannot derive from $CaSiO_3$-perovskite, unless the diamond around the inclusion expands by ~30% in volume.

Keywords

Diamond; inclusion; sub-lithospheric mantle; Juina; $CaSiO_3$-walstromite; $CaSiO_3$-perovskite

3.1 Introduction

Diamonds are the unique way to trap and convey fragments of deep material from the interior to the surface of our planet. Over the last thirty years, such material has enabled great strides to be made in understanding the Earth's deeper mantle, considerably helped by advances in technology and instrumentation. Nevertheless, it is only in the last fifteen years that a fuller range of mineral inclusion parageneses, thought to derive from the sub-lithospheric mantle, have been studied in some detail and mostly in diamonds from São Luiz (Juina, Brazil) (see Kaminsky, 2012 and references therein). These so-called "super-deep" diamonds represent only 6% of the whole diamond population (Stachel and Harris, 2008), but because of extensive studies these few localities are clearly overrepresented in any database and the percentage above is probably much lower (see Stachel and Harris, 2008). Such super-deep diamonds are believed to originate at depths between 300 and 800 km (Harte, 2010), and major inclusion phases within them are ferropericlase [(Fe,Mg)O)], enstatite ($MgSiO_3$), walstromite-structured $CaSiO_3$ (hereafter $CaSiO_3$-walstromite) and jeffbenite [$(Mg,Fe)_3Al_2Si_3O_{12}$], a tetragonal garnet formally known by the acronym TAPP, see Nestola et al. (2016).

$CaSiO_3$-walstromite is considered the most important Ca-bearing phase in super-deep diamonds (Pearson et al., 2014) and, over the years, the majority of scientists have speculated that it represents the retrograde transformation from $CaSiO_3$-perovskite (Harte et al., 1999; Joswig et al., 1999; Stachel et al., 2000; Hayman et al., 2005), a phase stable only below ~600 km depth (Kaminsky, 2012), and a speculation heightened by its coexistence with ferropericlase within some diamonds. This observation hints at a transition zone or lower-mantle origin for these diamonds, but the lack of concrete evidence in the form of a diffraction patterns or Raman spectra of surviving $CaSiO_3$-perovskite included in diamonds casts doubt as to whether it really is the ancestor of $CaSiO_3$-walstromite. Previous workers, (Walter et al., 2008; Bulanova et al., 2010; Armstrong et al., 2012; Thomson et al., 2014; Thomson et al., this issue), have also suggested the possibility that Ca-silicate inclusions in diamonds are not lower-mantle phases, on the basis of a near absence of $MgSiO_3$ component. For example, Walter et al. (2008) and Armstrong et al. (2012) experimentally demonstrated that subsolidus $CaSiO_3$-perovskite minerals at pressures above 20 GPa that are in equilibrium with a magnesium-rich phase always have a detectable magnesium component. The near absence of a magnesium component (<1 mol%) effectively precludes equilibration with $MgSiO_3$-perovskite and accordingly indicates a shallower paragenesis. For composite

$CaSiO_3$ + $CaTiSiO_3$ inclusions, these authors argue that unmixing originated at > ~10 GPa. In consequence, these authors consider that the absence of a serious Mg component, coupled with the characteristic high trace element signature of the Ca-silicate family of inclusions, likely indicates a low-degree, carbonatitic melt in the transition zone for their genesis. Another possible explanation is that $CaSiO_3$ inclusions represent material trapped at shallower depths in a region of diamond growth where the local chemistry is $CaSiO_3$-rich and not the bulk Earth composition (Brenker et al., 2005). A more recent study by Zedgenizov et al. (2014), suggests that Ca-silicate inclusions from São Luiz diamonds form at upper mantle or transition zone pressures via reaction of carbonatitic melts with peridotite.

Our aims are therefore to obtain for the first time the pressure of formation of $CaSiO_3$-walstromite and to determine by non-destructive methods whether $CaSiO_3$-walstromite could derive from $CaSiO_3$-perovskite or not. A non-destructive in-situ investigation of an inclusion in diamond is useful and important because: (a) some mineral inclusions under pressure, once extracted, would invert to lower-pressure phases: in particular synthesized $CaSiO_3$-perovskite is known to invert to glass after pressure release (Kanzaki et al., 1991); (b) the internal pressure on the inclusion can provide information about the formation pressure of the diamond (Izraeli et al., 1999; Sobolev et al., 2000; Nestola et al., 2011); (c) the morphology and orientation relationships of the inclusion with the host diamond can provide indications about its protogenetic vs. syngenetic and/or epigenetic nature (Nestola et al., 2014); and (d) preservation of the diamond surface growth features can provide indications of oxidation processes (Fedortchouk et al., 2011).

For the present paper we have probed 45 composite inclusions (numbered #1 to #45) in a single large (the longest dimension is ~3.5 mm) diamond (SL_FFM_08; Figure 3.1) with a combination of single-crystal X-ray diffraction (SCXRD) and micro-Raman spectroscopy, in order to determine the pressure at which they were trapped within this diamond. In addition, synchrotron X-ray diffraction data were collected from synthetic $CaSiO_3$-walstromite to obtain a new and updated equation of state (previously determined in 1997), to provide thermoelastic parameters for estimating the entrapment pressure. In support of the experimental high-pressure and high-temperature in-situ diffraction, we also performed Density Functional Theory (DFT) calculations. Finally, thermodynamic calculations were performed to verify if the $CaSiO_3$-perovskite – $CaSiO_3$-walstromite transformation could occur within diamonds.

Figure 3.1: Expanded view of the inclusion-bearing diamond studied in this work.

3.2 Material and methods

3.2.1 Samples

The diamond investigated in this study was recovered in the mid to late 1980's from alluvial deposits in the Juina area of south-western Brazil, from the São Luiz river (Harte et al., 1999; Kaminsky et al., 2001; Hayman et al., 2005).

The $CaSiO_3$-walstromite powder used for high-temperature synchrotron X-ray diffraction measurements came from the same experimental batch as that referred to in

Gasparik et al. (1994), synthesized at 2000 K and 9 GPa. The single $CaSiO_3$-walstromite crystal used for high-pressure measurements was extracted from the same material.

3.2.2 Synchrotron X-ray diffraction

High-pressure single-crystal X-ray diffraction was performed at the ID09A beamline (European Synchrotron Radiation Facility, Grenoble, France). We used the standard beamline setup (Merlini and Hanfland, 2013) with a monochromatic parallel beam of 0.4139 Å and approximately 30×30 µm^2 section on the sample. The synthetic $CaSiO_3$-walstromite fragment measured 40×40×20 µm^3. It was placed in a membrane type diamond-anvil cell, with a stainless-steel gasket and loaded with He gas as pressure medium. Pressure was determined from the shift of the lines of ruby (Mao et al., 1986). The diffraction patterns were recorded as step scans with a Mar555 flat panel detector, and the raw data were processed with the CrysAlis software (Rigaku Oxford Diffraction). Single-crystal structure refinements were performed with the Jana2006 software (Petříček et al., 2014) and the crystal structure data will be published separately. Structure and unit-cell parameters were determined at 8 different pressures up to about 8 GPa (Table 3.1).

Table 3.1: Lattice parameters and volume of $CaSiO_3$-walstromite as a function of pressure.

P (GPa)	a (Å)	b (Å)	c (Å)	α (°)	β (°)	γ (°)	V (Å^3)
0.99	6.661(1)	9.240(7)	6.616(1)	83.62(3)	76.32(1)	69.91(4)	371.4(3)
1.54	6.645(2)	9.203(6)	6.597(1)	83.71(3)	76.41(2)	70.08(4)	368.5(3)
2.4	6.619(2)	9.178(8)	6.572(1)	83.56(3)	76.51(2)	70.13(4)	364.9(4)
3.86	6.582(1)	9.141(9)	6.534 (1)	83.27(3)	76.63(2)	70.20(4)	359.5(4)
5.13	6.553(2)	9.100(9)	6.505(1)	83.08(4)	76.71(2)	70.21(5)	354.8(4)
6.12	6.532(2)	9.053(9)	6.479(2)	83.03(4)	76.82(2)	70.25(5)	350.7(4)
7.04	6.510(2)	9.037(9)	6.460 (1)	82.81(4)	76.85(2)	70.32(5)	347.9(4)
8.04	6.490(2)	9.015(9)	6.438(1)	82.76(4)	76.93(2)	70.36(5)	345.0(4)

High-temperature powder diffraction was performed at the "Materials Characterization by X-ray diffraction" beamline at the ELETTRA synchrotron facility (Trieste, Italy), using the high-resolution powder diffraction setup (Rebuffi et al., 2014). The sample was contained in a quartz capillary and diffraction patterns were collected with a monochromatic beam (0.688427 Å) and point detector in the 2ϑ angular interval 4-40°. In order to extract lattice parameters and monitor the high-temperature structural evolution, the diffraction patterns were fitted with the Rietveld method in the GSAS+EXPGUI software (Larson and Von Dreele, 1984; Toby, 2001). The unit-cell parameters were determined at 25 different temperatures up to about 1120 K (Table 3.2).

Table 3.2: Lattice parameters and volume of $CaSiO_3$-walstromite as a function of temperature.

T (K)	a (Å)	b (Å)	c (Å)	α (°)	β (°)	γ (°)	V (Å^3)
298	6.6915(2)	9.2927(3)	6.6518(2)	83.704(2)	76.165(2)	69.661(2)	376.42(2)
323	6.6926(2)	9.2962(3)	6.6532(2)	83.727(2)	76.175(2)	69.642(2)	376.68(2)
348	6.6945(2)	9.2992(3)	6.6545(2)	83.742(2)	76.188(2)	69.627(2)	376.97(2)
373	6.6955(2)	9.3028(3)	6.6550(2)	83.761(2)	76.197(2)	69.610(2)	377.18(2)
398	6.6966(2)	9.3064(3)	6.6559(2)	83.778(2)	76.210(2)	69.592(2)	377.42(2)
423	6.6972(2)	9.3095(3)	6.6577(2)	83.802(2)	76.222(2)	69.585(2)	377.69(2)
448	6.6985(2)	9.3126(3)	6.6579(2)	83.820(2)	76.233(2)	69.563(2)	377.87(2)
473	6.7007(2)	9.3166(3)	6.6587(2)	83.838(2)	76.245(2)	69.540(2)	378.16(2)
498	6.7016(2)	9.3205(3)	6.6603(2)	83.859(2)	76.257(2)	69.530(2)	378.46(2)
523	6.7034(2)	9.3247(3)	6.6615(2)	83.880(2)	76.267(2)	69.512(2)	378.77(2)
548	6.7048(2)	9.3290(4)	6.6629(3)	83.900(2)	76.279(2)	69.484(3)	379.06(3)
573	6.7060(2)	9.3320(3)	6.6636(2)	83.928(2)	76.294(2)	69.466(2)	379.28(2)
623	6.7095(2)	9.3403(3)	6.6663(2)	83.976(2)	76.320(2)	69.429(2)	379.93(2)
673	6.7109(3)	9.3462(4)	6.6677(3)	84.031(3)	76.355(2)	69.407(3)	380.34(3)
723	6.7148(2)	9.3546(4)	6.6715(3)	84.071(2)	76.374(2)	69.369(3)	381.06(3)
773	6.7182(2)	9.3625(3)	6.6745(2)	84.117(2)	76.398(2)	69.335(3)	381.70(3)
823	6.7215(3)	9.3703(4)	6.6771(3)	84.149(2)	76.411(2)	69.305(3)	382.31(3)
873	6.7240(2)	9.3790(3)	6.6810(3)	84.218(2)	76.453(2)	69.274(3)	383.03(3)
923	6.7269(2)	9.3860(3)	6.6839(2)	84.272(2)	76.481(2)	69.236(2)	383.60(2)
973	6.7296(2)	9.3928(3)	6.6877(2)	84.322(2)	76.507(2)	69.204(2)	384.22(3)
1023	6.7323(3)	9.4006(4)	6.6911(3)	84.382(2)	76.541(2)	69.172(2)	384.87(3)
1073	6.7341(3)	9.4079(3)	6.6941(3)	84.433(2)	76.572(2)	69.148(2)	385.44(3)
1123	6.7374(3)	9.4153(4)	6.6975(3)	84.486(3)	76.603(3)	69.123(3)	386.12(3)
987*	6.7298(2)	9.3959(3)	6.6881(2)	84.355(2)	76.526(2)	69.192(2)	384.39(2)
298*	6.6911(2)	9.2927(3)	6.6502(2)	83.714(2)	76.171(2)	69.659(2)	376.31(2)

*Decreasing temperature.

3.2.3 Density Functional Theory (DFT) calculations

Periodic DFT calculations were performed with the plane-wave VASP package (Kresse and Furthmüller, 1996a,b) within the GGA approximation (Perdew et al., 1996), with projector-augmented waves (Blöchl, 1994; Kresse and Joubert, 1999), and the PBEsol functional (Perdew et al., 2008). The unit cell of $CasiO_3$-walstromite was fully optimized with plane-wave cutoffs of 600 eV and a 4×3×4 k-mesh. The threshold for electronic and ionic convergence was set to 10-8 and 10-5 eV, respectively. A calculation at zero external pressure yielded a value of the optimized unit-cell volume (374.25 Å) in excellent agreement with the observed one (376.42 Å), the discrepancy being ~0.4%.

The value of the Voigt bulk modulus, which represents the stiffness of the material when subject to isotropic strain, was calculated by reducing the volume of the fully relaxed cell by 1%. Ionic positions within this reduced cell were optimized, and the stress tensor arising due to the volume reduction was calculated. The Voigt bulk modulus was then estimated from the formula $-K * (V_{red} - V_0)/V_0 = P$, where Vred stands here for reduced volume and P for mean stress averaged from the diagonal elements $P = (P_{xx} + P_{yy} + P_{zz})/3$ of the stress tensor of the uniformly reduced cell corrected for the residual stress of the unreduced cell, i.e. $P_{xx} = P_{xx}^{red} - P_{xx}^{0}$ (see Table 3.3).

Table 3.3: Diagonal elements of the stress matrix of $CaSiO_3$-walstromite calculated for the fully relaxed cell and the relaxed cell whose volume was reduced by 1%.

Cell	***V*** **($Å^3$)**	**P_{xx} (GPa)**	**P_{yy} (GPa)**	**P_{zz} (GPa)**	**$K_{Voigt,DFT}$ (GPa)**
Unreduced	374.25	-0.00055	-0.00075	0.00136	
Reduced	370.52	0.79610	0.91919	0.83837	85.4

3.2.4 In-situ X-ray diffraction of inclusions still trapped within the diamond

The SCXRD measurements were made in situ by mounting the diamond on a pin with wax. X-ray data were collected using a Rigaku Oxford Diffraction SuperNova goniometer, equipped with a Dectris Pilatus 200K area detector and with a Mova X-ray microsource. For the measurements, Mo$K\alpha$-radiation, operated at 50 kV and 0.8 mA, was used to minimize the absorption effects due to the large size of the host diamond. The sample to detector distance was 68 mm. Data reduction was performed using the CrysAlis software (Rigaku Oxford Diffraction) using frame scaling based on maximizing the agreement between intensities of symmetry-equivalent reflections (as described in Angel et al., 2016).

3.2.5 Micro-Raman Spectroscopy

Raman spectroscopy provides direct insight into the vibrational behaviour of ions or groups of ions bonded together, allowing a quick identification of phases, even if they are still contained within diamond hosts. Preliminary Raman analyses were carried out by means of a Renishaw RM-1000 micro-Raman spectrometer at the Geoscience Institute Frankfurt with a grating of 1800 grooves per mm in the optical path, and Si-based charge-coupled device detectors. Spectra were excited with a red He-Ne (633 nm) and a green YAG (532 nm) Laser. The wavenumber accuracy was ~0.5 cm^{-1} and the spectral resolution 0.8 cm^{-1}. The lateral and depth resolution was on the order of several to a few tens of micrometers depending on the actual sampling depth. Further Raman measurements were carried out with a Thermo Scientific™ DXR™ Raman Microscope using a 532 nm laser as excitation source at the Department of Geosciences, University of Padova. Reflected and transmitted light optics were used to select analysis locations. The analyses were performed using a 50× Long Working Distance objective with ~2.5 cm^{-1} spectral resolution and 1.1 μm spatial resolution at 10 mW of power. Spectra were recorded in the frequency range extending from 100 to 3500 cm^{-1}. To maximize the signal-to-noise ratio, each spectrum was collected four times using an exposure time of 30 s, and then merged together at the end of the acquisition. Spectral fitting was carried out using the Thermo Scientific™ OMNIC™ Spectra Software. Applying the Raman mapping technique (Nasdala et al., 2003), rectangular sample areas were analysed point-by-point. The map was obtained in confocal mode using a 25 μm pinhole to limit the unwanted signal from the surrounding diamond; each spectrum of the map was collected eight times using an exposure time of 60 s and spectra were obtained from a grid of points spaced 5 μm along X and 4 μm along Y. These measurements were carried out in situ without any sample preparation.

3.3 Results

3.3.1 Pressure-volume equation of state and thermal expansion of synthetic $CaSiO_3$-walstromite

The unit-cell volumes for $CaSiO_3$-walstromite at different pressures are reported in Table 3.1. The volume decreases smoothly with increasing pressure, as shown in Figure 3.2, up to 8.04 GPa. The P-V data were fitted using a 2nd order Birch-Murnaghan EoS (BM2-EoS, Birch, 1947), because an F_E-f_E plot of the data can be fitted by a horizontal line (Angel, 2000). The simultaneous refinement of the BM2-EoS coefficients using the program EoSFit7c (Angel et al., 2014a) yielded the values K_{0T} = 78.6(1.3) GPa with $K`_0$ fixed at 4.

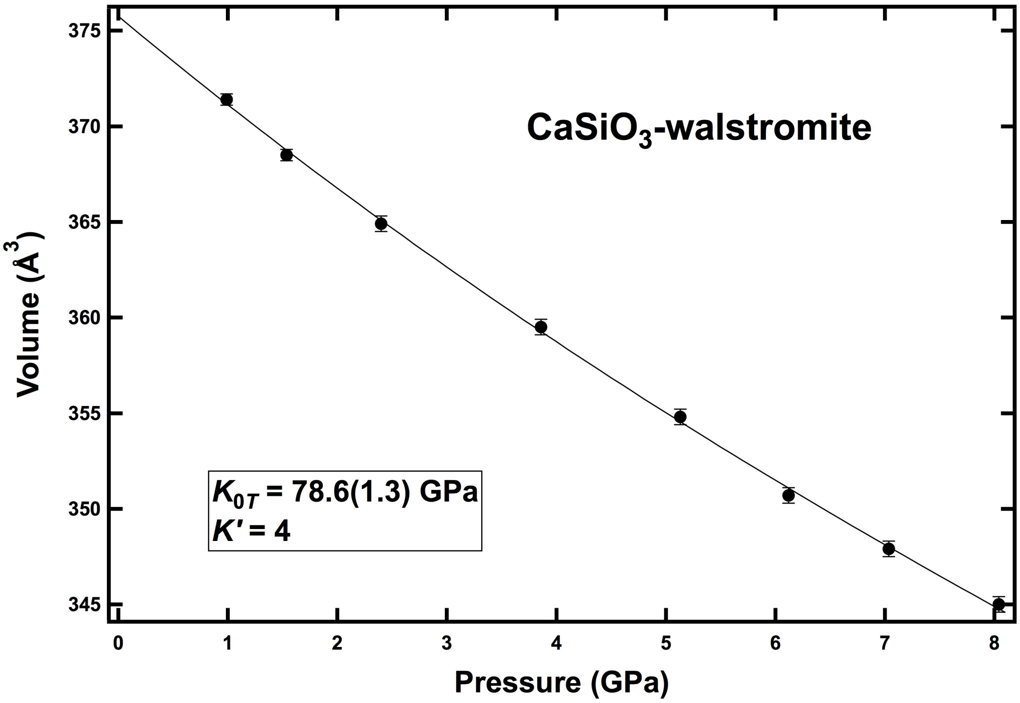

Figure 3.2: Pressure-volume behaviour of $CaSiO_3$-walstromite. The solid line is a 2nd order Birch-Murnaghan EoS fit to the data.

The unit-cell volumes for $CaSiO_3$-walstromite at different temperatures are reported in Table 3.2. The volume increases linearly with increasing temperature, as shown in Figure 3.3, up to 1123 K. The temperature-volume data were fitted using the software EoSFit7c (Angel et al., 2014a) to a thermal pressure EoS (Angel et al., 2014a) by adopting θ_E = 460 K (Holland and Powell, 2011). The thermal expansion coefficient obtained is α_0= 2.551(9) × 10^{-5} K^{-1} at 298 K.

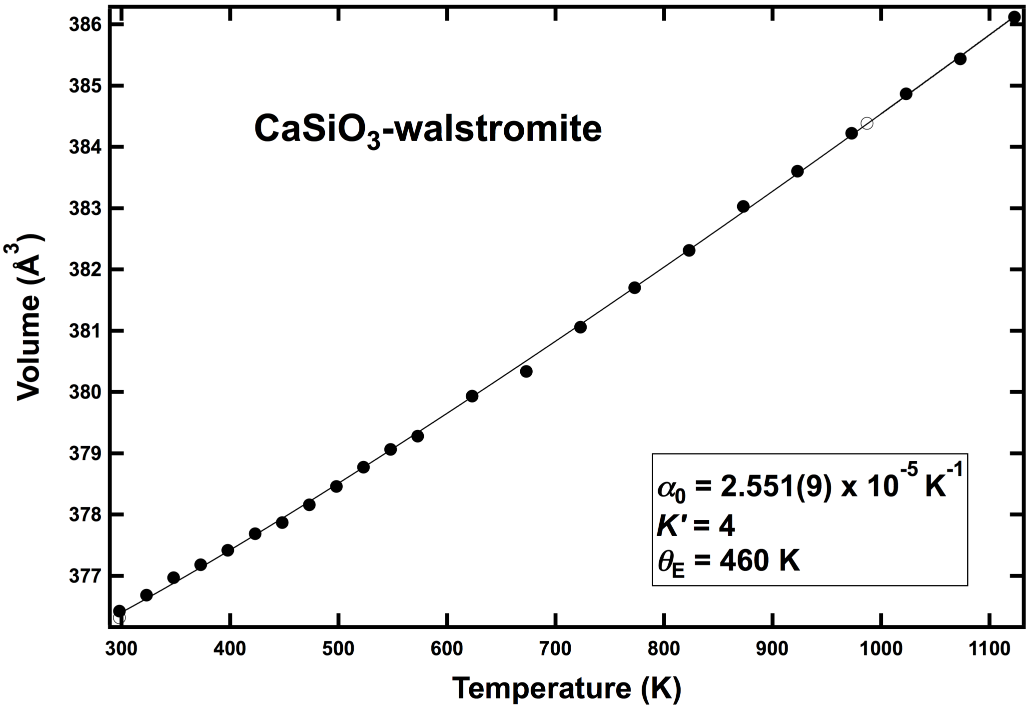

Figure 3.3: Temperature-volume behaviour of CaSiO$_3$-walstromite, where the solid dots represent data during heating, the open dots during cooling. The errors bars are within the symbols. The solid line is a thermal pressure EoS fit to the data.

CaSiO$_3$-walstromite is a triclinic mineral, characterized by three-membered rings of silicate tetrahedra constituting infinite parallel layers (Barkley et al., 2011) and, consequently, the directions of maximum and minimum compression under stress are not constrained to lie along the unit-cell axes (Nye, 1985). We therefore calculated the principal axes of compression of the structure from the changes in cell parameters measured at high pressure, using the software Win_Strain (www.rossangel.com): as expected, the stiffest principal axis lies in the (010) plane, because this plane is parallel to the layering, towards the $[2\ \bar{1}\ \bar{2}]$ direction; the softest axis is perpendicular to the layers, close to the $[1\ \bar{1}\ 2]$ direction; the intermediate axis is parallel to the $[\bar{2}\ \bar{1}\ 0]$ direction. The linear moduli of the principal strain axes were obtained by fitting them with a BM2-EoS and the room-pressure compressibilities are: $\beta_{[2\bar{1}\bar{2}]} = 1.70 \times 10^{-3}$ GPa^{-1}, $\beta_{[1\bar{1}2]} = 6.66 \times 10^{-3}$ GPa^{-1} and $\beta_{[2\bar{1}0]} = 4.55 \times 10^{-3}$ GPa^{-1}. These values mean that the direction perpendicular to the layers is ~3 times more compressible than directions parallel to the layers. This strain analysis provides a quantification of the compressional anisotropy of our phase, which in turn plays a key role in determining the appropriate bulk modulus to be used in this work to calculate the depth of entrapment of the diamond-$CaSiO_3$-walstromite pair (see the extensive explanation in the Discussion section).

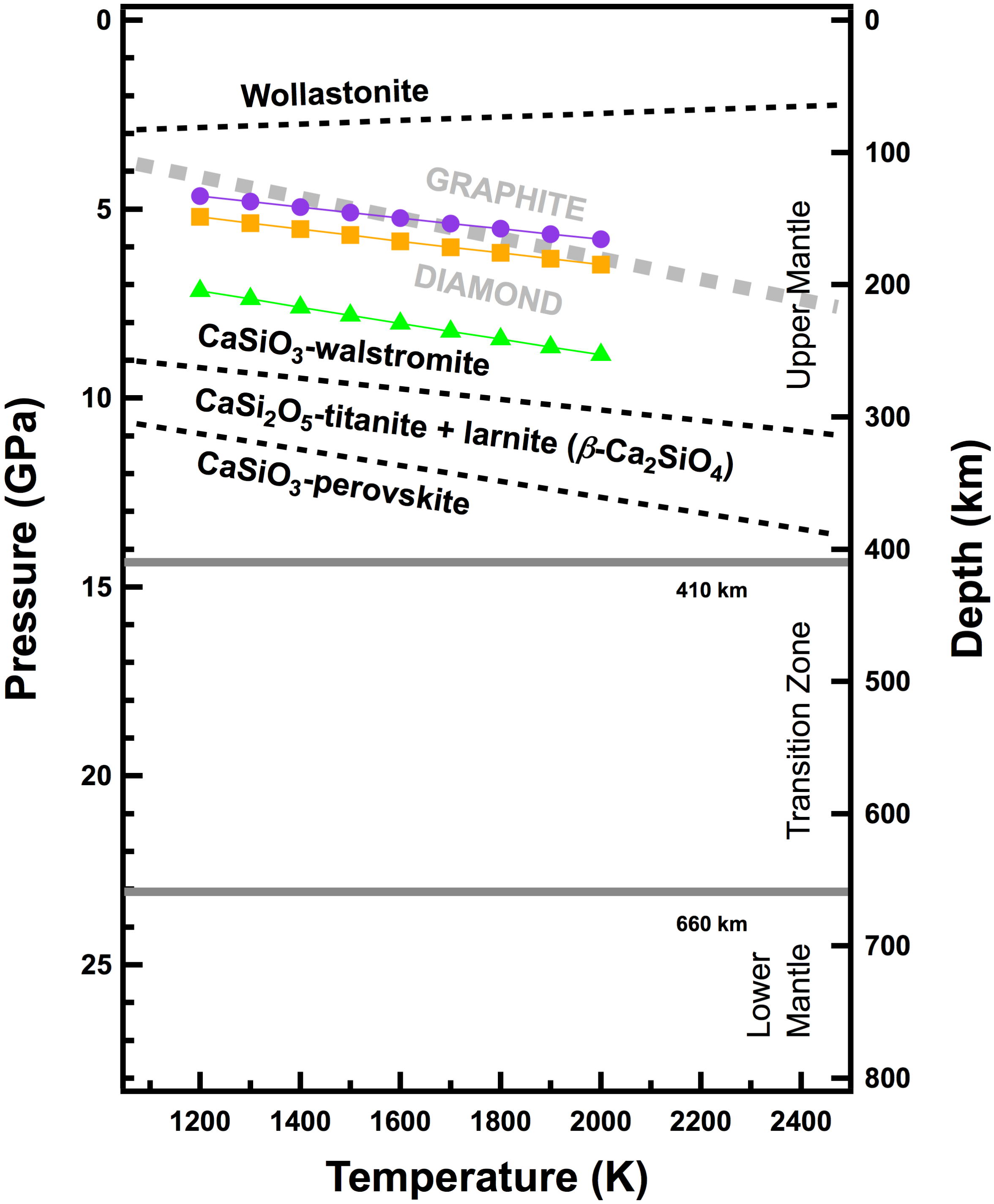

Figure 3.4: Phase diagram of the $CaSiO_3$ system, in which the phase boundaries are given as dotted lines (Gasparik et al., 1994; Essene, 1974). The graphite-diamond phase boundary is shown as a grey stippled line (Day, 2012). The 410 and 660 km discontinuities enclosing the transition zone are indicated by bold lines. Entrapment pressures are plotted for different values of $CaSiO_3$-walstromite bulk modulus: $K_{Reuss} = 78.6$ GPa with purple circles, $K_{Voigt,DFT} = 85.4$ GPa with orange squares and $K_{Voigt,MAX} = 107$ GPa with green triangles.

3.3.2 Inclusion phases

In-situ Raman microprobe analyses of diamond SL_FFM_08 showed that 30 out of the 45 inclusions that were investigated are single phases or assemblages of Ca-silicates, identified by comparison with spectra reported by Nasdala et al. (2003) and Brenker et al. (2005; 2007). The following single phases or assemblages were observed as inclusions:

$CaSiO_3$-walstromite (inclusions #1, 2, 6, 7, 8, 9, 12, 13, 14, 15, 17, 19, 20, 23, 24, 25, 26, 27, 29, 30, 33, 34, 36, 37, 38, 39);

$CaSiO_3$-walstromite + larnite (β-Ca_2SiO_4) (inclusions #10, 18, 21, 22);

$CaSiO_3$-walstromite + $CaSi_2O_5$-titanite (inclusions #40, 43);

$CaSiO_3$-walstromite + larnite (β-Ca_2SiO_4) + $CaSi_2O_5$-titanite (inclusion #11).

These are all stable phases in the $CaSiO_3$ phase diagram (Figure 3.4). At pressures above ~3 GPa $CaSiO_3$-walstromite structure becomes stable; above 10 GPa and 1773 K $CaSiO_3$-walstromite decomposes to larnite (β-Ca_2SiO_4) + $CaSi_2O_5$-titanite; this two-phase assemblage is stable from 10 to 12 GPa at 1773 K and then they recombine to form $CaSiO_3$-perovskite (Gasparik et al., 1994).

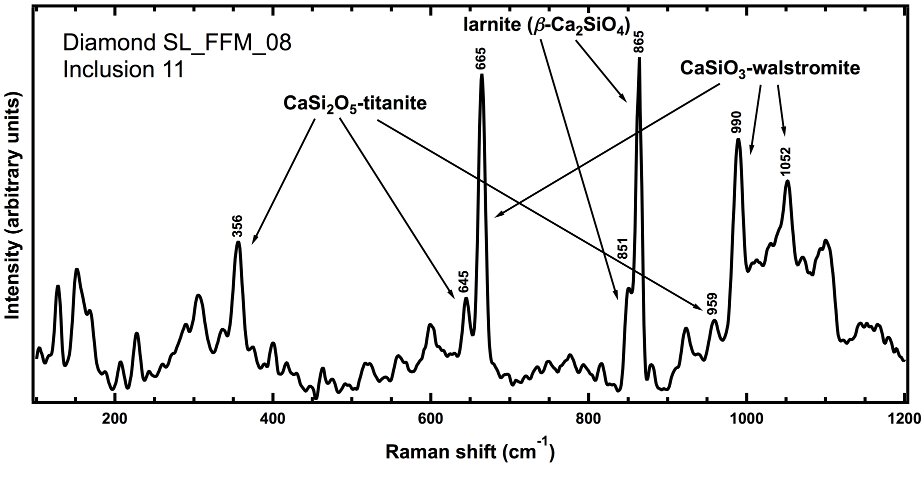

Figure 3.5: Raman spectrum of inclusion SL_FFM_08-#11, showing the coexistence of $CaSiO_3$-walstromite, larnite (β-Ca_2SiO_4) and $CaSi_2O_5$-titanite, which correspond to reference spectra reported by Nasdala et al. (2003) and Brenker et al. (2005; 2007).

Compared to room pressure spectra reported by Nasdala et al. (2003), we observed noticeable shifts in the Raman spectra of the Ca-silicates. For instance, the main Raman band of $CaSiO_3$-walstromite (~656 cm^{-1} at ambient pressure) was observed at a maximum of

671 cm^{-1} (#8) and at a minimum of 658 cm^{-1} (#14, 23), the main Raman band of larnite (~859 cm^{-1} at ambient pressure) was observed at a maximum of 866 cm^{-1} (#21) and at a minimum of 861 cm^{-1} (#11), and the main Raman band of $CaSi_2O_5$-titanite (~356 cm^{-1} at ambient pressure) was observed at a maximum of 357 cm^{-1} (#11) and at a minimum of 352 cm^{-1} (#40). All of these observations indicate that the inclusions are under stress, even though visible fractures are present around them, (see Figure 3.1). For complete characterization of inclusion #11 (dimensions 30×28 µm), which contains all three Ca-silicate phases coexisting together (see Figure 3.5), Raman microprobe mapping (Nasdala et al., 2003) was applied. The generated images (Figure 3.6) represent two-dimensional sections (with limited integration over the third dimension) through the inclusion and clearly depict the spatial distribution of the three phases. More specifically, larnite (β-Ca_2SiO_4) occupies the upper left portion of the inclusion (c), $CaSi_2O_5$-titanite occupies the lower right part of the inclusion (d) and $CaSiO_3$-walstromite is located between the two (b). The presence of larnite (β-Ca_2SiO_4) and $CaSi_2O_5$-titanite in unequal proportions indicates that the bulk composition of $CaSiO_3$ is not respected, although the system is closed.

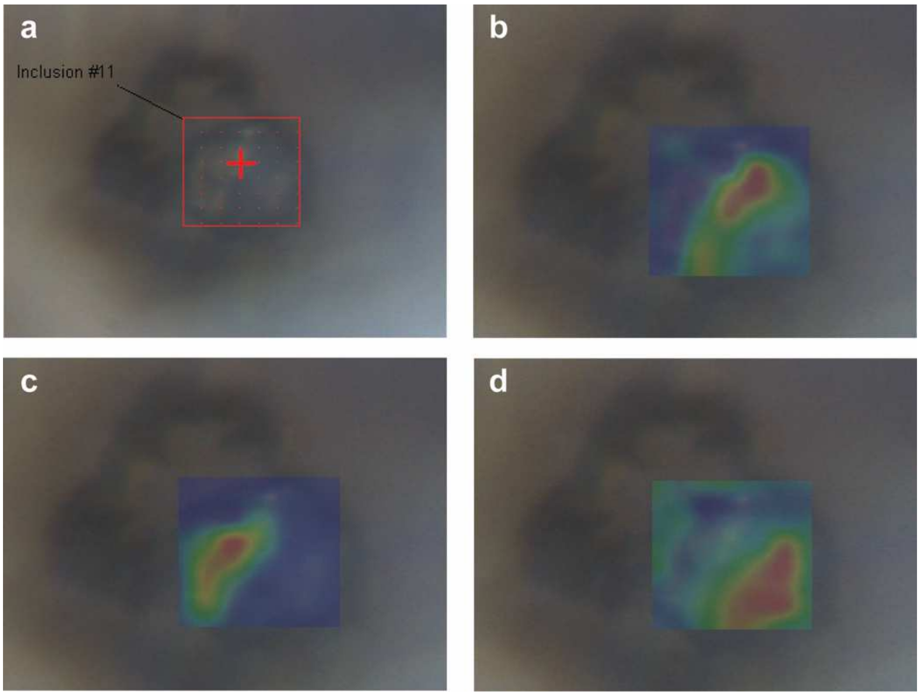

Figure 3.6: a) Close-up of inclusion #11; b) Raman intensity at 664 cm^{-1} (characteristic of $CaSiO_3$-walstromite); c) Raman intensity at 864 cm^{-1} (characteristic of larnite (β-Ca_2SiO_4)); d) Raman intensity at 355 cm^{-1} (characteristic of $CaSi_2O_5$-titanite). The map area is 30×28 µm^2. Raman intensity is function of colour: blue indicates minimum intensity, red indicates maximum intensity.

3.3.3 Inclusion residual pressures

Ten inclusions out of the 33 Ca-silicate inclusions listed in the previous section were individually investigated by SCXRD. The lattice parameters obtained for each inclusion are shown in Table 3.4. Because of the extreme proximity of inclusions #8, 9, 10 and 13, it was not possible to discriminate between them and to assign them the corresponding cell parameters. For this reason, they have been labelled simply as "Group 8". All of the inclusions have unit-cell volumes less than the room pressure volume of $CaSiO_3$-walstromite (~376 Å^3), confirming the Raman results that these inclusions retain a remnant pressure. We have determined their residual pressures, which range from ~0.17 (#26) to ~1.8 GPa (#Group 8), by using the thermoelastic parameters for $CaSiO_3$-walstromite reported in Table 6. The presence of fractures around our inclusions explains why they exhibit lower pressure than the residual pressure of 2.38 GPa inferred from the difference between the previously reported V = 365.39 Å^3 for a $CaSiO_3$-walstromite inclusion and the volume of the same inclusion after release from its diamond host, which is V = 375.16 Å^3 (Joswig et al., 2003).

Table 3.4: Unit-cell parameters and volumes of ten $CaSiO_3$-walstromite inclusions trapped within diamond SL_FFM_08.

Inclusion	a (Å)	b (Å)	c (Å)	α (°)	β (°)	γ (°)	V (Å^3)
2	6.580(1)	6.636(3)	9.248(2)	69.81(3)	83.85(2)	77.20(2)	369.4(2)
12	6.593(2)	6.642(2)	9.263(3)	69.85(3)	83.84(3)	77.06(3)	370.9(2)
6	6.579(3)	6.625(4)	9.238(4)	70.03(5)	83.74(4)	77.13(4)	368.7(3)
27	6.607(17)	6.63(2)	9.25(3)	70.4(3)	84.0(3)	77.3(2)	373(2)
24	6.58(2)	6.66(1)	9.28(2)	69.5(2)	84.4(2)	77.1(2)	372(2)
26	6.595(9)	6.649(9)	9.35(3)	70.01(18)	83.97(16)	76.93(11)	375(1)
Group 8	6.582(11)	6.646(12)	9.263(15)	70.12(15)	83.91(13)	76.74(15)	371(1)
Group 8	6.576(5)	6.622(7)	9.235(6)	70.15(8)	83.95(6)	76.96(7)	368.3(5)
Group 8	6.596(8)	6.615(8)	9.247(16)	69.97(14)	83.80(12)	76.99(11)	369.2(9)
Group 8	6.583(12)	6.619(11)	9.253(18)	69.94(17)	84.28(16)	76.77(15)	369(1)

3.4 Discussion

3.4.1 Depth of formation of the $CaSiO_3$-walstromite – diamond pair by single-inclusion elastic barometry

The presence within the same Ca-silicate inclusions of $CaSiO_3$-walstromite with either larnite but no detectable $CaSi_2O_5$-titanite, or vice-versa, suggests that the initial Ca-silicate inclusions were trapped by diamond growth at conditions near to the $CaSiO_3$-walstromite = larnite (β-Ca_2SiO_4) + $CaSi_2O_5$-titanite equilibrium phase boundary, at about 10 GPa at 1500 K.

Both our Raman and X-ray diffraction measurements show that the inclusions are under a residual pressure as a consequence of differences in the thermoelastic properties between the diamond and the inclusion phase. In principle, this residual pressure, measured at ambient conditions, can be used to estimate the formation pressure conditions of the diamond-inclusion pair if the equations of state of the mineral inclusion and the host diamond are known. The key concept of this approach is that, at the moment of encapsulation, the inclusion and its cavity in the diamond host have the same volume and experience the same P and T (Izraeli et al., 1999; Nestola et al., 2012; Angel et al., 2014b). This in turn allows the depth of formation of the diamond to be estimated.

However, "single-inclusion elastic barometry" can only be applied within some boundary conditions. One is that the deformation in the host and the inclusion has been purely elastic. If inclusions are surrounded by cracks, the brittle deformation would have resulted in a partial or a complete release of the P_{inc}, so in this case the calculated entrapment pressures are minimum estimates.

Another assumption is that both the diamond and its inclusion are elastically isotropic (Angel et al., 2014b), and thus the inclusion is under isotropic stress (i.e. P). An inclusion contained within a diamond is under uniform strain because its host is cubic. The volume response of a material to the application of uniform strain is quantified by K_{Voigt} (Voigt, 1928), while the response of a material to the application of uniform stress (i.e. the one we have determined by high-pressure X-ray diffraction of a crystal in a fluid medium) is quantified by K_{Reuss} (Reuss, 1929). K_{Voigt} and K_{Reuss} represent the upper and lower bounds of the effective bulk modulus, respectively, and they are only equal for cubic materials. But we know from the high-pressure X-ray diffraction measurements of its unit-cell parameters that $CaSiO_3$-walstromite is anisotropic, therefore K_{Voigt} is greater than K_{Reuss}. We would therefore need the EoS of $CaSiO_3$-walstromite under uniform strain, but this is not possible because its full stiffness matrix is unknown. By using as constraints the Reuss bulk modulus (K_{0T}) and the linear bulk moduli ($M_{0,\mathrm{a}}$, $M_{0,\mathrm{b}}$, $M_{0,\mathrm{c}}$) determined from diffraction, which depend on the stiffness matrix C_{ij}, and its inverse (compliance) matrix S_{ij}, the value of K_{Voigt} of $CaSiO_3$-walstromite must be less than 107 GPa ($K_{\mathrm{Voigt,MAX}}$). If we use systematic patterns of C_{ij} in layered materials to estimate K_{Voigt}, the most likely value for K_{Voigt} is in the range 80-90 GPa. This estimate is supported by DFT calculations performed in this work which provided a $K_{\mathrm{Voigt}} = 85.4$ GPa ($K_{\mathrm{Voigt,DFT}}$). We assume a K'_0 fixed at 4.

Table 3.5: Isomeke calculations for the diamond-$CaSiO_3$-walstromite host-inclusion system: effect of $CaSiO_3$-walstromite bulk modulus (expressed in GPa).

Temperature (K)	P_{e} ($K_{\mathrm{Reuss}} = 78.6$)	P_{e} ($K_{\mathrm{Voigt,DFT}} = 85.4$)	P_{e} ($K_{\mathrm{Voigt,max}} = 107$)
1200	4.660	5.208	7.161
1300	4.808	5.372	7.381
1400	4.954	5.533	7.598
1500	5.097	5.692	7.812
1600	5.240	5.850	8.024
1700	5.381	6.007	8.235
1800	5.521	6.162	8.443
1900	5.660	6.316	8.651
2000	5.798	6.470	8.857

Note: P_{e} are expressed in GPa.

The calculation of the pressure of formation ($P_{\mathrm{e)}}$ for the $CaSiO_3$-walstromite – diamond pair was performed with the software EoSFit7c (Angel et al., 2014a), by following the same method described in Angel et al. (2014b). We used thermal expansion and compressibility data for $CaSiO_3$-walstromite obtained in this work, thermoelastic properties for diamond from the review of Angel et al. (2015) (Table 3.6) and the residual pressure obtained by using the volume reported by Joswig et al. (2003), interpreted in terms of our EoS, which is 2.38 GPa, as explained in § 3.3. No entrapment pressure calculations on multiphase inclusions were performed because the stress state for mixed-phase inclusions is not well defined.

Table 3.6: Thermoelastic parameters used in the thermodynamic calculations.

	$CaSiO_3$-walstromite	**$CaSiO_3$-perovskite**	**Diamond**
K_{0T} (GPa)	85.4 (this work, Voigt modulus)	236 (Holland and Powell, 2011)	444 (Angel et al., 2015)
K'	4.0 (this work)	3.9 (Holland and Powell, 2011)	4 (Angel et al., 2015)
a_0 (10^{-5}/K^{-1})	2.551 (this work)	1.87 (Holland and Powell, 2011)	0.27 (Angel et al., 2015)
$\boldsymbol{\theta}_E$ (K)	460 (Holland and Powell, 2011)	1000 (Holland and Powell, 2011)	1500 (Angel et al., 2015)
V_0 (cm^3/mol)	37.58 (this work)	27.45 (Holland and Powell, 2011)	45.40 (Angel et al., 2015)
$\Delta H^{\circ}_{f,298}$ (kJ/mol)	14.79 ± 4.41 (Kojitani et al., 2001)	-78.90 ± 1.42 (Kojitani et al., 2001)	

Assuming a temperature range between 1200 K and 2000 K for $CaSiO_3$-walstromite formation (i.e. the same temperature range at which $CaSiO_3$-walstromite was successfully synthesized by Gasparik et al., 1994), and considering three possible bulk moduli, we obtained entrapment pressures ranging from 4.66 to 5.80 GPa ($K_{\mathrm{Reuss}} = 78.6$ GPa), from 5.21 to 6.47 GPa ($K_{\mathrm{Voigt,DFT}} = 85.4$ GPa) and from 7.16 to 8.86 GPa ($K_{\mathrm{Voigt,MAX}} = 107$ GPa) (Table 3.5). The entrapment pressures calculated with K_{Reuss} (purple circles) fall partially into the stability field of graphite, confirming that K_{Reuss} is not appropriate for a triclinic mineral like $CaSiO_3$-walstromite. Conversely both entrapment pressures calculated with $K_{\mathrm{Voigt,DFT}}$ (orange squares), which is our best estimate, and $K_{\mathrm{Voigt,MAX}}$ (green triangles) fall into the stability fields of both diamond and $CaSiO_3$-walstromite (Figure 3.4). Moreover, the presence of fractures around the inclusions indicates these are only minimum estimates, and it is possible that the entrapment pressure may will be at least on the boundary between $CaSiO_3$-

walstromite and larnite + $CaSi_2O_5$-titanite, consistent with the observations of coexistent $CaSiO_3$-walstromite, larnite and $CaSi_2O_5$-titanite in a single inclusion.

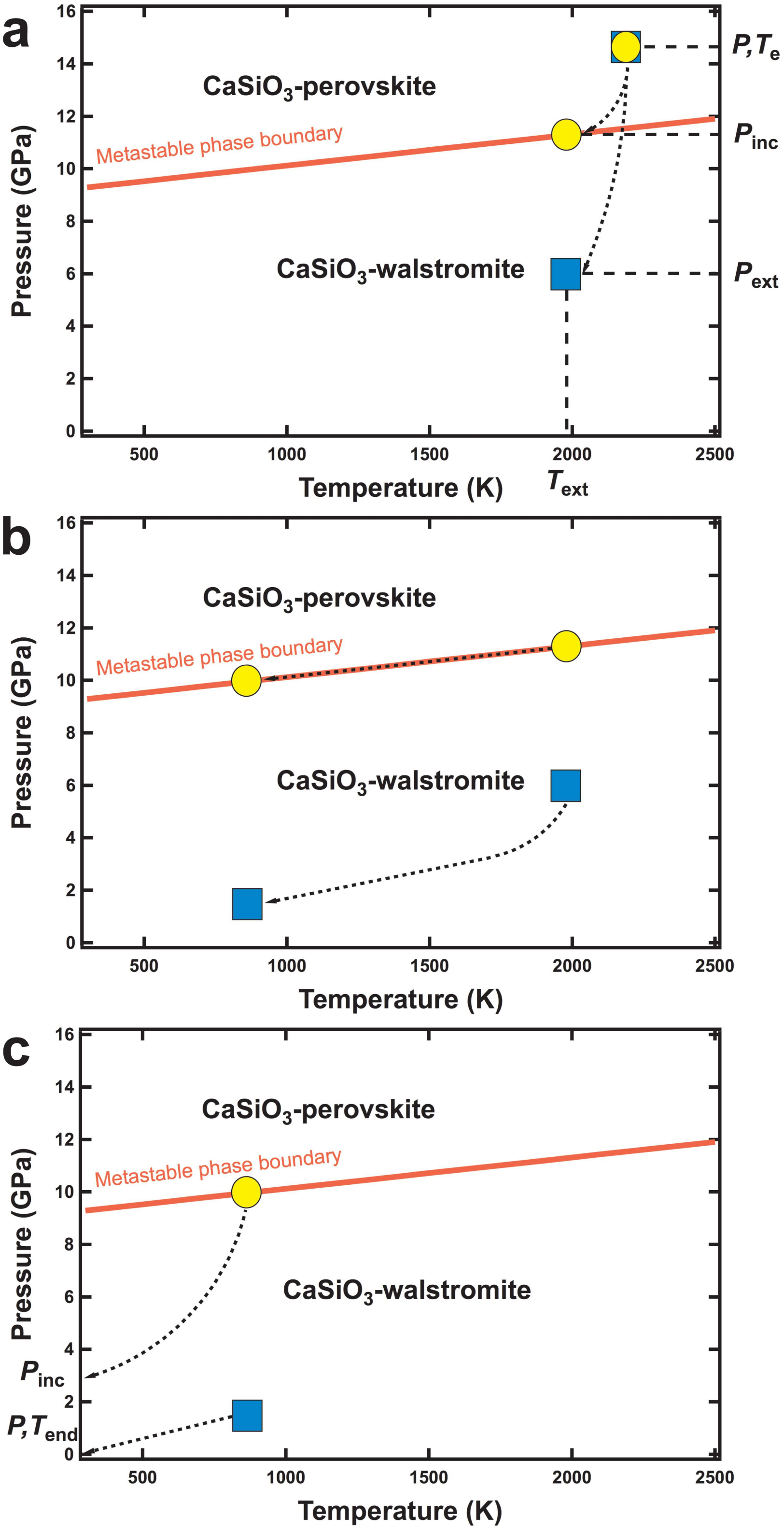

Figure 3.7: a) During exhumation from a certain entrapment pressure and temperature condition (P,T_e) the inclusion (orange circle), which is softer than the diamond, cannot expand and remains at a pressure higher (P_{inc}) than the external pressure exerted on the diamond (P_{ext}). When this internal pressure reaches the phase boundary (Kojitani et al., 2001), $CaSiO_3$-perovskite starts to transform to $CaSiO_3$-walstromite; b) During the process of transformation, the inclusion pressure is buffered to the pressure of the phase boundary, because the inclusion is a closed chemical system. The inclusion pressure remains at the phase boundary pressure until complete transformation; c) Once the transformation is complete, the inclusion pressure leaves the phase boundary.

3.4.2 Thermodynamic calculations

It has been suggested that $CaSiO_3$-walstromite inclusions are the retrograde transformation product of $CaSiO_3$-perovskite, implying diamond growth and $CaSiO_3$-perovskite entrapment in the lower mantle (Harte et al., 1999; Joswig et al., 1999; Stachel et al., 2000; Hayman et al., 2005). After the identification of monophase $CaSiO_3$-walstromite inclusions in diamond SL_FFM_08, we have performed some thermodynamic calculations in order to understand if these inclusions could derive from $CaSiO_3$-perovskite or not. The key concept behind our argument is the following – see Figure 3.7: since the diamond host and the inclusion have different compressibilities, during exhumation from a certain entrapment pressure and temperature condition (P, T_e) the inclusion (yellow circle) wants to expand more, but, being confined by the stiff diamond (blue square), it cannot and remains at a pressure higher (P_{inc}) than the external pressure exerted on the diamond (P_{ext}). When this internal pressure reaches the phase boundary (Kojitani et al., 2001), $CaSiO_3$-perovskite starts to transform to $CaSiO_3$-walstromite (Figure 3.7a). During the process of transformation, the inclusion pressure must be buffered to the pressure of the phase boundary, because the inclusion is a closed chemical system. Therefore, the inclusion pressure remains at the phase boundary pressure (at the T_{ext}) until complete transformation (Figure 3.7b), even while the external T_{ext} and P_{ext} on the diamond decrease due to exhumation. Once the transformation is complete, which means when all of the $CaSiO_3$-perovskite has been transformed to $CaSiO_3$-walstromite, the inclusion pressure is no longer buffered and it finally becomes less than the phase boundary pressure (Figure 3.7c). We can calculate the fraction of $CaSiO_3$-perovskite transformed to $CaSiO_3$-walstromite from the ΔV of the inclusion and the ΔV of the hole within the diamond between the start and the end of the path in P, T space. A step-by-step explanation of this argument is provided in the Appendix.

The direct transformation of $CaSiO_3$-perovskite → $CaSiO_3$-walstromite involves a ΔV of 30% at high pressure and temperature, but typical volume changes for diamonds by cooling and decompression can be calculated from the EoS of the diamond to be of the order of 1-3%, depending on the exact path. This means if we start with $CaSiO_3$-perovskite, it would never completely transform to $CaSiO_3$-walstromite, unless the diamond expanded by 30%. The maximum amount of transformation occurs when ΔV of diamond is maximized, which means when the path followed by the diamond terminates at room temperature. The amount of transformation is also maximised by entrapment of the inclusion directly on the phase boundary, because then there is no volume expansion contribution due to exhumation of the $CaSiO_3$-perovskite to the P and T of the phase boundary. Using the EoS parameters reported in Table 3.6 multiple calculations with different paths and different entrapment conditions were performed, but the maximum fraction of $CaSiO_3$-perovskite transformed to $CaSiO_3$-walstromite is ~25%, provided the behaviour of diamond is purely elastic. Two other non-elastic processes could play a role in generating the volume change in the diamond to allow the remaining 75% of $CaSiO_3$-perovskite to transform to $CaSiO_3$-walstromite: brittle failure (at low temperatures and high stress rates) and plastic deformation (at high temperatures). However, to obtain 30% of expansion by brittle failure, one would need cracks around the inclusion in three perpendicular planes all direction, each with widths of 10% of the diameter of the inclusion. These are not visible in our diamond. With respect to plastic deformation, at the moment there are no available data on the relationship between plastic deformation and volume change in diamonds. In any case, the greater the depth of entrapment of the $CaSiO_3$-perovskite, the higher the amount of plastic deformation and fractures needed to allow complete transformation from $CaSiO_3$-perovskite to $CaSiO_3$-walstromite.

3.5 Conclusions

Here we report for the first time an estimate of the depth of formation for the diamond-$CaSiO_3$-walstromite pair by “single-inclusion elastic barometry”, which is ~5.7 GPa (~180 km) at 1500 K, although the presence of fractures at the diamond-inclusion interface indicates this is only a minimum estimate. If $CaSiO_3$-walstromite were the product of retrograde transformation from $CaSiO_3$-perovskite, any Ca-silicate inclusion, which represents a chemically closed system, should show the bulk composition of $CaSiO_3$. The observation of a multiphase inclusion containing unequal proportions of larnite (β-Ca_2SiO_4)

and $CaSi_2O_5$-titanite coexisting with $CaSiO_3$-walstromite (see our micro-Raman map) is therefore inconsistent with a model of retrograde transformation from lower mantle or transition zone precursors (Brenker et al., 2005). Further, our thermodynamic calculations suggest that the interpretation of single $CaSiO_3$-walstromite inclusions as the retrograde product from $CaSiO_3$-perovskite would require a very large (~30%) expansion of diamond. However, the coexistence of $CaSiO_3$-walstromite, larnite (β-Ca_2SiO_4) and $CaSi_2O_5$-titanite suggests a simple explanation of entrapment in the two-phase field of larnite (β-Ca_2SiO_4) + $CaSi_2O_5$-titanite (between ~9.5 and ~11.5 GPa at 1500 K) and demonstrates that the sample investigated is a sub-lithospheric diamond. These observations suggest that so-called "super-deep diamonds" in many cases may not be so super deep and instead form in the region of the deep upper mantle and transition zone, which would be consistent with the recent model of Thomson et al. (2016) and with the range of pressure recorded by majoritic garnets, which in some cases are found in the same diamonds as Ca-silicate inclusions.

Acknowledgments

This work was supported by Fondazione Cassa di Risparmio di Padova e Rovigo and by the project INDIMEDEA, funded by the ERC Starting Grant 2012 to FN (agreement N° 307322). MD acknowledges computational grant G62-24 at Interdisciplinary Centre for Mathematical and Computational Modelling (ICM) of the University of Warsaw. We are grateful to M.J. Walter and an anonymous referee for reviewing the manuscript. The Diamond Trading Company (a member of the DeBeers Group of Companies) is thanked for the donation of the diamond to JWH. We thank the European Synchrotron Radiation Facility (Grenoble, France) for access to beamline ID09A and the ELETTRA synchrotron facility (Trieste, Italy) for access to the "Materials Characterization by X-ray diffraction" beamline, that contributed to the results presented here. Stefano Castelli is thanked for providing the macrophotography of the diamond.

Appendix

If we choose some entrapment pressure and temperature conditions (P_e and T_e) and a path in P, T space, we can calculate the external P and T (P_{ext} and T_{ext}, respectively) exerted on the diamond when the $CaSiO_3$-perovskite inclusion reaches the phase boundary. The key parameters now are the volume of the hole ($V_{hole,0}$) and hence of the inclusion ($V_{pv,0}$) at P_{ext} and T_{ext}. To test the fraction of transformation from $CaSiO_3$-perovskite to $CaSiO_3$-walstromite at the end of the path, we choose P_{end} and T_{end} and we suppose transformation was not complete, which means the inclusion pressure remains buffered at $P_{inc} = P_{boundary}$, at T_{end}.

The fractional change of the hole in the diamond, from P_{ext} and T_{ext} when the inclusion pressure reaches the phase boundary, to the final external conditions P_{end} and T_{end} is $\frac{\Delta V_{hole}}{V_{hole,0}} = \frac{V_{hole,end} - V_{hole,0}}{V_{hole,0}}$. If there was no transformation this volume would be occupied by the $CaSiO_3$-perovskite, and then

$$\frac{V_{hole,end} - V_{hole,0}}{V_{hole,0}} = \frac{V_{pv,end} - V_{pv,0}}{V_{pv,0}}.$$

However, if a volume fraction x of the $CaSiO_3$-perovskite transforms to $CaSiO_3$-walstromite, the volume of the two phases occupying the inclusion will be $\left[(1-x)V_{pv,end} + xV_{wal,end}\right]$ instead. Then:

$$\frac{V_{hole,end} - V_{hole,0}}{V_{hole,0}} = \frac{\left[(1-x)V_{pv,end} + xV_{wal,end}\right] - V_{pv,0}}{V_{pv,0}}.$$

Re-arrangement of this equation yields the volume fraction of $CaSiO_3$-perovskite transformed to $CaSiO_3$-walstromite as: $x = \left[\left(\frac{V_{pv,0}}{V_{hole,0}}\right)V_{hole,end} - V_{pv,end}\right] \cdot \frac{1}{V_{wal,end} - V_{pv,end}}$. Provided the calculated value of x remains less than 1.0, the inclusion pressure remains buffered at the phase boundary, and the derivation and calculation is valid.

References

Angel, R.J., 2000. Equations of state. Reviews in Mineralogy and Geochemistry 41, 35-59.

Angel, R.J., Alvaro, M., Gonzalez-Platas, J., 2014a. EosFit7c and a Fortran module (library) for equation of state calculations. Zeitschrift für Kristallographie 229, 405-419.

Angel, R.J., Mazzucchelli, M.L., Alvaro, M., Nimis, P., Nestola, F., 2014b. Geobarometry from host-inclusion systems: The role of elastic relaxation. American Mineralogist 99, 2146-2149.

Angel, R.J., Alvaro, M., Nestola, F., Mazzucchelli, M.L., 2015. Diamond thermoelastic properties and implications for determining the pressure of formation of diamond-inclusion systems. Russian Geology and Geophysics 56, 211-220.

Angel, R.J., Milani, S., Alvaro, M., Nestola, F., 2016. High quality structures at high pressure? Insights from inclusions in diamonds. Zeitschrift für Kristallographie 231, 467-473.

Armstrong, L., Walter, M., Tuff, J., Lord, O.T., Lennie, A., Kleppe, A., Clark, S., 2012. Perovskite phase relations in the system CaO–MgO–TiO_2–SiO_2 and implications for deep mantle lithologies. Journal of Petrology 53, 611-635.

Barkley, M.C., Downs, R.T., Yang, H., 2011. Structure of walstromite, $BaCa_2Si_3O_9$, and its relationship to $CaSiO_3$-walstromite and wollastonite-II. American Mineralogist 96, 797-801.

Birch, F., 1947. Finite elastic strain of cubic crystals. Physical Review 71, 809.

Blöchl, P.E., 1994. Projector augmented-wave method. Physical Review B 50, 17953.

Brenker, F.E., Vincze, L., Vekemans, B., Nasdala, L., Stachel, T., Vollmer, C., Kersten, M., Somogyi, A., Adams, F., Joswig, W., 2005. Detection of a Ca-rich lithology in the Earth's deep (> 300 km) convecting mantle. Earth and Planetary Science Letters 236, 579-587.

Brenker, F.E., Vollmer, C., Vincze, L., Vekemans, B., Szymanski, A., Janssens, K., Szaloki, I., Nasdala, L., Joswig, W., Kaminsky, F., 2007. Carbonates from the lower part of transition zone or even the lower mantle. Earth and Planetary Science Letters 260, 1-9.

Bulanova, G.P., Walter, M.J., Smith, C.B., Kohn, S.C., Armstrong, L.S., Blundy, J., Gobbo, L., 2010. Mineral inclusions in sublithospheric diamonds from Collier 4 kimberlite pipe, Juina, Brazil: subducted protoliths, carbonated melts and primary kimberlite magmatism. Contributions to Mineralogy and Petrology 160, 489-510.

Day, H.W., 2012. A revised diamond-graphite transition curve. American Mineralogist 97, 52-62.

Essene, E., 1974. High-pressure transformations in $CaSiO_3$. Contributions to Mineralogy and Petrology 45, 247-250.

Fedortchouk, Y., Manghnani, M.H., Hushur, A., Shiryaev, A., Nestola, F., 2011. An atomic force microscopy study of diamond dissolution features: The effect of H_2O and CO_2 in the fluid on diamond morphology. American Mineralogist 96, 1768-1775.

Gasparik, T., Wolf, K., Smith, C.M., 1994. Experimental determination of phase relations in the $CaSiO_3$ system from 8 to 15 GPa. American Mineralogist 79, 1219-1222.

Harte, B., 2010. Diamond formation in the deep mantle: the record of mineral inclusions and their distribution in relation to mantle dehydration zones. Mineralogical Magazine 74, 189-215.

Harte, B., Harris, J., Hutchison, M., Watt, G., Wilding, M., 1999. Lower mantle mineral associations in diamonds from São Luiz, Brazil. Mantle petrology: Field observations and high-pressure experimentation: A tribute to Francis R.(Joe) Boyd 6, 125-153.

Hayman, P.C., Kopylova, M.G., Kaminsky, F.V., 2005. Lower mantle diamonds from Rio Soriso (Juina area, Mato Grosso, Brazil). Contributions to Mineralogy and Petrology 149, 430-445.

Holland, T., Powell, R., 2011. An improved and extended internally consistent thermodynamic dataset for phases of petrological interest, involving a new equation of state for solids. Journal of Metamorphic Geology 29, 333-383.

Izraeli, E., Harris, J., Navon, O., 1999. Raman barometry of diamond formation. Earth and Planetary Science Letters 173, 351-360.

Joswig, W., Paulus, E.F., Winkler, B., Milman, V., 2003. The crystal structure of

$CaSiO_3$-walstromite, a special isomorph of wollastonite-II. Zeitschrift für Kristallographie 218, 811-818.

Joswig, W., Stachel, T., Harris, J.W., Baur, W.H., Brey, G.P., 1999. New Ca-silicate inclusions in diamonds – tracers from the lower mantle. Earth and Planetary Science Letters 173, 1-6.

Kaminsky, F., Zakharchenko, O., Davies, R., Griffin, W., Khachatryan-Blinova, G., Shiryaev, A., 2001. Superdeep diamonds from the Juina area, Mato Grosso State, Brazil. Contributions to Mineralogy and Petrology 140, 734-753.

Kaminsky, F., 2012. Mineralogy of the lower mantle: A review of 'super-deep' mineral inclusions in diamond. Earth Science Reviews 110, 127-147.

Kanzaki, M., Stebbins, J.F., Xue, X., 1991. Characterization of quenched high pressure phases in $CaSiO_3$ system by XRD and ^{29}Si NMR. Geophysical Research Letters 18, 463-466.

Kojitani, H., Navrotsky, A., Akaogi, M., 2001. Calorimetric study of perovskite solid solutions in the $CaSiO_3$–$CaGeO_3$ system. Physics and Chemistry of Minerals 28, 413-420.

Kresse, G., Furthmüller, J., 1996a. Efficiency of ab-initio total-energy calculations for metals and semiconductors using a plane-wave basis set. Computational Materials Science 6, 15-50.

Kresse, G., Furthmüller, J., 1996b. Efficient iterative schemes for ab-initio total-energy calculations using a plane-wave basis set. Physical Review B 54, 11169.

Kresse, G., Joubert, D., 1999. From ultrasoft pseudopotentials to the projector augmented-wave method. Physical Review B 59, 1758.

Larson, A.C., Von Dreele, R.B., 1994. GSAS. General Structure Analysis System. LANSCE, MS-H805, Los Alamos, New Mexico.

Mao, H., Xu, J., Bell, P., 1986. Calibration of the ruby pressure gauge to 800 kbar under quasi-hydrostatic conditions. Journal of Geophysical Research 91, 4673-4676.

Merlini, M., Hanfland, M., 2013. Single-crystal diffraction at megabar conditions by synchrotron radiation. High Pressure Research 33, 511-522.

Nasdala, L., Brenker, F.E., Glinnemann, J., Hofmeister, W., Gasparik, T., Harris, J.W., Stachel, T., Reese, I., 2003. Spectroscopic 2D-tomography Residual pressure and strain around mineral inclusions in diamonds. European Journal of Mineralogy 15, 931-935.

Nestola, F., Nimis, P., Ziberna, L., Longo, M., Marzoli, A., Harris, J.W., Manghnani, M.H., Fedortchouk, Y., 2011. First crystal-structure determination of olivine in diamond: Composition and implications for provenance in the Earth's mantle. Earth and Planetary Science Letters 305, 249-255.

Nestola, F., Merli, M., Nimis, P., Parisatto, M., Kopylova, M., De Stefano, A., Longo, M., Ziberna, L., Manghnani, M., 2012. In situ analysis of garnet inclusion in diamond using single-crystal X-ray diffraction and X-ray micro-tomography. European Journal of Mineralogy 24, 599-606.

Nestola, F., Nimis, P., Angel, R., Milani, S., Bruno, M., Prencipe, M., Harris, J., 2014. Olivine with diamond-imposed morphology included in diamonds. Syngenesis or protogenesis?. International Geology Review 56, 1658-1667.

Nestola, F., Burnham, A.D., Peruzzo, L., Tauro, L., Alvaro, M., Walter, M.J., Gunter, M., Anzolini, C., Kohn, S.C., 2016. Tetragonal Almandine-Pyrope Phase, TAPP: finally a name for it, the new mineral jeffbenite. Mineralogical Magazine, doi: 10.1180/minmag.2016.080.059.

Nye, J.F., 1985. Physical properties of crystals: their representation by tensors and matrices. Oxford University Press.

Pearson, D., Brenker, F., Nestola, F., McNeill, J., Nasdala, L., Hutchison, M., Matveev, S., Mather, K., Silversmit, G., Schmitz, S., 2014. Hydrous mantle transition zone indicated by ringwoodite included within diamond. Nature 507, 221-224.

Perdew, J.P., Burke, K., Ernzerhof, M., 1996. Generalized gradient approximation made simple. Physical Review Letters 77, 3865.

Perdew, J.P., Ruzsinszky, A., Csonka, G.I., Vydrov, O.A., Scuseria, G.E., Constantin, L.A., Zhou, X., Burke, K., 2008. Restoring the density-gradient expansion for exchange in solids and surfaces. Physical Review Letters 100, 136406.

Petříček, V., Dušek, M., Palatinus, L., 2014. Crystallographic computing system JANA2006: general features. Zeitschrift für Kristallographie 229, 345-352.

Rebuffi, L., Plaisier, J.R., Abdellatief, M., Lausi, A., Scardi, P., 2014. MCX: a Synchrotron Radiation Beamline for X-ray Diffraction Line Profile Analysis. Zeitschrift für Anorganische und Allgemeine Chemie 640, 3100-3106.

Reuss, A., 1929. Berechnung der fließgrenze von mischkristallen auf grund der plastizitätsbedingung für einkristalle. Journal of Applied Mathematics and Mechanics 9, 49-58.

Sobolev, N.V., Fursenko, B.A., Goryainov, S.V., Shu, J., Hemley, R.J., Mao, A., Boyd, F.R., 2000. Fossilized high pressure from the Earth's deep interior: the coesite-in-diamond barometer. Proceedings of the National Academy of Sciences of the United States of America 97, 11875-11879.

Stachel, T., Harris, J. W., 2008. The origin of cratonic diamonds—constraints from mineral inclusions. Ore Geology Reviews 34, 5-32.

Stachel, T., Harris, J.W., Brey, G.P., Joswig, W., 2000. Kankan diamonds (Guinea) II: lower mantle inclusion parageneses. Contributions to Mineralogy and Petrology 140, 16-27.

Thomson, A.R., Walter, M.J., Kohn, S.C., Brooker, R.A., 2016. Slab melting as a barrier to deep carbon subduction. Nature 529, 76-79.

Thomson, A.R., Kohn, S.C., Bulanova, G.P., Smith, C.B., Araujo, D., Walter, M.J., 2014. Origin of sub-lithospheric diamonds from the Juina-5 kimberlite (Brazil): constraints from carbon isotopes and inclusion compositions. Contributions to Mineralogy and Petrology 168, 1-29.

Thomson, A.R., Kohn, S.C., Bulanova, G.P., Smith, C.B., Araujo, D., Walter, M.J., 2016. Trace element composition of silicate inclusions in sub-lithospheric diamonds from the Juina-5 kimberlite: evidence for diamond growth from slab melts. In press, this issue.

Toby, B.H., 2001. EXPGUI, a graphical user interface for GSAS. Journal of Applied Crystallography 34, 210-213.

Voigt, W., 1928. Lehrbuch der Kristallphysik (mit Ausschluss der Kristalloptik), edited by BG Teubner and JW Edwards, Leipzig Berlin. Ann Arbor, Mich.

Walter, M.J., Bulanova, G.P., Armstrong, L.S., Keshav, S., Blundy, J.D., Gudfinnsson, G., Lord, O.T., Lennie, A.R., Clark, S.M., Smith, C.B., 2008. Primary carbonatite melt from deeply subducted oceanic crust. Nature 454, 622-625.

Zedgenizov, D.A., Kagi, H., Shatsky, V.S., Ragozin, A.L., 2014. Local variations of carbon isotope composition in diamonds from São-Luis (Brazil): evidence for heterogenous carbon reservoir in sublithospheric mantle. Chemical Geology 363, 114-124.

4 Depth of formation of super-deep diamonds: Raman barometry of $CaSiO_3$-walstromite inclusions

Chiara Anzolini[1], Mauro Prencipe[2], Matteo Alvaro[3], Claudia Romano[4], Alessandro Vona[4], Sofia Lorenzon[1], Evan M. Smith[5], Frank E. Brenker[6] and Fabrizio Nestola[1]

[1]Department of Geosciences, University of Padova, Via G. Gradenigo 6, 35131 Padova, Italy

[2]Department of Earth Sciences, University of Torino, Via Valperga Caluso 35, 10125 Torino, Italy

[3]Department of Earth and Environmental Sciences, University of Pavia, Via Ferrata 1, 27100 Pavia, Italy

[4]Department of Sciences, University of Roma Tre, Largo S. Leonardo Murialdo 1, 00146 Roma, Italy

[5]Gemological Institute of America, 50 W 47th Street, NY 10036, New York, United States of America

[6]Geoscience Institute – Nanogeoscience, Goethe University, Altenhöferallee 1, 60438 Frankfurt am Main, Germany

The paper has been published in *American Mineralogist* Vol. 103(1), pp. 69–74, 2018.

The layout has been revised.

Abstract

"Super-deep" diamonds are thought to have a sub-lithospheric origin (i.e. below ~300 km depth) because some of the mineral phases entrapped within them as inclusions are considered to be the products of retrograde transformation from lower-mantle or transition-zone precursors. $CaSiO_3$-walstromite, the most abundant Ca-bearing mineral inclusion found in super-deep diamonds, is believed to derive from $CaSiO_3$-perovskite, which is stable only below ~600 km depth, although its real depth of origin is controversial. The remnant pressure (P_{inc}) retained by an inclusion, combined with the thermoelastic parameters of the mineral inclusion and the diamond host, allows calculation of the entrapment pressure of the diamond-inclusion pair. Raman spectroscopy, together with X-ray diffraction, is the most commonly used method for measuring the P_{inc} without damaging the diamond host.

In the present study we provide, for the first time, a calibration curve to determine the P_{inc} of a $CaSiO_3$-walstromite inclusion by means of Raman spectroscopy without breaking the diamond. To do so, we performed high-pressure micro-Raman investigations on a $CaSiO_3$-walstromite crystal under hydrostatic stress conditions within a diamond-anvil cell. We additionally calculated the Raman spectrum of $CaSiO_3$-walstromite by ab initio methods both under hydrostatic and non-hydrostatic stress conditions to avoid misinterpretation of the results caused by the possible presence of deviatoric stresses causing anomalous shift of $CaSiO_3$-walstromite Raman peaks. Lastly, we applied single-inclusion elastic barometry to estimate the minimum entrapment pressure of a $CaSiO_3$-walstromite inclusion trapped in a natural diamond, which is ~9 GPa (~260 km) at 1800 K. These results suggest that the diamond investigated is certainly sub-lithospheric and endorse the hypothesis that the presence of $CaSiO_3$-walstromite is a strong indication of super-deep origin.

Keywords

Diamond, inclusion, $CaSiO_3$-walstromite, micro-Raman spectroscopy, ab initio methods, elastic geobarometry

4.1 Introduction

Diamonds and the mineral inclusions that they trap during growth provide a unique window on the deep Earth. A small portion (~6%) of diamonds (Stachel and Harris 2008) are interpreted to crystallize between 300 and 800 km depth (Harte 2010) because some of the inclusions entrapped are considered to be the products of retrograde transformation from lower-mantle or transition-zone precursors. However, in many cases undisputed evidence of these purported high-pressure precursors as inclusions in diamonds is lacking, and, consequently, their real depth of origin has been proven only in rare cases (e.g. Brenker et al. 2002; Pearson et al. 2014). Most so-called "super-deep diamonds" contain mainly walstromite-structured $CaSiO_3$ (hereafter $CaSiO_3$-walstromite), ferropericlase ((Fe,Mg)O)), enstatite ($MgSiO_3$) and jeffbenite ($(Mg,Fe)_3Al_2Si_3O_{12}$), a tetragonal phase with garnet-like stoichiometry previously known by the acronym TAPP, (see Nestola et al. 2016), and it is through the study of these mineral phases that the depth of formation of super-deep diamonds can be retrieved.

$CaSiO_3$-walstromite is the dominant Ca-bearing phase in super-deep diamonds (Joswig et al. 1999) and in almost all cases it is considered the product of back transformation from $CaSiO_3$-perovskite, which is stable only below ~600 km depth within the regular high-pressure assemblage of peridotitic/eclogitic mantle rocks (Frost 2008; Kaminsky 2012). However, there is compelling evidence that at least some $CaSiO_3$-walstromite originate within the upper mantle (Brenker et al. 2005; Anzolini et al. 2016), although this would require a substantial change in the source rock chemistry. Assuming peridotitic/eclogitic mantle chemistries, $CaSiO_3$-perovskite is the main Ca-host in the lower mantle (Ringwood 1991), but is also present in the lowermost transition zone, where it exsolves from majoritic garnet at pressures greater than 20 GPa (Irifune and Ringwood 1987). Nevertheless, there are currently no reliable literature data on the exact pressure at which $CaSiO_3$ inclusions originally crystallize and therefore no valid evidence whether or not each $CaSiO_3$-walstromite derives from $CaSiO_3$-perovskite.

Single-inclusion elastic barometry, a method recently improved by Angel et al. (2014a, 2014b, 2015a, 2015b), allows us to estimate the pressure and temperature conditions of entrapment for an inclusion within a diamond by knowing its residual pressure (P_{inc}), measured while the host is at ambient conditions, and the thermoelastic parameters of the mineral inclusion and the diamond host. In principle, the P_{inc} sustained by an inclusion while still entrapped within a diamond can be determined mainly in two ways: 1) by comparing the unit-cell volume of the inclusion before and after release from its host; 2) by comparing the Raman spectrum of the inclusion still trapped within the diamond and the Raman spectrum of the same mineral phase at room pressure. The first method requires inclusions large enough to be analyzed by single-crystal X-ray diffraction, but large inclusions are more likely to fracture the surrounding host during exhumation (Van der Molen and Van Roermund 1986; Artioli et al. 2008), and therefore their internal pressure is largely released. The second method allows to analyze tiny inclusions, which commonly preserve higher internal pressures, and, on the other hand, to prevent the host-inclusion system from destruction or damages. The host-inclusion system integrity preserves information about both the pressure exerted by the diamond on the inclusion and the relationships between the two, which may provide further details on the diamond-inclusion growth mechanisms (e.g. CORs crystallographic orientation relationships Nestola et al. 2014; Angel et al. 2015b; Milani et al. 2016; Nestola et al. 2017).

In this light, we have determined experimentally the pressure-induced shift of Raman peaks for a synthetic $CaSiO_3$-walstromite up to 7.5 GPa under hydrostatic conditions to obtain a calibration system that enables us to determine the P_{inc} of a $CaSiO_3$-walstromite inclusion without breaking the diamond host. However, the effect of the elastic anisotropy of the host and the inclusion and the effect of a deviatoric stress field on the stress state of the inclusion arising from the absence of fluids at the interface between diamond and inclusion (see Nimis et al. 2016) are still unknown. Therefore, to prevent any misinterpretation of our results in terms of Raman peak shifts we calculated the Raman spectrum of $CaSiO_3$-walstromite by ab initio methods both under hydrostatic and non-hydrostatic conditions. Lastly, we estimated the entrapment pressure of a $CaSiO_3$-

walstromite inclusion found in a diamond by single-inclusion elastic barometry.

4.2 Experimental methods

4.2.1 Samples

The single $CaSiO_3$-walstromite crystal, whose longest dimension is 40 μm, used for the high-pressure Raman investigations came from the experimental batch of Gasparik et al. (1994), synthesized at 2000 K and 9 GPa.

The diamond investigated in this study (Figure 4.1a) was a 2.70-carat oval cut Type-II diamond. The inclusion investigated (Figure 4.1b) was a $CaSiO_3$-walstromite, identified by comparison with Raman spectra reported by Nasdala et al. (2003) and Brenker et al. (2005, 2007).

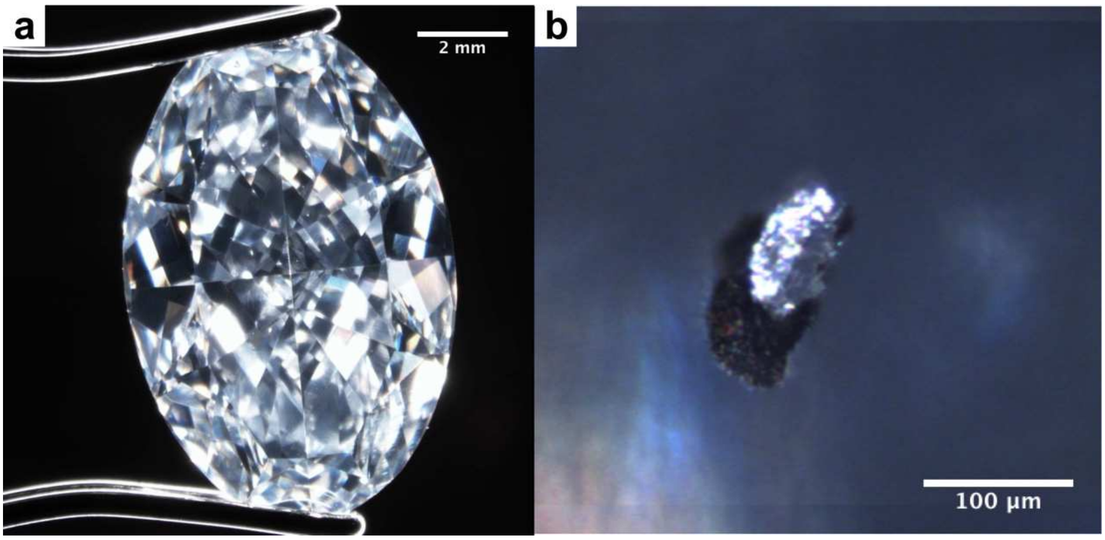

Figure 4.1: a) Expanded view of the inclusion-bearing diamond studied in this work; b) Close-up of the $CaSiO_3$-walstromite inclusion investigated. The black halo around the inclusion indicates the presence of graphitization inside a fracture.

4.2.2 Experimental in situ calibration of $CaSiO_3$-walstromite Raman spectra at high pressure

The ambient pressure Raman spectrum of the synthetic single crystal of $CaSiO_3$-walstromite was collected with a Thermo Scientific™ DXR™ Raman Microscope using a green solid state laser (532 nm) as excitation source at the Department of Geosciences, University of Padova. The analyses were performed using a 50× Long Working Distance (LWD) objective with ~2.5 cm^{-1} spectral resolution and 1 μm spatial resolution at 10 mW of power. The Raman system was set with 900 lines/mm grating and a 25 µm pinhole. Spectra were recorded in the frequency range extending from 100 to 3500 cm^{-1}; to maximize the signal-to-noise ratio, each spectrum was collected ten times using an exposure time of 20 s, and then merged together at the end of the acquisition. The instrument was calibrated by using the calibration tool provided by Thermo Scientific^{TM}.

The high-pressure Raman spectra were collected at the Department of Sciences, University of Roma Tre, with a Horiba LabRam HR micro-Raman spectrometer equipped with a green solid state laser (532 nm) focused through a 20× LWD objective. A ETH diamond-anvil cell with 600 µm size culets was loaded with the crystal of $CaSiO_3$-walstromite and a 4:1 mixture of methanol:ethanol as pressure-transmitting medium. Pressure was determined by the calibrated shift of the R_1 ruby fluorescence band (Mao et al. 1986). The spatial resolution was ~1 µm and the spectral resolution was 0.3 cm^{-1}. For the ruby, optical filters were employed in order to achieve ~1 mW at the sample surface; the Raman system was set with 1800 lines/mm grating, exposure time 1 s (3 times), confocal hole of 300 µm and slit of 200 µm. For the $CaSiO_3$-walstromite, optical filters were employed in order to achieve ~50 mW at the sample surface; the Raman system was set with 1800 lines/mm grating, exposure time 60 s (3 times), confocal hole of 100 µm and slit of 100 µm. The calibration was done using the main Raman line (520.5 cm^{-1}) of a silicon standard.

The Raman spectrum of the $CaSiO_3$-walstromite inclusion was collected at the Gemological Institute of America with a Renishaw inVia Raman microscope using the 514.5 nm output wavelength of a 150 mW argon-ion laser, at 100% output power. The analyses were performed using 50× LWD lens with a 0.55 numerical aperture and the system was set with 1800 lines/mm grating. Spectra were recorded in the frequency range extending from 100 to 1200 cm^{-1}; to maximize the signal-to-noise ratio, each spectrum was collected four times using an exposure time of 60 s, and then merged together at the end of the acquisition. The calibration was done using an internal silicon standard (inside the instrument) using its main Raman line (520.5 cm^{-1}).

The baseline subtraction with a quadratic function and the Lorentzian fitting were carried out using the Thermo Scientific^{TM} OMNIC^{TM} Spectra Software.

4.2.3 Ab initio calibration of $CaSiO_3$-walstromite Raman spectra at high pressure

The ab initio calculation of the vibrational frequencies and intensities of the Raman-active modes was performed by using the CRYSTAL14 software (Dovesi et al. 2014). A hybrid HF/DFT Hamiltonian was used (WC1LYP) which employs the Wu-Cohen DFT exchange functional (Wu and Cohen 2006) corrected with a fraction (20%) of the exact non-local Hartree-Fock exchange, and the Lee-Young-Parr DFT correlation functional (Lee et al. 1988). The grid for the evaluation of the DFT exchange–correlation functionals was chosen by the keyword XLGRID of the CRYSTAL14 user manual (Dovesi et al. 2014) and corresponds to a total of 345185 points in the unit cell. A measure of the excellent numerical accuracy provided by such a grid is the evaluation of the total number of electrons in the unit cell, by the numerical integration of the electron density over the cell volume: 348.000013 electrons out of 348. The atomic basis sets employed were from the CRYSTAL online library at the address www.crystal.unito.it/basis-sets.php. More precisely, they were 86-511G(2d) for Ca, 86-311G(*1d*) for Si and 8-411G(2d) for O, where the symbols 1d and 2d stand for the presence of one and two polarization functions, respectively. The thresholds controlling the accuracy of the calculation of Coulomb and exchange integrals were set to 8 (ITOL1 to ITOL4) and 18 (Dovesi et al. 2014). The diagonalization of the Hamiltonian matrix was performed at 8 independent $\underline{k}$ vectors in the reciprocal space (Monkhorst net; Monkhorst and Pack 1976) by setting to 2 the shrinking factor IS (Dovesi et al. 2014). Cell parameters and fractional coordinates were optimized by analytical gradient methods, as implemented in CRYSTAL14 (Dovesi et al. 2014; Civalleri et al. 2001). Geometry optimization was considered converged when each component of the gradient (TOLDEG parameter in CRYSTAL14) was smaller than 0.00003 hartree/bohr and displacements (TOLDEX) were smaller than 0.00012 bohr with respect to the previous step. Lattice parameters and fractional coordinates were optimized at the WC1LYP level (static values: no zero point and thermal effects included), at the static pressures of 0 and 4 GPa, and at four other *non-hydrostatic* stress conditions specified by matrices representing the stress tensor in a Cartesian frame (with $\underline{e}_1$, $\underline{e}_2$, $\underline{e}_3$ basis vectors), where the $\underline{e}_2$ vector is parallel to the $\underline{b}$ lattice vector; the $\underline{e}_1$, and $\underline{e}_3$ vectors are respectively subparallel to the $\underline{a}$, and $\underline{c}$ lattice vectors, derived from a standard orthogonalization of the lattice basis. The chosen four stress matrices corresponded to a hydrostatic component of 4 GPa plus deviatoric stresses (pure shear, traceless stress matrices) having eigenvalues 1, –0.5 and –0.5 GPa, and directions of maximum compression (eigenvalue 1 GPa) respectively along $\underline{e}_1$, $\underline{e}_2$, $\underline{e}_3$ and the softest direction$[1\bar{1}2]$, (the latter one is given with reference to the crystal lattice basis). Vibrational frequencies were calculated at 0, 4 GPa and at the four non-hydrostatic stress conditions, as the eigenvalues of the matrix of the second derivatives of the full potential of the crystal with respect the mass-weighted nuclear displacements (Hessian matrix; Pascale 2004). Relative intensities of the Raman signals are computed using a fully analytical approach formulated and implemented in the CRYSTAL14 program (Maschio et al. 2012, 2013).

4.3 Results

4.3.1 Raman spectrum at ambient pressure

Before performing the high-pressure Raman measurements, we examined the Raman spectrum of the synthetic $CaSiO_3$-walstromite at ambient conditions (Figure 4.2). The three main Raman peaks, in order of decreasing intensity, were observed at 656, 977 and 1037 cm^{-1} (hereafter called Peak 1, 2 and 3, respectively). The raw spectrum (Figure 4.7) shows also lower intensity peaks in the 200-590 cm^{-1} region (the main ones at 301, 328, 349, 396 and 512 cm^{-1}) and in the 810-950 cm^{-1} region (the main ones at 813, 838, 857 and 950 cm^{-1}); another peak is centered at 1055 cm^{-1}. Our ambient Raman frequencies agree with those reported in previous studies within the experimental uncertainty (Nasdala et al. 2003; Brenker et al. 2005, 2007).

4.3.2 Effect of hydrostatic pressure on the Raman frequencies: comparison between experiment and simulation

In situ Raman spectra of the three main peaks (656, 977 and 1037 cm^{-1}) of crystalline $CaSiO_3$-walstromite, measured as a function of pressure up to 7.5 GPa, are shown in Figure

4.2. Data analysis of the spectra was carried out using Thermo Scientific™ OMNIC™ Spectra Software with Gaussian function. The measured frequencies are reported in Table 4.1.

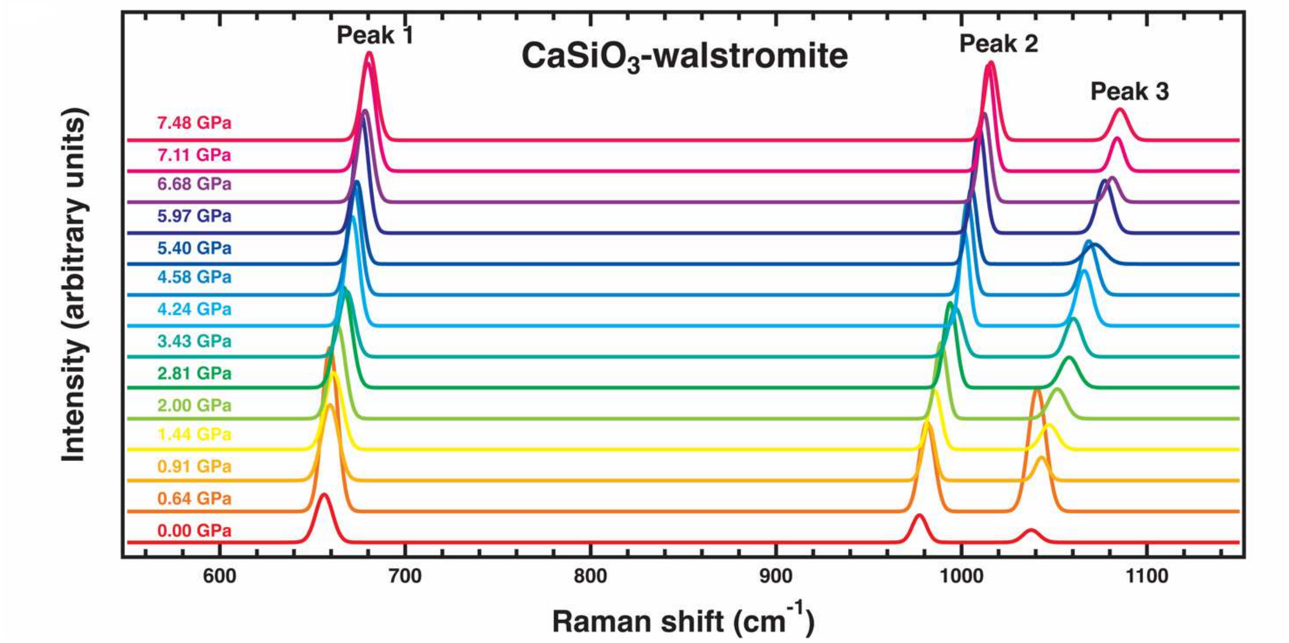

Figure 4.2: Raman spectra of synthetic CaSiO$_3$-walstromite up to 7.5 GPa.

Table 4.1: Experimental frequencies of the three main peaks of CaSiO$_3$-walstromite up to 7.5 GPa.

Pressure (GPa)	Peak 1	Peak 2	Peak 3
	Frequency (cm^{-1})	Frequency (cm^{-1})	Frequency (cm^{-1})
0.00[a]	656.3	977.3	1037.6
0.64	659.4	981.4	1040.8
0.91	659.4	982.3	1043.2
1.44	661.4	985.5	1047.2
2.00	663.5	989.0	1051.6
2.81	666.7	993.9	1058.0
3.43	668.5	996.8	1060.3
4.24	671.3	1001.6	1066.1
4.58	672.5	1003.3	1068.6
5.40[b]	673.9	1005.4	1071.8
5.97	676.3	1009.5	1077.3
6.68[b]	678.3	1012.3	1081.3
7.11[b]	679.7	1014.4	1083.9
7.48	680.6	1016.0	1085.4

Notes: [a]Raman spectrum measured at room pressure with the crystal in air. [b]Data taken during pressure unloading.

It is evident that all Raman peaks shift continuously toward higher wavenumbers with increasing pressure throughout the pressure range. In particular, Peaks 1 and 2 show an almost linear trend. The pressure-dependence of the three main Raman bands was fitted with a weighted linear regression and the resulting pressure coefficients were: $\mathrm{d}v/\mathrm{d}P$ = 3.22(±0.05) cm^{-1} GPa^{-1} for Peak 1, $\mathrm{d}v/\mathrm{d}P$ = 5.16(±0.09) cm^{-1} GPa^{-1} for Peak 2 and $\mathrm{d}v/\mathrm{d}P$ = 6.5(±0.1) cm^{-1} GPa^{-1} for Peak 3 (Figure 3a). Minor peaks were too weak to be fitted accurately at high pressure; therefore they were not considered for the calculation of the pressure coefficients.

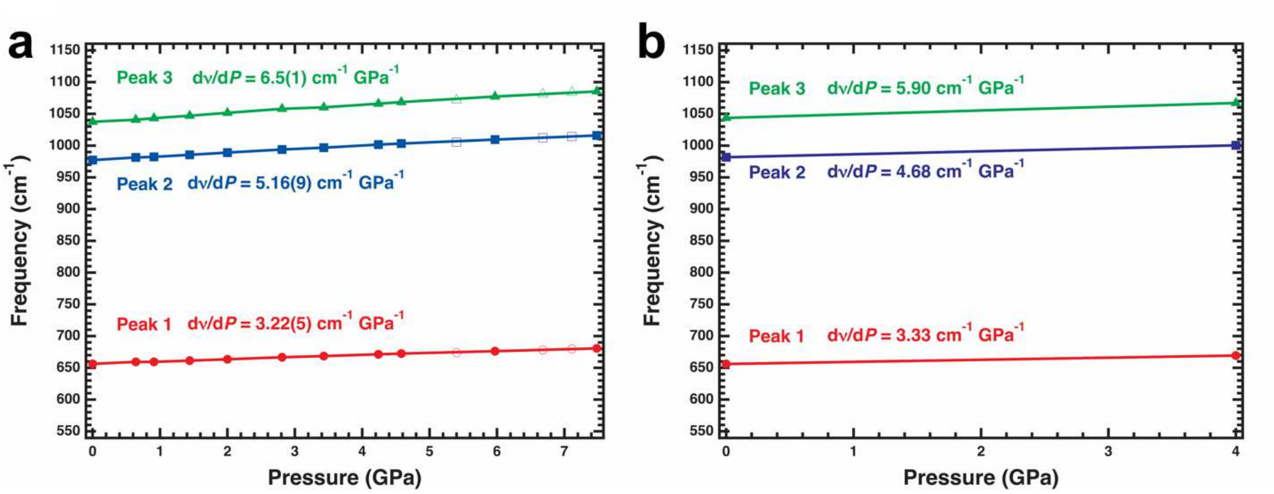

Figure 4.3: a) Experimental and b) calculated pressure-dependencies of the main Raman peaks of CaSiO$_3$-walstromite under hydrostatic conditions. In a) compression and decompression are represented by solid and open symbols, respectively. The error bars lie within the symbols.

Our calculated Raman spectra (Table 4.2) are comparable with the experimental frequencies reported in Table 4.1.

Table 4.1 within 1 or 2 standard deviations (σ). All Raman frequencies systematically increase with increasing pressure. The pressure-dependence of the three main Raman bands was fitted with a weighted linear regression and the resulting pressure coefficients were: $\mathrm{d}v/\mathrm{d}P$ = 3.33 cm^{-1} GPa^{-1} for Peak 1, $\mathrm{d}v/\mathrm{d}P$ = 4.68 cm^{-1} GPa^{-1} for Peak 2 and $\mathrm{d}v/\mathrm{d}P$ = 5.90 cm^{-1} GPa^{-1} for Peak 3 (Figure 3b). These pressure-dependencies match well with the experimental ones within 1 or 2 standard deviations (σ).

Table 4.2: Calculated Raman frequencies of the three main peaks of $CaSiO_3$-walstromite under hydrostatic pressure and their relative intensities normalized to 1000. Differences Δν are with respect to our calculated data at ambient pressure.

$P_{\text{hydrostatic}} = 0$ GPa		$P_{\text{hydrostatic}} = 4$ GPa	
Frequency (cm^{-1})	Relative intensity	Frequency (cm^{-1})	Δν (cm^{-1})
656.1	1000	669.4	13.3
981.8	342	1000.5	18.7
1043.6	165	1067.2	23.5
Note: the complete table, which reports all calculated Raman peaks and relative intensities, is deposited with the journal.			

4.3.3 Effect of non-hydrostatic pressure on the Raman frequencies

The ab initio calculated peak shifts under non-hydrostatic stresses show patterns similar to those under hydrostatic pressure (Figure 4.4). Also, the pressure-dependencies of the three main peaks under non-hydrostatic stresses are comparable to those calculated under hydrostatic pressure, the differences being less than 2 σ (Table 4.3). Relative to the values under hydrostatic pressure, Peak 1 and Peak 3 show negative shifts under any non-hydrostatic stress state: the mean differences of the Δν are −1.4 cm^{-1} for Peak 1 and −1.0

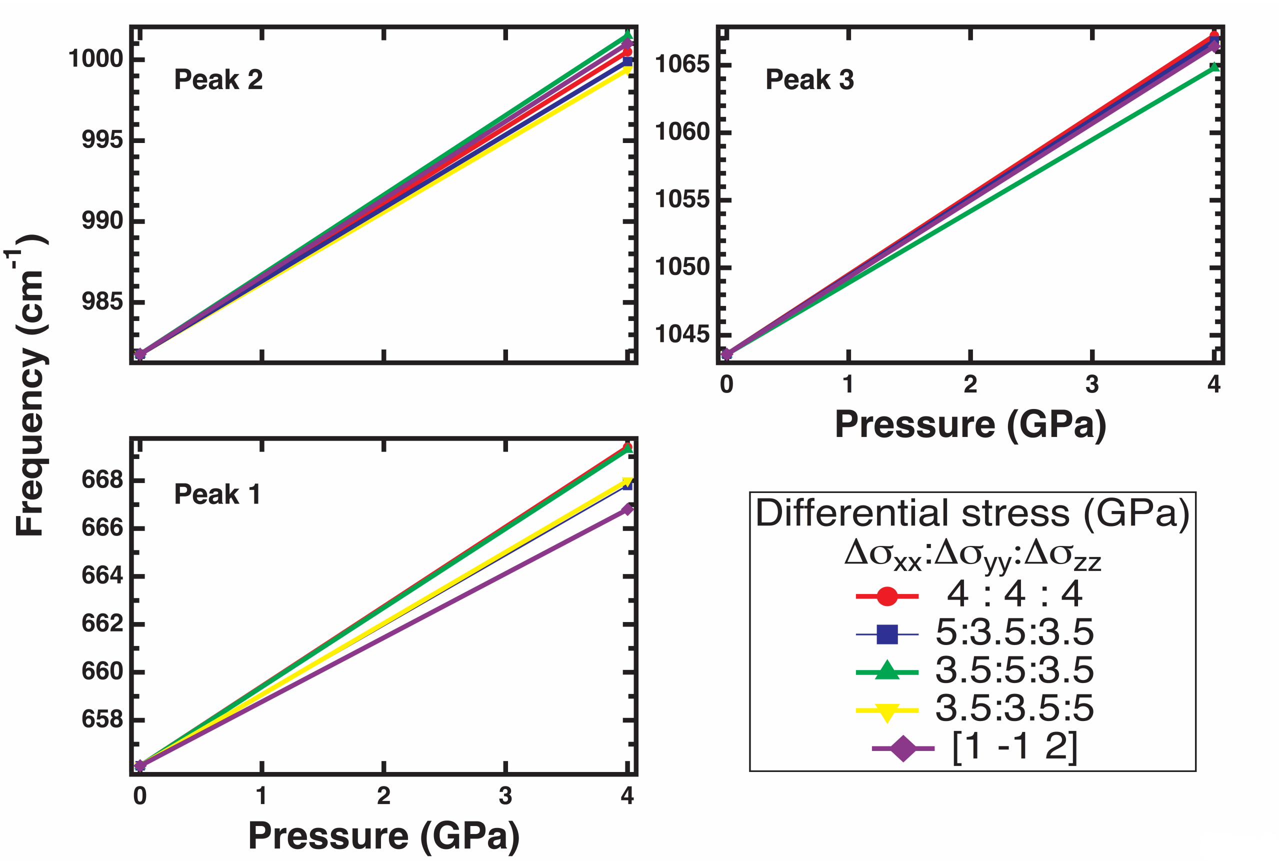

Figure 4.4: Calculated pressure-dependencies of the three main Raman vibrational frequencies of $CaSiO_3$-walstromite at different stress states.

cm^{-1} for Peak 3, which correspond to a mean difference of the ΔP of -0.5 and -0.19 GPa, respectively. Conversely, Peak 2 shows a negative shift when the maximum compression is along $\underline{e}_1$ (i.e. subparallel to the a lattice vector) and $\underline{e}_3$ (i.e. subparallel to the c lattice vector), but a positive shift when the maximum compression is along $\underline{e}_2$ (i.e. parallel to the b lattice vector) and $[1\bar{1}2]$ (i.e. the softest direction, perpendicular to the layers): the mean difference of the $\Delta\nu$ is -0.1 cm^{-1}, which corresponds to a mean difference of the ΔP of -0.02 GPa. This indicates that Peak 2 is the least sensitive to the application of differential stresses, and therefore it is the most reliable peak to be used as a calibrant to calculate the P_{inc} of a $CaSiO_3$-walstromite inclusion.

4.3.4 Inclusion residual pressure

The least sensitive peak to the deviatoric stress suffered by the $CaSiO_3$-walstromite inclusion enclosed in the diamond is Peak 2, as explained in the previous paragraph. For this reason, we used the experimental pressure coefficient for Peak 2, which is 5.16(±0.09) cm^{-1} GPa^{-1}, to calculate the residual pressure (P_{inc}) retained by the $CaSiO_3$-walstromite inclusion found in the natural diamond (Figure 4.1). The main Raman peaks of that inclusion were observed at 669, 999 and 1061 cm^{-1} (Figure 4.5), which are the highest frequencies ever reported in literature for a $CaSiO_3$-walstromite still trapped within its diamond host. The calculation lead to the following residual pressure: 4.26(±0.07) GPa.

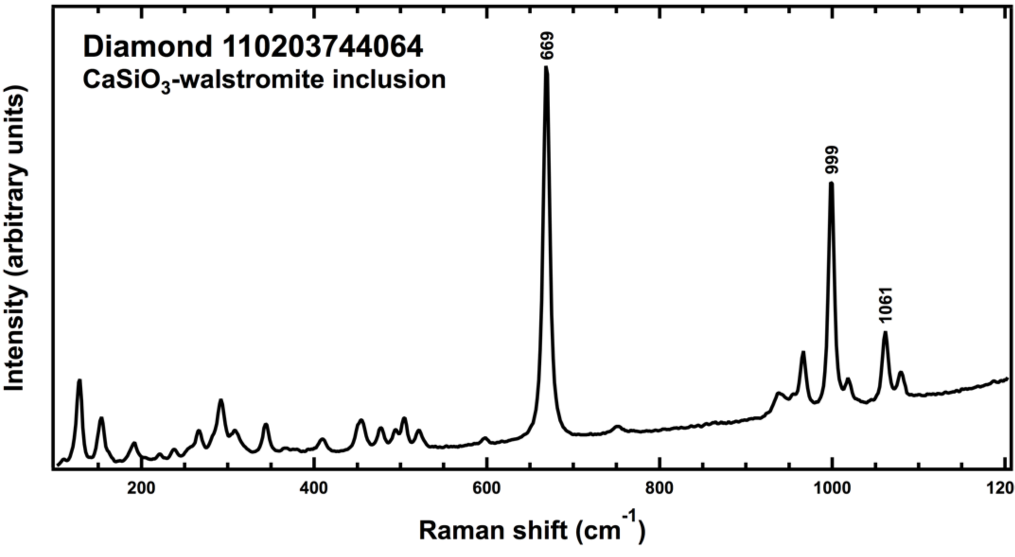

Figure 4.5: Raman spectrum of the $CaSiO_3$-walstromite inclusion found in the natural diamond.

Table 4.3: Calculated shifts of Raman frequencies under hydrostatic and non-hydrostatic stresses. Differences Δν and ΔP are with respect to the hydrostatic value.

State of stress	Peak 1				Peak 2				Peak 3			
	ν (cm^{-1})	Δν (cm^{-1})	dν/dP (cm^{-1}/GPa)	ΔP (GPa)	ν (cm^{-1})	Δν (cm^{-1})	dν/dP (cm^{-1}/GPa)	ΔP (GPa)	ν (cm^{-1})	Δν (cm^{-1})	dν/dP (cm^{-1}/GPa)	ΔP (GPa)
Hydrostatic	669.4	–	3.33	–	1000.5	–	4.68	–	1067.2	–	5.90	–
Non-hydrostatic along $\underline{e}_1$	667.8	–1.6	2.93	-0.5	999.9	–0.6	4.53	-0.13	1066.8	–0.4	5.80	-0.07
Non-hydrostatic along $\underline{e}_2$	669.3	–0.1	3.30	0.0	1001.5	1.0	4.93	0.21	1064.8	–2.4	5.30	-0.45
Non-hydrostatic along $\underline{e}_3$	668.0	–1.4	2.98	-0.5	999.4	–1.1	4.40	-0.26	1066.5	–0.7	5.73	-0.11
Non-hydrostatic along [1 -1 2]	666.8	–2.6	2.68	-1.0	1001.0	0.5	4.80	0.10	1066.4	–0.7	5.70	-0.12
	$\overline{\Delta v}$	–1.4	$\overline{\Delta P}$	-0.5	$\overline{\Delta v}$	–0.1	$\overline{\Delta P}$	-0.02	$\overline{\Delta v}$	–1.0	$\overline{\Delta P}$	-0.19

Notes: positive values mean shift toward higher frequencies, negative values mean shift toward lower frequencies. $\overline{\boldsymbol{\Delta v}}$ and $\overline{\boldsymbol{\Delta P}}$ are the mean difference of the frequency and of the pressure, respectively, evaluated over the set of total numbers of peaks.

4.4 Discussion

The Raman measurements show that the $CaSiO_3$-walstromite inclusion retains a residual pressure, as a consequence of the difference between the thermoelastic properties of the diamond host and those of the $CaSiO_3$-walstromite inclusion. This residual pressure, measured at ambient conditions, can be used to calculate the entrapment pressure and temperature conditions of the host-inclusion pair, provided that the equations of state of the mineral phase and the diamond are known and reliable. The basic concept behind this approach is that, at the moment of entrapment, the host fits the inclusion perfectly and the two are under the same P and T conditions (Izraeli et al. 1999; Howell et al. 2012; Nestola et al. 2012; Angel et al. 2014b, 2015b). However, this method relies on some assumptions: (i) the inclusion is spherical (Eshelby 1957, 1959; Mazzucchelli et al. 2017), (ii) both the host and inclusion are elastically isotropic and homogeneous (Angel et al. 2014b), (iii) at the moment of formation the inclusion perfectly fits in the diamond, (iv) deformation of both the host and the inclusion is elastic and no brittle or plastic deformation has occurred. The assumption that both the host and the inclusion are elastically isotropic implies that the inclusion is under isotropic strains. But the stress state in an anisotropic inclusion subject to isotropic strains (e.g. there is no fluid at the interface, see Nimis et al. 2016) such as $CaSiO_3$-walstromite is never hydrostatic (Anzolini et al. 2016) and, therefore, its Raman shifts may potentially be affected by such non-isotropic deformation. Nevertheless, our results indicate that the second highest peak of $CaSiO_3$-walstromite, located at 977 cm^{-1}, is not very sensitive to non-hydrostatic stress, being the mean difference of the ΔP with respect to the hydrostatic value only -0.02 GPa (see Table 4.3), and thus it is suitable to estimate the remnant pressure of a $CaSiO_3$-walstromite inclusion within a negligible error.

The calculation of the pressure of formation (P_e) for the $CaSiO_3$-walstromite – diamond pair was performed with the software EoSFit7c (Angel et al. 2014a), by following the same method described in Angel et al. (2014b). We used thermal expansion and compressibility data for $CaSiO_3$-walstromite reported in Anzolini et al. (2016), thermoelastic properties for diamond from the review of Angel et al. (2015a) and the residual pressure obtained in this work, which is 4.26(±0.07) GPa.

Assuming a temperature range between 1200 K and 2000 K for $CaSiO_3$-walstromite formation (i.e. the same temperature range at which $CaSiO_3$-walstromite was successfully synthesized by Gasparik et al. 1994), we obtained entrapment pressures ranging from 8.10 to 9.27 GPa (P_{inc} = 4.26(±0.07) GPa) (Table 4.4), corresponding to 240-280 km depth (Figure 4.6). Such pressure can be considered as a minimum estimate because of the presence of cracks around the inclusion (Figure 4.1b), which would partly release the stress (see

Mazzucchelli et al. 2016), and the effect of plastic deformation of diamond, which, if present, is not quantifiable yet. Taking this into consideration, the entrapment pressure could be set at higher values, at least on the boundary between $CaSiO_3$-walstromite and larnite + $CaSi_2O_5$-titanite. Considering instead Peak 1 or Peak 3 with the hydrostatic calibration, the arising error in the entrapment pressure would be ~0.5 and ~0.9 GPa, respectively, corresponding to an underestimation of the depth of about 10-20 km.

Table 4.4: Isomeke calculations for the diamond-$CaSiO_3$-walstromite host-inclusion system.

T (K)	P_e (GPa)
1200	8.100
1300	8.253
1400	8.403
1500	8.551
1600	8.697
1700	8.841
1800	8.984
1900	9.126
2000	9.267

4.5 Implications

In the present work, we provide the first experimental calibration of the Raman shifts of $CaSiO_3$-walstromite under hydrostatic conditions. Our ab initio simulation shows excellent agreement between calculated and experimentally measured Raman vibrational frequencies and intensities. We also present for the first time one possible method to assess the reliability of the hydrostatic calibration for a mineral elastically non-isotropic or subject to non-hydrostatic stress field showing that a careful analysis can provide fundamental insight on the Raman peaks to be used for determining the entrapment pressure for a host-inclusion pair. For example, our results on $CaSiO_3$-walstromite indicate that the main Raman peaks of $CaSiO_3$-walstromite are sensitive to deviatoric stress, with Peak 1 (656 cm^{-1}) and Peak 2 (977 cm^{-1}) showing the largest and smallest shifts, respectively. As a general rule, the use of these peaks is not ideal to retrieve reliable pressures from the Raman shifts. On the other hand, Peak 2, being the least sensitive to deviatoric stresses, can be used as in the present study to calibrate the residual pressure retained by a $CaSiO_3$-walstromite inclusion still trapped in a diamond within a negligible error. This residual pressure was in turn used to estimate, by single-inclusion elastic barometry, the formation depth of the diamond-$CaSiO_3$-walstromite pair, which resulted in $P = \sim 9$ GPa (~260 km) at 1800 K. This can be considered as a minimum value, as the presence of fractures at the diamond-inclusion interface would partly release the internal pressure of the inclusion. These results suggest that the diamond investigated is certainly sub-lithospheric and endorse the hypothesis that the presence of $CaSiO_3$-walstromite is a strong indication of super-deep origin.

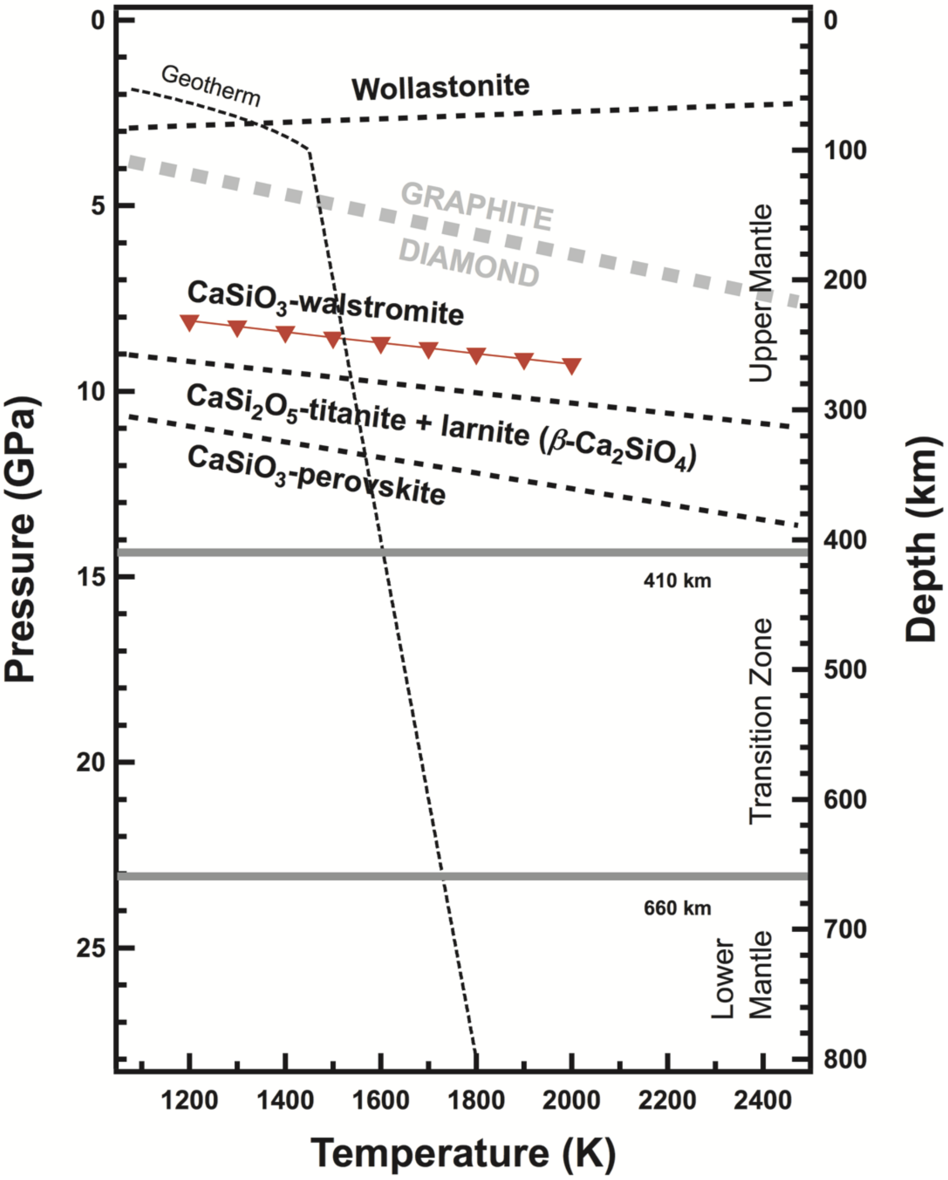

Figure 4.6: Phase diagram of the $CaSiO_3$ system, in which the phase boundaries are given as dotted lines (Essene 1974; Gasparik et al. 1994). The graphite-diamond phase boundary is shown as a grey dashed line (Day 2012). The geotherm is shown as a black dashed line (Turcotte and Schubert 2014). The 410 and 660 km discontinuities enclosing the transition zone are indicated by bold lines. Entrapment pressures from which our sample may have originated are represented with red symbols.

Acknowledgments

This investigation was financially supported by Fondazione Cassa di Risparmio di Padova e Rovigo and by the project INDIMEDEA, funded by the ERC-StG 2012 to F.N. (grant number 307322). M.A. has been supported by the Italian SIR-MIUR MILE DEEp (grant number RBSI140351) and the ERC-StG 2016 TRUE DEPTHS (grant number 714936). Ross J. Angel is thanked for advice and discussion. We are also grateful to H.M. Lamadrid for reviewing the manuscript.

References cited

Angel, R.J., Alvaro, M., and Gonzalez-Platas, J. (2014a) EosFit7c and a Fortran module (library) for equation of state calculations. Zeitschrift für Kristallographie-Crystalline Materials, 229, 405-419.

Angel, R.J., Mazzucchelli, M.L., Alvaro, M., Nimis, P., and Nestola, F. (2014b) Geobarometry from host-inclusion systems: The role of elastic relaxation. American Mineralogist, 99, 2146-2149.

Angel, R.J., Alvaro, M., Nestola, F., and Mazzucchelli, M.L. (2015a) Diamond thermoelastic properties and implications for determining the pressure of formation of diamond-inclusion systems. Russian Geology and Geophysics, 56, 211-220.

Angel, R.J., Nimis, P., Mazzucchelli, M.L., Alvaro, M., and Nestola, F. (2015b) How large are departures from lithostatic pressure? Constraints from host–inclusion elasticity. Journal of Metamorphic Geology, 33, 801-813.

Anzolini, C., Angel, R.J., Merlini, M., Derzsi, M., Tokár, K., Milani, S., Krebs, M.Y., Brenker, F.E., Nestola, F., and Harris, J.W. (2016) Depth of formation of $CaSiO_3$-walstromite included in super-deep diamonds. Lithos, 265, 138-147.

Artioli, G., Angelini, I., and Polla, A. (2008) Crystals and phase transitions in protohistoric glass materials. Phase Transitions, 81, 233-252.

Brenker, F.E., Stachel, T., and Harris, J.W. (2002) Exhumation of lower mantle inclusions in diamond: ATEM investigation of retrograde phase transitions, reactions and exsolution. Earth and Planetary Science Letters, 198, 1-9.

Brenker, F.E., Vincze, L., Vekemans, B., Nasdala, L., Stachel, T., Vollmer, C., Kersten, M., Somogyi, A., Adams, F., and Joswig, W. (2005) Detection of a Ca-rich lithology in the Earth's deep (> 300 km) convecting mantle. Earth and Planetary Science Letters, 236, 579-587.

Brenker, F.E., Vollmer, C., Vincze, L., Vekemans, B., Szymanski, A., Janssens, K., Szaloki, I., Nasdala, L., Joswig, W., and Kaminsky, F. (2007) Carbonates from the lower part of transition zone or even the lower mantle. Earth and Planetary Science Letters, 260, 1-9.

Civalleri, B., D'Arco, P., Orlando, R., Saunders, V., and Dovesi, R. (2001) Hartree–Fock geometry optimisation of periodic systems with the CRYSTAL code. Chemical Physics Letters, 348, 131-138.

Day, H.W. (2012) A revised diamond-graphite transition curve. American Mineralogist, 97, 52-62.

Dovesi, R., Saunders, V., Roetti, C., Orlando, R., Zicovich-Wilson, C., Pascale, F., Civalleri, B., Doll, K., Harrison, N., and Bush, I. (2014) CRYSTAL14 User's Manual. University of Torino, Torino.

Eshelby, J.D. (1957) The determination of the elastic field of an ellipsoidal inclusion, and related problems. In Proceedings of the Royal Society of London A: Mathematical, Physical and Engineering Sciences, p. 376-396. The Royal Society.

Eshelby, J.D. (1959) The elastic field outside an ellipsoidal inclusion. In Proceedings of the Royal Society of London A: Mathematical, Physical and Engineering Sciences, p. 561-569. The Royal Society.

Essene, E. (1974) High-pressure transformations in $CaSiO_3$. Contributions to Mineralogy and Petrology, 45, 247-250.

Frost, D.J. (2008) The upper mantle and transition zone. Elements, 4, 171-176.

Gasparik, T., Wolf, K., and Smith, C.M. (1994) Experimental determination of phase relations in the $CaSiO_3$ system from 8 to 15 GPa. American Mineralogist, 79, 1219-1222.

Harte, B. (2010) Diamond formation in the deep mantle: the record of mineral inclusions and their distribution in relation to mantle dehydration zones. Mineralogical Magazine, 74, 189-215.

Howell, D., Wood, I.G., Nestola, F., Nimis, P. and Nasdala, L. (2012) Inclusions under remnant pressure in diamond: a multi-technique approach. European Journal of Mineralogy, 4, 563-573.

Irifune, T., and Ringwood, A. (1987) Phase transformations in a harzburgite composition to 26 GPa: implications for dynamical behaviour of the subducting slab. Earth and Planetary Science Letters, 86, 365-376.

Izraeli, E., Harris, J., and Navon, O. (1999) Raman barometry of diamond formation. Earth and Planetary Science Letters, 173, 351-360.

Joswig, W., Stachel, T., Harris, J.W., Baur, W.H., and Brey, G.P. (1999) New Ca-silicate inclusions in diamonds—tracers from the lower mantle. Earth and Planetary Science Letters, 173, 1-6.

Kaminsky, F. (2012) Mineralogy of the lower mantle: A review of 'super-deep' mineral inclusions in diamond. Earth-Science Reviews, 110, 127-147.

Lee, C., Yang, W., and Parr, R.G. (1988) Development of the Colle-Salvetti correlation-energy formula into a functional of the electron density. Physical review B, 37, 785.

Mao, H., Xu, J., and Bell, P. (1986) Calibration of the ruby pressure gauge to 800 kbar under quasi-hydrostatic conditions. Journal of Geophysical Research: Solid Earth, 91, 4673-4676.

Maschio, L., Kirtman, B., Orlando, R., and Rèrat, M. (2012) Ab initio analytical infrared intensities for periodic systems through a coupled perturbed Hartree-Fock/Kohn-Sham method. The Journal of chemical physics, 137, 204113.

Maschio, L., Kirtman, B., Rérat, M., Orlando, R., and Dovesi, R. (2013) Ab initio analytical Raman intensities for periodic systems through a coupled perturbed Hartree-Fock/Kohn-Sham method in an atomic orbital basis. I. Theory. The Journal of chemical physics, 139, 164101.

Mazzucchelli, M.L., Angel, R.J., Rustioni, G., Milani, S., Nimis, P., Domeneghetti, M.C., Marone, F., Harris, J.W., Nestola, F., and Alvaro, M. (2016) Elastic geobarometry and the role of brittle failure on pressure release. In EGU General Assembly Conference Abstracts, p. 13569.

Mazzucchelli, M.L., Burnley, P.C., Angel, R.J., Domeneghetti, M.C., Nestola, F., and Alvaro, M. (2017) Elastic geobarometry: uncertainties arising from the geometry of the host-inclusion system, In EGU General Assembly Conference Abstracts, p. 2060.

Milani, S., Nestola, F., Angel, R., Nimis, P., and Harris, J. (2016) Crystallographic orientations of olivine inclusions in diamonds. Lithos, 265, 312-316.

Monkhorst, H.J., and Pack, J.D. (1976) Special points for Brillouin-zone integrations. Physical review B, 13, 5188.

Nasdala, L., Brenker, F.E., Glinnemann, J., Hofmeister, W., Gasparik, T., Harris, J.W., Stachel, T., and Reese, I. (2003) Spectroscopic 2D-tomography Residual pressure and strain around mineral inclusions in diamonds. European journal of mineralogy, 15, 931-935.

Nestola, F., Merli, M., Nimis, P., Parisatto, M., Kopylova, M., De Stefano, A., Longo, M., Ziberna, L., and Manghnani, M. (2012) In situ analysis of garnet inclusion in diamond using single-crystal X-ray diffraction and X-ray micro-tomography. European Journal of Mineralogy, 24, 599-606.

Nestola, F., Nimis, P., Angel, R., Milani, S., Bruno, M., Prencipe, M., and Harris, J. (2014) Olivine with diamond-imposed morphology included in diamonds. Syngenesis or protogenesis?. International Geology Review, 56, 1658-1667.

Nestola, F., Burnham, A.D., Peruzzo, L., Tauro, L., Alvaro, M., Walter, M.J., Gunter, M., Anzolini, C., and Kohn, S.C. (2016) Tetragonal Almandine-Pyrope Phase, TAPP: finally a name for it, the new mineral jeffbenite. Mineralogical Magazine, 80, 1219-1232.

Nestola, F., Jung, H. and Taylor, L.A. (2017) Mineral inclusions in diamonds may be synchronous but not syngenetic. Nature communications, 14168.

Nimis, P., Alvaro, M., Nestola, F., Angel, R.J., Marquardt, K., Rustioni, G., Harris, J.W., and Marone, F. (2016) First evidence of hydrous silicic fluid films around solid inclusions in gem-quality diamonds. Lithos, 260, 384-389.

Pascale, F., Zicovich-Wilson, C.M., Lopez Gejo, F., Civalleri, B., Orlando, R., and Dovesi, R. (2004) The calculation of the vibrational frequencies of crystalline compounds and its implementation in the CRYSTAL code. Journal of computational chemistry, 25, 888-897.

Pearson, D., Brenker, F., Nestola, F., McNeill, J., Nasdala, L., Hutchison, M., Matveev, S., Mather, K., Silversmit, G., and Schmitz, S. (2014) Hydrous mantle transition zone indicated by ringwoodite included within diamond. Nature, 507, 221-224.

Ringwood, A. (1991) Phase transformations and their bearing on the constitution and dynamics of the mantle. Geochimica et Cosmochimica Acta, 55, 2083-2110.

Stachel, T., and Harris, J. (2008) The origin of cratonic diamonds – constraints from mineral inclusions. Ore Geology Reviews, 34, 5-32.

Turcotte, D., and Schubert, G. (2014) Geodynamics, 3rd ed. Cambridge University Press.

Van der Molen, I., and Van Roermund, H. (1986) The pressure path of solid inclusions in minerals: the retention of coesite inclusions during uplift. Lithos, 19, 317-324.

Wu, Z., and Cohen, R.E. (2006) More accurate generalized gradient approximation for solids. Physical Review B, 73, 235-116.

Supplementary material

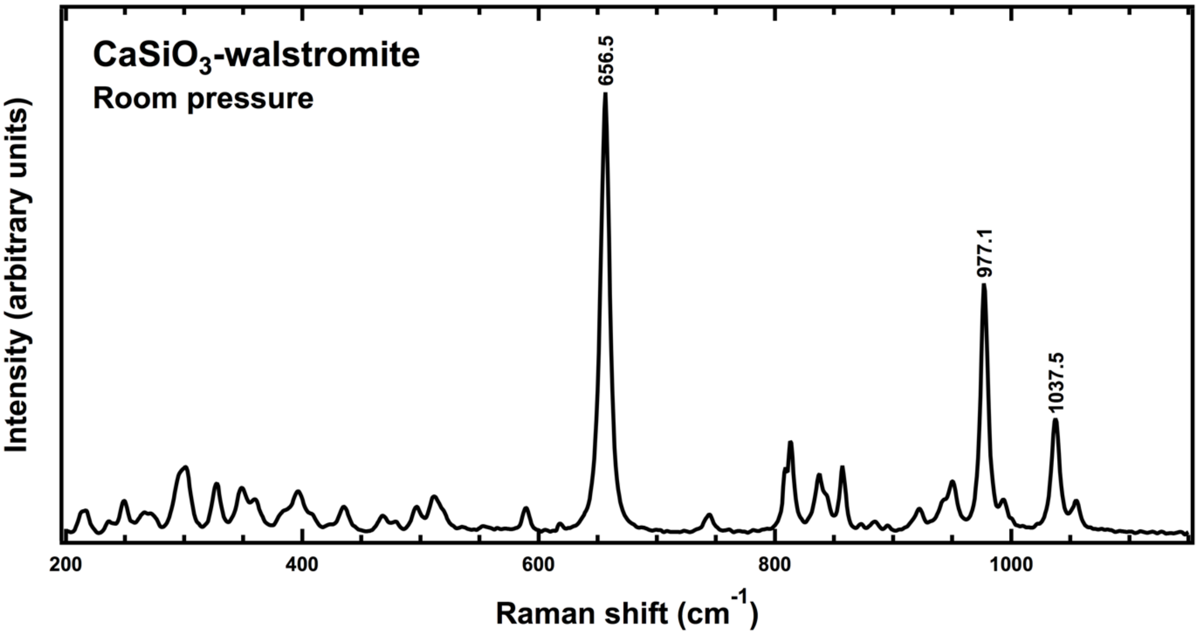

Figure 4.7: Raw Raman spectrum of synthetic CaSiO$_3$-walstromite at room pressure.

$P_{\text{hydrostatic}} = 0$ GPa		$P_{\text{hydrostatic}} = 4$ GPa	
Frequency (cm^{-1})	Relative intensity	Frequency (cm^{-1})	$\Delta\nu$ (cm^{-1})
80.6	60	88.3	7.7
99.8	12	109.6	9.8
111.0	24	120.2	9.2
133.7	101	134.5	0.8
153.0	23	155.3	2.3
153.5	20	159.6	6.1
165.2	58	166.1	0.9
179.7	57	191.3	11.6
189.3	8	197.6	8.3
203.6	34	209.4	5.8
213.4	20	221.8	8.4
218.2	66	237.9	19.7
239.3	43	257.2	17.9
252.7	48	265.2	12.5
256.1	3	269.2	13.1
273.0	30	286.4	13.4
277.2	35	295.9	18.7
293.3	19	305.2	11.9
299.6	53	312.2	12.6
305.4	64	322.2	16.8
328.8	81	344.6	15.8
352.4	71	370.1	17.7
364.6	61	381.9	17.3
385.9	24	397.3	11.4
399.5	65	412.3	12.8
442.0	39	451.2	9.2
447.0	7	457.9	10.9
469.8	40	476.7	6.9
480.0	37	494.3	14.3
496.9	42	502.7	5.8
510.6	35	519.7	9.1
513.3	35	523.0	9.7
595.4	40	602.2	6.8
656.1	1000	669.4	13.3
749.1	9	755.9	6.8
753.8	32	760.3	6.5
865.7	4	870.0	4.3
920.8	13	938.5	17.7
939.6	2	948.0	8.4
952.9	66	959.9	7.0
957.8	45	970.2	12.4
981.8	342	1000.5	18.7
995.6	22	1018.5	22.9
1043.6	165	1067.2	23.6
1063.7	36	1084.3	20.6

5 New stability field of jeffbenite (ex-“TAPP”): possible marker for diamonds super-deep origin

Chiara Anzolini[1], James W.E. Drewitt[2], Oliver T. Lord[2], Michael J. Walter[2] and Fabrizio Nestola[1]

[1]Department of Geosciences, University of Padova, Via G. Gradenigo 6, 35131 Padova, Italy

[2]School of Earth Sciences, University of Bristol, Queens Road, Bristol BS8 1RJ, United Kingdom

The paper has to be submitted.

Abstract

Jeffbenite is a new tetragonal phase with garnet-like stoichiometry previously referred to as TAPP (Tetragonal Almandine-Pyrope Phase), which is found exclusively in nature as inclusions in super-deep diamonds and may provide key information about their depth of formation. Nevertheless, whether jeffbenite forms as a primary phase in the transition zone or in the lower mantle, or is the product of retrogression from high-pressure mantle phases is still controversial. The only previously experimentally determined stability field for jeffbenite provides a maximum stability pressure of ~13 GPa (~320 km) at 1700 K. This suggested that jeffbenite is a sub-lithospheric mineral and could be stable in the shallower part of the transition zone, but ruled out its direct incorporation into diamond at the transition zone-lower mantle boundary or further down. These results were obtained on a Ti-rich jeffbenite, which is usually found as part of composite inclusions, and not on a Ti-free jeffbenite, which occurs as single-crystal inclusions within diamonds. We therefore performed new laser heated diamond-anvil cell experiments from 5 to 30 GPa on a synthetic Ti-free jeffbenite, in order to determine the role that TiO_2 plays in its stability field and to determine if jeffbenite can be directly incorporated into diamond in the deep transition zone or lower mantle. Our results indicate that the absence of TiO_2 extends the stability field of jeffbenite to ~23 GPa (~660 km) at 1600 K, demonstrating that Ti-free jeffbenite may represent one of the most reliable markers for the origin of super-deep diamonds.

5.1 Introduction

Diamonds and the mineral inclusions that they trap during growth provide a unique window on the deep Earth. A rare group (~6%) of diamonds (Stachel and Harris, 2008) is interpreted to crystallize between 300 and 800 km depth (Harte, 2010) because many of the inclusions entrapped are composites of multiple minerals and show evidence of retrograde transformation from lower-mantle or transition-zone precursors. However, undisputed evidence of these purported high-pressure precursors as inclusions in diamonds is frequently missing, and, consequently, their real depth of origin has been proven only in few cases (e.g. Brenker et al., 2002; Pearson et al., 2014; Smith et al., 2016). Most so-called "super-deep diamonds" contain mainly walstromite-structured $CaSiO_3$, ferropericlase [(Fe,Mg)O)], enstatite-structured $MgSiO_3$ and jeffbenite $[(Mg,Fe)_3Al_2Si_3O_{12}]$.

Jeffbenite is a new official mineral (IMA No. 2014-097; Nestola et al., 2016), previously referred to as TAPP (Tetragonal Almandine-Pyrope Phase), which occurs in nature exclusively as composite or homogeneous inclusions in super-deep diamonds, and, thus, may provide key information about their depth of formation. Jeffbenite is a tetragonal phase with garnet-like stoichiometry discovered as small inclusions of 30-100 μm in diameter in diamonds from the São Luiz placer deposit in the Juina area, Brazil (Harte and Harris, 1994; Harris et al., 1997; Harte et al., 1999; Zedgenizov et al., 2014). Subsequently, it was identified in diamonds from other placers and kimberlite pipes of the same area and in Guinea placer, Kankan (Stachel et al., 2000; Kaminsky et al., 2001; Hayman et al., 2005; Burnham et al., 2016). Based on all possible compositions reported in literature so far, jeffbenite can be classified in three main compositional groups: 1) Ti-free and low-Fe jeffbenite; 2) Ti-rich and high-Fe jeffbenite; and 3) Ti-rich and low-Fe jeffbenite (Nestola et al., 2016). Among these, Ti-free and Fe-rich jeffbenites occur as up to ~100 μm single-phase inclusions, while Ti-rich jeffbenites are found as composite inclusions in diamonds.

Since its first discovery, whether jeffbenite is a primary phase or the retrograde transformation product from other high-pressure precursors has been controversial and two schools of thought have developed. Based upon the coexistence of jeffbenite with other purported deep mantle phases, such as ferropericlase, retrogressed enstatite and retrogressed $CaSiO_3$-walstromite (Harris et al., 1997; Harte et al., 1999; Hutchison et al., 2001; Kaminsky et al., 2001; Brenker et al., 2002; Hayman et al., 2005;), and its capacity to hold ferric iron, as it was demonstrated that in deep mantle silicates Fe^{3+} is significantly abundant (McCammon et al., 1997; Harte, 2010), it has been suggested that jeffbenite is a primary phase with a limited stability field at the transition zone-lower mantle boundary. By contrast, the absence of octahedral silicon in the crystal structure, which is typical of high-pressure silicates below 200 km depth, makes a lower-mantle origin difficult to explain if the jeffbenite structure is primary (Harris et al., 1997; Finger and Conrad, 2000).

A first attempt to solve this debate was done by Armstrong and Walter in 2012, when they performed laser heating diamond-anvil cell (LH-DAC) experiments from 6 to 48 GPa and 1300-2100 K on an average Ti-bearing jeffbenite bulk composition and showed that it is stable at a maximum of ~13 GPa (~360 km) at 1700 K, which is consistent with tetrahedrally coordinated Si in the jeffbenite inclusions (Finger and Conrad, 2000). This confirms that jeffbenite is a sub-lithospheric mineral that could crystallize in the shallower part of the transition zone, but rules out direct incorporation of jeffbenite in diamond at the transition zone-lower mantle boundary or deeper. On the basis of this, two possibilities were proposed for its formation: 1) entrapment as a primary mineral by diamond in the upper mantle at pressures up to 13 GPa (Armstrong and Walter, 2012); 2) retrograde formation from a bridgmanite or a majoritic garnet below 13 GPa (Brenker et al., 2002; Armstrong and Walter, 2012; Harte and Hudson, 2013). However, these results were obtained on a Ti-rich jeffbenite, which is usually found as part of composite inclusions, and not on a Ti-free jeffbenite, which occurs as single-crystal inclusions within diamonds (Nestola et al., 2016).

We therefore report here new LH-DAC experiments from 5 to 30 GPa on a synthetic Ti-free jeffbenite, in order to determine the role that TiO_2 plays in the stability field of jeffbenite and to figure out if the latter can be directly incorporated into diamond in the deepest regions of the transition zone or in the lower mantle, thus, representing one of the most reliable markers for the origin of super-deep diamonds.

5.2 Methods

5.2.1 Starting materials

The glass starting material, based on the composition of the Ti-free jeffbenite inclusion extracted from a diamond and reported in Nestola et al. (2016), was formed by laser melting a pellet of oxide starting material within an aerodynamic levitation with CO_2 laser heating device at the Institut de Physique du Globe de Paris. Fragments of the resulting glass were mounted in epoxy and polished, then analyzed using a Cameca SX100 electron microprobe at the University of Bristol. Operating conditions were 20 kV and 10 nA with a beam size of 5 μm. The chemical compositions of the glasses used in this study are listed in Table 5.1.

Table 5.1: Chemical composition of starting materials compared to the composition of the holotype of jeffbenite.

Oxide (wt.%)	**H_1**	**H_4**	**H_5**	**B_1**	**B_3**	**B_7**	**Holotype** (Nestola et al., 2016)
SiO_2	43.507	43.497	41.299	41.230	42.510	42.988	41.740
TiO_2	0.043	0.029	0.044	0.005	0.001	0.009	0.060
Al_2O_3	24.039	24.462	25.816	24.696	23.947	24.285	23.840
Cr_2O_3	1.371	1.092	0.906	2.517	1.471	0.984	2.860
FeO_{tot}	4.752	4.614	3.843	4.783	5.471	5.403	4.590
MnO	0.764	0.761	0.717	0.027	0.009	0.003	0.790
MgO	25.416	25.682	27.259	26.483	26.490	26.040	25.160
Total	99.891	100.137	99.885	99.741	99.900	99.712	99.230

For the DAC experiments, fragments of glass were double polished to a thickness of 10-20 μm. Discs of glass with a diameter of 80 μm were cut out of the polished slabs using an UV laser and cleaned in acetone. A second batch of glass was ground to a fine powder and mixed together: glasses with the prefix "H" resulted in a final mixture labelled "H_ox", glasses with the prefix "B" resulted in a final mixture labelled "B_ox" (see Table 5.2).

5.2.2 Diamond-anvil cell experiments

LH-DAC experiments were performed in symmetric diamond-anvil cells with culet sizes of 250 μm. Rhenium gaskets were pre-indented to a thickness of ~50 μm. In the first set of experiments the glass sample discs were loaded in between SiO_2 insulators into 90 μm diameter laser-drilled sample chambers. In a second set of experiments, the powdered-glass starting material, mixed with 10 wt% Pt black as a laser absorber, was loaded into four 30 μm diameter chambers laser-drilled in the indentation. This four-chamber design has the advantage to allow a range of temperatures and pressures to be investigated in a single run. In this case, the chamber size was purposefully optimized to match the laser focal size in order to heat as much of the sample as uniformly as possible, so as to minimize the amount of unreacted or partially reacted material that can complicate interpretation of diffraction measurements. To prevent contamination, no insulating material was used. In both the sets of experiments the pressure was measured from the Raman shift of the singlet peak of diamond culet (Hanfland et al., 1986). In this way, we avoid putting ruby (Al_2O_3) grains in the sample chamber for a pressure marker and, unlike ruby, the signal from this peak remains strong and highly resolvable even to the Mbar range. Raman measurements are made with a Jobin-Yvon T64000 Raman spectrometer using a confocal aperture of 200 µm and the Raman shift is calibrated relative to the ruby scale (Mao et al., 1986). The precision to which pressure can be measured with the Raman peak is about 0.1 GPa, although the accuracy is poorer (~2 GPa) due to uncertainty in measuring the ruby pressure. Pressures are measured before and after heating. Typically, post-heating pressures are within 5% of the pre-heating pressure. All reported pressures are post-heating measurements. In experiments without insulators, thermal pressure has not been taken into account as it is calculated to be approximately 10% of the sample pressure at low temperatures (Heinz, 1990).

Double-sided laser heating was performed at the University of Bristol, where 100 W fiber lasers produced heated spots that were 20-30 µm in diameter. Samples were heated to a target maximum temperature and held for between 30 and 60 min before quenching by shutting off the laser power. Mean temperature is calculated as the average of all temperatures measured across a 20-25 µm strip across the sample and throughout the duration of the experiment and uncertainty estimated as $\pm 2\sigma$ of the mean. Here we will refer to mean temperatures when discussing experimental conditions, and all subsolidus data points are plotted on the basis of mean temperatures. The configuration of the laser heating setup and the spectroradiometric method employed for temperature measurement are detailed by Walter and Koga (2004) and Lord et al. (2014).

5.2.3 Synchrotron X-ray diffraction

Synchrotron X-ray powder diffraction measurements were made for the P-T quenched samples at beamline I15 of the Diamond Light Source (DLS) at the Rutherford Appleton Laboratory, UK. The monochromatic X-ray beam had a diameter of ~6 µm and a wavelength of 0.4133 Å. The acquisition time was typically 10 s and the sample to detector distance was calibrated using a CeO_2 standard. Diffraction patterns were preliminarily integrated into 1-

D spectra using the program Dioptas (Prescher and Prakapenka, 2015) and then fitted and indexed with the software HighScore Plus (PANalytical).

5.3 Results

LH-DAC experiments were performed at pressures from 5 to 30 GPa and temperatures from 1600 to 1800 K with the aim of locating the *P*-*T* stability field of Ti-free jeffbenite. Experimental phase conditions and resulting phase assemblages determined by X-ray diffraction are listed in Table 5.2 and shown in Figure 5.2. Due to heating issues, experiments performed on glass discs were excluded. Experiments on ground glass sometimes contain traces of stishovite as a result of steeper temperature gradients that occur due to the lack of insulating material, resulting in more pronounced Soret diffusion, which can cause Si to diffuse to regions of hotter temperature (Andrault and Fiquet, 2001; Sinmyo and Hirose, 2010; Armstrong et al., 2012).

Table 5.2: Experimental conditions and run products of LH-DAC experiments on jeffbenite bulk compositions.

Sample name	**Starting material**	**Final *P* (GPa)**	**Temperature (K)**	**Duration (min)**	**Run products**
H_ox_2_A	Ground glass	6.0	1700	60	En + PBrk
H_ox_4_A	Ground glass	6.5	1750	50	En
H_ox_2_C	Ground glass	8.5	1600	30	En + Ol +PBrk
H_ox_2_B	Ground glass	9.5	1700	60	En + Ol + PBrk
H_ox_4_B	Ground glass	9.5	1750	50	En + PBrk
H_ox_6_C	Ground glass + Pt black	10.5	1600	30	En + Ol + PBrk
H_ox_3_A	Ground glass	10.5	1800	30	Grt + En
H_ox_3_B	Ground glass	11.5	1600	40	Grt + En +Ol + PBrk
H_ox_1_B	Ground glass	13.5	1600	60	Grt + PBrk
H_ox_2_D	Ground glass	15.5	1600	45	Grt + En + PBrk + Coe + Sti
H_ox_5_A	Ground glass + Pt black	16.0	1600	55	Grt + Jfb + Sti
H_ox_1_C	Ground glass	16.5	1600	20	En + PBrk
H_ox_7_B	Ground glass + Pt black	18.0	1800	45	Brd + Grt + Sti
B_ox_1_C	Ground glass	18.5	1600	30	Grt + PBrk
H_ox_5_B	Ground glass + Pt black	23.0	1600	50	Jfb + Sti
H_ox_3_C	Ground glass	24.0	1800	60	Grt
H_ox_1_D	Ground glass	25.5	1600	30	Grt + Sti
H_ox_3_D	Ground glass	31.0	1600	60	Grt + Sti

En=enstatite, PBrk=pseudobrookite, Ol=olivine, Grt=garnet, Coe=coesite, Sti=stishovite, Jfb=jeffbenite, Brd=bridgmanite. Note: all the diffractograms are reported in Appendix B.

In the lowest-pressure experiments carried out, in the range 5–10 GPa, enstatite coexists with olivine, plus minor amounts of pseudobrookite. At ~10 GPa garnet starts to crystallize and often coexists with enstatite and/or pseudobrookite; in two runs also traces of stishovite are present. At 18 GPa a mixture of garnet and bridgmanite with small amounts of stishovite formed. From ~24 to 31 GPa majoritic garnet is the only mineral to crystallize, with minor amounts of stishovite. Ti-free jeffbenite was synthesized at 16 GPa, together with garnet, and at 23 GPa at 1600 K (Figure 5.1); in both runs also traces of stishovite are present.

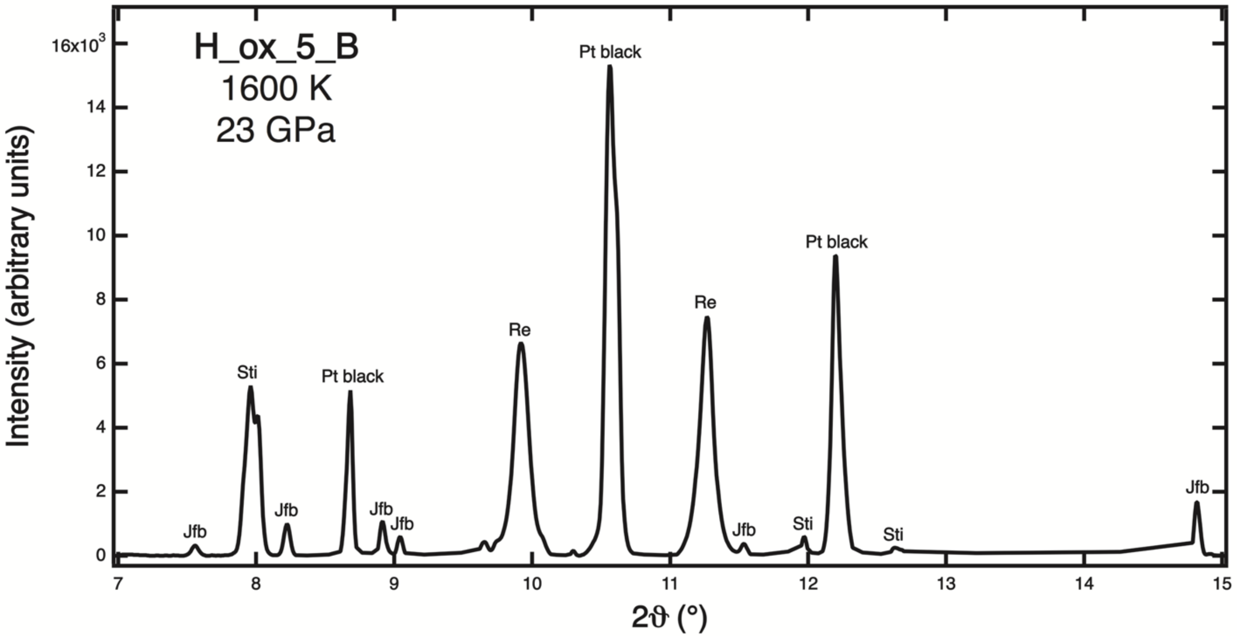

Figure 5.1: Powder diffraction pattern of jeffbenite + stishovite quenched from 23 GPa to 1600 K (run H_ox_5_B).

Due to the widespread presence of pseudobrookite, maybe attributable to poor oxide mixing, and to the fact that its second most intense peak (2.656 Å) is located approximately at the same *d* spacing of the most intense peak of jeffbenite (2.647 Å), it is possible neither to confirm nor exclude the presence of the latter in most of the runs carried out. Despite this, we can affirm that Ti-free jeffbenite is stable at 16 and 23 GPa. This indicates that the absence of Ti extends the stability field of jeffbenite to higher pressures (green area) than previously determined (yellow area).

5.4 Discussion and Conclusions

The main argument in favor of a super-deep origin for jeffbenite is its coexistence in the same diamond with minerals, which are interpreted to have crystallized in the transition zone or lower mantle (Harris et al., 1997; Harte et al., 1999; Hutchison et al., 2001; Brenker et al., 2002; Hayman et al., 2005; Kaminsky, 2012). An origin for jeffbenite in the lower mantle is also supported by its capacity to hold ferric iron (McCammon et al., 1997; Harte, 2010). On the other hand, its relatively low density and low cation coordination numbers, which would be unusual for a lower-mantle phase, favor a region of jeffbenite stability at shallower depths (Harris et al., 1997; Finger and Conrad, 2000). Thus, whether jeffbenite forms as a primary phase in the lower mantle or is the product of retrogression from high-pressure mantle phases has been a matter of important debate during the years.

The first experimentally determined stability field for jeffbenite (Armstrong and Walter, 2012), provided a maximum pressure for a Ti-rich jeffbenite stability of ~13 GPa (~360 km) at 1700 K (Figure 5.2). According to this result, the authors ruled out a lower-mantle origin for jeffbenite and drew the conclusion that it is either trapped as a primary phase in the upper mantle, or it originates as a high-pressure phase with a different structure, perhaps bridgmanite or majoritic garnet, and it reverses during exhumation. These conclusions were also accepted by Harte and Hudson (2013), with only slight reservations.

Our new results obtained on a Ti-free jeffbenite, instead, indicate that it is stable at a maximum of ~23 GPa (~660 km) at 1600 K (Figure 5.2). This admits direct incorporation of jeffbenite in diamonds at the base of the transition zone or top of the lower mantle, along with the other purported high-pressure precursors found in jeffbenite-bearing diamonds (Harris et al., 1997; Harte et al., 1999; Hutchison et al., 2001), but still does not explain the formation of jeffbenite-bearing composite inclusions unless such composite inclusions were trapped at high pressure as a mixture of several phases (Armstrong and Walter, 2012).

We therefore propose that Ti-rich jeffbenite, which is found as part of polyphase inclusions, and Ti-free jeffbenite, which occurs as single-phase inclusions, form by two different processes. Ti-rich jeffbenite, which was found to be stable at a maximum of ~13

GPa at 1700 K, is likely to be the retrograde transformation product from a high-pressure phase. In the majority of cases this precursor phase can be reasonably thought to be bridgmanite (Armstrong and Walter, 2012; Harte and Hudson, 2013), while when jeffbenite occurs in a composite inclusion with NaAl-pyroxene (Brenker et al., 2002), this clearly indicates formation from a majoritic garnet (Armstrong and Walter, 2012; Harte and Hudson, 2013). For some unusual composite inclusions, such those reported by Hutchison et al. (2001) and Hayman et al. (2005), instead, another high-pressure precursor must be considered.

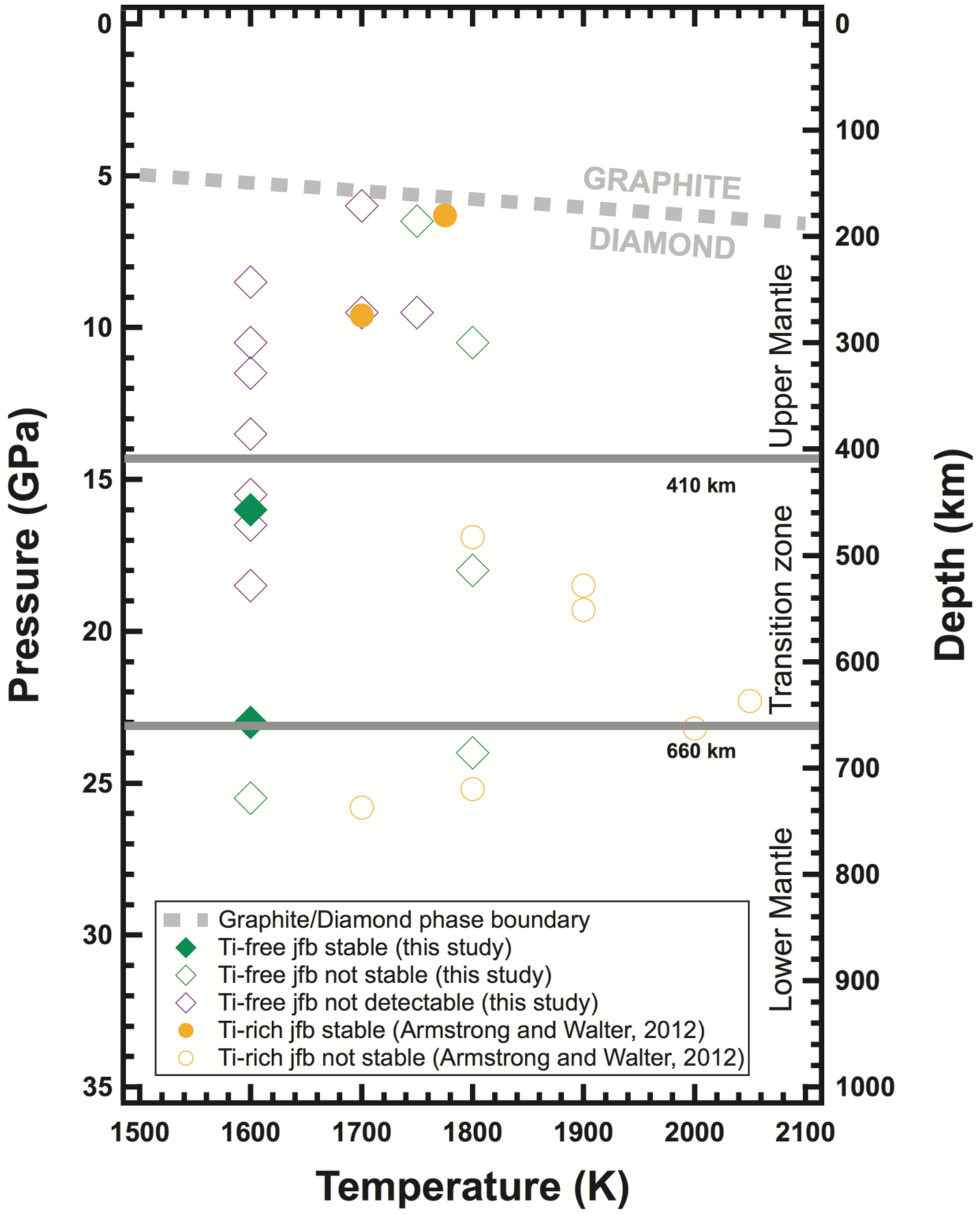

Figure 5.2: Results of phase equilibria experiments from 5 to 30 GPa and from 1600 to 1800 K. For a purpose of comparison, results by Armstrong and Walter (2012) are also plotted. Full symbols represent runs were jeffbenite was stable; empty symbols were jeffbenite was either not stable or not detectable because of the overlapping with pseudobrookite.

Ti-free jeffbenite, on the other hand, which we demonstrated forms at a maximum of ~23 GPa at 1600 K, is likely to be stable only over a narrow range of *P* and *T* and, over this span, only in very specific bulk compositions, as first suggested by Harris et al. (1997) and Harte et al. (1999). This would also explain why jeffbenite has been missed in prior experimental studies, allows encapsulation of it as a primary phase within diamonds at *P*-*T* conditions corresponding to its stability field, i.e. transition zone – uppermost lower mantle, and confirming what many authors proposed so far (Harris et al., 1997; McCammon et al., 1997; Harte et al., 1999; Hutchison et al., 2001; Kaminsky et al., 2001; Brenker et al., 2002; Hayman et al., 2005; Harte, 2010; Bulanova et al., 2010; Zedgenizov et al., 2014). Thus, in conclusion, Ti-free jeffbenite could be considered one of the most reliable markers for diamonds super-deep origin.

Acknowledgments

This work was supported by Fondazione Cassa di Risparmio di Padova e Rovigo, NERC Grant NE/M000419/1 to MJW, NERC Fellowship Grant NE/J018945/1 to OTL and ERC Starting Grant INDIMEDEA ERC-2012-StG-307322 to FN. We thank Diamond Light Source for access to beamline I15 that contributed to the results presented here, and for assistance from Simone Anzellini and Dominik Daisenberger in operating the beamline. We are grateful to James Badro, Richard Brooker and Andrew R. Thomson for helping with the sample preparation and to Stuart Kearns and Benjamin Buse for contributing microprobe time. Federico Zorzi is thanked for aiding with the use of HighScore Plus.

References cited

Andrault, D., and Fiquet, G., 2001, Synchrotron radiation and laser heating in a diamond anvil cell: Review of Scientific Instruments, v. 72, no. 2, p. 1283-1288.

Anzolini, C., Nestola, F., Burnham, A.D., et al., 2015, Diffraction and spectroscopic characterization of jeffbenite: a high-pressure marker in diamonds: Periodico di Mineralogia, no. ECMS, p. 21-22.

Armstrong, L.S., and Walter, M.J., 2012, Tetragonal almandine pyrope phase (TAPP): retrograde Mg-perovskite from subducted oceanic crust?: European Journal of

Mineralogy, v. 24, no. 4, p. 587-597.

Armstrong, L., Walter, M., Tuff, J., Lord, O., Lennie, A., Kleppe, A., and Clark, S., 2012, Perovskite phase relations in the system CaO–MgO–TiO_2–SiO_2 and implications for deep mantle lithologies: Journal of Petrology, v. 53, no. 3, p. 611-635.

Brenker, F.E., Stachel, T., and Harris, J.W., 2002, Exhumation of lower mantle inclusions in diamond: ATEM investigation of retrograde phase transitions, reactions and exsolution: Earth and Planetary Science Letters, v. 198, no. 1, p. 1-9.

Burnham, A., Bulanova, G., Smith, C., Whitehead, S., Kohn, S., Gobbo, L., and Walter, M., 2016, Diamonds from the Machado River alluvial deposit, Rondônia, Brazil, derived from both lithospheric and sublithospheric mantle: Lithos, v. 265, p. 199-213.

Finger, L.W., and Conrad, P.G., 2000, The crystal structure of “tetragonal almandine-pyrope phase” (TAPP): A reexamination: American Mineralogist, v. 85, no. 11-12, p. 1804-1807.

Hanfland, M., Syassen, K., Fahy, S., Louie, S.G., and Cohen, M.L., 1986, The first-order Raman mode of diamond under pressure: Physica B C, v. 139, p. 516-519.

Harris, J., Hutchison, M., Hursthouse, M., Light, M., and Harte, B., 1997, A new tetragonal silicate mineral occurring as inclusions in lower-mantle diamonds: Nature, v. 387, no. 6632, p. 486-488.

Harte, B., 2010, Diamond formation in the deep mantle: the record of mineral inclusions and their distribution in relation to mantle dehydration zones: Mineralogical Magazine, v. 74, no. 2, p. 189-215.

Harte, B., and Harris, J., 1994, Lower mantle mineral associations preserved in diamonds: Mineralogical Magazine, v. 58, no. AK, p. 384-385.

Harte, B., Harris, J., Hutchison, M., Watt, G., and Wilding, M., 1999, Lower mantle mineral associations in diamonds from Sao Luiz, Brazil: Mantle petrology: Field observations and high-pressure experimentation: A tribute to Francis R.(Joe) Boyd, v. 6, p. 125-153.

Harte, B., and Hudson, N.F., 2013, Mineral associations in diamonds from the lowermost upper mantle and uppermost lower mantle, *in* Proceedings of 10th International

Kimberlite Conference, Springer, p. 235-253.

Hayman, P.C., Kopylova, M.G., and Kaminsky, F.V., 2005, Lower mantle diamonds from Rio Soriso (Juina area, Mato Grosso, Brazil): Contributions to Mineralogy and Petrology, v. 149, no. 4, p. 430-445.

Heinz, D.L., 1990, Thermal pressure in the laser-heated diamond anvil cell: Geophysical Research Letters, v. 17, no. 8, p. 1161-1164.

Hutchison, M.T., Hursthouse, M., and Light, M., 2001, Mineral inclusions in diamonds: associations and chemical distinctions around the 670-km discontinuity: Contributions to Mineralogy and Petrology, v. 142, no. 1, p. 119-126.

Kaminsky, F., Zakharchenko, O., Davies, R., Griffin, W., Khachatryan-Blinova, G., and Shiryaev, A., 2001, Superdeep diamonds from the Juina area, Mato Grosso State, Brazil: Contributions to Mineralogy and Petrology, v. 140, no. 6, p. 734-753.

Kaminsky, F., 2012, Mineralogy of the lower mantle: A review of ‘super-deep’ mineral inclusions in diamond: Earth-Science Reviews, v. 110, no. 1, p. 127-147.

Lord, O.T., Wann, E.T., Hunt, S.A., et al., 2014, The NiSi melting curve to 70 GPa: Physics of the Earth and Planetary Interiors, v. 233, p. 13-23.

Mao, H., Xu, J., and Bell, P., 1986, Calibration of the ruby pressure gauge to 800 kbar under quasi-hydrostatic conditions: Journal of Geophysical Research: Solid Earth, v. 91, no. B5, p. 4673-4676.

McCammon, C., Hutchison, M., and Harris, J., 1997, Ferric iron content of mineral inclusions in diamonds from Sao Luiz: a view into the lower mantle: Science, v. 278, no. 5337, p. 434-436.

Nestola, F., Burnham, A.D., Peruzzo, L., et al., 2016, Tetragonal Almandine-Pyrope Phase, TAPP: finally a name for it, the new mineral jeffbenite: Mineralogical Magazine, v. 80, no. 7, p. 1219-1232.

Pearson, D., Brenker, F., Nestola, F., et al., 2014, Hydrous mantle transition zone indicated by ringwoodite included within diamond: Nature, v. 507, no. 7491, p. 221-224.

Prescher, C., and Prakapenka, V.B., 2015, DIOPTAS: a program for reduction of two-dimensional X-ray diffraction data and data exploration: High Pressure Research, v. 35, no. 3, p. 223-230.

Sinmyo, R., and Hirose, K., 2010, The Soret diffusion in laser-heated diamond-anvil cell: Physics of the Earth and Planetary Interiors, v. 180, no. 3, p. 172-178.

Smith, E.M., Shirey, S.B., Nestola, F., Bullock, E.S., Wang, J., Richardson, S.H., and Wang, W., 2016, Large gem diamonds from metallic liquid in Earth's deep mantle: Science (New York, N.Y.), v. 354, no. 6318, p. 1403-1405.

Stachel, T., and Harris, J., 2008, The origin of cratonic diamonds—constraints from mineral inclusions: Ore Geology Reviews, v. 34, no. 1, p. 5-32.

Stachel, T., Harris, J.W., Brey, G.P., and Joswig, W., 2000, Kankan diamonds (Guinea) II: lower mantle inclusion parageneses: Contributions to Mineralogy and Petrology, v. 140, no. 1, p. 16-27.

Walter, M.J., and Koga, K.T., 2004, The effects of chromatic dispersion on temperature measurement in the laser-heated diamond anvil cell: Physics of the Earth and Planetary Interiors, v. 143, p. 541-558.

Zedgenizov, D., Kagi, H., Shatsky, V., and Ragozin, A., 2014, Local variations of carbon isotope composition in diamonds from São-Luis (Brazil): evidence for heterogenous carbon reservoir in sublithospheric mantle: Chemical Geology, v. 363, p. 114-124.

6 Depth of formation of ferropericlase included in super-deep diamonds

Chiara Anzolini[1], Fabrizio Nestola[1], Matteo Alvaro[2], Andrea Gianese[1], Paolo Nimis[1] and Jeffrey W. Harris[2]

[1]Department of Geosciences, University of Padova, Via G. Gradenigo 6, 35131 Padova, Italy

[2]Department of Earth and Environmental Sciences, University of Pavia, Via A. Ferrata, 1, 27100 Pavia, Italy

[3]School of Geographical and Earth Sciences, University of Glasgow, G12 8QQ Glasgow, United Kingdom

The paper is in preparation.

Abstract

Super-deep diamonds are considered to be sub-lithospheric on the basis of the inclusions trapped within them. Ferropericlase is the most abundant phase found in super-deep diamonds, and, when associated with low-Ni enstatite in a diamond, is considered proof of lower-mantle origin. In previous studies, the discovery of nanometer-sized exsolutions of magnesioferrite within inclusions of ferropericlase seemed to validate the lower-mantle hypothesis. However, a newly reported phase diagram for magnesioferrite demonstrates that this cannot exsolve from ferropericlase at lower-mantle conditions.

Here, we report the study of two ferropericlases, extracted from a single super-deep diamond, by Synchrotron X-ray Tomographic Microscopy (SRXTM), Single-Crystal X-ray Diffraction (SCXRD) and Field Emission Gun–Scanning Electron Microscopy (FEG-SEM). SRXTM did not show any fractures around the ferropericlase inclusions. Beyond the diffraction reflections belonging to ferropericlase, SCXRD revealed the presence of a second phase identified as magnesioferrite. FEG-SEM analysis showed that magnesioferrite occurs as nanometer-sized exsolutions within ferropericlase. We also completed elastic geobarometry, which provided an estimate for the depth of entrapment of the two ferropericlase – diamond pairs and placed their origin between the upper mantle and the transition zone, at ~12 GPa (~340 km) at 1500 K. These results strengthen the hypothesis that single ferropericlase inclusions might not be reliable markers for a lower-mantle provenance of super-deep diamonds, although they indicate a sub-lithospheric origin at least within the deepest regions of the upper mantle and/or within the transition zone.

6.1 Introduction

Diamonds and the mineral inclusions that they trap during growth are among the most studied geological "samples" as they provide unique information about the deepest regions of the Earth, which cannot be directly investigated. Such diamonds can be conveniently subdivided in two main categories: lithospheric and sub-lithospheric or "super-deep". In terms of relative abundance, within the global diamond population, 94% are represented by lithospheric diamonds and only 6% by super-deep diamonds (Stachel and

Harris, 2008). Lithospheric diamonds form at depths ranging between 120 and 250 km, whilst super-deep diamonds are interpreted to crystallize between 300 km and 800 km depth (Harte, 2010), because some of the inclusions trapped within them are considered to be primary or the products of retrograde transformation from lower-mantle or transition-zone precursors. However, due to the lack of experimental evidence relating composite inclusions directly to high-pressure precursors, the real depth of origin of super-deep diamonds is still uncertain.

The most common mineral inclusion in super-deep diamonds is ferropericlase, (Mg,Fe)O (see Kaminsky, 2012 and references therein). Based on experimental observations, ferropericlase is the second most abundant mineral in the lower mantle, comprising approximately 16–20 wt% (660 to 2900 km depth), and, consequently, inclusions of ferropericlase in diamond, especially when associated with low-Ni enstatite, are often considered to indicate a lower-mantle origin (Harte et al., 1999; Stachel et al., 2000; McCammon, 2001). Such origin is based on two facts that apply only to this particular mineral pair, and, moreover, such a pair is rarely found in one diamond: 1) the two minerals would recombine to form olivine at shallower depths; 2) an enstatite enriched in Al and depleted in Ni is considered to be the decompression product of bridgmanite (Stachel et al., 2000). The situation is different, however, if only ferropericlase is found as an inclusion, which happens much more frequently. Minerals with the broad chemistry of ferropericlase are stable within the entire range of pressure and temperature conditions from lower mantle to the Earth's surface (Brey et al., 2004) and it can form not only by decomposition of ringwoodite, but also by decarbonation processes (Brenker et al., 2007).

In addition, samples from São Luiz, Juina, Brazil, which is considered the main world source of super-deep diamonds, are noteworthy for containing nanometer-sized magnesioferrite (Harte et al., 1999; Wirth et al., 2014; Kaminsky et al., 2015). Based upon a phase diagram valid for 1 atm, such exsolutions would place the origin of this assemblage in the uppermost part of the lower mantle (Palot et al., 2016). However, a newly reported phase diagram for magnesioferrite demonstrates that the latter is not stable at such pressures and, thus, it cannot exsolve directly from ferropericlase at lower-mantle conditions (Uenver-

Thiele et al., 2017a,b).

The aim of this study is therefore to obtain the entrapment pressures (P_e) of two ferropericlase inclusions contained in a single São Luiz diamond (AZ1, Figure 6.1). Such inclusions were investigated by a combination of Synchrotron X-ray Tomographic Microscopy (SRXTM), Single-Crystal X-ray Diffraction (SCXRD) and Field Emission Gun–Scanning Electron Microscopy (FEG-SEM). SRXTM confirmed the absence of fractures around the inclusions, and both SCXRD and FEG-SEM techniques showed nanometer-sized exsolutions of magnesioferrite within the two ferropericlases. Lastly, we completed elastic geobarometry, which determined an estimate for the depth of entrapment of the two ferropericlase – diamond pairs.

6.2 Material and methods

6.2.1 Sample

Figure 6.1 shows the diamond investigated in this study, which was recovered in the mid to late 1980s from alluvial deposits in the Juina area of south-western Brazil, from the São Luiz river (Harte et al., 1999; Hayman et al., 2005; Kaminsky et al., 2001). The sample contains two main black tabular inclusions, identified as ferropericlase by SCXRD. The smaller one, whose longest dimension is ~160 µm, is named AZ1_1; the bigger one, whose longest dimension is ~280 µm, is named AZ1_2.

6.2.2 Synchrotron X-ray Tomographic Microscopy

This non-destructive, high-resolution technique allows to acquire three-dimensional maps of the variations of the X-ray attenuation coefficient within a sample. X-ray micro-tomography experiments were carried out at the Swiss Light Source (SLS) at TOMCAT, a beamline for tomographic microscopy and coherent radiology experiments. Measurements were performed at 13.5 keV in order to maximize contrast. A total of 1501 X-ray radiographs were acquired for each sample from different angular positions around a vertical rotation axis. A mathematical algorithm (Marone and Stampanoni, 2012) was used for the reconstruction of 2160 cross-sectional slices of 2560 × 2560 pixels, with a pixel size of 0.33 μm.

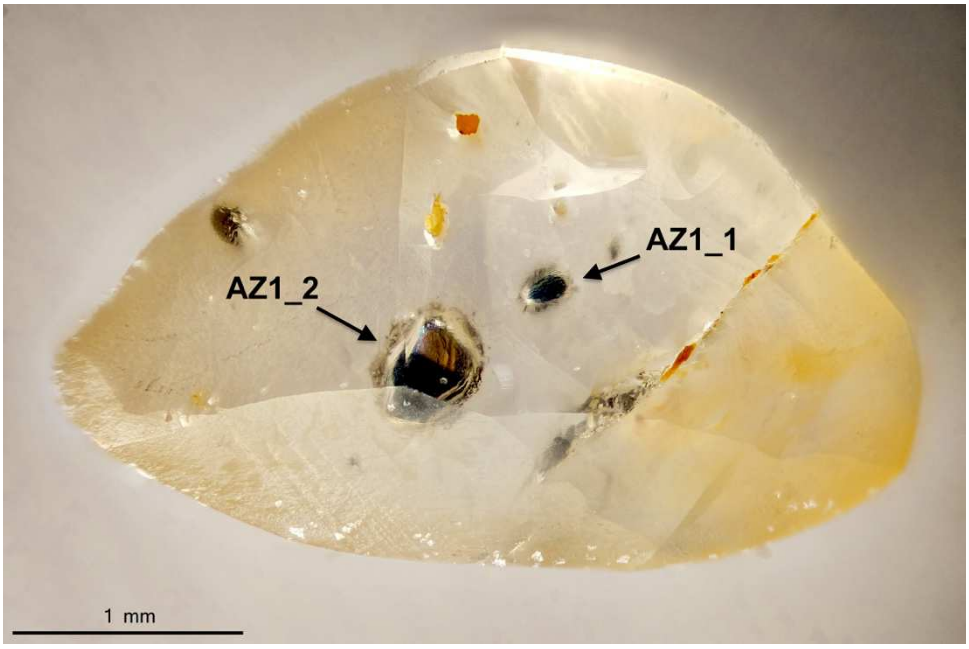

Figure 6.1: Expanded view of the inclusion-bearing diamond studied in this work.

6.2.3 Single-Crystal X-ray Diffraction

SCXRD measurements were performed on the ferropericlase inclusions both before and after release from their diamond host at the Department of Geosciences (University of Padova). X-ray data were collected using a Rigaku Oxford Diffraction *SuperNova* single-crystal diffractometer, equipped with a Dectris *Pilatus* 200 K area detector and with a *Mova* X-ray microsource. A monochromatized Mo*K*a radiation ($\lambda = 0.71073$ Å), working at 50 kV and 0.8 mA, was used. The sample-to-detector distance was 68 mm. Data reduction was performed using the CrysAlisPro software (Rigaku Oxford Diffraction).

6.2.4 Field Emission Gun – Scanning Electron Microscopy

The two ferropericlase inclusions were first extracted by mechanical crushing of the host, then polished in a three-steps process and finally carbon coated. FEG-SEM measurements were carried out at the Department of Physics and Astronomy (University of Padova), using a *Zeiss* SIGMA HD FEG-SEM microscope operating at 20 kV, with a spotsize of ~1 nm. Imaging was performed using an InLens secondary electron detector.

Compositional analysis was performed using an energy dispersive X-ray spectrometer (EDX by Oxford Instruments). The spatial resolution in microanalysis was of ~1 μm.

6.3 Results

6.3.1 Inclusion X-ray tomography

Owing to the high absorption contrast between diamond (highly transparent to X-rays) and the mineral phases, the high-absorbing inclusions could be easily distinguished from the host crystal.

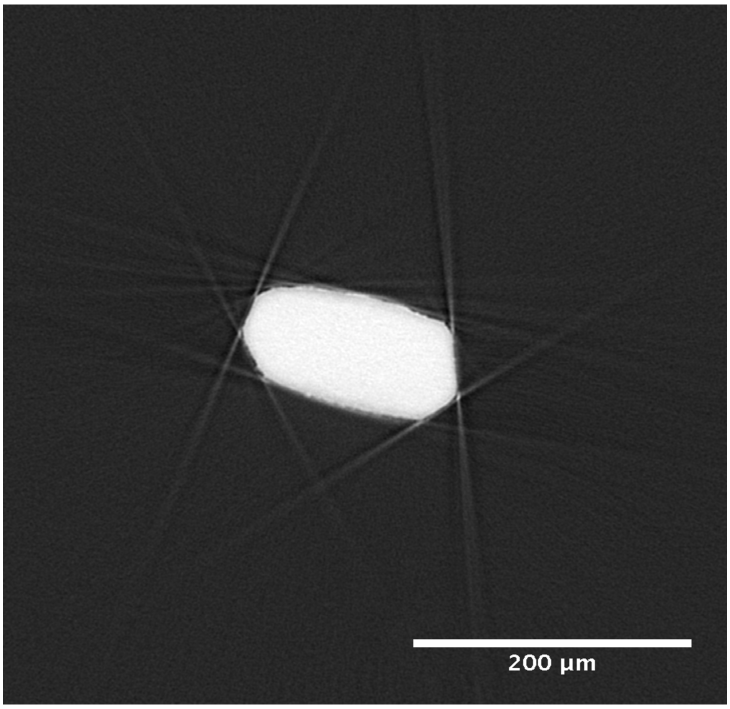

Figure 6.2: A representative SRXTM image of inclusion AZ1_1. Straight bright lines departing from the inclusion edges are imaging artifacts.

A single X-ray radiograph (Figure 6.2) and the final 3-D reconstruction (Figure 6.3) of inclusion AZ1_1 show the absence of fractures at the diamond-inclusion interface. This makes AZ1_1 a good candidate for the application of the "elastic geobarometry" method, because the presence of fractures would cause a partial release of the residual pressure retained by the inclusion and, therefore, an underestimation of the final entrapment pressure determined by elastic geobarometry.

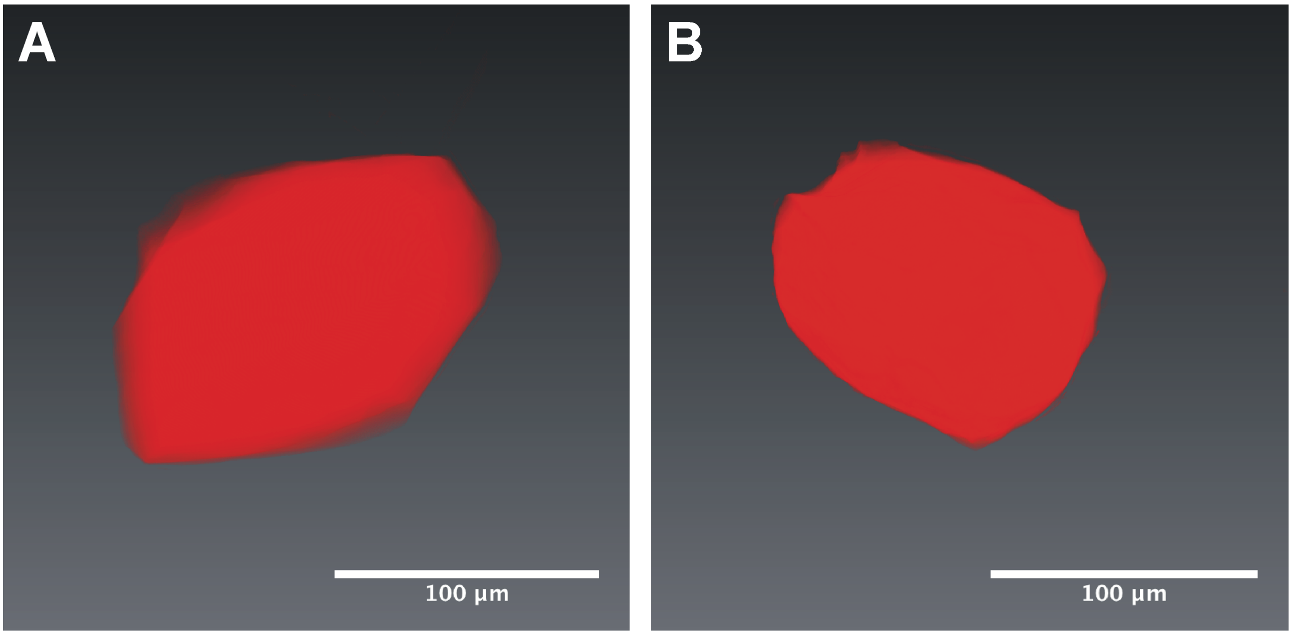

Figure 6.3: The 3-D reconstruction of inclusion AZ1_1 from two points of view. Both show there are no fractures around the inclusion.

6.3.2 Inclusion residual pressures

As predicted by optical examination, SCXRD measurements identified both the inclusions as ferropericlase. However, they also revealed the presence of another phase, which was identified as magnesioferrite. Diffraction images (Figure 6.4) only show the second (1.49 Å) and the third (2.44 Å) most intense peaks of ferropericlase, as the main peak (2.10 Å) cannot be detected due to an overlap with the most intense diamond peak, located at the same *d* spacing (2.07 Å). In addition, the first (2.53 Å) and the third (2.97 Å) most intense peaks of magnesioferrite are visible. Again, the second peak in order of intensity (1.48 Å) cannot be unambiguously detected due to overlapping with the peak of ferropericlase placed at the same *d* spacing (1.49 Å). As indicated by the diffraction data, ferropericlase and the exsolutions of magnesioferrite show an almost identical crystallographic orientation. In order to produce pseudo-single-crystal X-ray diffraction spots like those shown in Figure 6.4, there must be a high density of nanometer-sized magnesioferrite grains in topotaxial relation to the ferropericlase, which was subsequently confirmed by SEM observations.

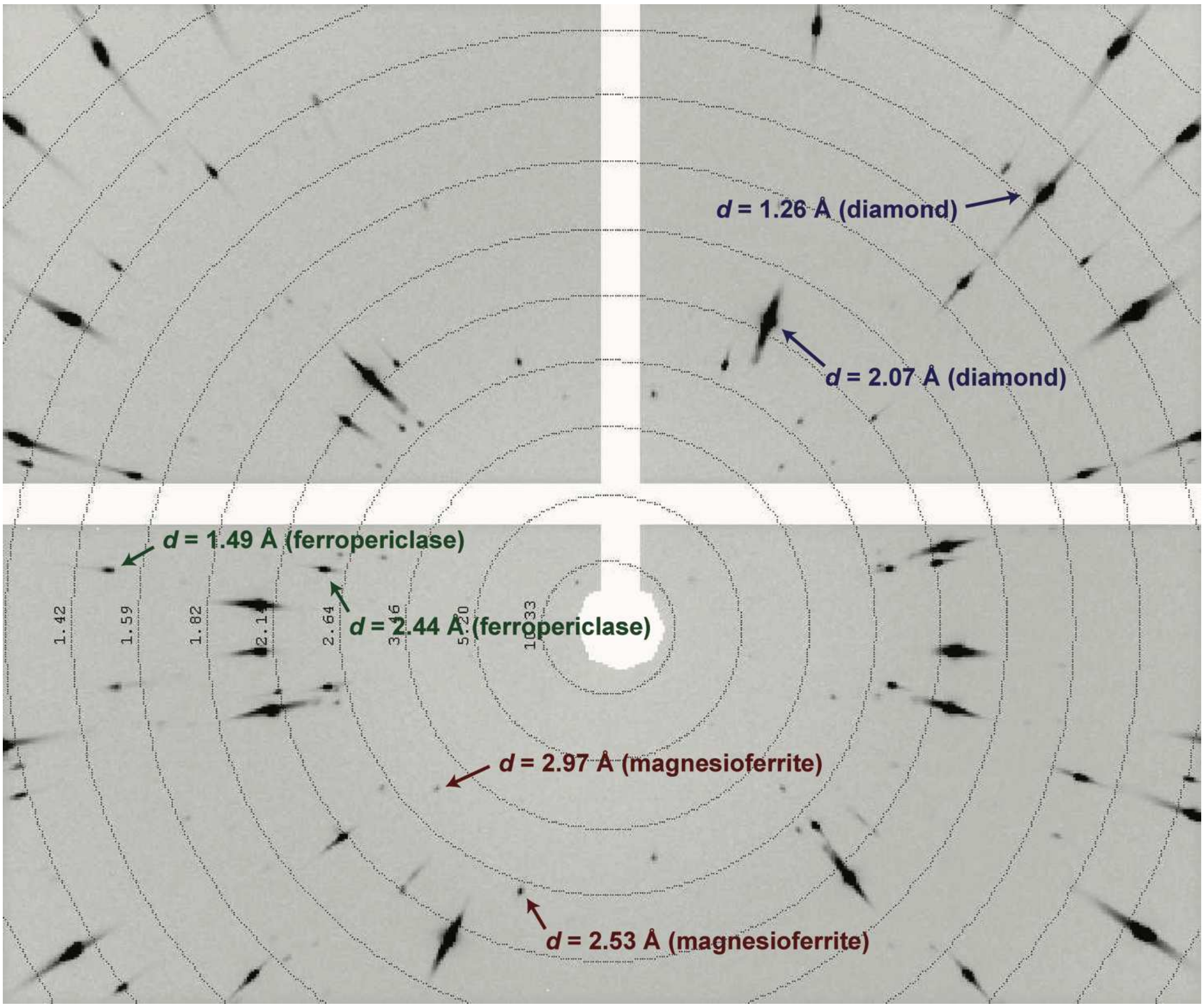

Figure 6.4: Single-crystal X-ray diffraction images of inclusion AZ1_2 showing the second and the third diffraction peaks of ferropericlase together with the first and the third most intense peaks of magnesioferrite. Peaks at 2.07 Å and 1.26 Å belong to diamond.

X-ray analyses also provided the lattice parameters and relative unit-cell volumes reported in Table 6.1. By comparing the unit-cell volumes before (V) and after (V_0) release from the diamond host and using the P-V-T equation of state for ferropericlase reported in Angel et al. (2017), we obtained the inclusion residual pressures (P_{inc}). Based on the X-ray tomography observations, such residual pressures could be considered definitively reliable as they are not affected by fracture systems around the inclusions, as typically observed for ferropericlase inclusions in diamond. The calculated residual pressures are in turn used to determine the depth of formation of a diamond-inclusion pair by elastic geobarometry.

Table 6.1: Lattice parameter and unit-cell volume of the two ferropericlase inclusions. The residual pressure is calculated by comparing the volume before (V) and after (V_0) release from the diamond host.

Inclusion	***a*** **(Å)**	a_0 **(Å)**	***V*** **(Å^3)**	V_0 **(Å^3)**	P_{inc} **(GPa)**
AZ1_1	4.253(4)	4.2685(2)	76.91(12)	77.770(5)	1.84
AZ1_2	4.256(8)	4.2689(3)	77.1(2)	77.795(9)	1.48

6.3.3 Magnesioferrite exsolutions within ferropericlase inclusions

The polished surface of both inclusion AZ1_1 and AZ1_2 (Figure 6.5) exhibit pervasively and homogeneously distributed nanometer-sized exsolutions of magnesioferrite, which represent ~6% of the total area (calculated using the ImageJ software, Abràmoff et al., 2004). The average grain size of the magnesioferrite exsolutions is ~200 nm and they often coalesce in chains of 2–3 μm long. EDX analyses provide a similar composition for both the ferropericlase inclusions with composition approximately $(Mg_{0.6}Fe_{0.4})O$. Due to limitations in the EDX resolution, the composition measured on a magnesioferrite vein is an average composition affected by the surrounding ferropericlase matrix (Figure 6.5d). Therefore, to estimate the magnesioferrite composition we followed the following logical steps: 1) the spot size of the EDX is 1 μm (green circle); 2) image analysis suggests that the average composition obtained analysing the magnesioferrite vein is affected for ~28% by the magnesioferrite and for ~72% by the ferropericlase; 3) the specific composition of the ferropericlase in inclusion AZ1_2 is known and is $(Mg_{0.59}Fe_{0.39})O$; 4) by subtracting the weighted matrix component it is possible to obtain a reasonable estimate for the magnesioferrite composition, which results to be $[Mg_{0.72}Fe_{0.23}(Mn,Na,Al,Cr)_{0.04}]Fe_2O_4$. This result is consistent with previously reported compositions of magnesioferrite exsolutions in ferropericlase inclusions in diamonds (Wirth et al., 2014).

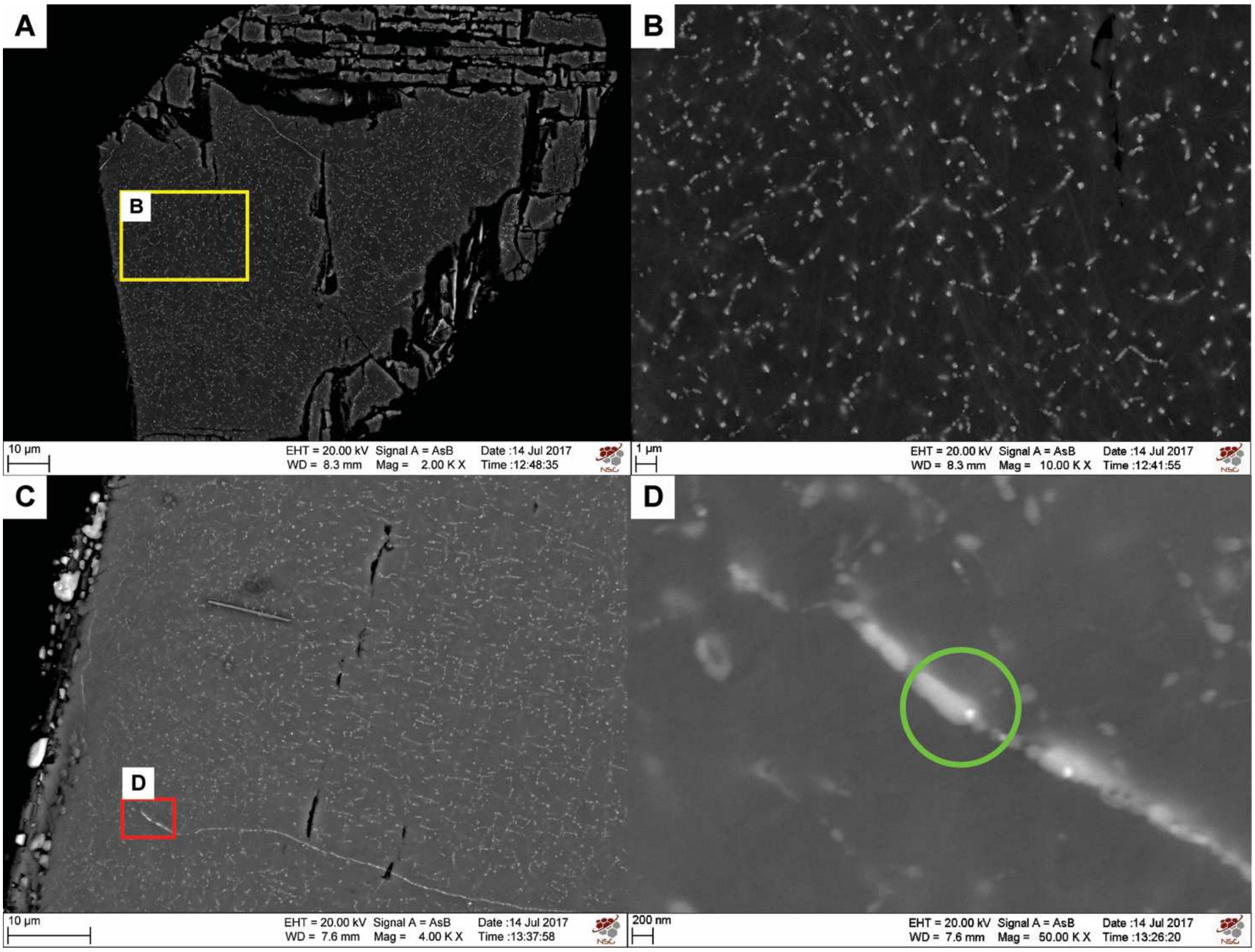

Figure 6.5: SEM images of A) inclusion AZ1_1; B) portion of inclusion AZ1_1; C) portion of inclusion AZ1_2; D) close-up of a mfr vein: within the EDX spectrometer spot area (green circle) the mfr exsolution represents ~28%, the fPer matrix represents the remaining ~78%.

6.3.4 Depth of formation of the ferropericlase – diamond pair by elastic geobarometry

The calculation of the pressure of formation for the two ferropericlase – diamond pairs was performed using the software EoSFit7c (Angel et al., 2014a), by following the same method described in Angel et al. (2014b). We used thermal expansion and compressibility data for ferropericlase reported in Angel et al. (2017), thermoelastic properties for diamond from the review of Angel et al. (2015) and the residual pressures calculated in section 6.3.2 (1.84 GPa for AZ1_1 and 1.48 GPa for AZ1_2). In the temperature range between 1200 and 2000 K, we obtained entrapment pressures ranging between 10.29 and 14.10 GPa (~290-410 km depth) for AZ1_1 and between 9.47 and 13.29 GPa (~270-390 km depth) for AZ1_2 (Table 6.2).

Table 6.2: Isomeke calculations for the two diamond-ferropericlase host-inclusion systems studied in this work.

T (K)	AZ1_1	AZ1_2
	P_e (P_{inc} = 1.84)	P_e (P_{inc} = 1.48)
1200	10.285	9.473
1300	10.839	10.025
1400	11.371	10.555
1500	11.880	11.063
1600	12.367	11.550
1700	12.833	12.015
1800	13.278	12.460
1900	13.701	12.884
2000	14.104	13.288

Note: P_e and P_{inc} are expressed in GPa.

The entrapment pressures in Table 6.2 fall in the lowermost part of the upper mantle – uppermost part of the transition zone (Figure 6.6). However, the elastic geobarometry method used in this work at the moment does not take into account the effect that the presence of the exsolutions could have on the residual pressure and, in turn, on the entire entrapment pressure determination. Therefore, our results must be considered only a minimum estimate of the real depth on formation.

6.4 Conclusions

Here we report an estimate of the depth of formation for the diamond-ferropericlase pair by “elastic geobarometry”, which is ~12 GPa (~340 km) at 1500 K, although the presence of magnesioferrite exsolutions within the ferropericlase indicate this is only a minimum estimate. Our conclusions can be summarized as follow:

1) ferropericlase inclusions in diamonds are often to be characterized by the presence of pervasive exsolutions of magnesioferrite; in Harte et al. (1999) the authors estimated that 25% of ferropericlases contain such exsolutions;
2) the advantage of having an isotropic inclusion within an isotropic host in the ferropericlase-diamond system, which would result in the absence of anisotropic effects, could be nullified by the presence of magnesioferrite exsolutions, as their effect on the elastic properties of mineral inclusions is not known yet;

3) based upon recent data, the exsolution of magnesioferrite from ferropericlase would occur at P <~9 GPa in the upper mantle (Uenver-Thiele et al., 2017a,b), thus, at present, single ferropericlase inclusions cannot be considered markers for a lower-mantle provenance of super-deep diamonds although their presence certainly indicate a sub-lithospheric origin at least between the deepest regions of the upper mantle and the transition zone.

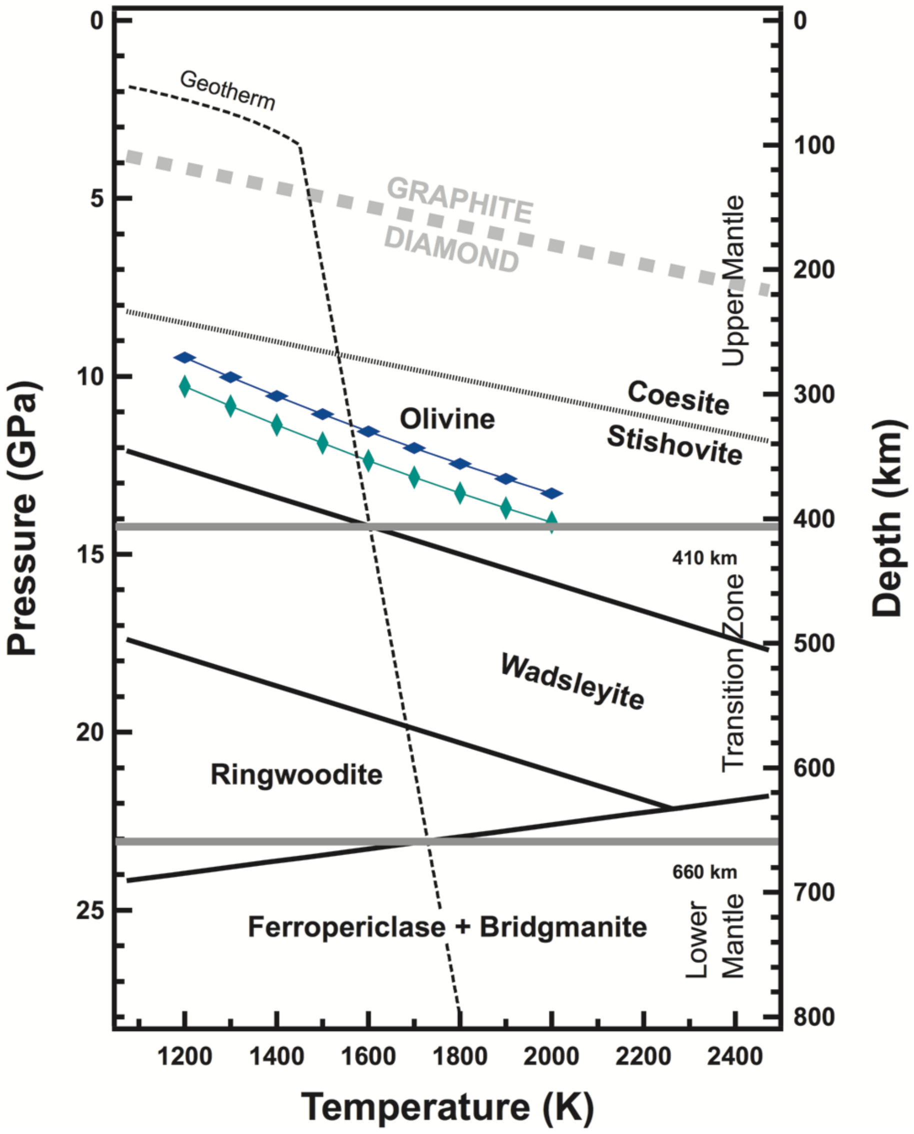

Figure 6.6: Phase diagram in which the phase boundaries are given as solid lines (Katsura and Ito, 1989; Katsura et al., 2003; Katsura et al., 2004). The coesite-stishovite phase boundary is displayed as a black dotted line (Zhang et al., 1996). The graphite-diamond phase boundary is shown as a grey stippled line (Day, 2012). The geotherm is shown as a black dashed line (Turcotte and Schubert, 2014). The 410 and 660 km discontinuities enclosing the transition zone are indicated by bold lines. Entrapment pressures values for inclusions AZ1_1 and AZ1_2 are represented with green and blue diamonds, respectively.

Acknowledgements

This investigation was financially supported by Fondazione Cassa di Risparmio di Padova e Rovigo and by the project INDIMEDEA, funded by the ERC-StG 2012 to FN (grant number 307322). MA has been supported by the Italian SIR-MIUR MILE DEEp (grant number RBSI140351) and the ERC-StG 2016 TRUE DEPTHS (grant number 714936). Part of this research was carried out at the synchrotron beamline TOMCAT at the Swiss Light Source (Paul Scherrer Institut, Switzerland). The authors thank F. Marone, M. Stampanoni, S. Milani and G. Rustioni for help during synchrotron work. L. Tauro and N. Michieli are acknowledged for their help in the SEM-EDX sample preparation and analysis, respectively. S. Castelli is thanked for providing the macrophotography of the diamond. The DeBeers Group of Companies is thanked for the donation of the diamond to JWH.

References

Abràmoff, M.D., Magalhães, P.J. and Ram, S.J. (2004) Image processing with ImageJ. Biophotonics International, 7, 36-42.

Angel, R.J., Mazzucchelli, M.L., Alvaro, M. and Nestola, F. (2017) EosFit-Pinc: A simple GUI for host-inclusion elastic thermobarometry. American Mineralogist, 1957–1960.

Angel, R.J., Alvaro, M., Nestola, F. and Mazzucchelli, M.L. (2015) Diamond thermoelastic properties and implications for determining the pressure of formation of diamond-inclusion systems. Russian Geology and Geophysics, 1-2, 211-220.

Angel, R.J., Alvaro, M. and Gonzalez-Platas, J. (2014a) EosFit7c and a Fortran module (library) for equation of state calculations. Zeitschrift für Kristallographie-Crystalline Materials, 5, 405-419.

Angel, R.J., Mazzucchelli, M.L., Alvaro, M., Nimis, P. and Nestola, F. (2014b) Geobarometry from host-inclusion systems: The role of elastic relaxation. American Mineralogist, 10, 2146-2149.

Brenker, F.E., Vollmer, C., Vincze, L., Vekemans, B., Szymanski, A., Janssens, K., Szaloki, I., Nasdala, L., Joswig, W. and Kaminsky, F. (2007) Carbonates from the lower part of transition zone or even the lower mantle. Earth and Planetary Science Letters, 1, 1-9.

Brey, G.P., Bulatov, V., Girnis, A., Harris, J.W. and Stachel, T. (2004) Ferropericlase—a lower mantle phase in the upper mantle. Lithos, 1, 655-663.

Day, H.W. (2012) A revised diamond-graphite transition curve. American Mineralogist, 1, 52-62.

Harte, B. (2010) Diamond formation in the deep mantle: the record of mineral inclusions and their distribution in relation to mantle dehydration zones. Mineralogical Magazine, 2, 189-215.

Harte, B., Harris, J.W., Hutchison, M.T., Watt, G.R. and Wilding, M.C. (1999) Lower mantle mineral associations in diamonds from Sao Luiz, Brazil. Mantle petrology: Field observations and high-pressure experimentation: A tribute to Francis R.(Joe) Boyd, 125-153.

Hayman, P.C., Kopylova, M.G. and Kaminsky, F.V. (2005) Lower mantle diamonds from Rio Soriso (Juina area, Mato Grosso, Brazil). Contributions to Mineralogy and Petrology, 4, 430-445.

Kaminsky, F., Zakharchenko, O., Davies, R., Griffin, W., Khachatryan-Blinova, G. and Shiryaev, A. (2001) Superdeep diamonds from the Juina area, Mato Grosso State, Brazil. Contributions to Mineralogy and Petrology, 6, 734-753.

Kaminsky, F. (2012) Mineralogy of the lower mantle: A review of 'super-deep' mineral inclusions in diamond. Earth-Science Reviews, 1, 127-147.

Kaminsky, F.V., Ryabchikov, I.D., McCammon, C.A., Longo, M., Abakumov, A.M., Turner, S. and Heidari, H. (2015) Oxidation potential in the Earth's lower mantle as recorded by ferropericlase inclusions in diamond. Earth and Planetary Science Letters, 49-56.

Katsura, T. and Ito, E. (1989) The system $Mg_2SiO_4Fe_2SiO_4$ at high pressures and temperatures: Precise determination of stabilities of olivine, modified spinel, and spinel. Journal of Geophysical Research: Solid Earth, B11, 15663-15670.

Katsura, T., Yamada, H., Nishikawa, O., Song, M., Kubo, A., Shinmei, T., Yokoshi, S., Aizawa, Y., Yoshino, T. and Walter, M.J. (2004) Olivinewadsleyite transition in the system $(Mg,Fe)_2SiO_4$. Journal of Geophysical Research: Solid Earth, B2.

Katsura, T., Yamada, H., Shinmei, T., Kubo, A., Ono, S., Kanzaki, M., Yoneda, A., Walter, M.J., Ito, E. and Urakawa, S. (2003) Post-spinel transition in Mg_2SiO_4 determined by high P–T in situ X-ray diffractometry. Physics of the Earth and Planetary Interiors, 1, 11-24.

Marone, F. and Stampanoni, M. (2012) Regridding reconstruction algorithm for real-time tomographic imaging. Journal of synchrotron radiation, 6, 1029-1037.

McCammon, C. (2001) Geophysics. Deep diamond mysteries. Science (New York, N.Y.), 5531, 813-814.

Palot, M., Jacobsen, S.D., Townsend, J.P., Nestola, F., Marquardt, K., Miyajima, N., Harris, J.W., Stachel, T., McCammon, C.A. and Pearson, D.G. (2016) Evidence for H_2O-bearing fluids in the lower mantle from diamond inclusion, 237-243.

Stachel, T. and Harris, J.W. (2008) The origin of cratonic diamonds—constraints from mineral inclusions. Ore Geology Reviews, 1, 5-32.

Stachel, T., Harris, J.W., Brey, G.P. and Joswig, W. (2000) Kankan diamonds (Guinea) II: lower mantle inclusion parageneses. Contributions to Mineralogy and Petrology, 1, 16-27.

Turcotte, D. and Schubert, G. (2014) Geodynamics, ed. 3rd Cambridge University Press.

Uenver-Thiele, L., Woodland, A.B., Boffa Ballaran, T., Miyajima, N. and Frost, D.J. (2017a) Phase relations of $MgFe_2O_4$ at conditions of the deep upper mantle and transition zone. American Mineralogist, 3, 632-642.

Uenver-Thiele, L., Woodland, A.B., Boffa Ballaran, T., Miyajima, N. and Frost, D.J. (2017b) Phase relations of Fe-Mg spinels including new high-pressure post-spinel phases and implications for natural samples. American Mineralogist, 10, 2054-2064.

Wirth, R., Dobrzhinetskaya, L., Harte, B., Schreiber, A. and Green, H.W. (2014) High-Fe (Mg,Fe)O inclusion in diamond apparently from the lowermost mantle. Earth and Planetary Science Letters, 365-375.

Zhang, J., Li, B., Utsumi, W. and Liebermann, R.C. (1996) In situ X-ray observations of the coesite-stishovite transition: reversed phase boundary and kinetics. Physics and Chemistry of Minerals, 1, 1-10.

7 Conclusions

7.1 Summary

Super-deep diamonds are the deepest samples available from the Earth's interior. They are believed to originate from depths between 300 and 800 km, regions which cannot be directly investigated, on the basis of the inclusions they contain, which are considered to be retrograde transformation products from lower-mantle or transition-zone precursors. However, due to the lack of experimental evidence relating these mineral phases with their purported high-pressure precursors, the real depth of origin of super-deep diamonds is still uncertain. Therefore, super-deep diamonds and their inclusions could in principle provide a unique information about the otherwise inaccessible Earth's mantle, provided their real depth of provenance being known.

As highlighted in the introduction chapter, the application of classical geobarometry to determine the depth of formation of diamonds is often not possible, due to the lack of appropriate mineral inclusion assemblages. Elastic geobarometry, on the other hand, being based solely on the thermoelastic parameters of host and inclusion, which are known or can be determined with high accuracy and precision, has the double advantage of being applied to a larger number of diamonds and in a non-destructive way.

This Ph.D. project aimed to obtain the real pressure of formation of super-deep diamonds by studying three among the most common mineral inclusions found within them ($CaSiO_3$-walstromite, jeffbenite and ferropericlase) by non-destructive methods. For this purpose, we have studied about 40 diamonds coming from Juina locality, the main world source of sub-lithospheric diamonds, and containing $CaSiO_3$-walstromite or ferropericlase using in-house single-crystal X-ray diffraction and micro-Raman spectroscopy. Field emission gun-scanning electron microscopy, synchrotron X-ray tomographic microscopy and synchrotron Mössbauer source at outside Institutions were also used. In addition, laser-heating diamond-anvil cell experiments were performed on a synthetic Ti-free jeffbenite to determine if the absence of Ti extends the stability field of such mineral compared to previous studies. Finally, elastic geobarometry, which provides the depth of formation of a diamond-inclusion pair, has been completed both on ferropericlase and $CaSiO_3$-walstromite, in this last case combined with thermodynamic and first-principles calculations. All the results have been summarized in Figure 7.1.

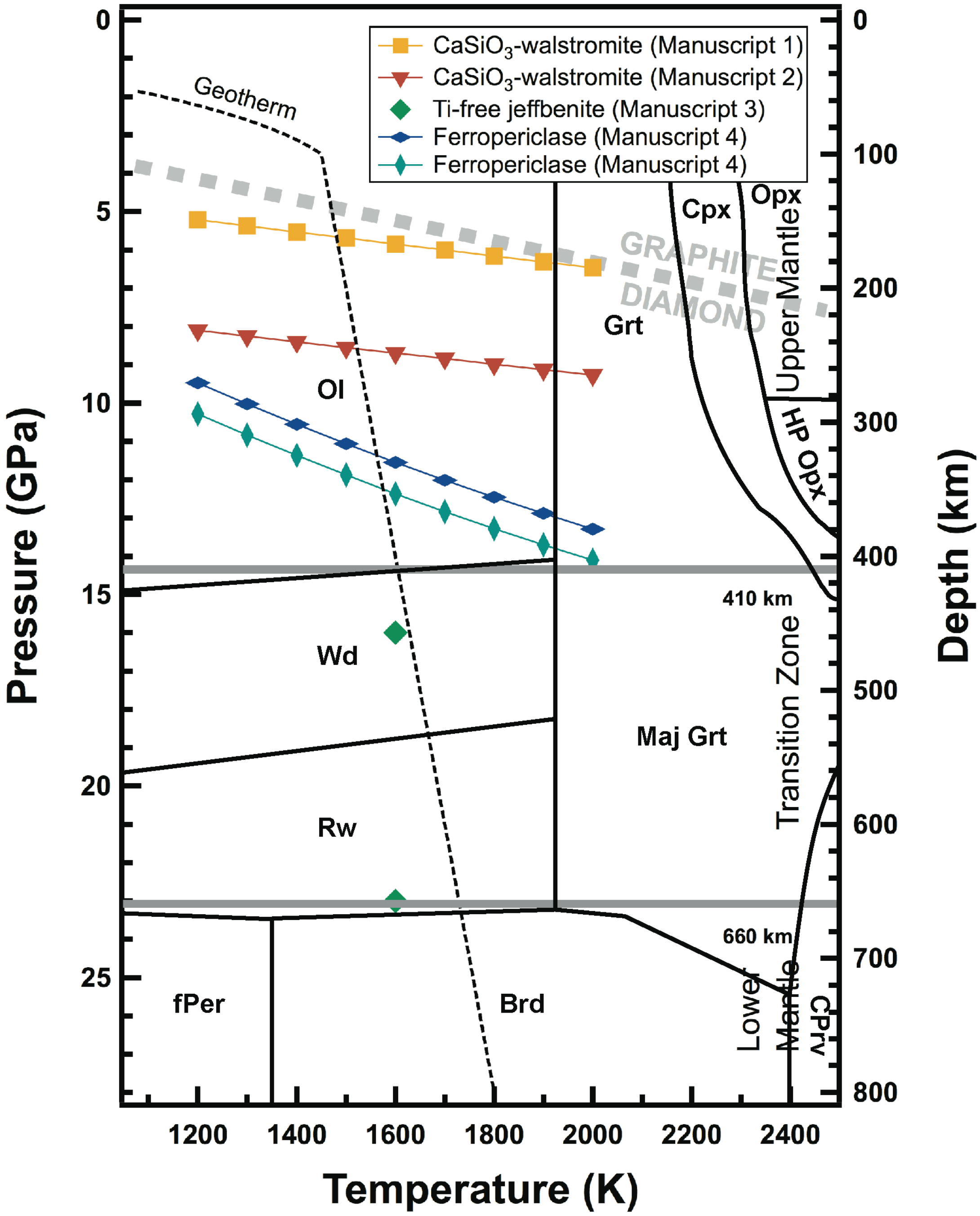

Figure 7.1: Phase diagram in which the phase boundaries are given as solid lines (Stixrude and Bertelloni, 2007). The graphite-diamond phase boundary is shown as a grey stippled line (Day, 2012). The geotherm is shown as a black dashed line (Turcotte and Schubert, 2014). The 410 and 660 km discontinuities enclosing the transition zone are indicated by bold lines.

In the first manuscript, we investigated several single phases and assemblages of Ca-silicate inclusions still trapped in a diamond by in-situ single-crystal X-ray diffraction and micro-Raman spectroscopy and we obtained a minimum entrapment pressure of ~5.7 GPa (~180 km) at 1500 K (Figure 7.1). However, the observed coexistence of $CaSiO_3$-walstromite, larnite (β-Ca_2SiO_4) and $CaSi_2O_5$-titanite in one multiphase inclusion within the same diamond indicates that the sample investigated is sub-lithospheric with entrapment pressure between ~9.5 and ~11.5 GPa at 1500 K, based on experimentally-determined phase equilibria. In addition, thermodynamic calculations suggested that, within a diamond, single inclusions of $CaSiO_3$-walstromite cannot derive from $CaSiO_3$-perovskite, unless the diamond expands by ~30% in volume, but typical volume changes for diamonds by cooling and decompression are of the order of 1-3%, depending on the exact path.

In the second manuscript, we provided the first calibration curve to determine the P_{inc} of a $CaSiO_3$-walstromite inclusion by means of Raman spectroscopy without breaking the diamond. To do so, we performed high-pressure micro-Raman investigations on a $CaSiO_3$-walstromite crystal under hydrostatic stress conditions within a diamond-anvil cell. We also calculated at different pressures the Raman spectrum of $CaSiO_3$-walstromite by ab initio methods both under hydrostatic and non-hydrostatic stress conditions to avoid misinterpretation of the results caused by the possible presence of deviatoric stresses causing anomalous shift of $CaSiO_3$-walstromite Raman peaks. Finally, we applied elastic geobarometry to estimate the minimum entrapment pressure of a $CaSiO_3$-walstromite inclusion trapped in a natural diamond, which resulted to be ~9 GPa (~260 km) at 1800 K (Figure 7.1). These results indicated that the diamond investigated was certainly sub-lithospheric.

In the third manuscript, we performed laser heated diamond-anvil cell experiments on a synthetic Ti-free jeffbenite, in order to determine the role that TiO_2 plays in its stability field and to determine if this mineral could be directly incorporated into diamond in the deep transition zone or lower mantle. With respect to previous studies, our results indicated that the absence of TiO_2 extends the stability field of jeffbenite to ~23 GPa (~660 km) at

1600 K (Figure 7.1), demonstrating that Ti-free jeffbenite may represent one of the most reliable markers for diamonds super-deep origin.

In the fourth manuscript, we reported the study of two ferropericlases, extracted from a single diamond, by Synchrotron X-ray Tomographic Microscopy (SRXTM), Single-Crystal X-ray Diffraction (SCXRD) and Field Emission Gun–Scanning Electron Microscopy (FEG-SEM). SRXTM did not show any fractures around the ferropericlase inclusions. Both SCXRD and FEG-SEM showed nanometer-sized exsolutions of magnesioferrite within the inclusions. We also completed elastic geobarometry, which provided an estimate for the depth of entrapment of the two ferropericlase–diamond pairs and placed their origin between the upper mantle and the transition zone, at ~12 GPa (~340 km) at 1500 K (Figure 7.1). These results strengthened the hypothesis that single ferropericlase inclusions might not be reliable markers for a lower-mantle provenance of super-deep diamonds, although their presence indicates a sub-lithospheric origin.

7.2 Concluding remarks

Our concluding remarks can be summarized as follows:

1) Single $CaSiO_3$-walstromite and ferropericlase inclusions cannot currently suggest a lower-mantle origin for super-deep diamonds, although their presence indicates a sub-lithospheric origin.
2) Ti-free jeffbenite and ringwoodite inclusions are, at the moment, the only examples of mineral phases found within diamonds which unambiguously indicate a diamond origin down to ~660 km depth.
3) Elastic geobarometry, being based upon several assumptions (enlisted in § 2.6), is often able to provide only a minimum estimate for the depth of entrapment of an inclusion within its host. However, the possibility of being applied to any diamond-inclusion couple allowed us to confirm that super-deep diamonds, in the specific sense of sub-lithospheric, definitely exist.

8 References

Akaogi, M. (2007) Phase transitions of minerals in the transition zone and upper part of the lower mantle. Geological Society of America Special Papers, 1-13.

Andreazza, P., Kaminsky, F.V., Sablukov, S.M., Belousova, E.A., Tremblay, M. and Griffin, W.L. (2008) Kimberlitic sources of super-deep diamonds in the Juina area, Mato Grosso State, Brazil. In 9th International Kimberlite Conference Extended Abstracts, 9IKC-A-00004, Frankfurt.

Angel, R.J., Mazzucchelli, M.L., Alvaro, M. and Nestola, F. (2017) EosFit-Pinc: A simple GUI for host-inclusion elastic thermobarometry. American Mineralogist, 1957–1960

Angel, R.J., Alvaro, M., Nestola, F. and Mazzucchelli, M.L. (2015a) Diamond thermoelastic properties and implications for determining the pressure of formation of diamond-inclusion systems. Russian Geology and Geophysics, 1-2, 211-220.

Angel, R.J., Nimis, P., Mazzucchelli, M.L., Alvaro, M. and Nestola, F. (2015b) How large are departures from lithostatic pressure? Constraints from host–inclusion elasticity. Journal of Metamorphic Geology, 8, 801-813.

Angel, R.J., Alvaro, M. and Gonzalez-Platas, J. (2014a) EosFit7c and a Fortran module (library) for equation of state calculations. Zeitschrift für Kristallographie-Crystalline Materials, 5, 405-419.

Angel, R.J., Mazzucchelli, M.L., Alvaro, M., Nimis, P. and Nestola, F. (2014b) Geobarometry from host-inclusion systems: The role of elastic relaxation. American Mineralogist, 10, 2146-2149.

Anzolini, C., Angel, R.J., Merlini, M., Derzsi, M., Tokár, K., Milani, S., Krebs, M.Y., Brenker, F.E., Nestola, F. and Harris, J.W. (2016) Depth of formation of CaSiO3-walstromite included in super-deep diamonds. Lithos, 265, 138-147.

Araujo, D.P., Gaspar, J.C., Bulanova, G.P., Smith, C.B., Kohn, S.C., Walter, M.J. and Hauri, E.H. (2013) Juina diamonds from kimberlites and alluvials: a comparison of morphology, spectral characteristics and carbon isotope composition. In 10th International

Kimberlite Conference, p. 255-269. Springer, Bangalore.

Barron, L.M., Mernagh, T.P. and Barron, B.J. (2008) Using strain birefringence in diamond to estimate the remnant pressure on an inclusion. Australian Journal of Earth Sciences, 2, 159-165.

Brenker, F.E., Stachel, T. and Harris, J.W. (2002) Exhumation of lower mantle inclusions in diamond: ATEM investigation of retrograde phase transitions, reactions and exsolution. Earth and Planetary Science Letters, 1, 1-9.

Brenker, F.E., Vollmer, C., Vincze, L., Vekemans, B., Szymanski, A., Janssens, K., Szaloki, I., Nasdala, L., Joswig, W. and Kaminsky, F. (2007) Carbonates from the lower part of transition zone or even the lower mantle. Earth and Planetary Science Letters, 1, 1-9.

Brey, G.P., Bulatov, V., Girnis, A., Harris, J.W. and Stachel, T. (2004) Ferropericlase—a lower mantle phase in the upper mantle. Lithos, 1, 655-663.

Burnham, A.D., Bulanova, G.P., Smith, C.B., Whitehead, S.C., Kohn, S.C., Gobbo, L. and Walter, M.J. (2016) Diamonds from the Machado River alluvial deposit, Rondônia, Brazil, derived from both lithospheric and sublithospheric mantle. Lithos, 265, 199-213.

Cayzer, N.J., Odake, S., Harte, B. and Kagi, H. (2008) Plastic deformation of lower mantle diamonds by inclusion phase transformations. European Journal of Mineralogy, 3, 333-339.

Chinn, J.L., Milledge, H.J. and Gurney, J.J. (1998) Diamonds and inclusions from the Jagersfontein kimberlite. In 7th International Kimberlite Conference, p. 156-157, Cape Town.

Day, H.W. (2012) A revised diamond-graphite transition curve. American Mineralogist, 1, 52-62.

Eshelby, J.D. (1959) The elastic field outside an ellipsoidal inclusion. In Proceedings of the Royal Society of London A: Mathematical, Physical and Engineering Sciences, p. 561-569. The Royal Society.

Eshelby, J.D. (1957) The determination of the elastic field of an ellipsoidal inclusion, and related problems. In Proceedings of the Royal Society of London A: Mathematical, Physical and Engineering Sciences, p. 376-396. The Royal Society.

Fedortchouk, Y., Manghnani, M.H., Hushur, A., Shiryaev, A. and Nestola, F. (2011) An atomic force microscopy study of diamond dissolution features: The effect of H2O and CO2 in the fluid on diamond morphology. American Mineralogist, 11-12, 1768-1775.

Fei, Y. and Bertka, C.M. (1999) Phase transitions in the Earth's mantle and mantle mineralogy. Mantle petrology: field observations and high pressure experimentation, 189-207.

Fei, Y., Wang, Y. and Finger, L.W. (1996) Maximum solubility of FeO in (Mg, Fe) SiO3-perovskite as a function of temperature at 26 GPa: Implication for FeO content in the lower mantle. Journal of Geophysical Research: Solid Earth, B5, 11525-11530.

Funamori, N., Jeanloz, R., Miyajima, N. and Fujino, K. (2000) Mineral assemblages of basalt in the lower mantle. Journal of Geophysical Research: Solid Earth, B11, 26037-26043.

Gasparik, T., Wolf, K. and Smith, C.M. (1994) Experimental determination of phase relations in the CaSiO3 system from 8 to 15 GPa. American Mineralogist, 11-12, 1219-1222.

Gibson, S.A., Thompson, R.N., Leonardos, O.H., Dickin, A.P. and Mitchell, J.G. (1995) The Late Cretaceous impact of the Trindade mantle plume: evidence from large-volume, mafic, potassic magmatism in SE Brazil. Journal of Petrology, 1, 189-229.

Guarino, V., Wu, F., Lustrino, M., Melluso, L., Brotzu, P., de Barros Gomes, C., Ruberti, E., Tassinari, C.C.G. and Svisero, D.P. (2013) U–Pb ages, Sr–Nd-isotope geochemistry, and petrogenesis of kimberlites, kamafugites and phlogopite-picrites of the Alto Paranaíba Igneous Province, Brazil. Chemical Geology, 65-82.

Gurney, J.J., Helmstaedt, H.H., Richardson, S.H. and Shirey, S.B. (2010) Diamonds through time. Economic Geology, 3, 689-712.

Harlow, G.E. and Davies, R.M. (2005) Diamonds. Elements, 2, 67-70.

Harris, J.W., Milledge, H.J., Barron, T.H.K. and Munn, R.W. (1970) Thermal expansion of garnets included in diamond. Journal of Geophysical Research, 5775-5792.

Harris, J., Hutchison, M., Hursthouse, M., Light, M. and Harte, B. (1997) A new tetragonal silicate mineral occurring as inclusions in lower-mantle diamonds. Nature, 6632, 486-488.

Harte, B. (2010) Diamond formation in the deep mantle: the record of mineral inclusions and their distribution in relation to mantle dehydration zones. Mineralogical Magazine, 2, 189-215.

Harte, B. and Harris, J.W. (1994) Lower mantle mineral associations preserved in diamonds. Mineralogical Magazine, AK, 384-385.

Harte, B., Harris, J.W., Hutchison, M.T., Watt, G.R. and Wilding, M.C. (1999) Lower mantle mineral associations in diamonds from Sao Luiz, Brazil. Mantle petrology: Field observations and high-pressure experimentation: A tribute to Francis R.(Joe) Boyd, 125-153.

Harte, B. and Hudson, N.F. (2013) Mineral associations in diamonds from the lowermost upper mantle and uppermost lower mantle. In 10th International Kimberlite Conference, p. 235-253. Springer, Bangalore.

Hayman, P.C., Kopylova, M.G. and Kaminsky, F.V. (2005) Lower mantle diamonds from Rio Soriso (Juina area, Mato Grosso, Brazil). Contributions to Mineralogy and Petrology, 4, 430-445.

Heaman, L., Teixeira, N.A., Gobbo, L. and Gaspar, J.C. (1998) U-Pb mantle zircon ages for kimberlites from the Juina and Paranatinga provinces, Brazil. In 7th International Kimberlite Conference, p. 322-324, Cape Town.

Hirose, K., Fei, Y., Ma, Y. and Mao, H. (1999) The fate of subducted basaltic crust in the Earth's lower mantle. Nature, 6714, 53-56.

Howell, D., Wood, I.G., Dobson, D.P., Jones, A.P., Nasdala, L. and Harris, J.W. (2010) Quantifying strain birefringence halos around inclusions in diamond. Contributions to Mineralogy and Petrology, 5, 705-717.

Howell, D., Wood, I.G., Nestola, F., Nimis, P. and Nasdala, L. (2012) Inclusions under remnant pressure in diamond: a multi-technique approach. European Journal of Mineralogy, 4, 563-573.

Hutchison, M.T., Hursthouse, M.B. and Light, M.E. (2001) Mineral inclusions in diamonds: associations and chemical distinctions around the 670-km discontinuity. Contributions to Mineralogy and Petrology, 1, 119-126.

Irifune, T. and Ringwood, A.E. (1993) Phase transformations in subducted oceanic crust and buoyancy relationships at depths of 600–800 km in the mantle. Earth and Planetary Science Letters, 1-2, 101-110.

Irifune, T. (1994) Absence of an aluminous phase in the upper part of the Earth's lower mantle. Nature, 6485, 131-133.

Irifune, T., Shinmei, T., McCammon, C.A., Miyajima, N., Rubie, D.C. and Frost, D.J. (2010) Iron partitioning and density changes of pyrolite in Earth's lower mantle. Science, 5962, 193-195.

Izraeli, E.S., Harris, J.W. and Navon, O. (1999) Raman barometry of diamond formation. Earth and Planetary Science Letters, 3, 351-360.

Kaminsky, F., Zakharchenko, O., Davies, R., Griffin, W., Khachatryan-Blinova, G. and Shiryaev, A. (2001) Superdeep diamonds from the Juina area, Mato Grosso State, Brazil. Contributions to Mineralogy and Petrology, 6, 734-753.

Kaminsky, F. (2012) Mineralogy of the lower mantle: A review of 'super-deep' mineral inclusions in diamond. Earth-Science Reviews, 1, 127-147.

Liu, L. (2002) An alternative interpretation of lower mantle mineral associations in diamonds. Contributions to Mineralogy and Petrology, 1, 16-21.

Mazzucchelli, M.L., Burnley, P., Angel, R.J., Chiara Domeneghetti, M., Nestola, F. and Alvaro, M. (2016) Elastic geobarometry: uncertainties arising from the geometry of the host-inclusion system. EGU General Assembly Conference Abstracts, 2060.

McCammon, C. (2001) Geophysics. Deep diamond mysteries. Science (New York, N.Y.), 5531, 813-814.

McCammon, C., Hutchison, M. and Harris, J. (1997) Ferric iron content of mineral inclusions in diamonds from Sao Luiz: a view into the lower mantle. Science, 5337, 434-436.

Moore, R.O. and Gurney, J.J. (1985) Pyroxene solid solution in garnets included in diamond. Nature, 6046, 553-555.

Nasdala, L., Brenker, F.E., Glinnemann, J., Hofmeister, W., Gasparik, T., Harris, J.W., Stachel, T. and Reese, I. (2003) Spectroscopic 2D-tomography Residual pressure and strain around mineral inclusions in diamonds. European Journal of Mineralogy, 6, 931-935.

Nestola, F., Nimis, P., Angel, R.J., Milani, S., Bruno, M., Prencipe, M. and Harris, J.W. (2014) Olivine with diamond-imposed morphology included in diamonds. Syngenesis or protogenesis?. International Geology Review, 13, 1658-1667.

Nestola, F. (2017) Inclusions in super-deep diamonds: windows on the very deep Earth. Rendiconti Lincei, 1-10.

Nestola, F., Nimis, P., Ziberna, L., Longo, M., Marzoli, A., Harris, J.W., Manghnani, M.H. and Fedortchouk, Y. (2011) First crystal-structure determination of olivine in diamond: Composition and implications for provenance in the Earth's mantle. Earth and Planetary Science Letters, 1, 249-255.

Nestola, F., Burnham, A.D., Peruzzo, L., Tauro, L., Alvaro, M., Walter, M.J., Gunter, M., Anzolini, C. and Kohn, S.C. (2016) Tetragonal Almandine-Pyrope Phase, TAPP: finally a name for it, the new mineral jeffbenite. Mineralogical Magazine, 7, 1219-1232.

Novella, D., Bolfan-Casanova, N., Nestola, F. and Harris, J.W. (2015) H2O in olivine and garnet inclusions still trapped in diamonds from the Siberian craton: Implications for the water content of cratonic lithosphere peridotites. Lithos, 230, 180-183.

Ono, S. (1999) High temperature stability limit of phase egg, AlSiO3(OH). Contributions to Mineralogy and Petrology, 1, 83-89.

Pearson, D.G., Brenker, F.E., Nestola, F., McNeill, J., Nasdala, L., Hutchison, M.T., Matveev, S., Mather, K., Silversmit, G. and Schmitz, S. (2014) Hydrous mantle transition zone indicated by ringwoodite included within diamond. Nature, 7491, 221-224.

Perrillat, J., Ricolleau, A., Daniel, I., Fiquet, G., Mezouar, M., Guignot, N. and Cardon, H. (2006) Phase transformations of subducted basaltic crust in the upmost lower mantle. Physics of the Earth and Planetary Interiors, 1, 139-149.

Prescher, C. and Prakapenka, V.B. (2015) DIOPTAS: a program for reduction of two-dimensional X-ray diffraction data and data exploration. High Pressure Research, 3, 223-230.

Riccomini, C., Velzquez, V.F. and Gomes, C.B. (2005) Tectonic controls of the Mesozoic and Cenozoic alkaline magmatism in central-southeastern Brazilian Platform. Mesozoic to Cenozoic alkaline magmatism in the Brazilian Platform, 31-56.

Sano, A., Ohtani, E., Kubo, T. and Funakoshi, K. (2004) In situ X-ray observation of decomposition of hydrous aluminum silicate AlSiO 3 OH and aluminum oxide hydroxide d-AlOOH at high pressure and temperature. Journal of Physics and Chemistry of Solids, 8, 1547-1554.

Shirey, S.B., Cartigny, P., Frost, D.J., Keshav, S., Nestola, F., Nimis, P., Pearson, D.G., Sobolev, N.V. and Walter, M.J. (2013) Diamonds and the geology of mantle carbon. Rev Mineral Geochem, 1, 355-421.

Smith, E.M., Shirey, S.B., Nestola, F., Bullock, E.S., Wang, J., Richardson, S.H. and Wang, W. (2016) Large gem diamonds from metallic liquid in Earth's deep mantle. Science (New York, N.Y.), 6318, 1403-1405.

Sobolev, N.V., Fursenko, B.A., Goryainov, S.V., Shu, J., Hemley, R.J., Mao, A. and Boyd, F.R. (2000) Fossilized high pressure from the Earth's deep interior: the coesite-in-diamond barometer. Proceedings of the National Academy of Sciences of the United States of America, 22, 11875-11879.

Stachel, T. and Harris, J.W. (2008) The origin of cratonic diamonds—constraints from mineral inclusions. Ore Geology Reviews, 1, 5-32.

Stachel, T., Brey, G.P. and Harris, J.W. (2005) Inclusions in sublithospheric diamonds: glimpses of deep Earth. Elements, 2, 73-78.

Stachel, T., Harris, J.W., Brey, G.P. and Joswig, W. (2000) Kankan diamonds (Guinea) II: lower mantle inclusion parageneses. Contributions to Mineralogy and Petrology, 1, 16-27.

Stixrude, L. and Lithgow-Bertelloni, C. (2005) Thermodynamics of mantle minerals–

I. Physical properties. Geophysical Journal International, 2, 610-632.

Tappert, R., Stachel, T., Harris, J.W., Muehlenbachs, K., Ludwig, T. and Brey, G.P. (2005) Diamonds from Jagersfontein (South Africa): messengers from the sublithospheric mantle. Contributions to Mineralogy and Petrology, 5, 505-522.

Tassinari, C.C. and Macambira, M.J. (1999) Geochronological provinces of the Amazonian Craton. Episodes-Newsmagazine of the International Union of Geological Sciences, 3, 174-182.

Thomson, A.R., Walter, M.J., Kohn, S.C. and Brooker, R.A. (2016) Slab melting as a barrier to deep carbon subduction. Nature, 7584, 76-79.

Tschauner, O., Ma, C., Beckett, J.R., Prescher, C., Prakapenka, V.B. and Rossman, G.R. (2014) Discovery of bridgmanite, the most abundant mineral in Earth, in a shocked meteorite. Science, 6213, 1100-1102.

Turcotte, D. and Schubert, G. (2014) Geodynamics, ed. 3rd Cambridge University Press.

Whitney, D.L. and Evans, B.W. (2010) Abbreviations for names of rock-forming minerals. American Mineralogist, 1, 185-187.

Wilding, M.C., Harte, B. and Harris, J.W. (1991) Evidence for a deep origin for Sao Luiz diamonds. In 5th International Kimberlite Conference, p. 456-458, Araxa.

Wirth, R., Dobrzhinetskaya, L., Harte, B., Schreiber, A. and Green, H.W. (2014) High-Fe (Mg,Fe)O inclusion in diamond apparently from the lowermost mantle. Earth and Planetary Science Letters, 365-375.

Wood, B.J. (2000) Phase transformations and partitioning relations in peridotite under lower mantle conditions. Earth and Planetary Science Letters, 3, 341-354.

Zedgenizov, D.A., Ragozin, A.L., Kalinina, V.V. and Kagi, H. (2016) The mineralogy of Ca-rich inclusions in sublithospheric diamonds. Geochemistry International, 10, 890-900.

9 Appendix A

High-pressure behaviour of CaSiO$_3$-walstromite

CaSiO$_3$-walstromite is a triclinic mineral and, consequently, the directions of maximum and minimum compression under stress are not constrained to lie along the unit-cell axes. Calculation of the principal axes of compression of the structure (with the software Win_Strain, www.rossangel.com) shows that the softest direction is approximately $[1\bar{1}\ 2]$ and the stiffest $[\bar{2}\,\bar{1}\,\bar{2}]$.

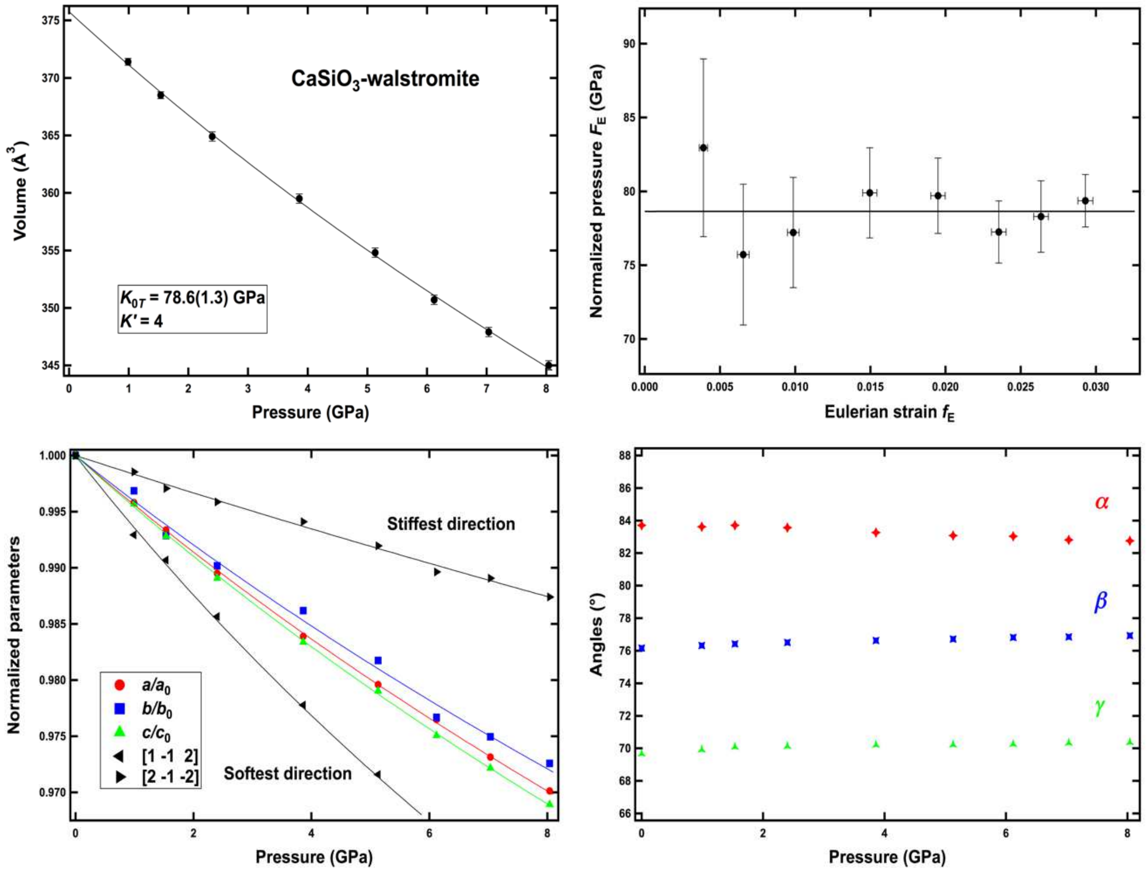

The structure of CaSiO$_3$-walstromite: rings of silicate tetrahedra (yellow) alternating with layers of calcium ions (red). The reason for the softest direction not being parallel to a unit-cell axis is no unit-cell axis is perpendicular to the layers.

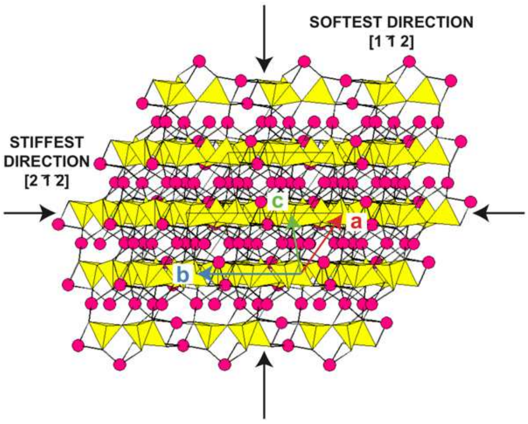

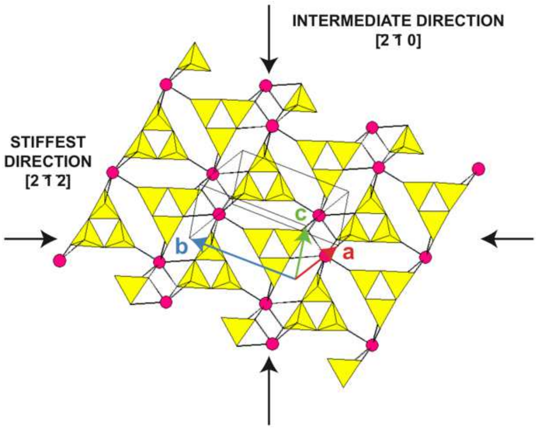

10 Appendix B

Diffractograms of run products of LH-DAC experiments on jeffbenite

List of abbreviations is reported in Table 5.2

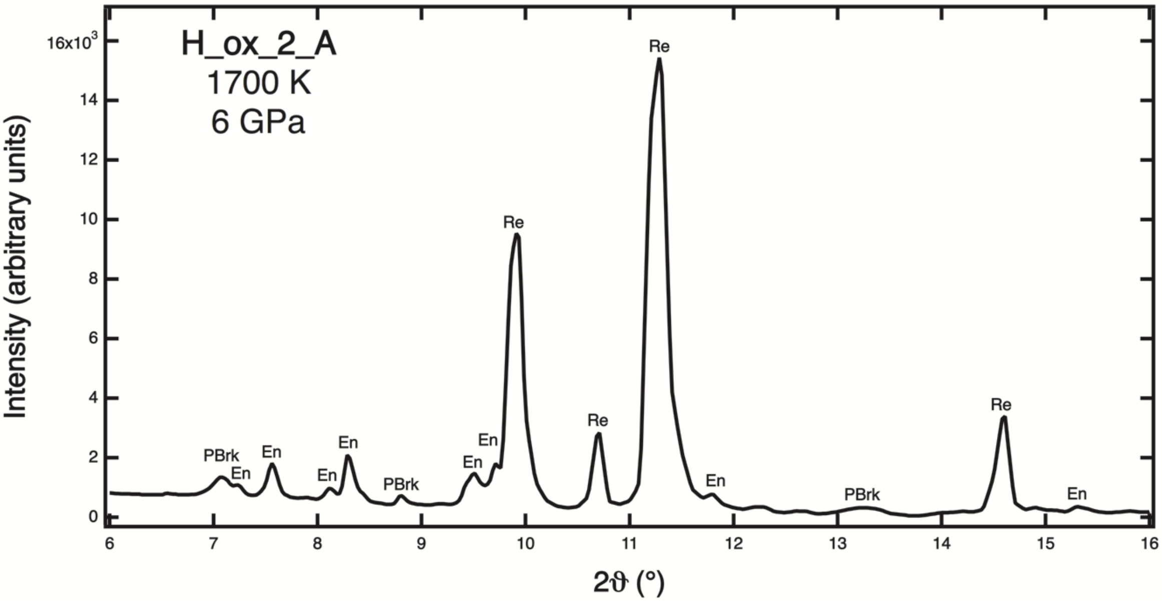
H_ox_2_A
1700 K
6 GPa
Intensity (arbitrary units)
16x10³
14
12
10
8
6
4
2
0
PBrk
En
En
En
En
PBrk
En
En
Re
Re
Re
En
PBrk
Re
En
6
7
8
9
10
11
12
13
14
15
16
2ϑ (°)

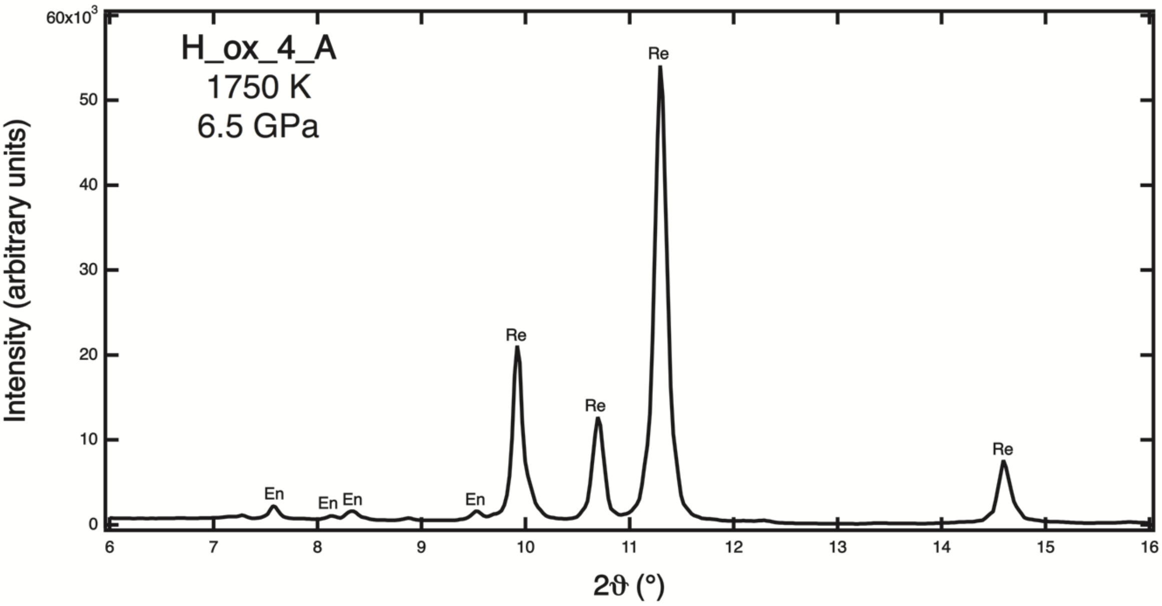
H_ox_4_A
1750 K
6.5 GPa
Intensity (arbitrary units)
60x10³
50
40
30
20
10
0
En
En
En
En
Re
Re
Re
Re
6
7
8
9
10
11
12
13
14
15
16
2ϑ (°)

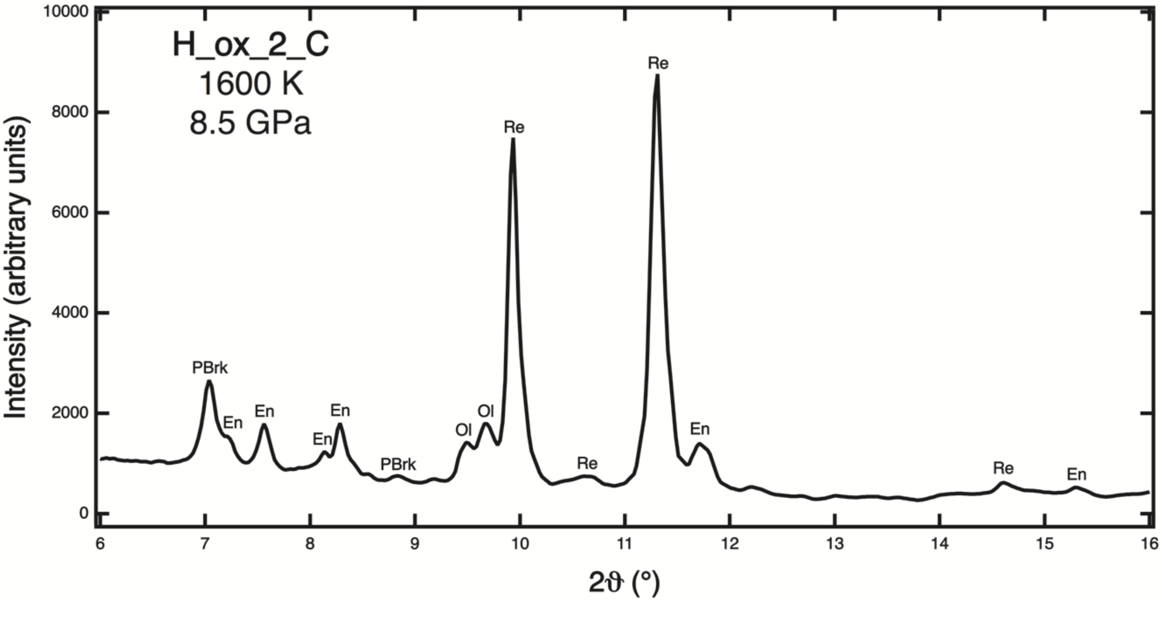
H_ox_2_C
1600 K
8.5 GPa
Intensity (arbitrary units)
10000
8000
6000
4000
2000
0
PBrk
En
En
En
En
PBrk
Ol
Ol
Re
Re
Re
En
Re
En
6
7
8
9
10
11
12
13
14
15
16
2ϑ (°)

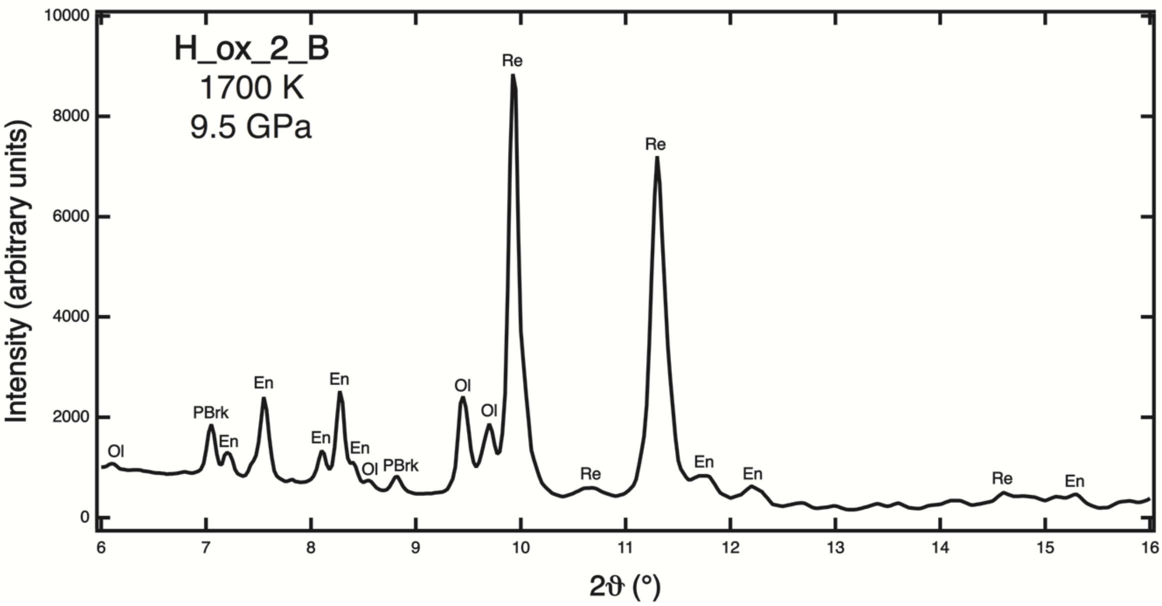
H_ox_2_B
1700 K
9.5 GPa
Intensity (arbitrary units)
10000
8000
6000
4000
2000
0
2ϑ (°)
6
7
8
9
10
11
12
13
14
15
16
Ol
PBrk
En
En
En
En
En
Ol
PBrk
Ol
Ol
Re
Re
Re
En
En
Re
En

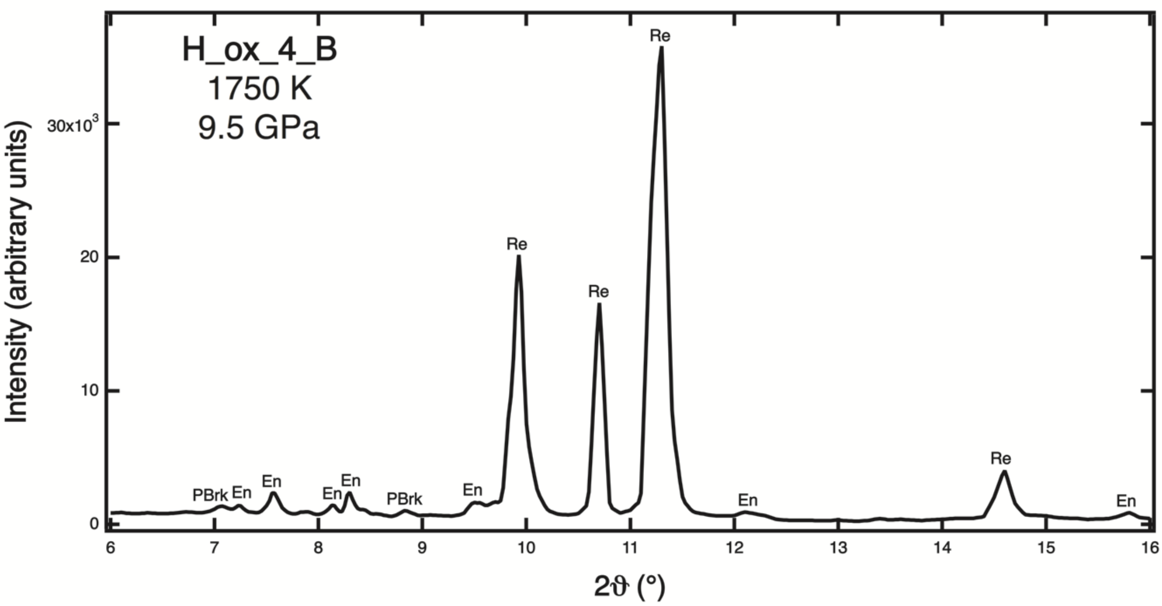
H_ox_4_B
1750 K
9.5 GPa
Intensity (arbitrary units)
30x10³
20
10
0
2ϑ (°)
6
7
8
9
10
11
12
13
14
15
16
PBrk
En
En
En
En
PBrk
En
Re
Re
Re
En
Re
En

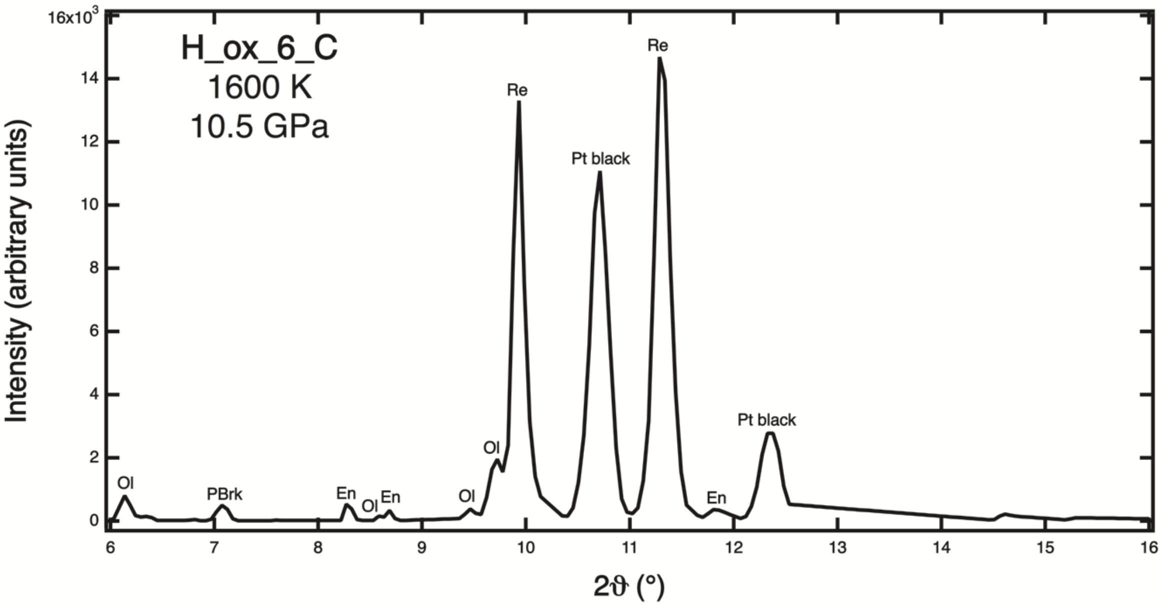
H_ox_6_C
1600 K
10.5 GPa
Intensity (arbitrary units)
16x10³
14
12
10
8
6
4
2
0
2ϑ (°)
6
7
8
9
10
11
12
13
14
15
16
Ol
PBrk
En
Ol
En
Ol
Ol
Re
Pt black
Re
En
Pt black

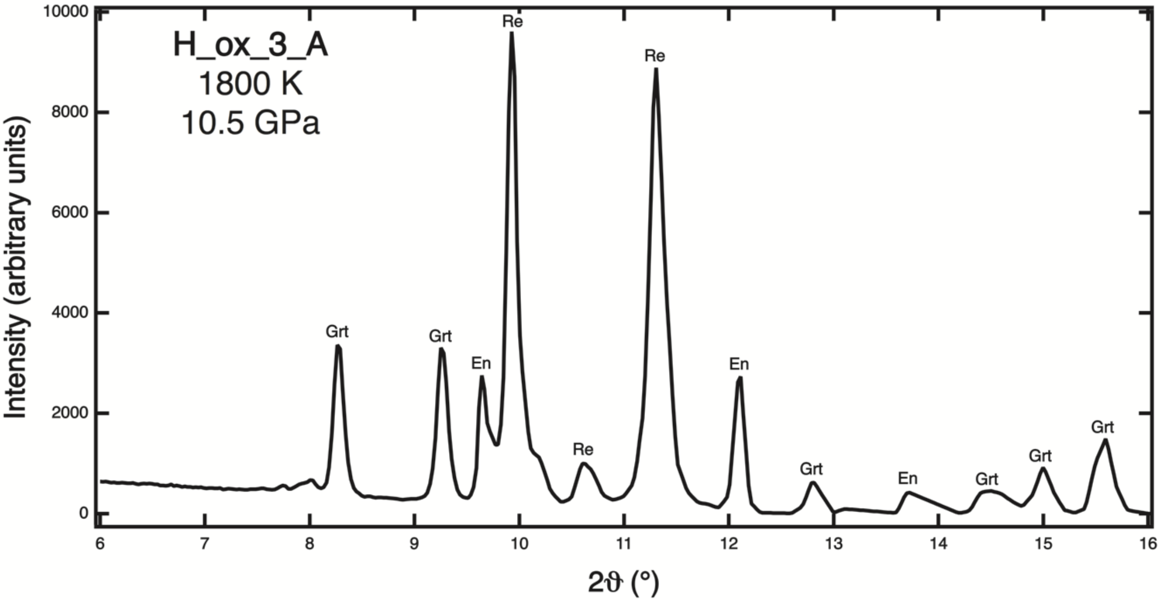
H_ox_3_A
1800 K
10.5 GPa
Intensity (arbitrary units)
2ϑ (°)
0
2000
4000
6000
8000
10000
6
7
8
9
10
11
12
13
14
15
16
Grt
Grt
En
Re
Re
Re
En
Grt
En
Grt
Grt
Grt

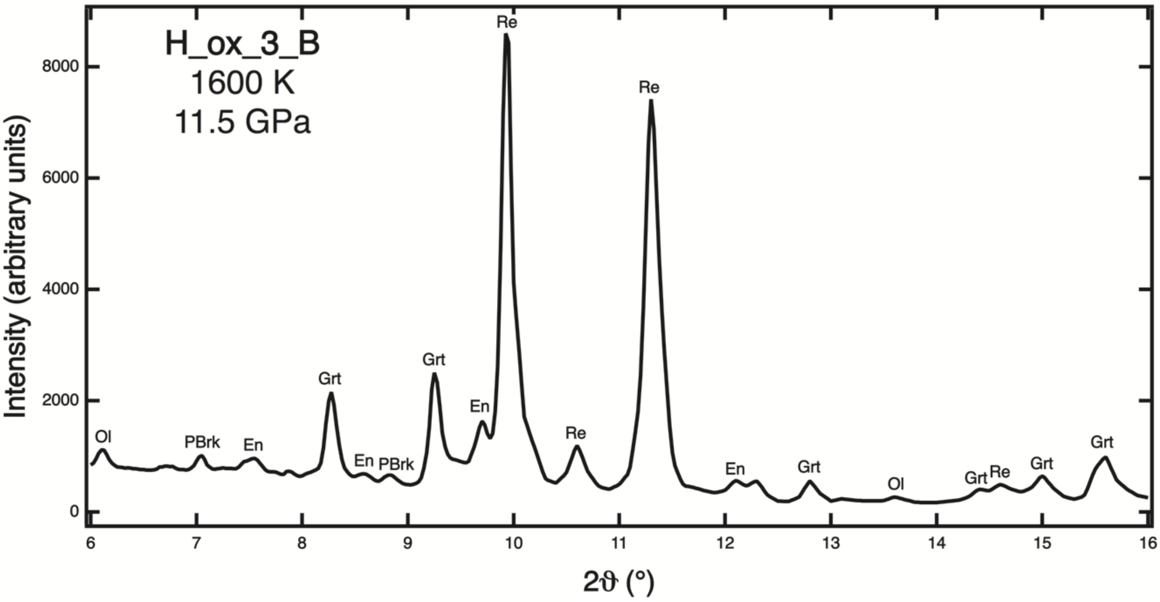
H_ox_3_B
1600 K
11.5 GPa
Intensity (arbitrary units)
2ϑ (°)
0
2000
4000
6000
8000
6
7
8
9
10
11
12
13
14
15
16
Ol
PBrk
En
Grt
En
PBrk
Grt
En
Re
Re
Re
En
Grt
Ol
Grt
Re
Grt
Grt

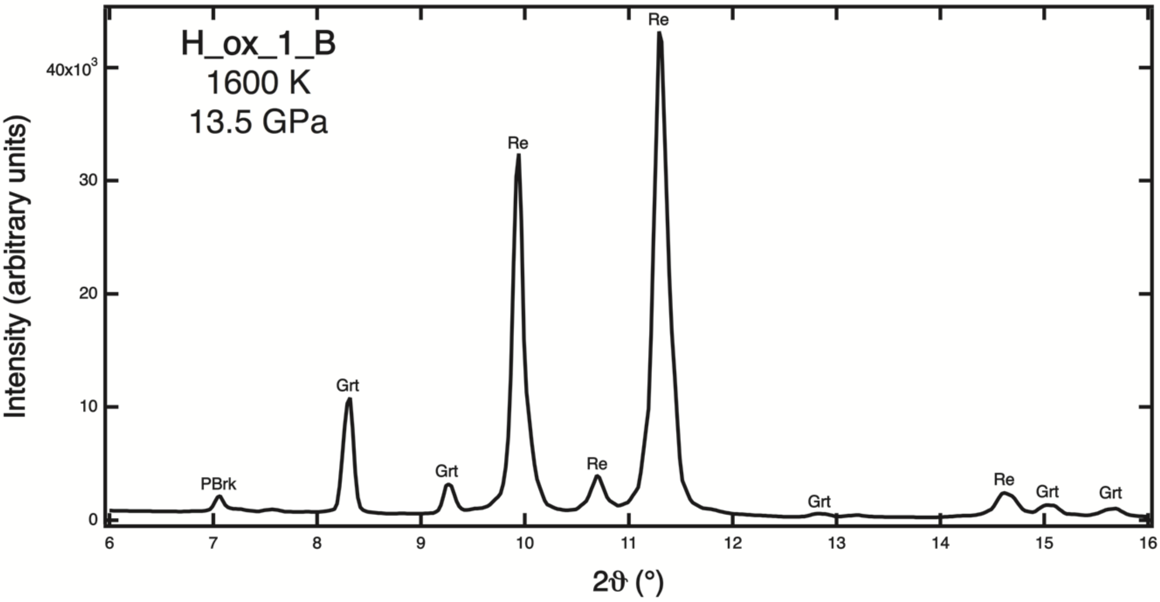
H_ox_1_B
1600 K
13.5 GPa
Intensity (arbitrary units)
2ϑ (°)
0
10
20
30
40x10³
6
7
8
9
10
11
12
13
14
15
16
PBrk
Grt
Grt
Re
Re
Re
Grt
Re
Grt
Grt

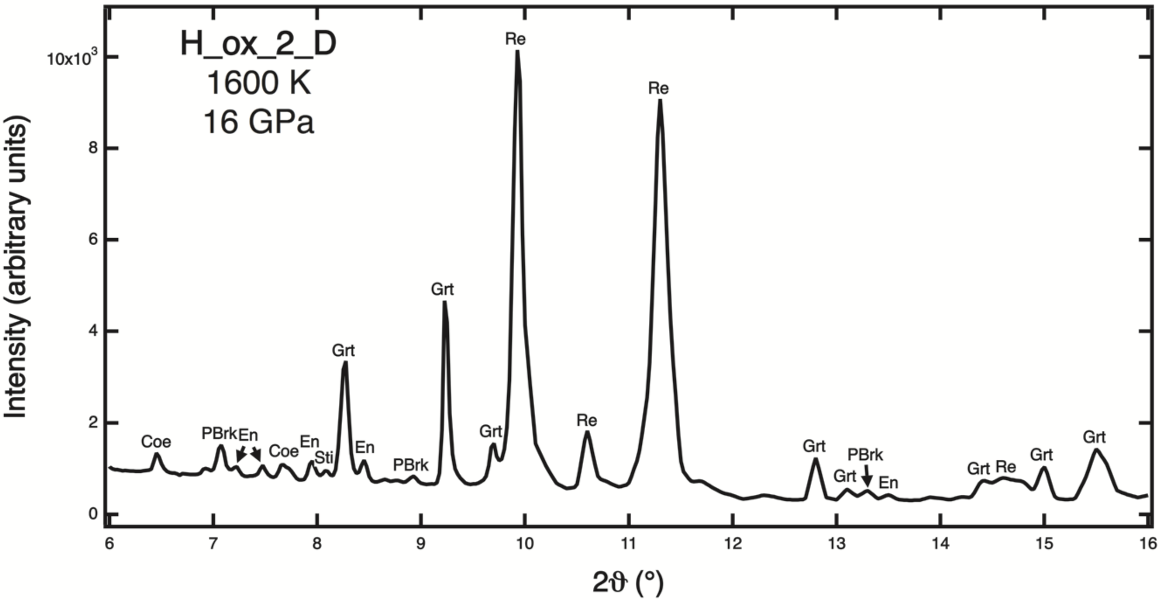
H_ox_2_D
1600 K
16 GPa
Intensity (arbitrary units)
10x10³
8
6
4
2
0
Coe
PBrk
En
Coe
En
Sti
Grt
En
PBrk
Grt
Grt
Re
Re
Re
Grt
Grt
PBrk
En
Grt
Re
Grt
Grt
6
7
8
9
10
11
12
13
14
15
16
2ϑ (°)

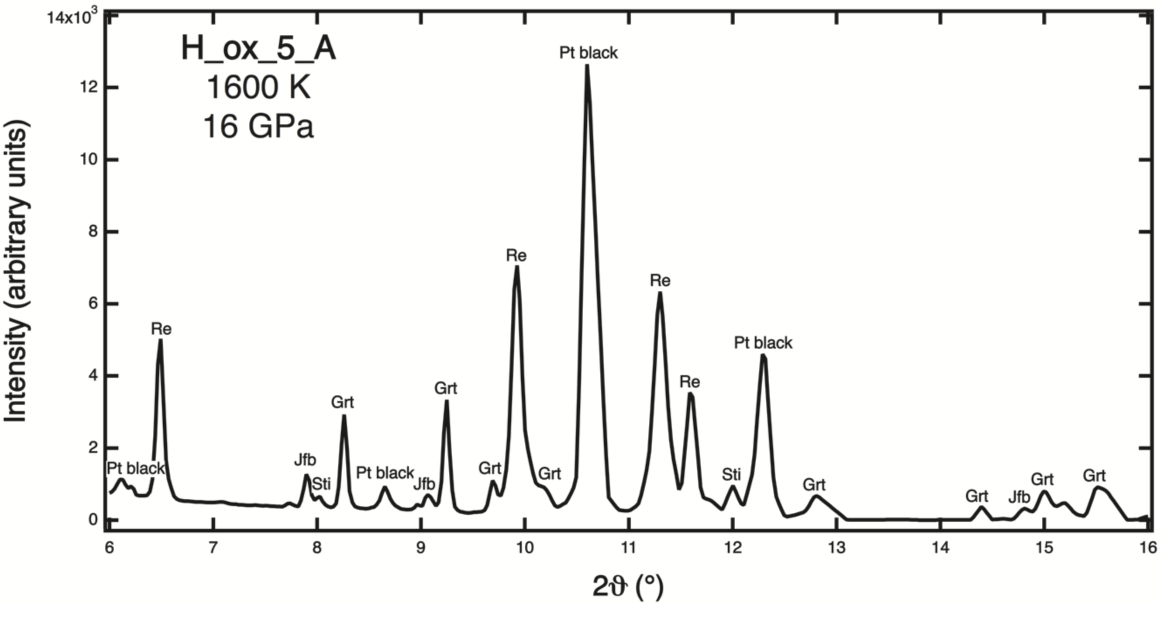
H_ox_5_A
1600 K
16 GPa
Intensity (arbitrary units)
14x10³
12
10
8
6
4
2
0
Pt black
Re
Jfb
Sti
Grt
Pt black
Jfb
Grt
Grt
Re
Grt
Pt black
Re
Re
Sti
Pt black
Grt
Grt
Jfb
Grt
Grt
6
7
8
9
10
11
12
13
14
15
16
2ϑ (°)

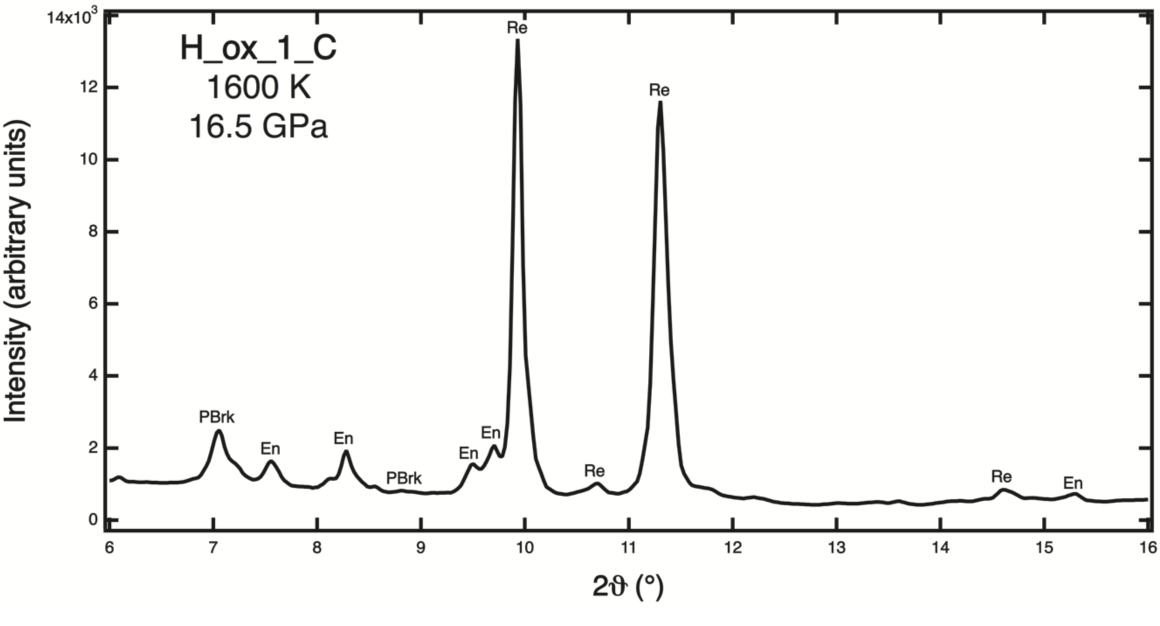
H_ox_1_C
1600 K
16.5 GPa
Intensity (arbitrary units)
14x10³
12
10
8
6
4
2
0
PBrk
En
En
PBrk
En
En
Re
Re
Re
Re
En
6
7
8
9
10
11
12
13
14
15
16
2ϑ (°)

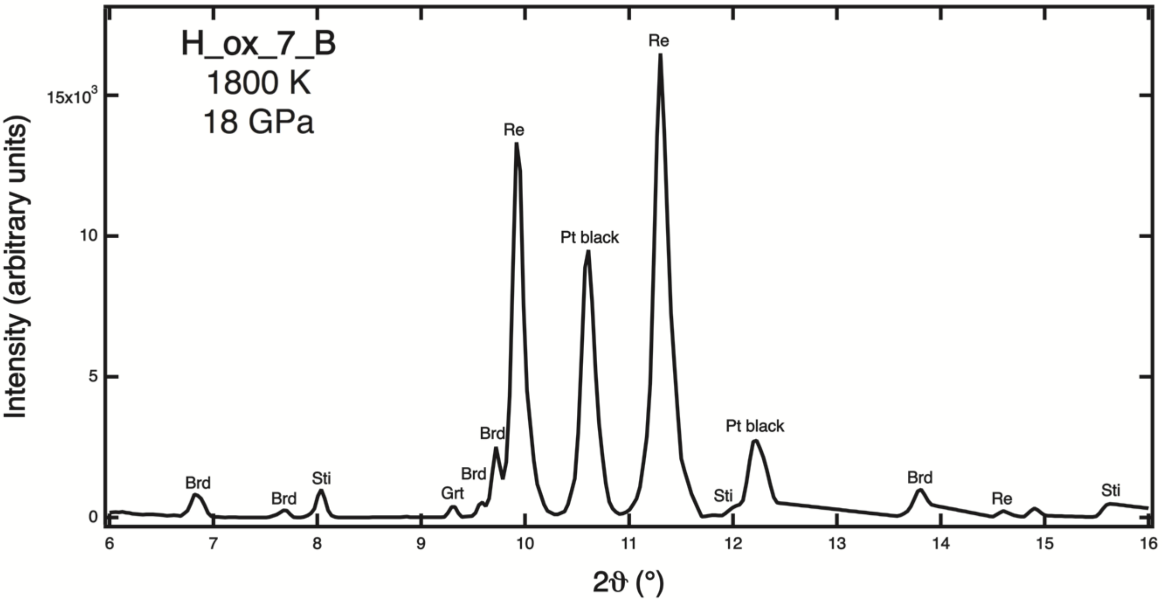
H_ox_7_B
1800 K
18 GPa
Intensity (arbitrary units)
15x10^3
10
5
0
2ϑ (°)
6
7
8
9
10
11
12
13
14
15
16
Brd
Brd
Sti
Grt
Brd
Brd
Re
Pt black
Re
Sti
Pt black
Brd
Re
Sti

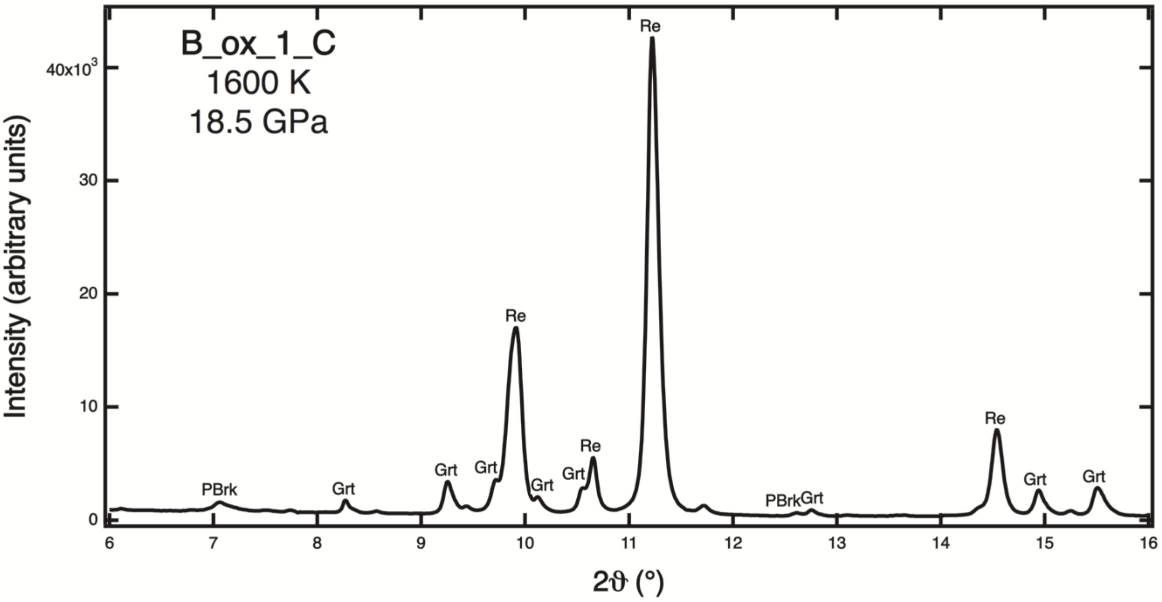
B_ox_1_C
1600 K
18.5 GPa
Intensity (arbitrary units)
40x10^3
30
20
10
0
2ϑ (°)
6
7
8
9
10
11
12
13
14
15
16
PBrk
Grt
Grt
Grt
Re
Grt
Grt
Re
Re
PBrk
Grt
Re
Grt
Grt

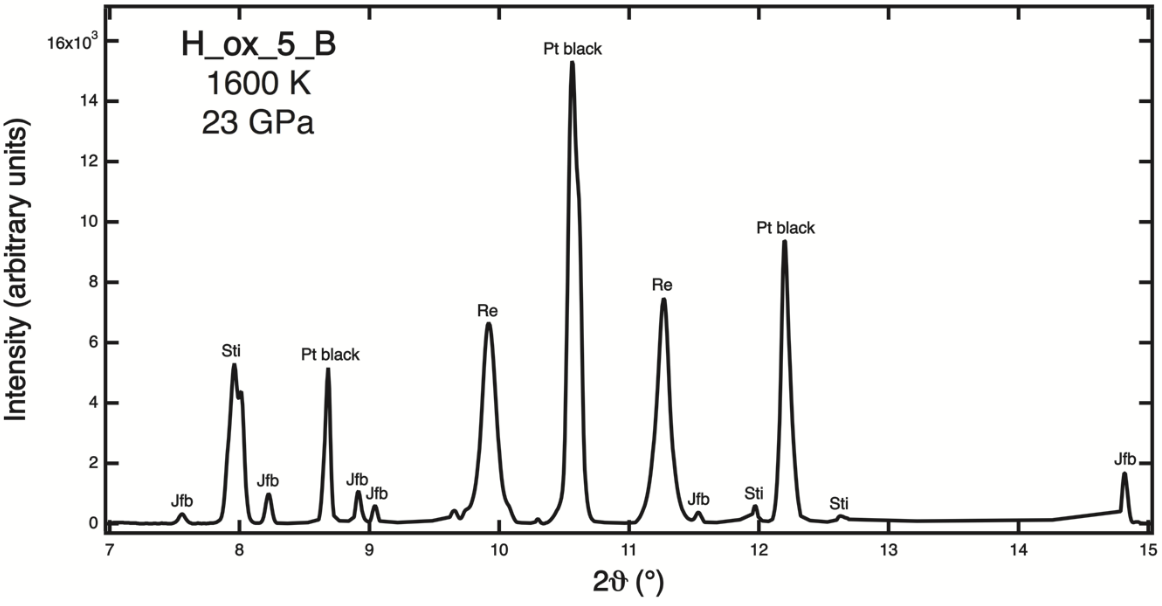
H_ox_5_B
1600 K
23 GPa
Intensity (arbitrary units)
16x10^3
14
12
10
8
6
4
2
0
2ϑ (°)
7
8
9
10
11
12
13
14
15
Jfb
Sti
Jfb
Pt black
Jfb
Jfb
Re
Pt black
Re
Jfb
Sti
Pt black
Sti
Jfb

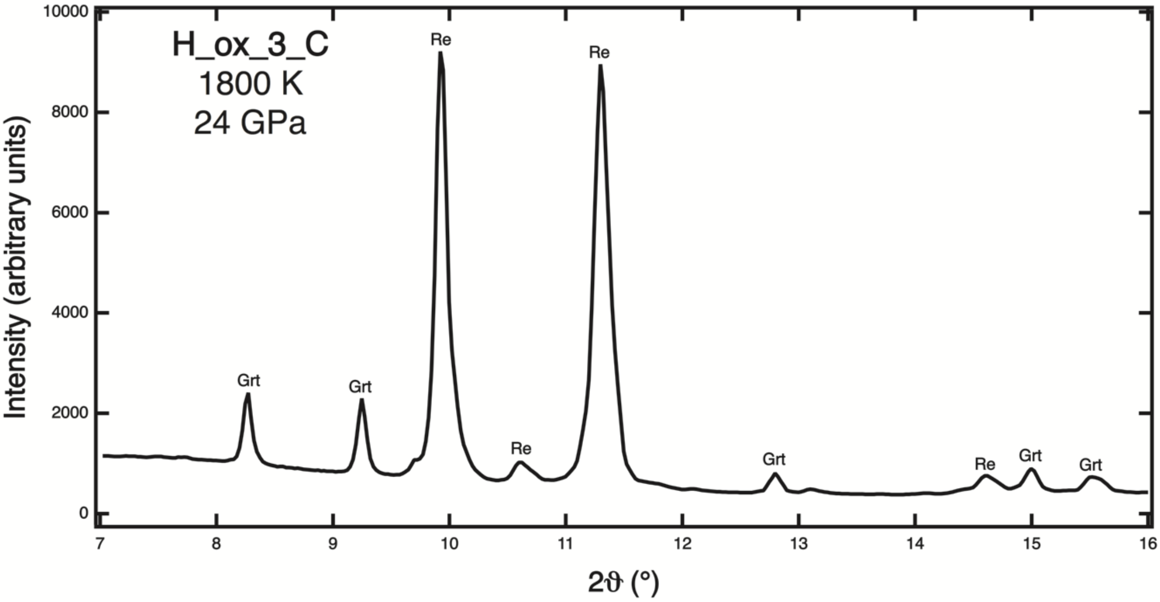
H_ox_3_C
1800 K
24 GPa
Re
Re
Grt
Grt
Re
Grt
Re
Grt
Grt
Intensity (arbitrary units)
10000
8000
6000
4000
2000
0
7
8
9
10
11
12
13
14
15
16
2ϑ (°)

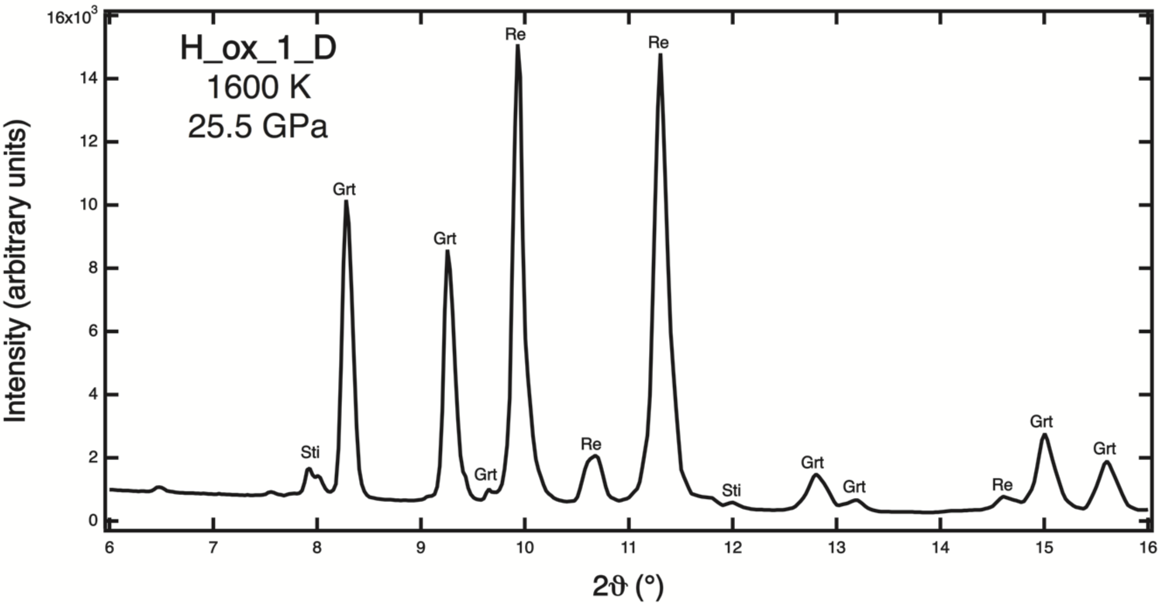
H_ox_1_D
1600 K
25.5 GPa
Re
Re
Grt
Grt
Sti
Grt
Re
Sti
Grt
Grt
Re
Grt
Grt
Intensity (arbitrary units)
16x10^3
14
12
10
8
6
4
2
0
6
7
8
9
10
11
12
13
14
15
16
2ϑ (°)

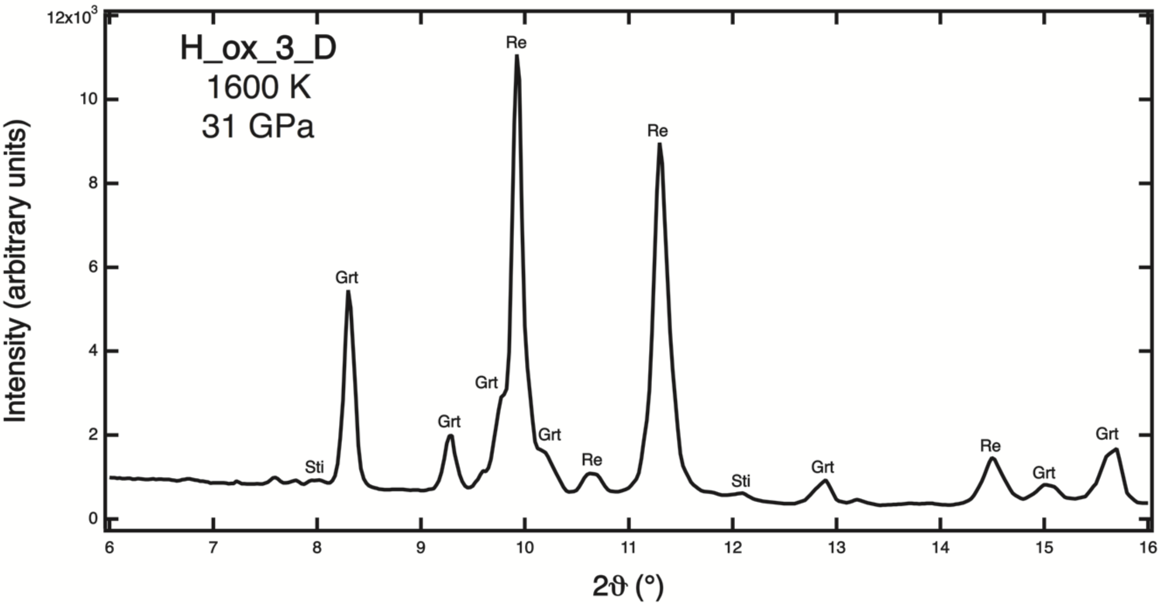
H_ox_3_D
1600 K
31 GPa
Re
Re
Grt
Grt
Grt
Grt
Sti
Re
Sti
Grt
Re
Grt
Grt
Intensity (arbitrary units)
12x10^3
10
8
6
4
2
0
6
7
8
9
10
11
12
13
14
15
16
2ϑ (°)

11 Appendix C

Other related publications

Mineralogical Magazine, 2015, Vol. 79(2), pp. 285–294

Equation of state of hercynite, $FeAl_2O_4$, and high-pressure systematics of Mg-Fe-Cr-Al spinels

F. NESTOLA[1,]*, B. PERIOTTO[1], C. ANZOLINI[2], G. B. ANDREOZZI[2], A. B. WOODLAND[3], D. LENAZ[4], M. ALVARO[1] AND F. PRINCIVALLE[4]

[1] Dipartimento di Geoscienze, Università degli Studi di Padova, Via Gradenigo 6, I-35131 Padova, Italy
[2] Dipartimento di Scienze della Terra, Sapienza Università di Roma, Piazzale Aldo Moro 5, I-00185 Roma, Italy
[3] Institut für Geowissenschaften, Geozentrum der Goethe-Universität, Altenhöferallee 1, D-60438, Frankfurt am Main, Germany
[4] Dipartimento di Matematica e Geoscienze, Università degli Studi di Trieste, Via Weiss 8, I-34127 Trieste, Italy

[*Received 25 June 2014; Accepted 14 August 2014; Associate Editor: E. Grew*]

ABSTRACT

In this work a single crystal of synthetic hercynite, $FeAl_2O_4$, was investigated by X-ray diffraction up to 7.5 GPa and at room temperature, in order to determine its pressure−volume equation of state. The unit-cell volume decreases non-linearly with a reduction of 3.4% (i.e. 18.43 Å^3). The pressure−volume data were fitted to a third-order Birch-Murnaghan equation of state providing the following coefficients: V_0 = 542.58(3) Å^3, K_{T0} = 193.9(1.7) GPa, K' = 6.0(5). These results are consistent with previous investigations of Cr and Al spinels measured with the same experimental approach but the K_{T0} differs significantly from the experimental determination carried out more than 40 years ago by Wang and Simmons (1972) by the pulse echo overlap method. Our new results were used to re-determine the $FeAl_2O_{4(\text{hercynite})} = FeO_{(\text{wüstite})} + Al_2O_{3(\text{corundum})}$ equilibrium in $P-T$ space and obtain geobarometric information for Cr-Al spinels found as inclusions in diamond.

KEYWORDS: hercynite, X-ray diffraction, high pressure, bulk modulus, diamond, spinel.

Introduction

DUE to their abundance in several geological environments, spinels have an important place in Earth science. An incredibly large number of scientific papers have been published on their stability and behaviour and, more recently, several studies have focused on their elastic behaviour under extreme conditions of temperature and pressure, which can be used to determine the conditions at which spinels crystallize (Sack and Ghiorso, 1991; Andreozzi and Lucchesi, 2002; Bosi *et al.*, 2008; Lenaz *et al.*, 2009; Lenaz *et al.*, 2013; Princivalle *et al.*, 2012; Perinelli *et al.*, 2012; Lenaz and Skogby, 2013; Perinelli *et al.*, 2014; Nestola *et al.*, 2014). In detail, spinels from a high-pressure mantle origin represent one of the most common inclusions found in diamonds and consequently they can provide significant indications about the environment of formation of diamonds. In this specific case, the most common spinels are represented by the Cr-spinels, mainly by solid solutions comprising magnesiochromite, $MgCr_2O_4$ and chromite, $FeCr_2O_4$. However, the hercynite component, $FeAl_2O_4$, is significant in high-pressure spinels with percentages reaching 10−15%, whereas the spinel (*sensu stricto*), $MgAl_2O_4$, only constitutes a few percent (see Stachel and Harris, 2008 and Lenaz *et al.*, 2009 for a review). The natural magnesiochromite–chromite–hercynite–spinel (*sensu stricto*) solid solutions have often been used as geothermometers (Fabriès, 1979; Ballhaus *et al.*, 1990), geobarometers (O'Neill, 1981; O'Neill and Wall,

---

* E-mail: fabrizio.nestola@unipd.it
DOI: 10.1180/minmag.2015.079.2.07

1987) and oxygen barometers (Ballhaus *et al.*, 1991). However, whereas the high-pressure behaviour of $MgCr_2O_4$, $FeCr_2O_4$ and $MgAl_2O_4$ has been the subject of several recent investigations (i.e. Nestola *et al.*, 2007, 2009, 2014; Taran *et al.*, 2014), the elastic behaviour of hercynite remains to be investigated and compared with that of the other endmembers. Data on the high-pressure behaviour of hercynite are also needed to constrain the influence of Al-Cr substitution at high pressure on the elasticity of natural, complex Cr-rich spinels. It has been demonstrated experimentally that hercynite can be stable at high-pressure conditions up to 7–8.5 GPa at temperatures >1000ºC (Schollenbruch *et al.*, 2010) and this explains why it could be an important component of Cr-spinels included in diamonds. In addition, a few mineral equilibria involving $FeAl_2O_4$ hercynite have been investigated at high pressure in order to calibrate certain spinel-based geobarometers (i.e. Bohlen *et al.*, 1986; Shulters and Bohlen, 1989). As mentioned, the most recent work in which the stability field of hercynite has been defined is from Schollenbruch *et al.* (2010). In this work the authors used the bulk modulus, K, published in the thermodynamic database by Holland and Powell (1998, 1990) who reported a value of 210 GPa at room temperature, with a fixed $K' = 4$. Such a value of bulk modulus, as reported in their table A1 Appendix 2 (specified in Holland and Powell, 1998), is clearly indicated as "estimated" and reports no obvious errors. To the best of our knowledge, the only further datum on the bulk modulus of hercynite was published more than 40 years ago by Wang and Simmons (1972) using ultrasonic measurements. Those authors reported an adiabatic bulk modulus K_S value of 210.3 GPa (corresponding to a static bulk modulus K_T of 209 GPa as reported by Stixrude and Lithgow-Bertelloni, 2005) but also reported no error relative to their bulk modulus. However, both the "estimated" values from Holland and Powell (1998) and Wang and Simmons (1972) appear to be too high when compared to previous values measured on $MgCr_2O_4$, $FeCr_2O_4$ and $MgAl_2O_4$, which show K_T of 182.5(1.4), 184.8(1.7) (Nestola *et al.*, 2014) and 193(1) GPa (Nestola *et al.*, 2007), respectively. In detail, we observe that for Mg-bearing spinels, substituting Cr for Al, an increase of K_T from 182.5 to 193 GPa (an increase of ~5%) is obtained. Instead, for the Fe-bearing spinels, if we assume that the estimated value of bulk modulus by Holland and Powell (1998) and that measured by Wang and Simmons (1972) are correct, the substitution of Cr for Al would cause an increase in K_T from 184.8 to ~210 GPa (i.e. an increase of >13%), which appears to be anomalously high. In order to test this anomalous behaviour a synthetic single crystal of pure hercynite, $FeAl_2O_4$, was investigated by X-ray diffraction (XRD) under high-pressure conditions and room temperature using a diamond-anvil cell up to ~7.5 GPa. For the purposes of comparison the same experimental approach was used as in Nestola *et al.* (2014) on $MgCr_2O_4$ and $FeCr_2O_4$ and Nestola *et al.* (2007) on $MgAl_2O_4$. The results obtained are expected to be crucial in determining the correct stability field and entrapment pressure of spinels in diamonds, which are based on host and inclusion thermodynamic properties, such as the bulk modulus K_{T0} (see Angel *et al.*, 2015; Milani *et al.*, 2015).

Experimental

Sample

The sample studied here is a synthetic hercynite single crystal, with dark green to black colour, regular octahedral shape and ~100 μm in size (see Fig. 1), corresponding to the sample He100g studied by Hålenius *et al.* (2002). The hercynite endmember was produced using a flux-growth method starting from $Al(OH)_3$, MgO and Fe_2O_3 reagents and with $Na_2B_4O_7$ used as a flux, under a strongly reducing atmosphere obtained through

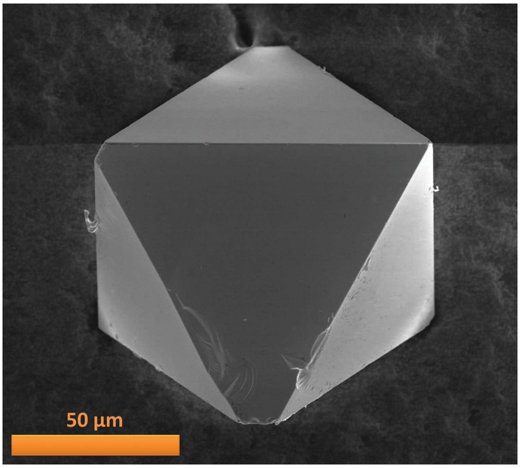

FIG. 1. High-magnification scanning electron microscope image of the He100 single crystal studied in the present study.

continuous flow of CO_2 and H_2 gases. Many experiments at increasingly reducing conditions (CO_2:H_2 from 2:1 to 1:2 gas-mixing ratio) were undertaken to minimize the spinel Fe^{3+} content, but Fe^{3+} could not be completely reduced. The proof of the ubiquitous presence of Fe^{3+} and its quantification were obtained by Mössbauer spectroscopy and further confirmed by optical absorption spectroscopy (see Hålenius *et al.*, 2002 for more details). For He100g, the sample closest to the ideal endmember, previous authors obtained the following composition (wt.%): FeO = 41.1(3), Fe_2O_3 = 1.2(3), Al_2O_3 = 57.5(4). The corresponding chemical formula $Fe^{2+}[Al_{1.973(6)}Fe^{3+}_{0.027(6)}]O_4$ indicates the presence of 1.35 mole% magnetite in solid solution with hercynite.

In situ high-pressure XRD

The single crystal selected for the high-pressure experiments for this work was free of twinning and inclusions, and showed sharp diffraction profiles. The crystal size of the sample was 120 μm × 100 μm × 40 μm. The sample was loaded in an Eidgenössische Technische Hochschule (ETH)-type diamond-anvil cell (DAC) equipped with Be backing-plates (Miletich *et al.*, 2000) for the determination of unit-cell parameters by means of *in situ* high-pressure single-crystal XRD at the Department of Geosciences of the University of Padova (Italy). The ETH-type DAC has stainless steel gaskets pre-indented to a thickness of 90 μm with a spark-eroded hole of 250 μm in diameter. A mixture of methanol and ethanol with 4:1 ratio was used as pressure medium, which remains hydrostatic up to pressures greater than those reached in this present work (Angel *et al.*, 2007). The diameter of the diamond culets was 600 μm. To determine the pressure–volume equation of state (EoS), the sample was loaded together with a single crystal of quartz used as an internal pressure standard (Angel *et al.*, 1997). The measurements of the unit-cell parameters were carried out on a four-circle STOE STADI IV diffractometer at the Department of Geosciences of the University of Padova (Italy) equipped with a point detector and controlled by the *SINGLE* software package (Angel and Finger, 2011). *SINGLE* software is based on the 8-position centring method (King and Finger, 1979; Angel *et al.*, 2000) and vector least-squares refinement of the unit-cell parameters (Ralph and Finger, 1982). The data were acquired using Mo*K*α radiation at 50 kV and 40 mA. The unit-cell edge was determined from the centring of an average of 25 reflections, in the 2θ range 14–33° at 12 different pressures up to 7.456 GPa.

Results

Pressure–volume equation of state of hercynite

The unit-cell volume *vs.* pressure for the hercynite crystal studied in this work is shown in Fig. 2. The volume shows a significant decrease (>18 Å^3,

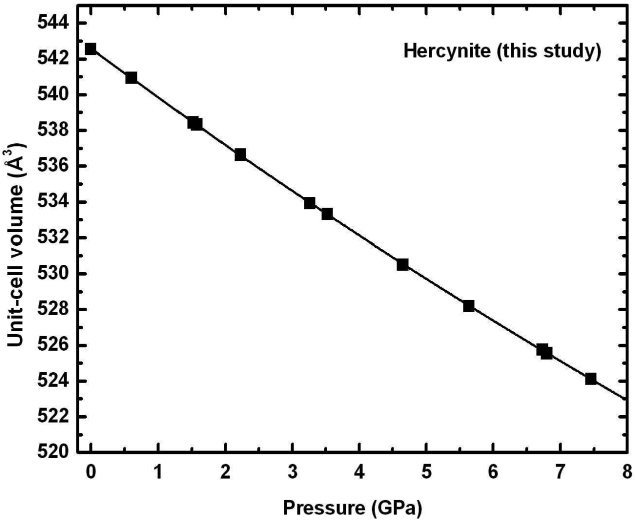

FIG. 2. Pressure–volume trend for hercynite investigated here.

TABLE 1. Unit-cell parameters at different pressures for $FeAl_2O_4$ studied in this work. Standard deviations in the last digits are in parentheses.

P (GPa)	a (Å)	V (Å^3)
0.00010(1)	8.1560(2)	542.54(4)
0.603(6)	8.1479(2)	540.93(4)
1.523(6)*	8.1353(2)	538.42(4)
1.576(5)	8.1348(2)	538.32(4)
2.227(7)	8.1262(2)	536.62(4)
3.265(8)	8.1125(2)	533.91(4)
3.525(7)*	8.1094(2)	533.30(4)
4.653(7)	8.0952(2)	530.50(4)
5.641(9)	8.0833(2)	528.17(4)
6.734(9)*	8.0710(2)	525.74(4)
6.797(10)	8.0699(2)	525.54(4)
7.456(11)	8.0626(2)	524.11(4)

* Data collected during decompression.

~3.4%) up to ~7.5 GPa. The volume compression over pressure is marked by a slight curvature, which becomes more evident above 4 GPa. In order to provide a clear idea of the deviation from linearity we can calculate that at the maximum pressure reached in this present work (7.5 GPa) the difference between the observed volume (524.1 Å^3) and that calculated (522.8 Å^3) assuming linear evolution with pressure for the data above 4 GPa is ~1.3 Å^3. This volume difference, for a stiff structure such as that of hercynite, would correspond to a compression of ~0.55 GPa (using the EoS coefficients for our sample reported below). This highlights how crucial it is to choose the correct EoS to fit the pressure–volume data (see Angel *et al.*, 2014*a*,*b*). In order to define which is the best EoS to adequately describe the pressure–volume data for hercynite (see Table 1) an F_E–f_E plot (Angel, 2000) was constructed, with F_E being the normalized stress given as $[P/(3f_E)\cdot(1+2f_E)^{5/2}]$ and f_E being the Eulerian strain given as $([(V_0/V)^{2/3}-1]/2)$ which is shown in Fig. 3. The plot shows clearly that the experimental data can be fitted adequately to a third-order Birch–Murnaghan EoS (hereafter BM3, Birch, 1947). The intercept of the dashed straight line at $f_E = 0$ (Fig. 3) gives K_{T0} = 195.4(1.3) GPa, whereas its slope [equal to $3K_{T0}(K'-4)/2$] provides the first pressure derivative K' with a value of 5.6(2). The fit of the pressure–volume data reported in Table 1 to a BM3 (using *EosFit7c*, Angel *et al.*, 2014*a*) provided the following EoS coefficients: V_0 = 542.58(3) Å^3, K_{T0} = 193.9(1.7) GPa, K' = 6.0(5). The quality of the diffraction data is also marked by the negligible difference (~1 estimated standard deviation) between the refined data and those obtained by the plot in Fig. 3.

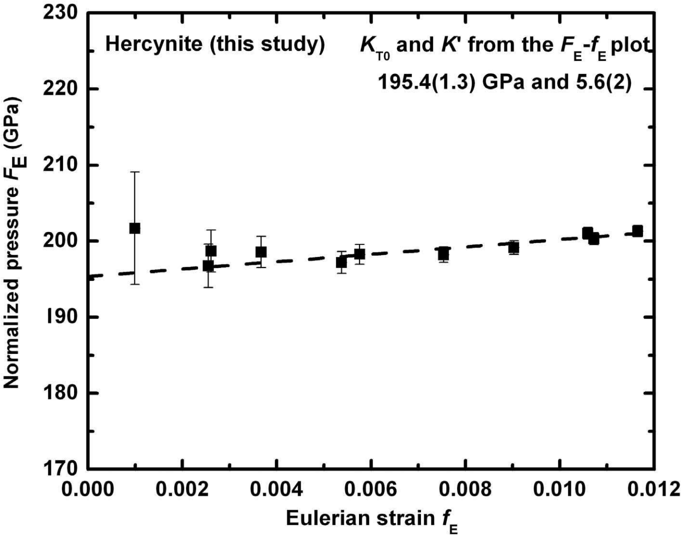

FIG. 3. $F_E - f_E$ plot for the sample studied in this work. The K_{T0} and its first pressure derivative, K', were obtained by the straight line intercept and its slope (Angel, 2000).

Comparison with previous work

As reported in the introduction section, the only data available in the literature for the bulk modulus of hercynite are from Holland and Powell (1998) and Wang and Simmons (1972). However, the bulk modulus provided by Holland and Powell (1998) was only "estimated" and the one measured by Wang and Simmons (1972) was obtained by a digital pulse echo overlap method, which does not provide a reliable set of results such as those obtained by modern techniques (i.e. *in situ* high-pressure XRD). These authors report a value of bulk modulus of 210.3 GPa (K_{VRH}) corresponding to a static bulk modulus K_{T0} of ~209 GPa as reported in the database by Stixrude and Lithgow-Bertelloni (2005). However, Wang and Simmons (1972) obtained no first pressure derivative for hercynite as their measurements were only performed at room pressure.

The bulk modulus from Wang and Simmons (1972) differs from that in the present study by ~7.2%, which is a significant difference. Although (1) it is well known that our bulk modulus is strongly related to its first pressure derivative and that (2) the two experimental methods used in Wang and Simmons (1972) and in the present work are different, we consider the above-mentioned bulk modulus difference to be too great. The reason for such a discrepancy is not so evident or trivial that it can be explained, but a first attempt to investigate it could be to analyse the materials investigated in the two works. The synthetic crystal used in Wang and Simmons (1972) was originally a very large single crystal, 4 mm × 4 mm × 10 mm in size, but they then reduced the crystal size to less than a half of the original size during sample preparation. In order to calculate the density they used the lattice parameter of Slack (1964). The density of 4.280 g/cm^3 used by Wang and Simmons (1972) is only slightly different from ours (~0.5%), which is 4.275 g/cm^3 (calculated using our volume in Table 1 and our chemical formula reported above), and we do not consider such a difference sufficient to justify the large change in bulk modulus, from 209 to 193.9 GPa. However, the unit-cell volume of 539.35 Å^3 provided by Slack (1964) for the synthetic crystal used in Wang and Simmons (1972) corresponds to a unit-cell parameter *a* of 8.1400 Å, much smaller than the value of 8.1560 Å that was measured for our He100g crystal. The sample studied by Slack (1964) using single-crystal XRD was reported to have some Fe^{2+} in the octahedral site, as a consequence of temperature-driven cation disorder. In detail, Slack (1964) reported ~15% of Fe^{2+} in octahedral coordination as a possible consequence of the sample annealing at 1200ºC. In our case, for hercynite crystals produced in the same experimental conditions as sample He100g, the structural characterization by Andreozzi and Lucchesi (2002) revealed 15% of Fe^{2+} in octahedral coordination; this result was obtained for samples annealed at a much lower temperature (i.e. 800ºC) however, in perfect agreement with the results of Harrison *et al.* (1998), who showed that in synthetic hercynite the Fe^{2+} disorder is linearly dependent on temperature up to 1150ºC. On the basis of our experiments and the literature data, we conclude that neither the cell parameter nor the Fe^{2+} disorder reported for the sample used in Wang and Simmons (1972) do not agree with the expected values for a defect-free hercynite annealed at 1200ºC.

The physical difference between our sample and the hercynite of Wang and Simmons (1972) is the real crystal volume: our sample has a real volume of 0.00048 mm^3 whereas the Wang and Simmons crystal had a volume of 160 mm^3. Such a difference cannot be negligible in terms of real and calculated density, as for a crystal of 160 mm^3 the degree of porosity and fractures can influence the material density and cause a non-negligible difference between real and calculated density by XRD. Furthermore, the crystal dimensions were actually too small for the technique used by Wang and Simmons. Indeed, the authors themselves state that for the pulse echo overlap method the crystal they used was clearly too small and this caused some problems with the travel time which was too small.

Bulk modulus systematics for Mg-Fe-Cr-Al spinels and stability field of hercynite

A direct comparison between our data and those obtained in previous studies on spinels can be carried out with respect to $MgCr_2O_4$, $FeCr_2O_4$ and $MgAl_2O_4$. These three endmembers were investigated by Nestola *et al.* (2007, 2009, 2014) using the same experimental approach as presented in the present work for $FeAl_2O_4$ spinel. The pressure–volume EoS of all these four endmembers is reported in Table 2. The data in Table 2 were all obtained using a third-order Birch-Murnaghan EoS and the confidence ellipses are

TABLE 2. Bulk modulus and its first pressure-derivative for $FeAl_2O_4$ in this study and for $MgAl_2O_4$ (Nestola *et al.*, 2007), $FeCr_2O_4$ and $MgCr_2O_4$ (Nestola *et al.*, 2014).

Compound	K_{T0} (GPa)	K'
$FeAl_2O_4$	193.9(1.7)	6.0(5)
$FeCr_2O_4$	184.8(1.7)	6.1(5)
$MgCr_2O_4$	182.5(1.4)	5.8(4)
$MgAl_2O_4$	193(1)	5.6(3) *ordered str.*
$MgAl_2O_4$	192(1)	5.4(3) *disordered str.*

shown in Fig. 4 as in Nestola *et al.* (2014), with the values of K_S (Wang and Simmons, 1972) and K' (Holland and Powell, 1990, 1998) from previous hercynite studies added for comparison.

The following results are shown in Fig. 4: (1) when Al substitutes for Cr the static bulk modulus shows a significant increase from an average value of 183.6 GPa to an average value of 193 GPa; (2) the Fe/Mg substitution does not affect significantly the bulk modulus for either Cr or Al spinels; (3) the first pressure derivative remains constant within 1–2 sigmas for all four endmembers $MgCr_2O_4$–$FeCr_2O_4$–$FeAl_2O_4$–$MgAl_2O_4$, with an average value being 5.8; and (4) the single bulk-modulus datum from a previous study on hercynite lies completely out of the range for the general Mg-Fe-Cr-Al spinels compared in this present work. Considering these four points together, we are confident that the EoS of our hercynite sample is consistent with the EoS of the other three spinels.

Using the new EoS of hercynite determined here we have re-calculated the equilibrium $FeAl_2O_{4(\text{hercynite})} = FeO_{(\text{wüstite})} + Al_2O_{3(\text{corundum})}$ in the P–T space as computed by Schollenbruch *et al.* (2010). The new equilibrium is shown in Fig. 5 compared with that of Schollenbruch *et al.* (2010), who used a bulk modulus of 210 GPa and a first pressure derivative $K' = 4$ (data extracted from Holland and Powell, 1990, 1998). The new equilibrium, calculated with our EoS data, shifts the value given by Schollenbruch *et al.* (2010) up to a maximum pressure of ~0.2 GPa (see Table 3 for the exact P–T values). Note that in Fig. 5 the differences between the two equilibria decrease slightly as a function of temperature. The uncertainties in the experimental conditions reported by Schollenbruch *et al.* (2010) (~0.5 GPa) along with further uncertainties due to their correction procedure, make the differences between the two equilibria in Fig. 5 insignificant.

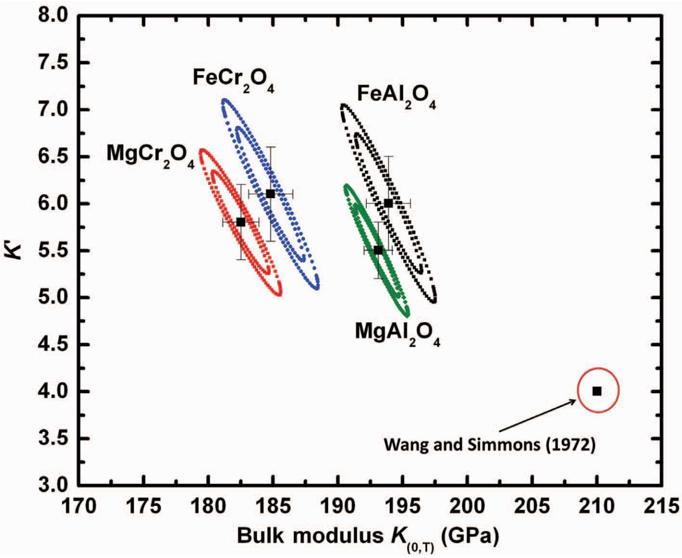

FIG. 4. Confidence ellipses [1 and 3 sigmas for small and large ellipses, respectively, see Angel (2000) for details] for four Cr-Al-Fe-Mg spinels including our hercynite $FeAl_2O_4$. In the red circle the value of K_S (Wang and Simmons, 1972) and K' (Holland and Powell, 1990, 1998) are reported for comparison.

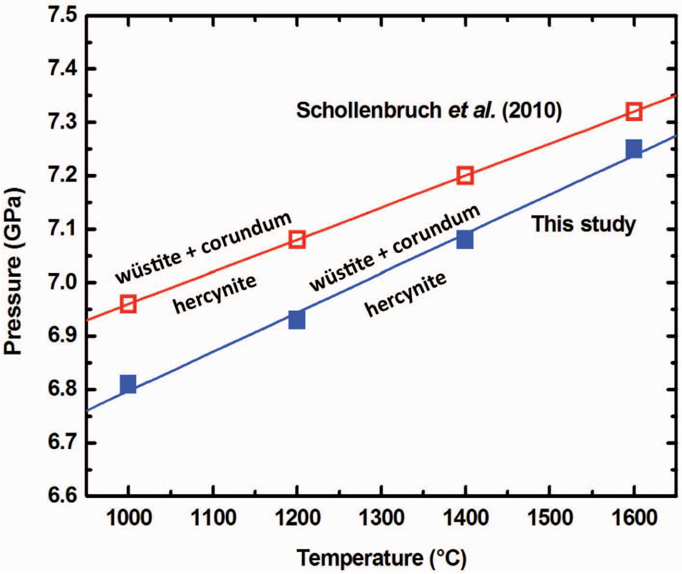

FIG. 5. Stability field in $P-T$ space for hercynite studied in this present work and that from Schollenbruch *et al.* (2010). The two curves mark the breakdown of hercynite to $FeO_{(wüstite)} + Al_2O_{3(corundum)}$ with increasing pressure.

Implications for diamond-inclusion geobarometry

As shown in the previous paragraph, the use of a bulk modulus ranging from ~194 to 209–210 GPa does not affect the boundary position of the equilibrium reaction $FeAl_2O_{4(hercynite)} = FeO_{(wüstite)} + Al_2O_{3(corundum)}$ in the $P-T$ space (probably due to the experimental conditions used by Schollenbruch *et al.*, 2010; this is not a general case for minerals, see for example the case of antigorite, Nestola *et al.*, 2010). However, the same does not apply when different EoS are used to obtain geobarometric information for a diamond-inclusion pair (i.e. Cr-Al spinels included in peridotitic diamonds). In detail, it was demonstrated recently that information about the pressure of formation of diamond and its mineral inclusions can be obtained with a new approach based entirely on their respective elastic properties (see Nestola *et al.*, 2011; Angel *et al.*, 2014*a*, 2015). However, such an approach relies on precise and accurate knowledge of the $P-V-T$ equations of state of diamond and its inclusions and therefore differences in bulk modulus and/or thermal expansion coefficient could be critical. In fact, we have shown how, considering a typical peridotitic diamond which includes Cr-Al spinels, the use of bulk modulus with a value of 210 GPa and a $K' = 4$ (Wang and Simmons, 1972; Holland and Powell, 1990, 1998) can provide a different pressure of formation with respect to that obtained with a bulk modulus with a value of 193.9 GPa and $K' = 6.0$ (present study). In general, the hercynite component for a Cr-spinel extracted from a diamond can reach 10–15% (see for example Lenaz *et al.*, 2009; Stachel and Harris, 2008). In this present work we used the thermal

TABLE 3. Pressure–temperature data relative to the hercynite = wüstite + corundum breakdown using the EoS coefficients of hercynite measured in this work compared with those used in Schollenbruch *et al.* (2010).

	P (GPa)	T (ºC)
Schollenbruch *et al.* (2010)	6.962	1000
This work	6.809	1000
Schollenbruch *et al.* (2010)	7.082	1200
This work	6.932	1200
Schollenbruch *et al.* (2010)	7.202	1400
This work	7.082	1400
Schollenbruch *et al.* (2010)	7.318	1600
This work	7.252	1600

expansion data for hercynite provided by Holland and Powell (1998) and a temperature dependency of the bulk modulus dK/dT was calculated, also following Holland and Powell (1998) [i.e. $K_T = K_{T0}\ (1 - 1.5{\cdot}10 - 4\ {\cdot}(T - 298)$]. Moreover, an internal pressure of the inclusion in diamond was assumed to be 0.5 GPa (typical values for minerals in lithospheric diamonds, see Nestola *et al.*, 2011, 2012) and a temperature of formation of 1200ºC. Based on these parameters, using (1) the bulk modulus of 209 GPa and first pressure derivative $K' = 4$ as reported in Wang and Simmons (1972) and Holland and Powell (1990, 1998) and (2) EoS parameters for diamond reported in Angel *et al.* (2014*a*), a calculation performed with the *ISOMEKE* subroutine (available in *EoSFit7c*, see Angel *et al.*, 2014*a*,*b*) provided a pressure of entrapment/formation $P_e = 6.26$ GPa (with a $dK/dT = -0.031$ GPa/ºC). Whereas, using our EoS coefficients and the same parameters (with a $dK/dT = -0.028$ GPa/ºC), a pressure of formation of $P_e = 5.71$ GPa was obtained.

This result has significant implications if we consider that the two major components in Cr-spinels found as inclusions in diamond are magnesiochromite ($MgCr_2O_4$) and chromite ($FeCr_2O_4$) (together summing up to 85–90%). Indeed, these two components show nearly identical thermo-elastic parameters; therefore, the only possible changes in the pressure of formation for the diamond-Cr-spinel pairs must be due to the hercynite component.

Acknowledgements

The research project was funded by the ERC Starting Grant INDIMEDEA (nº 307322) to FN.

References

Andreozzi, G.B. and Lucchesi, S. (2002) Intersite distribution of Fe^{2+} and Mg in the spinel (sensu stricto)–hercynite series by single-crystal X-ray diffraction. *American Mineralogist*, **87**, 1113–1120.

Angel, R.J. (2000) Equations of state. Pp. 35–59 in: *High-Temperature and High-Pressure Crystal Chemistry* (R.M. Hazen, R.T. Downs, editors). Reviews in Mineralogy & Geochemistry, **41**. Mineralogical Society of America and the Geochemical Society, Washington, DC.

Angel, R.J. and Finger, L. (2011) SINGLE: a program to control single-crystal diffractometers. *Journal of Applied Crystallography*, **44**, 247–251.

Angel, R.J., Allan, D., Miletich, R. and Finger, L. (1997) The use of quartz as an internal pressure standard in high-pressure crystallography. *Journal of Applied Crystallography*, **30**, 461–466.

Angel, R.J., Downs, R. and Finger, L. (2000) High-temperature–high-pressure diffractometry. Pp. 559–597 in: *High-Temperature and High-Pressure Crystal Chemistry* (R.M. Hazen, R.T. Downs, editors). Reviews in Mineralogy & Geochemistry, **41**. Mineralogical Society of America and the Geochemical Society, Washington, DC.

Angel, R.J., Bujak, M., Zhao, J., Gatta, G.D. and Jacobsen, S.D. (2007) Effective hydrostatic limits of pressure media for high-pressure crystallographic studies. *Journal of Applied Crystallography*, **40**, 26–32.

Angel, R.J., Gonzalez-Platas, J. and Alvaro, M. (2014*a*). EosFit7c and a Fortran module (library) for equation of state calculations. *Zeitschrift für Kristallographie*, **229**, 405–419.

Angel, R.J., Mazzucchelli, M.L., Alvaro, M., Nimis, P. and Nestola, F. (2014*b*) Geobarometry from host-inclusion systems: the role of elastic relaxation. *American Mineralogist*, **99(10)**, 2146–2149.

Angel, R.J., Alvaro, M., Nestola, F. and Mazzucchelli, M.L. (2015) Diamond thermoelastic properties and implications for determining the pressure of formation of diamond-inclusion systems. *Russian Geology and Geophysics*, **56**, 211–220.

Ballhaus, C., Berry, R. and Green, D. (1990) Oxygen fugacity controls in the Earth's upper mantle. *Nature*, **349**, 437–440.

Ballhaus, C., Berry, R. and Green, D. (1991) High pressure experimental calibration of the olivine-orthopyroxene-spinel oxygen geobarometer: implications for the oxidation state of the upper mantle. *Contributions to Mineralogy and Petrology*, **107**, 27–40.

Birch, F. (1947) Finite elastic strain of cubic crystals. *Physical Review*, **71**, 809.

Bohlen, S.R., Dollase, W.A. and Wall, V.J. (1986) Calibration and applications of spinel equilibria in the system FeO-Al_2O_3-SiO_2. *Journal of Petrology*, **27**, 1143–1156.

Bosi, F., Hålenius, U. and Skogby, H. (2008) Stoichiometry of synthetic ulvöspinel single crystals. *American Mineralogist*, **93**, 1312–1316.

Fabriès, J. (1979) Spinel-olivine geothermometry in peridotites from ultramafic complexes. *Contributions to Mineralogy and Petrology*, **69**, 329–336.

Hålenius, U., Skogby, H. and Andreozzi, G.B. (2002) Influence of cation distribution on the optical absorption spectra of Fe^{3+}-bearing spinel ss–hercynite crystals: evidence for electron transitions in $^{VI}Fe^{2+}$–$^{VI}Fe^{3+}$ clusters. *Physics and Chemistry of Minerals*, **29**, 319–330.

Harrison, R.J., Redfern, S.A.T. and O'Neill, H.St.C. (1998) The temperature dependence of the cation distribution in synthetic hercynite ($FeAl_2O_4$) from in-situ neutron diffraction refinements. *American Mineralogist*, **83**, 1092–1099.

Holland, T. and Powell, R. (1990) An enlarged and updated internally consistent thermodynamic dataset with uncertainties and correlations: the system $K_2O-Na_2O-CaO-MgO-MnO-FeO-Fe_2O_3-Al_2O_3-TiO_2-SiO_2-C-H_2-O_2$. *Journal of Metamorphic Geology*, **8**, 89–124.

Holland, T. and Powell, R. (1998) An internally consistent thermodynamic data set for phases of petrological interest. *Journal of Metamorphic Geology*, **16**, 309–343.

King, H. and Finger, L. (1979) Diffracted beam crystal centering and its application to high-pressure crystallography. *Journal of Applied Crystallography*, **12**, 374–378.

Lenaz, D. and Skogby, H. (2013) Structural changes in the $FeAl_2O_4$-$FeCr_2O_4$ solid solution series and their consequences on natural Cr-bearing spinels. *Physics and Chemistry of Minerals*, **40**, 587–595.

Lenaz, D., Logvinova, A.M., Princivalle, F. and Sobolev, N.V. (2009) Structural parameters of chromite included in diamond and kimberlites from Siberia: A new tool for discriminating ultramafic source. *American Mineralogist*, **94**, 1067–1070.

Lenaz, D., Skogby, H., Logvinova, A.M., Sobolev, N.V. and Princivalle, F. (2013) A micro-Mössbauer study of chromites included in diamond and other mantle-related rocks. *Physics and Chemistry of Minerals*, **40**, 671–679.

Milani, S., Nestola, F., Alvaro, M., Pasqual, D., Mazzucchelli, M.L., Domeneghetti, M.C. and Geiger, C.A. (2015) Diamond–garnet geobarometry: The role of garnet compressibility and expansivity. *Lithos*, **227**, 140–147.

Miletich, R., Allan, D.R. and Kuhs, W.F. (2000) High-pressure single-crystal techniques. Pp. 445–520 in: *High-Temperature and High-Pressure Crystal Chemistry* (R.M. Hazen, R.T. Downs, editors). Reviews in Mineralogy & Geochemistry, **41**. Mineralogical Society of America and the Geochemical Society, Washington, DC.

Nestola, F., Ballaran, T.B., Balic-Zunic, T., Princivalle, F., Secco, L. and Dal Negro, A. (2007) Comparative compressibility and structural behavior of spinel $MgAl_2O_4$ at high pressures: The independency on the degree of cation order. *American Mineralogist*, **92**, 1838–1843.

Nestola, F., Smyth, J.R., Parisatto, M., Secco, L., Princivalle, F., Bruno, M., Prencipe, M. and Dal Negro, A. (2009) Effects of non-stoichiometry on the spinel structure at high pressure: Implications for Earth's mantle mineralogy. *Geochimica et Cosmochimica Acta*, **73**, 489–492.

Nestola, F., Angel, R.J., Zhao, J., Garrido, C.J., Sánchez-Vizcaíno, V.L., Capitani, G. and Mellini, M. (2010) Antigorite equation of state and anomalous softening at 6 GPa: an in situ single-crystal X-ray diffraction study. *Contributions to Mineralogy and Petrology*, **160**, 33–43.

Nestola, F., Nimis, P., Ziberna, L., Longo, M., Marzoli, A., Harris, J.W., Manghnani, M.H. and Fedortchouk, Y. (2011) First crystal-structure determination of olivine in diamond: Composition and implications for provenance in the Earth's mantle. *Earth and Planetary Science Letters*, **305**, 249–255.

Nestola, F., Periotto, B., Andreozzi, G.B., Bruschini, E. and Bosi, F. (2014) Pressure-volume equation of state for chromite and magnesiochromite: a single-crystal X-ray diffraction investigation. *American Mineralogist*, **99**, 1248–1253.

O'Neill, H.St.C. (1981) The transition between spinel lherzolite and garnet lherzolite, and its use as a geobarometer. *Contributions to Mineralogy and Petrology*, **77**, 185–194.

O'Neill, H.St.C. and Wall, V. (1987) The Olivine–orthopyroxene–spinel oxygen geobarometer, the nickel precipitation curve, and the oxygen fugacity of the Earth's Upper Mantle. *Journal of Petrology*, **28**, 1169–1191.

Perinelli, C., Andreozzi, G.B., Conte, A.M., Oberti, R. and Armienti, P. (2012) Redox state of subcontinental lithospheric mantle and relationships with metasomatism: insights from spinel peridotites from northern Victoria Land (Antarctica). *Contributions to Mineralogy and Petrology*, **164**, 1053–1067.

Perinelli, C., Bosi, F., Andreozzi, G.B., Conte, A.M. and Armienti, P. (2014) Geothermometric study of Cr-spinels of peridotite mantle xenoliths from northern Victoria Land (Antarctica). *American Mineralogist*, **99**, 839–846.

Princivalle, F., Martignago, F., Nestola, F. and Negro, A.D. (2012) Kinetics of cation ordering in synthetic $Mg(Al,Fe^{3+})_2O_4$ spinels. *European Journal of Mineralogy*, **24**, 633–643.

Ralph, R. and Finger, L.W. (1982) A computer program for refinement of crystal orientation matrix and lattice constants from diffractometer data with lattice symmetry constraints. *Journal of Applied Crystallography*, **15**, 537–539.

Sack, R.O. and Ghiorso, M.S. (1991) Chromian spinels as petrogenetic indicators; thermodynamics and petrological applications. *American Mineralogist*, **76**, 827–847.

Schollenbruch, K., Woodland, A.B. and Frost, D.J. (2010) The stability of hercynite at high pressures and temperatures. *Physics and Chemistry of Minerals*, **37**, 137–143.

Shulters, J.C. and Bohlen, S.R. (1989) The stability of hercynite and hercynite-gahnite spinels in corundum- or quartz-bearing assemblages. *Journal of Petrology*, **30**, 1017–1031.

Slack, G.A. (1964) $FeAl_2O_4$-$MgAl_2O_4$: Growth and some thermal, optical, and magnetic properties of mixed single crystals. *Physical Review*, **134**, A1268.

Stachel, T. and Harris, J. (2008) The origin of cratonic diamonds – constraints from mineral inclusions. *Ore Geology Reviews*, **34**, 5–32.

Stixrude, L. and Lithgow-Bertelloni, C. (2005) Thermodynamics of mantle minerals–I. Physical properties. *Geophysical Journal International*, **162**, 610–632.

Taran, M.N., Parisi, F., Lenaz, D. and Vishnevskyy, A.A. (2014) Synthetic and natural chromium bearing spinels: an optical spectroscopy study. *Physics and Chemistry of Minerals*, **41**, 593–602.

Wang, H. and Simmons, G. (1972) Elasticity of some mantle crystal structures: 1. Pleonaste and hercynite spinel. *Journal of Geophysical Research*, **77**, 4379–4392.

Lithos 265 (2016) 328–333

Contents lists available at ScienceDirect

Lithos

journal homepage: www.elsevier.com/locate/lithos

Synchrotron Mössbauer Source technique for *in situ* measurement of iron-bearing inclusions in natural diamonds

F. Nestola [a,*], V. Cerantola [b], S. Milani [a], C. Anzolini [a], C. McCammon [c], D. Novella [d], I. Kupenko [e], A. Chumakov [b], R. Rüffer [b], J.W. Harris [f]

[a] *Dipartimento di Geoscienze, Università degli Studi di Padova, Via G. Gradenigo 6, I-35131 Padova, Italy*
[b] *European Synchrotron Radiation Facility (ESRF), F-38043 Grenoble, France*
[c] *Bayerisches Geoinstitut, University of Bayreuth, 95440 Bayreuth, Germany*
[d] *Lawrence Livermore National Laboratory, Livermore, CA 94550, USA*
[e] *Institut für Mineralogie, Universität Münster, Corrensstraße 24, 48149 Münster, Germany*
[f] *School of Geographical and Earth Sciences, University of Glasgow, Glasgow G12 8QQ, UK*

ARTICLE INFO

Article history:
Received 5 May 2016
Revised 11 June 2016
Accepted 17 June 2016
Available online 25 June 2016

Keywords:
Ferropericlase
Magnesioferrite
Ferric iron
Oxygen fugacity
Magnetism

ABSTRACT

We describe a new methodology to collect energy domain Mössbauer spectra of inclusions in natural diamonds using a Synchrotron Mössbauer Source (SMS). Measurements were carried out at the Nuclear Resonance beamline ID18 at the European Synchrotron Radiation Facility (Grenoble, France). We applied this non-destructive approach to collect SMS spectra of a ferropericlase inclusion still contained within its diamond host from Juina (Brazil). The high spatial resolution of the measurement (~15 μm) enabled multiple regions of the 190 × 105 μm^2 inclusion to be sampled and showed that while Fe^{3+}/Fe_{tot} values in ferropericlase were below the detection limit (0.02) overall, there was a magnetic component whose abundance varied systematically across the inclusion. Hyperfine parameters of the magnetic component are consistent with magnesioferrite, and the absence of superparamagnetism allows the minimum particle size to be estimated as ~30 nm. Bulk Fe^{3+}/Fe_{tot} values are similar to those reported for other ferropericlase inclusions from Juina, and their variation across the inclusion can provide constraints on its history.

1. Introduction

Natural diamonds containing silicate, oxide and sulfide inclusions are a popular focus of investigation as they uniquely provide a window into the conditions of the Earth's interior at extreme depths. Indeed, diamonds are probably the only natural sample capable of traveling from the deep mantle to the Earth's surface, bringing other “fragments” from great depths. Because of their unique physical properties, diamonds protect mineral inclusions from alteration over time and space and thus provide constraints on Earth's evolution over the past 3.2 billion years (Richardson and Harris, 1997). Studies of mineral inclusions in diamonds have yielded considerable geochemical and geophysical information. For reviews on mineralogy, geochemistry, pressure and temperature of formation, and diamond genesis ages, see *e.g.*, Stachel and Harris (2008) and Shirey et al. (2013). Recent discoveries based on investigations of deep diamonds have considerably improved our knowledge of the Earth's deep carbon and water cycles (see *e.g.*, Harte, 2010; Nestola and Smyth, 2016; Pearson et al., 2014; Walter et al., 2011) and the oxygen fugacity of the Earth's interior (*e.g.*, McCammon et al., 1997, 2004b; Pearson et al., 2014).

Most investigations take place after diamonds are broken open to expose the mineral inclusion. However, a non-destructive *in situ* approach to investigate inclusions entrapped in diamonds can be crucial for many reasons: (a) inclusions may be under pressure in the diamond, thus once opened they could invert to lower pressure phases on release (for example in a case of natural clinopyroxene, Alvaro et al., 2010); (b) the inclusions may retain significant residual pressure that can provide information about the depth of diamond formation (*e.g.*, Nestola et al., 2011; Sobolev et al., 2000) that would otherwise be lost on opening the diamond; (c) crystallographic orientation relationships between the inclusion and its diamond host can provide constraints on its protogenetic *versus* syngenetic nature (Nestola et al., 2014); and (d) preservation of diamond surface growth features can provide information on late oxidation processes (Fedortchouk et al., 2011).

The so-called ‘super deep’ diamonds are those that are believed to have formed at depths of at least 300 km and some evidence suggests depths of at least 800 km (Harte, 2010). A common mineral inclusion in these diamonds is ferropericlase, $(Mg,Fe^{2+})O$ (see Kaminsky, 2012 for an extensive review). Ferropericlase is the second most abundant mineral in the lower mantle, constituting up to about 20 mol% (660 to

---

* Corresponding author.
E-mail address: fabrizio.nestola@unipd.it (F. Nestola).

http://dx.doi.org/10.1016/j.lithos.2016.06.016

2900 km depth). Bridgmanite, the dominant lower mantle phase and the Earth's most abundant mineral, has an affinity for ferric iron that is so profound that Fe^{3+}/Fe_{tot} is determined by bulk composition instead of oxygen fugacity. In contrast, Fe^{3+}/Fe_{tot} of ferropericlase is a strong function of oxygen fugacity (*e.g.*, McCammon et al., 2004a) and provides a measure of the most recent redox conditions under which it equilibrated (Otsuka et al., 2013).

Two methods have been used to determine Fe^{3+}/Fe_{tot} of ferropericlase inclusions in diamond. Mössbauer spectroscopy with a ^{57}Co point source was used to study inclusions down to 100 μm in diameter (McCammon et al., 1997, 2004b), which is the limit using a radioactive point source (McCammon, 1994). Although the time required to collect Mössbauer spectra is long (at least one day per spectrum), the relative transparency of diamond to 14.4 keV gamma rays enables spectra of ferropericlase inclusions to be collected *in situ* through the diamond as demonstrated by McCammon et al. (1997). To measure Fe^{3+}/Fe_{tot} in smaller ferropericlase inclusions, Longo et al. (2011) calibrated the flank method for ferropericlase based on X-ray emission spectroscopy using the electron microprobe (Höfer and Brey, 2007 and references therein) and Kaminsky et al. (2015) applied the calibration to inclusions in diamonds from the Juina area, Brazil. Inclusions ranged in size between 20 and 50 μm, but had to be removed from the diamond prior to measurement due to the high absorption of electrons at the iron L-edge by diamond.

Results from Kaminsky et al. (2015) showed Fe^{3+}/Fe_{tot} values of 0.08–0.12 in ferropericlase inclusions, which are higher than values measured using Mössbauer spectroscopy for other ferropericlase inclusions from Juina diamonds (0.02–0.09) (McCammon et al., 1997). The difference can be attributed to the presence of exsolved Fe^{3+}-enriched clusters that were observed using a transmission electron microscope (TEM) (Kaminsky et al., 2015). The flank method measures the bulk value of Fe^{3+}/Fe_{tot} since it cannot distinguish between different phases, while Mössbauer spectroscopy records Fe^{3+}/Fe_{tot} for individual phases. The reason that these can be distinguished is because the sub-spectrum for exsolved Fe^{3+}-enriched clusters is magnetically ordered while the sub-spectrum for ferropericlase is not (see Longo et al., 2011). However, the signal to noise ratios of the Mössbauer spectra collected by McCammon et al. (1997) were not sufficiently high to resolve the small amount of exsolved Fe^{3+}-enriched clusters due to the physical limitations of the point source; hence only Fe^{3+} in ferropericlase was detected and lower Fe^{3+}/Fe_{tot} values were obtained.

An ideal method to measure Fe^{3+}/Fe_{tot} values of ferropericlase would combine (1) the advantage of Mössbauer spectroscopy to distinguish Fe^{3+} in different phases and measure inclusions while still in the diamond, with (2) the advantage of the flank method to conduct rapid measurements with high spatial resolution. Indeed, electron energy loss spectroscopy using a TEM and X-ray Absorption Near Edge Structure spectroscopy using a synchrotron provides high spatial resolution and the latter has been applied to *in situ* measurements of ferropericlase inclusions, although for iron phase identification rather than oxidation state determination (Silversmit et al., 2011). The only method that offers the possibility to satisfy all of these requirements is the Synchrotron Mössbauer Source (SMS) (Potapkin et al., 2012; Smirnov et al., 1997). In this work we report development of a methodology to apply SMS to *in situ* determination of Fe^{3+}/Fe_{tot} in ferropericlase inclusions still contained within their diamonds.

2. Experimental approach

The diamond used in our study came from a suite of alluvial diamonds from São Luiz (Juina, Brazil). This locality is considered the main world locality of super-deep diamonds (see Pearson et al., 2014). A black tabular inclusion (referred to as "AZ2", Fig. 1) with dimensions of roughly 192 × 85 × 105 μm^3 was identified as ferropericlase by single-crystal X-ray diffraction (see the same experimental setup in Nestola et al., 2016). The unit-cell edge is $a = 4.251(4)$ Å with volume $V = 76.82(12)$ $Å^3$. Based on the range of compositions reported for the Juina area (Fe# = Fe/(Mg + Fe) = 0.15–0.62) (Harte et al., 1999; Kaminsky, 2012), the dimensionless Mössbauer thickness of the inclusion lies between 4 and 13 (9–30 mg Fe/cm^2).

Fig. 1. Diamond containing ferropericlase inclusion AZ2 (indicated with a red circle).

SMS spectra were collected at the Nuclear Resonance beamline ID18 (Rüffer and Chumakov, 1996) using the nuclear monochromator as described by Potapkin et al. (2012) at the European Synchrotron Radiation Facility, Grenoble. The SMS provides ^{57}Fe resonant radiation at 14.4 keV within a bandwidth of ~6 neV, which is tunable in energy over a range of about ±0.6 μeV. In contrast to radioactive sources, the beam emitted by the SMS can be focused and it is fully resonant and up to 99% polarized. SMS spectra were collected during operation in multibunch mode (7/8 + 1 filling) with the beam focused to a spot size of roughly 10 × 15 μm^2 using Kirkpatrick–Baez multilayer optics. The SMS linewidth was controlled before and after each sample measurement using $K_2Mg^{57}Fe(CN)_6$, whose Mössbauer spectrum consists of a single line, and the velocity scale was calibrated using 25 μm thick natural α-iron foil. Spectra at spots #1–#5 were collected for 90 min while the spectrum at spot #6 was collected for 7 h. All spectra were fitted using the program MossA with the full transmission integral and a Lorentzian-squared source line shape (Prescher et al., 2012).

To overcome the technical challenge of accurately locating the ferropericlase inclusion in the X-ray beam, we employed the same approach as that used at ID18 to locate small samples (<50 μm diameter) in the diamond anvil cell (DAC). The set-up consists of a BX90 DAC (Kantor et al., 2012) mounted on the laser heating system platform in the experimental hutch, but no pressure or temperature is applied during sample alignment. The experimental procedure is as follows:

(1) The diamond with the selected inclusion is attached on the tungsten carbide seat using plasticine and superglue such that the inclusion is centered over the ~1 mm diameter hole in the seat (Fig. 2a).
(2) A Re gasket with thickness ranging from 30 to 100 μm and a hole of 300 μm diameter is carefully glued on the upper surface of the diamond such that the inclusion is centered in the gasket hole (Fig. 2b).
(3) The seat-diamond-gasket assembly is mounted on the lower half of the DAC (Fig. 2c), which is then placed in the DAC holder (Fig. 2d) and attached to a platform on a moveable table connected to high-precision motors (1 μm step) inside the experimental hutch (Fig. 2e).
(4) From the control cabin with the X-ray shutter open, the signal of the avalanche photodiode (APD) detector positioned roughly 1 m behind the sample is monitored as the table is moved in

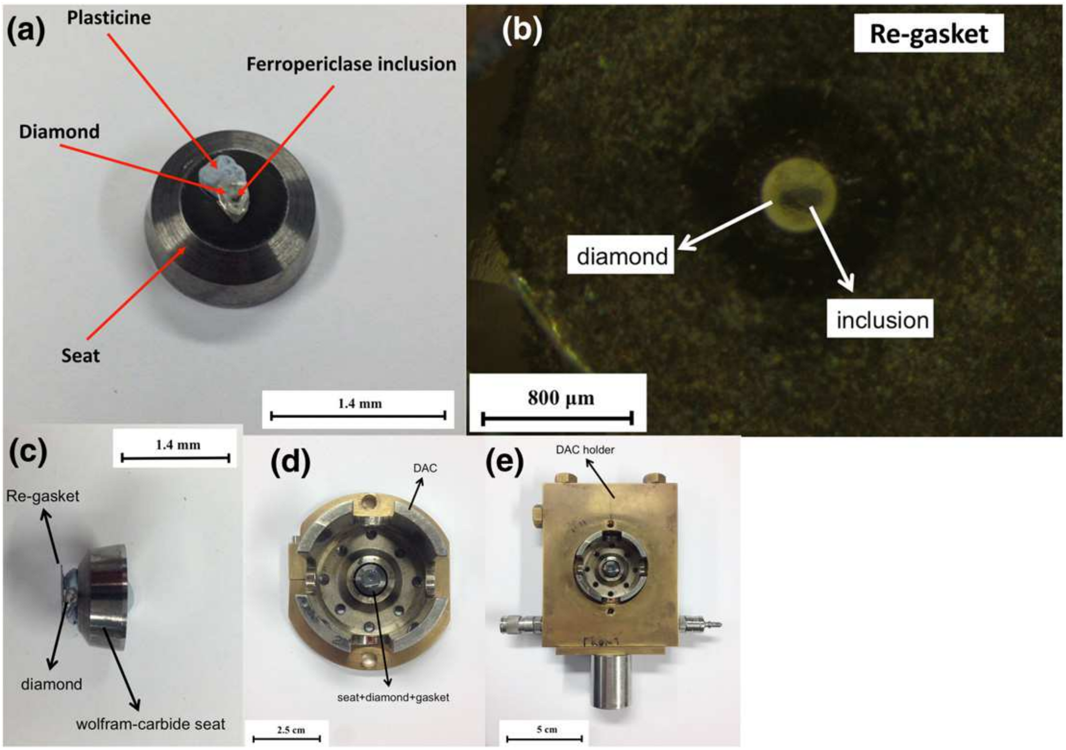

Fig. 2. (a) Tungsten carbide seat with the diamond centered over a ~1 mm diameter hole in the seat; (b) magnified image of inclusion AZ2 visible through the hole in the Re gasket; (c) side view of the seat-diamond-gasket assembly; (d) seat-diamond-gasket assembly attached to the bottom part of a BX90 DAC that is mounted inside a metallic ring; (e) DAC mounted on the DAC holder.

horizontal (y) and vertical directions (z). A maximum occurs when the X-rays pass through the gasket hole to reach the detector (Fig. 3).

(5) Once the inclusion has been located in the X-ray beam, absorption profiles are recorded and the DAC is moved to different positions so that different regions of the inclusion can be analyzed (Fig. 4). In this way the inclusion can be mapped without the use of an optical system.

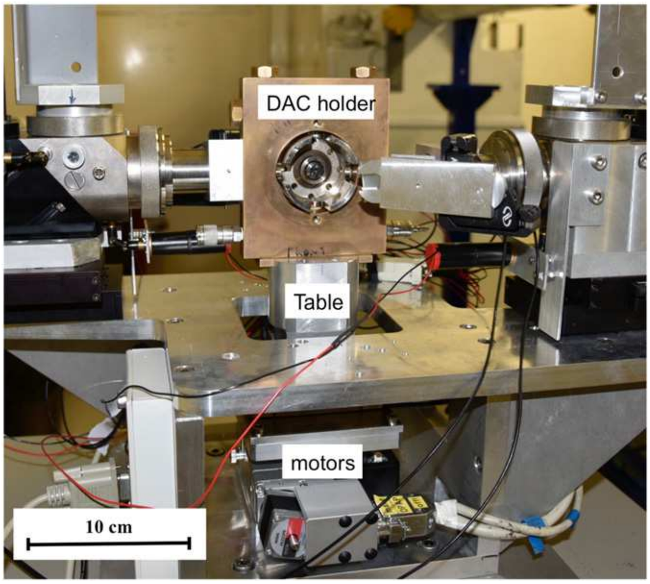

Fig. 3. DAC holder mounted on the laser heating platform inside the experimental hutch at beamline ID18. The table is moved by motors in the three directions x, y, z, with a step precision of 1 µm. The optics belonging to the double-sided laser heating system are visible on either side of the DAC. While the setup is normally used for high-pressure high-temperature DAC experiments, for this purpose only the positioning stage is needed.

3. Results and discussion

Mössbauer spectra collected from spots #1–#5 are dominated by a broad quadrupole doublet (Fig. 5). Qualitatively they look similar to spectra collected from ferropericlase inclusions in diamond using a radioactive source (McCammon et al., 1997, 2004b), but there are important differences. The SMS spectra have a significantly larger absorption (~70%) compared to radioactive source spectra (<1%) due to the lower background of the SMS, leading to a much higher signal to noise ratio despite the much shorter collection time for SMS spectra (radioactive source spectra of ferropericlase inclusions take several days to collect). In addition, SMS spectra probe individual regions of ~15 µm diameter while radioactive source spectra provide only an average measurement of the entire ferropericlase inclusion (>100 µm diameter).

SMS spectra collected from spots #1–#5 were fitted to a single Fe^{2+} quadrupole doublet with Voigt lineshape according to previous models (*e.g.*, Longo et al., 2011) (Table 1). Trials were conducted to test the addition of a quadrupole doublet corresponding to Fe^{3+}, but the presence of the doublet was not statistically significant in all cases. From these trials the detection limit for Fe^{3+}/Fe_{tot} in ferropericlase was estimated to be 0.02. However, there was evidence in all SMS spectra for deviations in the residual near −3 and 4.5 mm/s to varying degrees, suggesting the presence of a magnetically ordered component. Accordingly, the velocity scale was expanded and the X-ray beam was moved back to the vicinity of spot #5 where a new spectrum was collected over a longer period of time (spot #6).

The SMS spectrum from spot #6 shows clear evidence for absorption arising from magnetic hyperfine splitting (Fig. 6). We therefore added a magnetic sextet with the usual constraints (equal component widths and area ratios between the outer and inner components fixed to 3) but allowed all other parameters to vary. We then refit the original spectra from spots #1–#5 with the addition of a magnetic sextet where all parameters except area were fixed to the values from the spot #6 spectrum. All spots show the presence of the magnetic component at varying levels above experimental uncertainty (Table 1), and

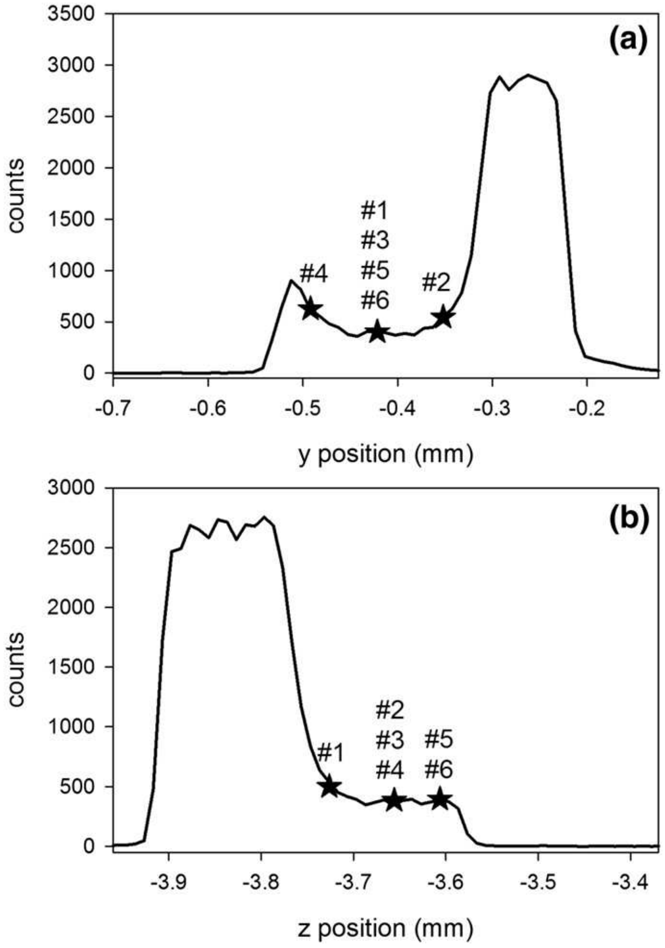

Fig. 4. Line profiles of the APD detector signal from inclusion AZ2 in the horizontal (top) and vertical (bottom) directions. The maxima correspond to the region in the gasket hole where there is no inclusion (Fig. 2b) and the relatively flat regions with non-zero counts adjacent to the maxima are from the inclusion. The widths indicate the approximate dimensions of the inclusion (150 × 150 μm^2) and the gasket hole (~300 μm diameter). The positions where the SMS spectra were collected are indicated with stars.

correlation of amounts with their estimated positions on the inclusion based on the absorption profiles (Fig. 4) reveal that the magnetic component abundance is highest in the centre and left region of the inclusion (Fig. 7).

The hyperfine parameters provide information about the magnetic component. The centre shift and magnetic hyperfine field (Table 1) are indicative of Fe^{3+} and fall close to values for synthetic $MgFe_2O_4$ (averaged CS = 0.32 mm/s relative to α-Fe, averaged BHF = 48 T; De Grave et al., 1979) and Fe_3O_4 (averaged CS = 0.49 mm/s relative to α-Fe, averaged BHF = 47 T; Häggström et al., 1978) as well as solid solutions in between (O'Neill et al., 1992). The hyperfine magnetic field is close to saturated and there is no evidence for superparamagnetism within the uncertainty of the data, where a superparamagnetic component would appear as a narrow line with the same centre shift as the magnetic component.

The absence of superparamagnetism provides information about the minimum particle size of the magnetic phase. Gonser et al. (1968) precipitated magnesioferrite by annealing synthetic ferropericlase in air, and Mössbauer spectra showed clear evidence for superparamagnetism. The amount decreased as annealing time increased, and they calculated the average size of the precipitates based on the temperature dependent behavior of the Mössbauer spectra. Room temperature spectra showed nearly complete superparamagnetism for an average particle diameter of 8 nm, while 20 nm particles were transitional between superparamagnetic and ferrimagnetic. A simple extension of their results based on magnetic relaxation time (their Eq. (3)) indicates that magnesioferrite precipitates of 30 nm diameter would give a fully ordered magnetic Mössbauer spectrum at room temperature. This result is consistent with data presented by Longo et al. (2011), where TEM images showed magnesioferrite impurities in synthetic ferropericlase of at least 40 nm in size and Mössbauer spectra showed a magnetically ordered component (Palot et al., 2016, reported magnesioferrite inclusions of similar size in ferropericlase within a diamond from the same locality).

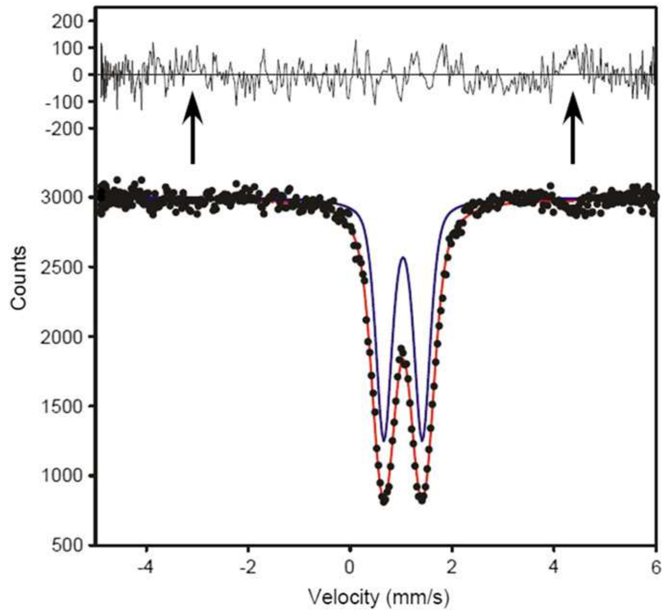

Fig. 5. Room temperature SMS spectrum of spot #5 on ferropericlase inclusion AZ2. Solid circles: experimental data; red line: full transmission integral fit. A single quadrupole doublet was fit to the spectrum (blue line), but note that it does not add up to the total spectrum due to the properties of the full transmission integral fit. The arrows indicate regions in the residual where there are positive deviations over multiple adjacent channels, suggesting the presence of absorption due to magnetic hyperfine splitting.

Previous TEM studies of ferropericlase inclusions in diamond show varying sizes of magnesioferrite precipitates. Both Harte et al. (1999) and Wirth et al. (2014) report features that exceed 100 nm in size and reach up to 3 μm long, while Kaminsky et al. (2015) report much smaller Fe^{3+}-rich regions that are less than 20 nm in size and as small as 1–2 nm. Results from the present study show a magnetic phase that is significantly larger than those observed by Kaminsky et al. (2015) in diamonds from kimberlite pipes in the same area (Juina, Brazil). Differences in size can be related to many parameters, including composition, oxygen fugacity and thermal history. While the TEM studies required removal of the inclusion from the diamond, the SMS approach provided constraints on the size of magnetic particles with the ferropericlase still in the diamond, keeping open the possibilities for further investigation using *in situ* techniques to elucidate its history.

Bulk ferropericlase Fe^{3+}/Fe$_{tot}$ ratios can be calculated based on the relative areas in SMS spectra assuming that the magnetic phase is endmember $MgFe_2O_4$ (Table 1). These ratios can be directly compared with values from bulk techniques such as the flank method that cannot distinguish between Fe^{3+} in different phases, and show a similar range to other ferropericlase inclusions from other Juina diamonds (Kaminsky et al., 2015). The different Fe^{3+}/Fe$_{tot}$ values observed in different regions of the AZ2 inclusion are a remarkable feature that provides potential information on the history of the inclusion, for example thermal or redox gradients that influenced magnesioferrite exsolution. The amount of the magnetic phase present in the different regions of the ferropericlase inclusion can be determined from the relative areas of the Mössbauer spectra based on the estimated iron concentration in

Table 1
Hyperfine parameters derived from room temperature SMS spectra of AZ2 ferropericlase inclusion.

Location	Component	CS[a] mm/s	QS[b] mm/s	Area %	Linewidth[c] mm/s	BHF[d] T	Fe^{3+}/Fe_{tot} bulk
Spot #1	Fe^{2+}	1.04(1)	0.76(1)	93(2)	0.39(1)	–	0.07(2)
	mag	*0.43*	*0.12*	7(2)	*1.0*	*43*	
Spot #2	Fe^{2+}	1.04(1)	0.75(1)	97(2)	0.38(1)	–	0.03(2)
	mag	*0.43*	*0.12*	3(2)	*1.0*	*43*	
Spot #3	Fe^{2+}	1.04(1)	0.75(1)	94(2)	0.37(1)	–	0.06(2)
	mag	*0.43*	*0.12*	6(2)	*1.0*	*43*	
Spot #4	Fe^{2+}	1.04(1)	0.76(1)	92(2)	0.38(1)	–	0.08(2)
	mag	*0.43*	*0.12*	8(2)	*1.0*	*43*	
Spot #5	Fe^{2+}	1.04(1)	0.76(1)	92(2)	0.37(2)	–	0.08(2)
	mag	*0.43*	*0.12*	8(2)	*1.0*	*43*	
Spot #6	Fe^{2+}	1.05(1)	0.77(1)	91(2)	0.38(2)	–	0.09(2)
	mag	0.43(12)	0.12(23)	9(2)	1.0(3)	43(5)	

Notes: values in italics were fixed during the fitting process.
[a] CS: center shift relative to α-Fe.
[b] QS: quadrupole splitting.
[c] Linewidth: full width at half maximum (including source linewidth).
[d] BHFe: magnetic hyperfine field ("magnetic sextet").

each phase. Assuming endmember magnesioferrite and an iron-poor ferropericlase composition (Fe# = 0.15), the volume fractions range between 0.5 and 2% for the different regions, while for an iron-rich composition (Fe# = 0.6) the range is 2 to 7%. The accuracy of these values can be improved by *in situ* determination of composition, for example using X-ray diffraction (Nestola et al., 2011).

4. Conclusions

We summarize our work as follows:

1) We described a new technique to collect Mössbauer spectra of inclusions in natural diamonds that does not require breaking open the diamond. The technique uses the recently developed Synchrotron Mössbauer Source and yields high quality spectra with low background and high spatial resolution (~15 μm) that can be collected in a few hours or less.
2) We collected SMS spectra at five different positions on a 150 × 150 μm^2 ferropericlase inclusion that showed low Fe^{3+}/Fe_{tot} overall (<0.02) but the presence of a magnetic component whose abundance varied systematically across the inclusion.
3) The well saturated hyperfine magnetic field rules out superparamagnetism and allowed the minimum particle size of the magnetic phase to be estimated as ~30 nm.
4) Bulk Fe^{3+}/Fe_{tot} values fall within the range observed for other ferropericlase inclusions in diamond reported in the literature and their variation across the inclusion provides potential constraints on the history of the inclusion.

This new experimental technique can be easily applied to investigate other iron-bearing inclusions in natural diamond. The wealth of information provided by Mössbauer spectroscopy opens a new possibility to obtain fundamental information on the Earth's interior.

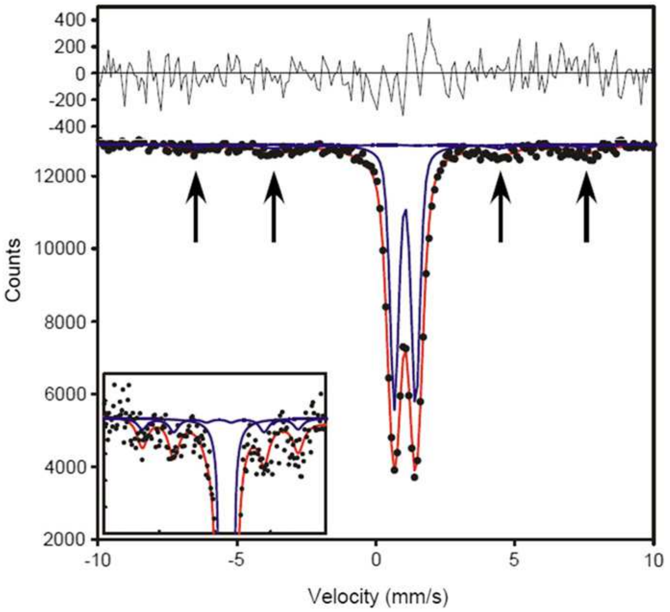

Fig. 6. Room temperature SMS spectrum of spot #6 on ferropericlase inclusion AZ2 collected over a large velocity range. The position of spot #6 is close to spot #5. The spectrum was fitted to one quadrupole doublet and one magnetic sextet where the symbols and lines are the same as in Fig. 5. The arrows indicate the positions of four peaks of the magnetic sextet, which can be seen more clearly in the inset that shows a magnified view near the baseline.

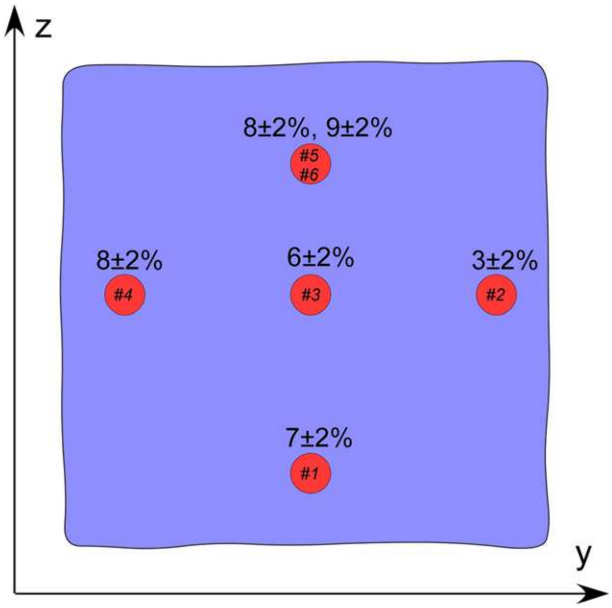

Fig. 7. Sketch of AZ2 ferropericlase inclusion. SMS spectra were collected at the red circles, where their size (~15 μm diameter) is scaled relative to the dimensions of the inclusion (150 × 150 μm^2). The spots (indicated by numbers) correspond to those in Fig. 4 and Table 1. Each spot is labeled with the relative area of the magnetic component measured at that position.

Acknowledgments

We thank the European Synchrotron Radiation Facility for provision of synchrotron radiation (ID18). Financial support was provided to FN by the European Research Council (project INDIMEDEA, agreement number 307322). The Diamond Trading Company (a member of the DeBeers Group of Companies) is thanked for the donation to JWH of the diamonds used in this study. Stefano Castelli is thanked for the picture in Fig. 1. Two anonymous referees are thanked for their useful suggestions.

References

Alvaro, M., Nestola, F., Boffa Ballaran, T., Camara, F., Domeneghetti, M.C., Tazzoli, V., 2010. High-pressure phase transition of a natural pigeonite. American Mineralogist 95, 300–311.

De Grave, E., Govaert, A., Chambaere, D., Robbrecht, G., 1979. Mössbauer effect study of MgFe$_2$O$_4$. Physica 96B, 103–110.

Fedortchouk, Y., Manghnani, M.H., Hushur, A., Shiryaev, A., Nestola, F., 2011. An atomic force microscopy study of diamond dissolution features: the effect of H2O and CO$_2$ in the fluid on diamond morphology. American Mineralogist 96, 1768–1775.

Gonser, U., Wiedersich, H., Grant, R.W., 1968. Mössbauer studies on the super-paramagnetic behavior of magnesioferrite precipitates. Journal of Applied Physics 39, 1004–1005.

Häggström, L., Annersten, H., Ericsson, T., Wäppling, R., Karner, W., Bjarman, S., 1978. Magnetic dipolar and electric quadrupolar effects on the Mössbauer spectra of magnetite above the Verwey transition. Hyperfine Interactions 5, 201–214.

Harte, B., 2010. Diamond formation in the deep mantle: the record of mineral inclusions and their distribution in relation to mantle dehydration zones. Mineralogical Magazine 74, 189–215.

Harte, B., Harris, J.W., Hutchison, M.T., Watt, G.R., Wilding, M.C., 1999. Lowe mantle mineral associations in diamonds from São Luiz, Brazil. In: Fei, Y., Bertka, C.M., Mysen, B.O. (Eds.), Mantle Petrology; Field Observations and High Pressure Experimentation: A Tribute to Francis R. (Joe) Boyd. The Geochemical Society, Special Publication No. 6, pp. 125–153.

Höfer, H.E., Brey, G., 2007. The iron oxidation state of garnet by electron microprobe: its determination with the flank method combined with major-elements analysis. American Mineralogist 92, 873–885.

Kaminsky, F., 2012. Mineralogy of the lower mantle: a review of 'super-deep' mineral inclusions in diamond. Earth-Science Reviews 110, 127–147.

Kaminsky, F.V., Ryabchikov, I.D., McCammon, C.A., Longo, M., Abakumov, A.M., Turner, S., Heidari, H., 2015. Oxidation potential in the Earth's lower mantle as recorded by ferropericlase inclusions in diamond. Earth and Planetary Science Letters 417, 49–56.

Kantor, I.Y., Prakapenka, V., Kantor, A., Dera, P., Kurnosov, A., Sinogeikin, S., Dubrovinskaia, N., Dubrovinsky, L., 2012. BX90: a new diamond anvil cell design for X-ray diffraction and optical measurements. Review of Scientific Instruments 83, 125102.

Longo, M., McCammon, C.A., Jacobsen, S.D., 2011. Microanalysis of the iron oxidation state in (Mg,Fe)O and application to the study of microscale processes. Contributions to Mineralogy and Petrology 162, 1249–1257.

McCammon, C.A., 1994. A Mössbauer milliprobe: practical considerations. Hyperfine Interactions 92, 1235–1239.

McCammon, C.A., Hutchison, M.T., Harris, J.W., 1997. Ferric iron content of mineral inclusions in diamonds from São Luiz: a view into the lower mantle. Science 278, 434–436.

McCammon, C.A., Lauterbach, S., Seifert, F., Langenhorst, F., van Aken, P.A., 2004a. Iron oxidation state in lower mantle mineral assemblages I. Empirical relations derived from high-pressure experiments. Earth and Planetary Science Letters 222, 435–449.

McCammon, C.A., Stachel, T., Harris, J.W., 2004b. Iron oxidation state in lower mantle mineral assemblages: II. Inclusions in diamonds from Kankan, Guinea. Earth and Planetary Science Letters 222, 423–434.

Nestola, F., Smyth, J.R., 2016. Diamonds and water in the deep earth: a new scenario. International Geology Review 58, 263–276.

Nestola, F., Nimis, P., Ziberna, L., Longo, M., Marzoli, A., Harris, J.W., Manghnani, M.H., Fedortchouk, Y., 2011. First crystal-structure determination of olivine in diamond: composition and implications for provenance in the Earth's mantle. Earth and Planetary Science Letters 305, 249–255.

Nestola, F., Nimis, P., Angel, R., Milani, S., Bruno, M., Prencipe, M., Harris, J., 2014. Olivine with diamond-imposed morphology included in diamonds. Syngenesis or protogenesis? International Geology Review 56, 1658–1667.

Nestola, F., Burnham, A.D., Peruzzo, L., Tauro, L., Alvaro, M., Walter, M.J., Gunter, M., Kohn, S.C., 2016. Tetragonal Almandine–Pyrope Phase, TAPP: finally a name for it, the new mineral jeffbenite. Mineralogical Magazine http://dx.doi.org/10.1180/minmag.2016.080.059.

O'Neill, H.S.C., Annersten, H., Virgo, D., 1992. The temperature dependence of the cation distribution in magnesioferrite (MgFe$_2$O$_4$) from powder XRD structural refinements and Mössbauer spectroscopy. American Mineralogist 77, 725–740.

Otsuka, K., Longo, M., McCammon, C.A., Karato, S., 2013. Ferric iron content of ferropericlase as a function of composition, oxygen fugacity, temperature and pressure: implications for redox conditions during diamond formation in the lower mantle. Earth and Planetary Science Letters 365, 7–16.

Palot, M., Jacobsen, S.D., Townsend, J.P., Nestola, F., Marquardt, K., Harris, J.W., Stachel, T., McCammon, C.A., Pearson, D.G., 2016. Evidence for H2O-bearing fluids in the lower mantle from diamond inclusion. Lithos 265, 237–243.

Pearson, D.G., Brenker, F., Nestola, F., McNeill, J., Nasdala, L., Hutchison, M.T., Matveev, S., Mather, K., Silversmit, G., Schmitz, S., Vekemans, B., Vincze, L., 2014. A hydrous mantle transition zone indicated by ringwoodite included within diamond. Nature 507, 221–224.

Potapkin, V., Chumakov, A.I., Smirnov, G.V., Celse, J.P., Rüffer, R., McCammon, C., Dubrovinsky, L., 2012. The ^{57}Fe synchrotron Mössbauer Source at the ESRF. Journal of Synchrotron Radiation 19, 559–569.

Prescher, C., McCammon, C., Dubrovinsky, L., 2012. MossA — a program for analyzing energy-domain Mossbauer spectra from conventional and synchrotron sources. Journal of Applied Crystallography 45, 329–331.

Richardson, S.H., Harris, J.W., 1997. Antiquity of peridotitic diamonds from the Siberian craton. Earth and Planetary Science Letters 151, 271–277.

Rüffer, R., Chumakov, A.I., 1996. Nuclear-resonance beamline at ESRF. Hyperfine Interactions 97-8, 589–604.

Shirey, S.B., Cartigny, P., Frost, D.J., Keshav, S., Nestola, F., Nimis, P., Pearson, D.G., Sobolev, N.V., Walter, M.J., 2013. Diamonds and the geology of mantle carbon. Reviews in Mineralogy and Geochemistry 75, 355–421.

Silversmit, G., Vekemans, B., Appel, K., Schmitz, S., Schoonjans, T., Brenker, F.E., Kaminsky, F., Vincze, L., 2011. Three-dimensional Fe speciation of an inclusion cloud within an ultradeep diamond by confocal μ-X-ray absorption near edge structure: evidence for late stage overprint. Analytical Chemistry 83, 6294–6299.

Smirnov, G.V., van Bürck, U., Chumakov, A.I., Baron, A.Q.R., Rüffer, R., 1997. Synchrotron Mössbauer source. Physical Review B 55, 5811–5815.

Sobolev, N.V., Fursenko, B.A., Goryainov, S.V., Shu, J., Hemley, R.J., Mao, A., Boyd, F.R., 2000. Fossilized high pressure from the Earth's deep interior: the coesite-in-diamond barometer. Proceedings of the National Academy of Sciences of the United States of America 97, 11875–11879.

Stachel, T., Harris, J.W., 2008. The origin of cratonic diamonds — constraints from mineral inclusions. Ore Geology Reviews 34, 5–32.

Walter, M.J., Kohn, S.C., Araujo, D., Bulanova, G.P., Smith, C.B., Gaillou, E., Wang, J., Steele, A., Shirey, S.B., 2011. Deep mantle cycling of oceanic crust: evidence from diamonds and their mineral inclusions. Science 334, 54–57.

Wirth, R., Dobrzhinetskaya, L., Harte, B., Schreiber, A., Green, H.W., 2014. High-Fe (Mg, Fe)O inclusion in diamond apparently from the lowermost mantle. Earth and Planetary Science Letters 404, 365–375.

Mineralogical Magazine, December 2016, Vol. 80(7), pp. 1219–1232

Tetragonal Almandine-Pyrope Phase, TAPP: finally a name for it, the new mineral jeffbenite

Fabrizio Nestola[1,*], Antony D. Burnham[2,6], Luca Peruzzo[3], Leonardo Tauro[1], Matteo Alvaro[4], Michael J. Walter[2], Mickey Gunter[5], Chiara Anzolini[1] and Simon C. Kohn[2]

[1] Dipartimento di Geoscienze, Università di Padova, Via Gradenigo, 6, I-35131 Padova, Italy
[2] School of Earth Sciences, University of Bristol, Queen's Road, Bristol BS8 1RJ, UK
[3] CNR-IGG, Padova, Via Gradenigo, 6, I-35131 Padova, Italy
[4] Dipartimento di Scienze della Terra e dell'Ambiente, Università di Pavia, Via Ferrata 1, 27100, Pavia, Italy
[5] Geological Sciences, University of Idaho, 875 Perimeter MS 3022, Moscow, 83844-3022, USA
[6] Now at Research School of Earth Sciences, Australian National University, Canberra, Australia

[*Received 5 July 2015; Accepted 16 November 2016; Associate Editor: Ed Grew*]

ABSTRACT

Jeffbenite, ideally $Mg_3Al_2Si_3O_8$, previously known as tetragonal-almandine-pyrope-phase ('TAPP'), has been characterized as a new mineral from an inclusion in an alluvial diamond from São Luiz river, Juina district of Mato Grosso, Brazil. Its density is 3.576 g/cm^3 and its microhardness is ~7. Jeffbenite is uniaxial (–) with refractive indexes $\omega = 1.733(5)$ and $\varepsilon = 1.721(5)$. The crystals are in general transparent emerald green.

Its approximate chemical formula is $(Mg_{2.62}Fe^{2+}_{0.27})(Al_{1.86}Cr_{0.16})(Si_{2.82}Al_{0.18})O_{12}$ with very minor amounts of Mn, Na and Ca. Laser ablation ICP-MS showed that jeffbenite has a very low concentration of trace elements. Jeffbenite is tetragonal with space group $I\bar{4}2d$, cell edges being $a = 6.5231(1)$ and $c = 18.1756(3)$ Å. The main diffraction lines of the powder diagram are [d (in Å), intensity, *hkl*]: 2.647, 100, 2 0 4; 1.625, 44, 3 2 5; 2.881, 24, 2 1 1; 2.220, 19, 2 0 6; 1.390, 13, 4 2 4; 3.069, 11, 2 0 2; 2.056, 11, 2 2 4; 1.372, 11, 2 0 12.

The structural formula of jeffbenite can be written as $(M1)(M2)_2(M3)_2(T1)(T2)_2O_{12}$ with M1 dominated by Mg, M2 dominated by Al, M3 dominated again by Mg and both T1 and T2 almost fully occupied by Si. The two tetrahedra do not share any oxygen with each other (i.e. jeffbenite is classified as an orthosilicate).

Jeffbenite was approved as a new mineral by the IMA Commission on New Minerals and Mineral Names with the code IMA 2014-097. Its name is after Jeffrey W. Harris and Ben Harte, two world-leading scientists in diamond research. The petrological importance of jeffbenite is related to its very deep origin, which may allow its use as a pressure marker for detecting super-deep diamonds. Previous experimental work carried out on a Ti-rich jeffbenite establishes that it can be formed at 13 GPa and 1700 K as maximum *P-T* conditions.

Keywords: TAPP, jeffbenite, physical properties, pressure/temperature conditions, diamond, São Luiz river, Brazil.

Introduction

Diamonds are able to preserve high-pressure phases as inclusions because of a combination of factors: (1) the strength of the diamond structure can maintain high pressures upon exhumation to the Earth's surface, commonly up to 2 or 3 GPa (e.g. Barron *et al.*, 2008; Howell *et al.*, 2012; Angel *et al.*, 2014; Angel *et al.*, 2015*a*,*b*), and thus limit the extent to which the stability field of a mineral is overstepped; (2) solvent/catalysts such as water and silicate melt do not come into contact with the inclusions because of the impervious nature of the diamond structure, which impedes retrogressive phase transitions; (3) the rapid ascent rate of kimberlites limits the time available for inclusions to undergo phase transitions at high temperature. Consequently, for example, coesite is a commonly encountered inclusion and, unlike most occurrences in metamorphic rocks (e.g. Chopin, 1984; Parkinson, 2000; Liou *et al.*, 2012)

*E-mail: fabrizio.nestola@unipd.it
DOI: 10.1180/minmag.2016.080.059

generally shows no signs of conversion to quartz (see Angel *et al.*, 2014 and Angel *et al.*, 2015*b*). Also encountered are majorite garnets that retain a silica excess (e.g. Stachel, 2001; Harte, 2010), unlike metamorphic examples where exsolution of the pyroxene component is complete (van Roermund and Drury, 1998 and references therein).

In this paper we present a new name for the phase commonly known as 'TAPP', Tetragonal Almandine-Pyrope Phase. 'TAPP' has been reported from numerous diamonds of sublithospheric origin since its original characterization (Harris *et al.*, 1997; Bulanova *et al.*, 2010; Armstrong and Walter, 2012; Kaminsky, 2012; Zedgenizov *et al.*, 2014). It has a composition that is very close to the stoichiometry of a garnet, but it lacks Ca and its structure is tetragonal (space group $I\bar{4}2d$; Finger and Conrad, 2000). It occurs as single grains (e.g. Harris *et al.*, 1997) or as one phase of composite, polyphase inclusions (e.g. Hutchison *et al.*, 2001; Brenker *et al.*, 2002; Walter *et al.*, 2011).

Jeffbenite is named in honour of two scientists, Jeffrey W. Harris (School of Geographical and Earth Sciences, University of Glasgow, UK; b. 1940) and Ben Harte (School of Geosciences, University of Edinburgh, UK; b. 1941), whose work on diamonds, and super-deep diamonds in particular, has shaped our understanding of mantle geochemical processes for years to come. Both were authors, together with Dr. Hutchison, Dr. Light and Prof. Hursthouse, of the original structural characterization of 'TAPP' published in *Nature* (Harris *et al.*, 1997).

Here we describe the new mineral jeffbenite in terms of its physical, chemical, optical and structural properties paying special attention to its stability field. Jeffbenite was approved in February 2015 as a new mineral by the IMA Commission on New Minerals and Mineral Names with the code IMA 2014-097. The holotype is deposited at the Museum of Mineralogy of the University of Padova under the catalogue number MMP M12660.

Historical overview

The mineral now called jeffbenite was first discovered in super-deep diamonds about 23 years ago and its occurrence was reported upon by Harte and Harris (1994). At that time these authors only had electron-microprobe (EMP) analyses of small inclusions and as it had the chemical composition of a pyrope-almandine garnet they referred to it as a 'garnet'. However, they noted the exceptional composition compared with other mantle-derived garnets; it was very poor in Ca and showed no majoritic substitution. Subsequent X-ray diffraction studies of the mineral showed that jeffbenite was not a garnet and the phase was described in detail by Harris *et al.* (1997) under the name 'Tetragonal-Almandine-Pyrope-Phase', or TAPP. The TAPP phase was never submitted to IMA for mineral approval and never described in detail, probably because of its extremely rare occurrence. For example, at the time its optical and physical properties were unknown. Only a few samples have been reported so far in the literature and very rarely as single crystals suitable for proper crystallographic, optical and physical characterization.

Jeffbenite has only been found as inclusions in diamond and, with the exception of a finding in a diamond from the Kankan alluvial deposits (Guinea) (Brenker *et al.*, 2002), only from the Juina region (Brazil).

In terms of mineral association, the most common associated phase with jeffbenite appears to be ferropericlase (e.g. Harte *et al.*, 1999), but olivine, $CaSiO_3$-walstromite, $MgSiO_3$ with enstatite structure and carbonates have also been recorded as coexisting inclusions (Hutchison *et al.*, 2001; Hayman *et al.*, 2005; Bulanova *et al.*, 2010; Thomson *et al.*, 2014).

Occurrence

The type specimen of jeffbenite studied in this work occurred as an inclusion in an alluvial diamond from São Luiz river, Juina district of Mato Grosso, Brazil (11°29′ S 59°02′ W), from which it was extracted by crushing the diamond. The jeffbenite sample formed part of a composite inclusion along with a grain of omphacitic pyroxene Between jeffbenite and omphacite we found no crystallographic relationships in terms of orientation and the two phases showed no orientation relationship with their diamond host (for an example of the procedure see Nestola *et al.*, 2014*a*). Within the same diamond, an inclusion of $CaSiO_3$-walstromite was also found.

One single crystal of jeffbenite with a size 0.07 mm × 0.05 mm × 0.03 mm was used for the present investigation (Fig. 1).

Appearance, physical and optical properties

Jeffbenite cannot be described in terms of morphology as it can be found only within diamond and thus we will never know its stable morphology.

FIG. 1. The single crystal of jeffbenite studied in this work on which the crystal structure was determined together with all further physical and optical properties. The emerald green colour is characteristic for this phase.

Figure 1 only provides an indicative idea of jeffbenite shape. The crystal appears transparent and deep emerald green in colour, the streak is white and the lustre is vitreous. It is non-fluorescent and shows a micro-Vickers hardness of 1346 corresponding to a Mohs hardness of ~7. The tenacity is brittle and no cleavage was observed. The fracture is irregular. The density of jeffbenite could not be determined by classical methods due to its limited crystal size. Its calculated density using X-ray diffraction and its empirical formula provide a density 3.576 g/cm^3.

In terms of optical properties, jeffbenite is uniaxial (–), with $\omega = 1.733(5)$ and $\varepsilon = 1.721(5)$ (measured using 589 nm radiation). Its pleochroism is ε = light blue and ω = colourless. Calculation of the Gladstone-Dale relationship yields a compatibility index, $1-(K_p/K_c) = -0.011$, which is in the 'superior' category (Mandarino, 1981).

Experimental methods

Scanning electron microscopy – energy dispersive spectroscopy (EDS) and chemical mapping

In order to verify the chemical homogeneity of jeffbenite the crystal in Fig. 1 was polished and analysed by a CamScan MX3000 electron microscope equipped with a LaB$_6$ source, four-quadrants solid-state back-scattered electron (BSE) detector and an EDAX EDS system for micro-analysis installed at Department of Geosciences of University of Padova. The analytical conditions were: accelerating voltage of 20 kV, filament emission of ~13 nA, and working distance of 27 mm. A BSE image of jeffbenite is shown in Fig. 2. On the same polished crystal a chemical map was performed to verify the homogeneity of the following elements: Si, Mg, Al, Fe, Mn, Cr and Ca. The chemical map is shown in Fig. 3.

Single-crystal X-ray diffraction

A complete set of X-ray diffraction intensities was collected using a new prototype instrument in the Department of Geosciences at the University of Padova (Angel and Nestola, 2015). The instrument consists of an Agilent Supernova goniometer equipped with an X-ray micro-source assembled with a Pilatus 200 K Dectris detector. The micro-X-ray source, Mo*K*α, operates at 50 kV and

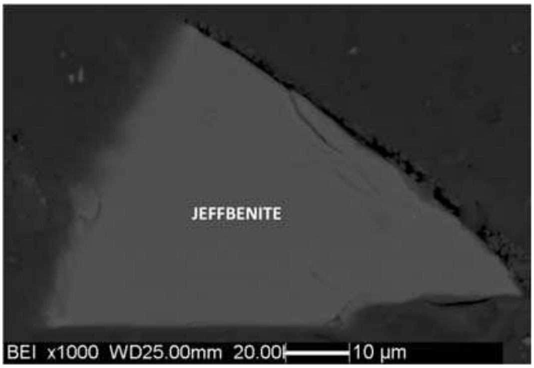

FIG. 2. A back-scattered electron image of the crystal shown in Fig. 1 after polishing. The chemical homogeneity is very evident.

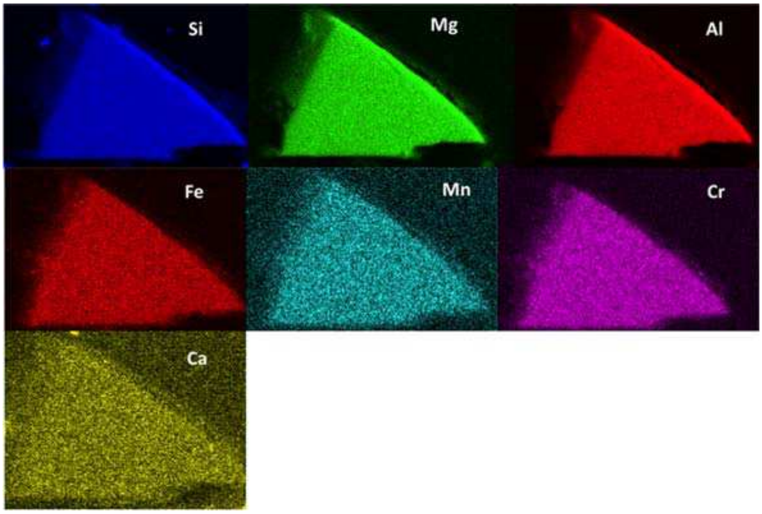

FIG. 3. Elemental distribution map of Si, Mg, Al, Fe, Mn, Cr and Ca for the jeffbenite crystal shown in Fig. 2. No further elements were mapped as the preliminary EDS results showed no other elements.

0.8 mA. The sample-to-detector distance was 68 mm. The micro source ensures a brilliance at least ten times higher than conventional sealed X-ray tubes and a beam spot of ~0.120 mm. At the same time the Pilatus 200 K detector ensures a very high sensitivity and negligible noise. The instrument is able to provide significant results on crystals of extremely small size, down to 0.01 mm. To obtain very reliable data on jeffbenite 2456 frames and 22,199 reflections were collected up to $2\theta_{max} = 80.49°$.

The redundancy was 28.9 and $F^2/\sigma(F^2) = 71.4$. The data completeness was 100% and the R_{int} (*I*4/*mmm*) was 0.039 up to maximum resolution. Data reduction was performed using *Crysalis* software (Agilent Technologies Ltd, Yarnton, UK), which corrected for Lp effects and absorption. Information relating to data collection and structure refinement, performed using *SHELX-97* (Sheldrick, 2008), is reported in Table 1. The refinement was performed using neutral scattering curves and all atoms were refined anisotropically. The starting model used was taken from Finger and Conrad (2000). Atom coordinates and U_{eq} parameters are given in Table 2. Structure factors and a crystallographic information file have been deposited with the Principal Editor of *Mineralogical Magazine* and are available from www.minersoc.org/pages/e_journals/dep_mat_mm.html. Selected bond distances are reported in Table 3. All crystal and refinement data are reported in Table 1.

Powder X-ray diffraction data were collected using the same instrument as above, which simulates a Gandolfi camera measurement mode.

TABLE 1. Crystal and refinement data for jeffbenite.

Crystal data	
Crystal size (mm)	0.070 × 0.050 × 0.030
Cell setting, space group	Tetragonal, $I\bar{4}2d$
a (Å)	6.5231(1)
c (Å)	18.1756(3)
V (Å^3)	773.38(5)
Z	4
Data collection and refinement	
Radiation, wavelength (Å)	Mo$K\alpha$, $\lambda = 0.71073$
Temperature (K)	293
$2\theta_{max}$	80.49
Measured reflections	28,735
Total unique reflections	1218
Reflections with $F_o > 4\sigma(F_o)$	1201
R_{int}	0.0389
Range of *h*, *k*, *l*	$-11 \le h \le 11$, $-11 \le k \le 11$, $-32 \le l \le 32$
R [$F_o > 4\sigma(F_o)$]	0.0179
R (all data)	0.0184
wR (on F_o^2)	0.0551
Goof	1.048
Number of least-squares parameters	52
Maximum and minimum residual peak (e Å^{-3})	0.42 –0.47

TABLE 2. Crystallographic sites, Wyckoff positions, site occupancies, atom coordinates, and equivalent anisotropic displacement parameters (Å^2) for jeffbenite.*

Atom	Site	Site occupancy	*x*	*y*	*z*	U_{eq}
T1	4b	Si	0.5	0.5	0	0.00537(8)
T2	8d	$Si_{0.91}Al_{0.09}$	–0.14975(5)	0.25	0.125	0.00249(7)
M1	4a	$Mg_{0.82}Fe^{3+}_{0.12}$	0	0	0	0.0124(1)
M2	8d	$Al_{0.93}Cr_{0.08}$	0.25918(6)	0.25	0.125	0.0086(1)
M3	8c	$Mg_{0.90}Fe^{2+}_{0.075}Mn_{0.025}Na_{0.005}Ca_{0.005}$	0	0.5	–0.02302(2)	0.0106(1)
O1	16e	O	0.01873(10)	0.28028(10)	0.05749(3)	0.0079(1)
O2	16e	O	–0.26098(11)	0.03758(10)	0.10130(4)	0.0088(1)
O3	16e	O	0.43666(11)	0.29614(10)	0.04693(4)	0.0081(1)

The structural data were obtained by refining the occupancy factors at M1, M2 and M3 sites. We did not refine the site occupancy of T1 and T2 as the T1–O and T2–O bond distances do not indicate any detectable Al substituting Si (see Table 3). In addition, it is well known that by X-ray diffraction refining Al against Si does not provide any realistic number having these two elements too close atomic numbers. For the M1, M2 and M3 sites we refined their occupancies using the scattering curve of neutral iron for all three as this approach provided the best match with the EMP analysis. We obtained the following occupancy factors: M1 = 0.560, M2 = 0.527, M3 = 0.479. The calculated electrons from such factors provide an M1 + M2 + M3 sum = 40.71 against 40.50 electrons obtained using the above cation occupancies, which are only based on the EMP analysis and on a Fe^{3+}/Fe$_{tot}$ ratio equal to 0.445 (see notes in Table 5 and/or text).

*Anisotropic displacement parameters are deposited with the cif at www.minersoc.org/pages/e_journals/dep_mat_mm.html

Data (in Å) are listed in Table 4. Unit-cell parameters were refined from the powder data using the method of Holland and Redfern (1997) on the basis of 21 unequivocally indexed reflections giving the following values: $a = 6.5355(2)$ Å, $c = 18.1576(11)$ Å, $V = 775.56(5)$ Å^3, in excellent agreement with the data measured by single-crystal X-ray diffraction.

Chemical data

Chemical analyses were carried out using a CAMECA SX50 electron microprobe (wavelength-dispersive spectroscopy mode, 20 kV, 20 nA, 2 μm beam diameter) installed at CNR-IGG Institute (hosted by the Department of Geosciences of University of Padova). Standards (analyser crystal, element, emission line) used were Kakanui pyrope (New Zealand) from the Smithsonian Museum (TAP, Mg$K\alpha$); Amelia albite (Virginia) (TAP, Na$K\alpha$); diopside (TAP, Si$K\alpha$; PET, Ca$K\alpha$); Al_2O_3 (TAP, Al$K\alpha$); $MnTiO_3$ (PET, Ti$K\alpha$; LIF, Mn$K\alpha$); Cr_2O_3 (LIF, Cr$K\alpha$); Fe_2O_3 (LIF, Fe$K\alpha$). Analytical data are given in Table 5.

Laser ablation inductively coupled plasma mass spectrometry (LA-ICP-MS) analysis was carried out using a LambdaPhysik Compex 110 Eximer 193 nm laser with a HelEX ablation chamber coupled to an Agilent 7700 series ICP-MS at the Research School of Earth Sciences in the Australian National University. The carrier gas was He–Ar, fluence was maintained at ~50 mJ and pulse rate was set to 5 Hz; two analyses were performed using a 40 μm spot size and one analysis was performed using a 100 μm spot size. The isotopes analysed were ^{23}Na, ^{29}Si, ^{89}Y, ^{90}Zr, ^{93}Nb, ^{139}La, ^{140}Ce, ^{141}Pr, ^{146}Nd, ^{147}Sm, ^{153}Eu, ^{157}Gd, ^{159}Dy, ^{163}Ho, ^{165}Er,

TABLE 3. Selected bond distances (Å) for jeffbenite.

T1–O3	1.6330(6) × 4
T2–O1	1.6591(7) × 2
T2–O2	1.6224(7) × 2
<T2–O>	1.6408
M1–O1	2.1093(2) × 4
M1–O2	2.5196(7) × 4
<M1–O>	2.3144
M2–O1	2.0012(7) × 2
M2–O2	1.9248(6) × 2
M2–O3	1.8559(7) × 2
<M2–O>	1.9273
M3–O1	2.0519(7) × 2
M3–O2	2.1249(7) × 2
M3–O3	2.0227(7) × 2
<M3–O>	2.0665

TABLE 4. Observed powder X-ray diffraction data for jeffbenite (for the observed *d*-spacings only those reflections with relative intensity >3% were reported).

Observed d-spacings (Å)	Relative intensity (%)	*h k l*	Calculated d-spacings (Å)	Calculated relative intensity (%)
6.140	4	1 0 1	6.140	2
4.126	5	1 1 2	4.113	5
3.177	9	1 0 5	3.175	12
3.069	**11**	**2 0 2**	3.070	3
2.881	**24**	**2 1 1**	2.880	17
2.647	**100**	**2 0 4**	2.650	100
2.275	8	2 1 5	2.275	2
2.220	**19**	**2 0 6**	2.220	20
2.056	**11**	**2 2 4**	2.057	4
2.013	7	3 1 2	2.012	4
1.939	5	2 1 7	1.940	5
1.871	3	3 0 5	1.878	1
1.800	5	3 2 1	1.800	4
1.705	8	3 1 6	1.705	7
1.664	7	2 1 9	1.660	4
1.625	**44**	**3 2 5**	1.618	21
1.521	6	3 3 2	1.527	2
1.484	9	3 2 7	1.484	7
1.447	6	4 1 5	1.440	1
1.390	**13**	**4 2 4**	1.390	10
1.372	**11**	**2 0 12**	1.374	6
1.318	6	4 2 6	1.314	4

Calculated *d*-spacings and relative intensities were calculated using the software *Highscore Plus* (PAnalytical) on the basis of the structural model given in Table 5.
The eight strongest reflections are given in bold.

TABLE 5. Chemical composition of the holotype of jeffbenite, determined by wavelength-dispersive spectroscopy.

Oxide wt.%	Range	Average
SiO_2	41.56–42.04	41.74(18)
TiO_2	0.04–0.07	0.06(1)
Al_2O_3	23.74–23.95	23.84(9)
Cr_2O_3	2.79–2.92	2.86(7)
FeO_{total}	4.55–4.62	4.59(3)
FeO	2.97–4.36	3.65(56)
Fe_2O_3	0.25–1.65	0.93(56)
MnO	0.75–0.85	0.79(4)
MgO	24.90–25.41	25.16(22)
CaO	0.08–0.10	0.09(1)
Na_2O	0.08–0.12	0.10(1)
Total	98.66–99.55	99.23

Total Fe as FeO. Fe^{3+}/Fe_{tot} was calculated using Droop's (1987) method.

TABLE 6. Trace element concentrations in jeffbenite, as determined by LA-ICP-MS. Analyses 1 and 2 were performed using a 40 μm spot size; analysis 3 was performed using a 100 μm spot size and the limit of detection (LOD) corresponding to this analysis is indicated.

	Analysis 1	Analysis 2	Analysis 3	LOD
Na_2O	5.34	2.22	3.38	–
Y	0.036	0.019	0.011	0.001
Zr	0.534	1.292	1.288	0.005
Nb	bdl	0.012	0.007	0.002
La	bdl	bdl	bdl	0.002
Ce	bdl	bdl	0.002	0.001
Pr	bdl	bdl	bdl	0.002
Nd	bdl	bdl	bdl	0.010
Sm	bdl	bdl	bdl	0.008
Eu	bdl	bdl	bdl	0.003
Gd	bdl	bdl	bdl	0.003
Tb	bdl	bdl	bdl	0.001
Dy	bdl	bdl	bdl	0.003
Ho	bdl	bdl	bdl	0.001
Er	bdl	bdl	bdl	0.004
Tm	bdl	bdl	bdl	0.002
Yb	bdl	0.007	0.004	0.003
Lu	bdl	bdl	bdl	0.002
Hf	0.030	0.046	0.048	0.003

The concentrations are provided in ppm except for Na, which is in wt.%

^{166}Tm, ^{172}Yb, ^{175}Lu and ^{176}Hf. GSD-1 g glass (Jochum *et al.*, 2005) was used as the external standard and Si was used as the internal standard (nominally set to 50% SiO_2 because analyses were partially contaminated by pyroxene, see below). The results are shown in Table 6.

Micro-Raman analysis

The same crystal investigated by X-ray diffraction and microprobe was also analysed by micro-Raman spectroscopy. To the best of our knowledge this is the first micro-Raman spectrum for this phase. Raman spectra were obtained using a ThermoScientific DXR Raman microscope

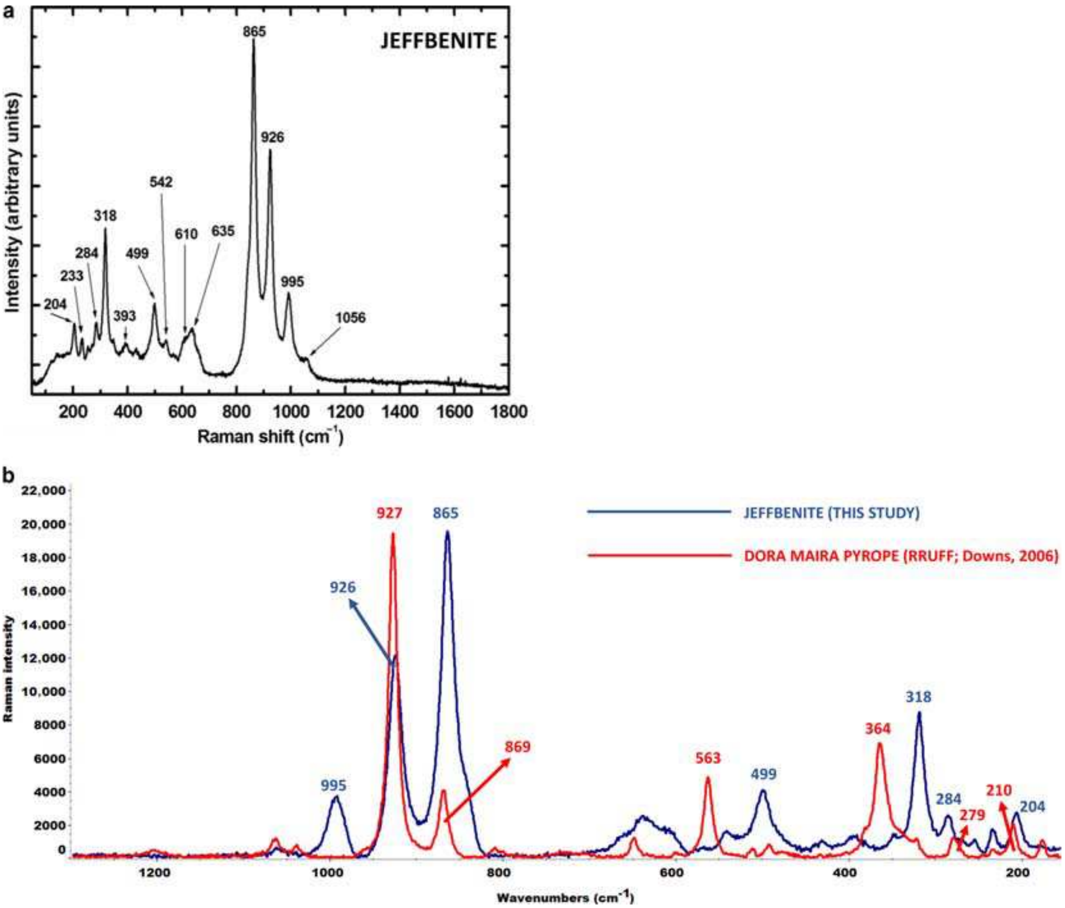

FIG. 4. Micro-Raman spectrum of jeffbenite carried out on the crystal in Fig. 1. Data were collected between 50 and 1800 cm^{-1} (see the text for more experimental details).

installed at the School of Earth Sciences of University of Bristol. A 532 nm excitation laser was used at a power of 3–5 mW to avoid any possible beam damage to the crystal; spectra were collected for ~220 s. The analysis was performed using a 50× objective with a spatial resolution of 1 μm and a spectral resolution estimated to be ~2.5 cm^{-1}. Data were collected between 50 and 1800 cm^{-1}. The Raman spectrum is shown in Fig. 4.

Results

Chemistry of jeffbenite

The empirical formula of jeffbenite, based on 12 oxygen atoms per formula unit (apfu), and on the data reported in Table 5 is the following:

$$(Mg_{0.82}Fe^{3+}_{0.12})_{\Sigma 0.95}(Al_{1.86}Cr_{0.16})_{\Sigma 2.02}(Mg_{1.80}Fe^{2+}_{0.15}Mn_{0.05}Ca_{0.01}Na_{0.01})_{\Sigma 2.02}(Si_{2.82}Al_{0.18})_{\Sigma 3.00}O_{12}.$$

No other elements were detected by EDS analysis.

The Fe^{3+}/Fe_{tot} ratio was calculated using Droop's (1987) method and for our data gives an average value of 0.18. However, the variation (see Table 5 for FeO and Fe_2O_3 wt.% calculation) is quite significant with a minimum of 0.048 and a maximum of 0.325. The only available Mössbauer measurements on the TAPP phase (McCammon *et al.*, 1997), provided much higher values of Fe^{3+}/Fe_{tot} between 0.66 and 0.74. However, a careful analysis of the chemical data on the McCammon *et al.* (1997) samples shows that using the Droop method with charge-balance considerations would give a much lower Fe^{3+}/Fe_{tot}

ratio. Their cation sum without any Fe correction and only considering the FeO_{tot} is between 7.91 and 7.95 (against the ideal value of 8), which would not require Fe^{3+} at all. We do not know the origin of this chemical discrepancy though it may lie in the low signal-to-noise ratio of the Mössbauer data. In order to obtain the best charge balance for our empirical formula we have used a value of $Fe^{3+}/Fe_{tot} = 0.445$, which is an intermediate value from our indirect determination by the Droop method and the direct Mössbauer measurement of McCammon *et al.* (1997).

The simplified formula of jeffbenite is $Mg_3Al_2Si_3O_{12}$, which requires MgO = 29.99, Al_2O_3 = 25.29, SiO_2 = 44.71 (total 100.00 wt.%).

The back-scattered electron images (Fig. 2) and X-ray maps (Fig. 3) indicate that the crystal studied is homogeneous in major-element composition and lacks exsolution features (in contrast to the specimen of Brenker *et al.*, 2002).

As reported by Armstrong and Walter (2012), 15 instances of jeffbenite have been reported in the literature up to that date. Since then, our jeffbenite sample, four inclusions found by Zegdenizov *et al.* (2014) and two more by Thomson *et al.* (2014) have been reported. Compositional data for jeffbenite were summarized by Armstrong and Walter (2012); in detail, they report six single inclusions of Ti-free and low-Fe jeffbenites, a further four composite inclusions of Ti-bearing and more ferroan jeffbenites and finally one Ti-bearing and extremely Fe-rich jeffbenite. To this list of jeffbenites, we must add our IMA approved jeffbenite, which is Ti-free and low-Fe; and a further Ti-bearing sample with very high Fe content analysed here by microprobe. This second jeffbenite has been identified in a diamond from the Collier-4 kimberlite in Brazil, and forms part of a polyphase inclusion with $(Mg,Fe)CO_3$. Electron microprobe data for our Ti-bearing and Fe-rich jeffbenite are given in Table 7. Its chemical formula is close to the jeffbenite analysed by Bulanova *et al.* (2010): see Table 8.

The concentrations of trace elements in jeffbenite (see Table 6) are low, with Zr and Hf being the most abundant of those measured, a feature also observed by Harte *et al.* (1999). The grain analysed in the present study (not the same crystal analysed by diffraction) is intergrown with a sodic pyroxene, and the three analyses all contained a contribution from this material (Na_2O varied from ~2.2–5.3%). This mixed nature of the analyses means that the SiO_2 content was assumed to be 50% (i.e. approximately halfway between jeffbenite and clinopyroxene) for processing the data, which introduces a relative uncertainty of ~10% for the bulk analyses; moreover there is no way to tell how the elements are distributed between the two phases. However, mass balance calculations

TABLE 7. Composition of Fe-rich jeffbenite and semi-quantitative analysis of coexisting magnesite in diamond RC2-7 from Collier-4 kimberlite, Brazil.

	Fe-rich jeffbenite	Magnesite
SiO_2	36.05	0.26
TiO_2	3.56	0.47
Al_2O_3	17.82	0.30
Cr_2O_3	0.01	0.03
FeO_{total}	20.12	16.51
MnO	0.37	0.62
MgO	17.99	34.05
CaO	0.04	0.42
Na_2O	0.10	0.11
K_2O	0.04	0.10
P_2O_5	0.02	–
CO_2*	–	47.12
Total	96.11	99.99

*Presence of carbonate indicated by Raman; CO_2 content inferred by difference.

TABLE 8. A comparison of the chemical compositions of Fe-rich jeffbenite, relative to 12 O per formula unit with respect to our Fe-poor jeffbenite.

Elements	(1)	(2)	(3)	(4)	(5)	(6)	(7)
Mg	2.62	2.10	1.83	1.92	2.03	2.24	2.71
Fe^{2+}	0.27	1.32	1.49	1.60	1.50	1.29	0.50
^{VI}Al	1.86	1.51	1.53	1.36	1.35	1.40	1.36
Ti	–	0.21	0.24	0.24	0.24	0.19	0.20
Si	2.91	2.86	2.72	2.84	2.81	2.87	2.78
^{IV}Al	0.09	0.14	0.28	0.16	0.19	0.13	0.22

Only the major elements are shown for comparison and all Fe was considered as Fe^{2+} even if it is known that that Fe^{3+} could be abundant. ^{IV}Al and ^{VI} Al are the aluminium in tetrahedral and octahedral coordination.

Sources: (1) this study; (2) this study; (3) Bulanova *et al.* (2010); (4) Thomson *et al.* (2014) diamond Ju5-43; (5) Thomson *et al.* (2014) diamond Ju5-102; (6) Thomson *et al.* (2014) diamond Ju5-117; (7) Ti-bearing jeffbenite reported by Armstrong and Walter (2012) averaging the jeffbenite inclusions from Harte *et al.* (1999), Kaminsky *et al.* (2001), Brenker *et al.* (2002), Hayman *et al.* (2005).

suggest that the trace-element content of jeffbenite must be in the range of zero to twice the measured concentrations. In many minerals, the rare-earth elements substitute for Ca, and the absence of Ca from jeffbenite may explain the remarkably low trace-element content.

Micro-Raman spectroscopy

The micro-Raman spectrum collected of jeffbenite is shown in Fig. 4*a*. The five main peaks, in order of decreasing intensity, are (in cm^{-1}): 865, 926, 318, 995 and 499. Lower intensity peaks are evident in the 540–640 cm^{-1} region, one peak is centred at 393 cm^{-1}, and three further peaks occur in the 200–300 cm^{-1} region. As we have no Raman spectrum of previous jeffbenites, we can only compare it with a chemically similar mineral like pyrope. Based on the work of Kolesov and Geiger (1998) on pyrope $Mg_3Al_2Si_3O_{12}$, we may divide the spectrum of jeffbenite into three main regions: (1) the 850–1060 cm^{-1} region is assigned to (Si–O) stretching modes; (2) the 490–640 cm^{-1} region is assigned to SiO_4 bending modes; (3) the 300–400 cm^{-1} region is typical of rotational modes of SiO_4^{4-} groups.

Peaks at <300 cm^{-1} may be assigned to the translational SiO_4^{4-} modes (i.e. 204 and 233 cm^{-1}) and to Mg–O vibrations (i.e. 284 cm^{-1}). The Raman spectrum of jeffbenite is distinctive and unlikely to be mistaken for other minerals.

In Fig. 4*b* we compared the Raman spectra of jeffbenite with that of pyrope from Dora Maira (Italy) and those selected from the RRUFF Raman database (Lafuente *et al.*, 2006; reference RRUFF number: R070637): in the spectra we can observe that a certain degree of overlapping is evident for peaks at 926–927, 865–869, 279–284 and 204–210 cm^{-1}. However, two important peaks of pyrope at 364 and 564 cm^{-1} are totally absent in jeffbenite and, on the contrary, the intense peak at 995 cm^{-1} is absent in pyrope. Therefore, jeffbenite can be identified confidently with respect to pyrope and any other minerals in the absence of XRD data (e.g. as part of composite inclusions).

The crystal structure of jeffbenite

The first crystallographic report for jeffbenite was published by Harris *et al.* (1997) and the same crystal studied in that work was then re-investigated by Finger and Conrad (2000). The necessity to reinvestigate jeffbenite by Finger and Conrad (2000) originated mainly because of some debate about the cation occupancies; Harris *et al.* (1997) had proposed some cation vacancies at the tetrahedral sites, which was not confirmed by Finger and Conrad (2000).

However, the structural models proposed in the two studies were nearly identical. The crystal structure of jeffbenite (Fig. 5) comprises five different cation positions. For comparison with

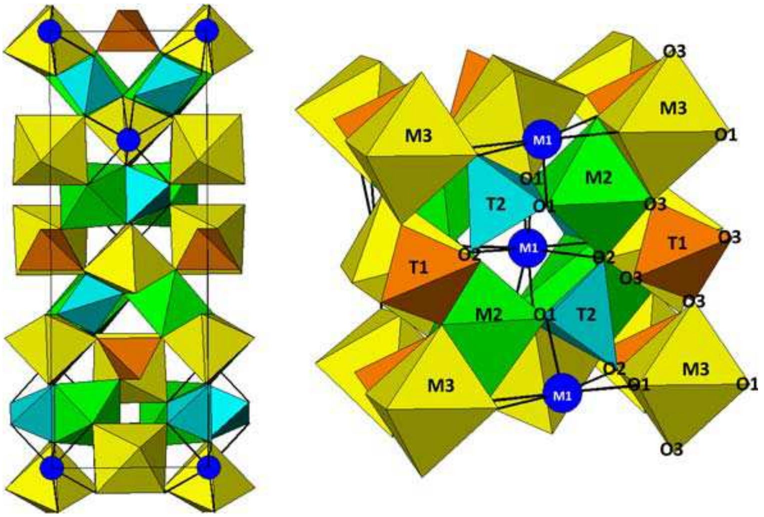

FIG. 5. Crystal structure of jeffbenite viewed perpendicular to *c* (left) and along a closed direction to the *c* axis (right) to better visualize the M1 site with the M1–O bonds.

Harris *et al.* (1997) and Finger and Conrad (2000) we used their same nomenclature: T1 and T2 are two symmetrically independent tetrahedral sites, M2 and M3 are two significantly different octahedral sites, the M1 site is represented by a capped tetrahedron.

The general formula could be (M1)$(M2)_2(M3)_2(T1)(T2)_2O_{12}$ with M1 dominated by Mg, M2 dominated by Al, M3 dominated again by Mg and both T1 and T2 almost fully occupied by Si. The two tetrahedra do not share any oxygen with each other. The T1 tetrahedron shares all its oxygen atoms with M2 and M3 octahedra, while T2 shares one edge with the M2 site and two oxygen vertices with one vertex of M2 and one vertex of M3. Therefore, jeffbenite can be classified as an orthosilicate. Comparison of our data in Table 3 with those of Finger and Conrad (2000) in their table 3 find no difference concerning bond distances, with identical values for all the crystallographic sites. This also explains why the unit-cell volumes between our sample and that of Finger and Conrad (2000) are very close (difference <0.2%).

Petrological importance of jeffbenite: deep or very deep phase?

The significance of jeffbenite and whether it is a primary phase or the product of retrogression of other mantle phases has been a matter of important debate, and viewpoints have changed as more information has become available. The initial recovery of the phase was as mineral grains (30 to 100 μm across) broken out of diamonds and occurring alongside grains of ferropericlase, MgSi-perovskite (bridgmanite) and CaSi-perovskite (Harte and Harris, 1994; Harris *et al.*, 1997; Harte *et al.*, 1999). This mineral association suggested to the above authors that jeffbenite had a limited stability field in the uppermost lower mantle. However, Harris *et al.* (1997) pointed out that jeffbenite had relatively low density and low cation coordination numbers for a lower mantle phase, and the possibility that the mineral was a retrograde product from another phase was not discounted. Finger and Conrad (2000) suggested, without definitive evidence, that jeffbenite crystallized during the ascent of the host diamond as a retrograde phase. In 1997, McCammon *et al.* measuring, by Mössbauer spectroscopy, the Fe^{3+}/Fe_{tot} content of mineral inclusions in diamonds from São Luiz (Brazil) suggested that jeffbenite could show Fe^{3+}/Fe_{tot} from 20 to 75% and that it, due to its association with ferropericlase and retrogressed enstatite, could be stable in the lower mantle.

Hutchison *et al.* (2001) proposed that jeffbenite in diamond has two mineralogical associations. The type-I association includes ferropericlase [(Mg,Fe)O], olivine [$(Mg,Fe)_2SiO_4$] and jeffbenite and is near the lower-mantle/upper-mantle boundary. The type-III association comprises jeffbenite/majoritic garnet, ferropericlase and $(Mg,Fe)SiO_3$ perovskite (bridgmanite) with Na_2O and Al_2O_3 components and is a lower mantle association, (Gasparik and Hutchison, 2000). In detail, Hutchison *et al.* (2001) reported the chemical composition of two jeffbenites in the diamond BZ243A from Sao Luiz region perfectly matching the analyses in our Table 5. Hutchison *et al.* (2001) agreed with Harris *et al.* (1997) and McCammon *et al.* (1997) about the depth of formation of jeffbenite, close to the boundary between the upper and lower mantle.

Kaminsky *et al.* (2001) reported that jeffbenite coexists with bridgmanite ($MgSiO_3$ perovskite); this mineral always being found retrogressed to enstatite in diamond. However, their supposed jeffbenite [similar to that reported by Harte *et al.* (1999)], which is in contact with bridgmanite, has a TiO_2 content of ~8% (almost double that of all other Ti-bearing jeffbenites) and Al_2O_3 of ~17%.

Brenker *et al.* (2002) reported jeffbenite as symplectitic intergrowths with diopside and olivine and associated in the same diamond with ferropericlase. The diamond studied in that work was from Kankan in Guinea. These authors then suggested that such an association could have a primary origin within the lower mantle but, based on their observations, they stated that jeffbenite could form as a retrograde phase within the transition zone of the Earth's mantle and need not be restricted to the upper part of the lower mantle. They also noted that high Fe^{3+} contents may favour the formation of jeffbenite. The samples studied by Brenker *et al.* (2002) are very similar to the chemical composition of jeffbenite studied in our work.

Hayman *et al.* (2005) investigated 69 alluvial diamonds from Rio Soriso (Juina area). In some of them they found jeffbenite. In detail, in one diamond they found jeffbenite in contact with ferropericlase and in a second diamond in contact with $MgSiO_3$ bridgmanite (assumed primary structure). Mainly based on the TiO_2 content of their jeffbenite (i.e. ~5%), Hayman *et al.* (2005) rejected the retrograde transition zone origin proposed by Brenker *et al.* (2002) in favour of a deeper origin at ~660 km depth, (the lower mantle boundary). The chemical composition of jeffbenite studied by Hayman *et al.* (2005) shows SiO_2 close to 40%, $TiO_2 \approx 5\%$, $Al_2O_3 \approx 19\%$. Also these authors found no symplectitic textures for touching jeffbenite-ferropericlase and jeffbenite-bridgmanite.

Bulanova *et al.* (2010) studied several diamonds from the Juina region reporting jeffbenite. The chemical analyses of their jeffbenite show low SiO_2 (i.e. ~35%) and Al_2O_3 (~20%), very high FeO (~23%) and TiO_2 (~4%) and very low MgO (~16%). This jeffbenite could contain almost 50% of the Fe-analogue and shows no symplectitic textures. Bulanova *et al.* (2010) suggested that estimates of depth for their sample could only be, by analogy with other previous works, typical of the boundary between the transition zone and lower mantle.

Harte (2010) in his review of mineral inclusions in deep diamonds noted that where experimental data for the transition zone and upper mantle find mineral assemblages containing majoritic garnet, then in the diamond inclusion associations the majoritic garnet often appears to be replaced by jeffbenite. Harte (2010) also suggested that although various interpretations on the occurrence of jeffbenite have been proposed, its capacity to hold ferric iron could represent further evidence of a deep origin, as it was demonstrated that in deep mantle silicates Fe^{3+} is, in general, significantly abundant (McCammon *et al.*, 2004; Frost *et al.*, 2004).

Armstrong and Walter (2012) performed, for the first time, a high pressure-temperature experimental study on jeffbenite synthesis using a laser-heated diamond-anvil-cell. These authors found that the phase assemblage determined by synchrotron X-ray diffraction consisted of jeffbenite + garnet + pseudobrookite + enstatite from 6 to 10 GPa. Using a Ti-rich jeffbenite bulk composition, these authors additionally found that jeffbenite is stable at a maximum pressure of 10–13 GPa at 1300–1700 K. At higher pressures either garnet (to ~20 GPa) or bridgmanite (>~20 GPa) was stable. Based on these results, the authors ruled out direct incorporation of jeffbenite in diamond at the transition zone – lower mantle boundary. Instead, they suggested (1) entrapment as a primary mineral by diamond in the upper mantle; or (2) retrograde formation from a high-pressure garnet or bridgmanite precursor. Armstrong and Walter (2012) proposed that jeffbenite originated as bridgmanite in the lower mantle in mafic protoliths and that it formed upon retrograde conversion at pressures less than ~13 GPa. With only slight reservations Harte and Hudson (2013) accepted the results of Armstrong and Walter (2012), and used a combined garnet-perovskite end-member mineral plot to show how jeffbenite might result from retrograde decomposition of both Al-bearing bridgmanite and majoritic garnet.

Finally, the most recent report of jeffbenite is from Zedgenizov *et al.* (2014), who placed jeffbenite in the transition zone – lower mantle boundary.

In general, all possible compositions of jeffbenites reported so far in the literature are shown in Table 8. Based on this table we can classify jeffbenites in three main compositional ranges: (1) Ti-free and low-Fe jeffbenite; (2) Ti-rich and high-Fe jeffbenites; and (3) Ti-rich and low Fe-jeffbenites. However, for Fe-rich jeffbenites it would be extremely important to analyse them by single-crystal X-ray diffraction to obtain the cation partitioning for Fe and Mg. Indeed, as we have shown in this work (see for example Table 2), the M1 site could host a considerable amount of iron and in the case of very Fe-rich jeffbenites like those found by Bulanova *et al.* (2010) and Thomson *et al.* (2014) we cannot exclude that this site could be dominated by Fe. This would correspond to a new mineral, the Fe-analogue of jeffbenite

Elastic properties of jeffbenite

Unfortunately, so far there are no literature data available for the compressibility and/or thermal expansion of jeffbenite. Such crucial thermodynamic properties could help in obtaining a thermodynamic stability field for different compositions. At the moment, in order to get the volume variation of jeffbenite as a function of pressure we can use the diffraction data in Armstrong and Walter (2012). In their table 4, these authors obtained a unit-cell volume of 783.51 Å^3 for their synthetic jeffbenite at room pressure and a volume of 749.02 Å^3 at 9.6 GPa. A simple calculation to obtain an indication of bulk modulus, K_T, could be performed applying the following relationship: K_T (GPa) = $\Delta P/(\Delta V/V_0)$. Applying this relationship we obtain $K_T = 218$ GPa.

Such a value is definitively larger than that of all pyrope-rich garnets ($\mathrm{K}_{\mathrm{T,pyrope\text{-}almandine}} = 164$–173 GPa; Milani *et al.*, 2015), majorite ($K_T =$ 160 GPa; Angel *et al.*, 1989) and of other Mg-rich high-pressure silicates like ringwoodite ($K_{\mathrm{T,Mg_2SiO_4\text{-}Fe_2SiO_4}} = 180$–190 GPa; Nestola *et al.*, 2010; Ganskow *et al.*, 2010; Ye *et al.*, 2012), wadsleyite ($K_T = 170$ GPa; Ye *et al.*, 2010) and oxides like Mg-Fe-Al-Cr spinels ($K_T \approx 185$ GPa; Nestola *et al.*, 2014*b*) and ferropericlase ($K_T =$ 150–160 GPa; Jacobsen *et al.*, 2002). Its bulk modulus, however, is lower than that of $MgSiO_3$ bridgmanite ($K_T = 253$ GPa; Vanpeteghem *et al.*, 2006), which is the only high-pressure Mg-silicate with a larger bulk modulus than jeffbenite.

Further work on the high-pressure and high-temperature behaviour of jeffbenite is in progress to define its experimental compressibility and thermal expansion.

Conclusions

The only experimentally determined stability field for jeffbenite available so far is that of Armstrong and Walter (2012) and this work provides the maximum pressure at which jeffbenite can be stable, i.e. 13 GPa at 1700 K. Based on the experimental stability field and the absence of jeffbenite from any other geological setting, we are confident that jeffbenite is entrapped in diamond in the deep upper mantle. Thus, in general, we can confirm that jeffbenite is without any doubt a sub-lithospheric mineral.

The results of Armstrong and Walter (2012) considerably affect the suggestions made in earlier work on the *P-T* stability field of jeffbenite, and cast doubt upon its occurrence as a primary phase in the lower part of the transition zone and the uppermost lower mantle. However, the stability field of Armstrong and Walter (2012) is that of a Ti-rich jeffbenite and not a Ti-free jeffbenite like the one investigated here. So, it is important to determine the roles that TiO_2 and also FeO and Fe_2O_3 play in extending the stability field of jeffbenite to higher or lower pressures.

Although these matters require further resolution, at the present time the two main possibilities for the formation of jeffbenite are: (1) entrapment as a primary mineral by diamond in the deepest regions of the upper mantle at pressures up to 10 to 13 GPa (Armstrong and Walter, 2012); (2) retrograde formation from a bridgmanite or high-pressure garnet (majoritic garnet) precursor below 13 GPa (Brenker *et al.*, 2002; Armstrong and Walter, 2012; Harte and Hudson, 2013).

Acknowledgements

This research was supported by the ERC Starting Grant 2012 to FN (agreement no. 307322) and NERC grant NE/J008583/1 to MJW and SCK. We are grateful to Chris Smith and Galina Bulanova for access to the Collier-4 diamond RC2-7. We thank M. Welch and a second anonymous referee for improving the manuscript.

References

Angel, R.J. and Nestola, F. (2015) A century of mineral structures: how well do we know them? *American Mineralogist*, **101**, 1036–1045.

Angel, R.J., Finger, L.W., Hazen, R.M., Kanzaki, M., Weidner, D.J., Liebermann, R.C. and Veblen, D.R. (1989) Structure and twinning of single-crystal $MgSiO_3$ garnet synthesized at 17 GPa and 1800°C. *American Mineralogist*, **74**, 509–512.

Angel, R.J., Mazzucchelli, M.L., Alvaro, M., Nimis, P. and Nestola, F. (2014) Geobarometry from host-inclusion systems: the role of elastic relaxation. *American Mineralogist*, **99**, 2146–214.

Angel, R.J., Alvaro, M., Nestola, F. and Mazzucchelli, M. L. (2015*a*) Diamond thermoelastic properties and implications for determining the pressure of formation of diamond inclusion systems. *Russian Geology and Geophysics*, **56**, 211–220.

Angel, R.J., Nimis, P., Mazzucchelli, M.L., Alvaro, M. and Nestola, F. (2015*b*) How large are departures from lithostatic pressure? Constraints from host-inclusion elasticity. *Journal of Metamorphic Geology*, https://doi.org/10.1111/jmg.12138.

Armstrong, L.S. and Walter, M.J. (2012) Tetragonal almandine pyrope phase (TAPP): retrograde Mg-perovskite from subducted oceanic crust? *European Journal of Mineralogy*, **24**, 587–597.

Barron, L.M., Barron, B.J., Mernagh, T.P. and Birch, W.D. (2008) Ultrahigh pressure macro diamonds from Copeton (New South Wales, Australia), based on Raman spectroscopy of inclusions. *Ore Geology Reviews*, **34**, 76–86.

Brenker, F.E., Stachel, T. and Harris, J.W. (2002) Exhumation of lower mantle inclusions in diamond: A TEM investigation of retrograde phase transitions, reactions and exsolution. *Earth and Planetary Science Letters*, **198**, 1–9.

Bulanova, G.P., Walter, M.J., Smith, C.B., Kohn, S.C., Armstrong, L.S., Blundy, J. and Gobbo, L. (2010) Mineral inclusions in sublithospehric diamonds from Collier 4 kimberlite pipe, Juina, Brazil: subducted protoliths, carbonated melts and primary kimberlite magmatism. *Contributions to Mineralogy and Petrology*, **160**, 489–510.

Chopin, C. (1984) Coesite and pure pyrope in high-grade blueschists of the Western Alps: a first record and some consequences. *Contributions to Mineralogy and Petrology*, **86**, 107–118.

Droop, G.T.R. (1987) A general equation for estimating Fe (super 3+) concentrations in ferromagnesian silicates and oxides from microprobe analyses, using stoichiometric criteria. *Mineralogical Magazine*, **51**, 431–435.

Finger, L.W. and Conrad, P.G. (2000) The crystal structure of "Tetragonal Almandine-Pyrope Phase" (TAPP): a re-examination. *American Mineralogist*, **85**, 1804–1807.

Frost, D.J., Liebske, C., Langenhorst, F., McCammon, C. A., Trunnes, R.G. and Rubie, D.C. (2004) Experimental evidence for the existence of iron-rich metal in the Earth's lower mantle. *Nature*, **428**, 409–412.

Ganskow, G., Ballaran, T.B. and Langenhorst, F. (2010) Effect of iron on the compressibility of hydrous ringwoodite. *American Mineralogist*, **95**, 747–753.

Gasparik, T. and Hutchison, M.T. (2000) Experimental evidence for the origin of two kinds of inclusions in diamonds from the deep mantle. *Earth and Planetary Science Letters*, **181**, 103–114.

Harris, J.W., Hutchison, M.T., Hursthouse, M., Light, M. and Harte, B. (1997) A new tetragonal silicate mineral occurring as inclusions in lower mantle diamonds. *Nature*, **387**, 486–488.

Harte, B. (2010) Diamond formation in the deep mantle: the record of mineral inclusions and their distribution in relation to mantle dehydration zones. *Mineralogical Magazine*, **74**, 189–215.

Harte, B. and Harris, J.W. (1994) Lower mantle mineral associations preserved in diamonds. *Mineralogical Magazine*, **58A**, 384–385.

Harte, B. and Hudson, N.F.C. (2013) Mineral associations in diamonds from the lowermost Upper mantle and uppermost lower mantle. *Proceedings of 10th International Kimberlite Conference*, 235–253.

Harte, B., Harris, J.W., Hutchison, M.T., Watt, G.R. and Wilding, M.C. (1999) Lower mantle mineral associations in diamonds from Sao Luiz, Brazil. Pp. 125–153 in: *Mantle Petrology: Field Observations and High Pressure Experimentation: A Tribute to Francis R. (Joe) Boyd* (Y. Fei, C.M. Bertka and B.O. Mysen, editors). The Geochemical Society, Houston, Texas, USA.

Hayman, P.C., Kopylova, M.G. and Kaminsky, F.V. (2005) Lower mantle diamonds from Rio Soriso (Juina area, Mato Grosso, Brazil). *Contributions to Mineralogy and Petrology*, **149**, 430–445.

Holland, T.J.B. and Redfern, S.A.T. (1997) Unit cell refinement from powder diffraction data: The use of regression diagnostics. *Mineralogical Magazine*, **61**, 65–77.

Howell, D., Wood, I.G., Nestola, F., Nimis, P. and Nasdala, L. (2012) Inclusions under remnant pressure in diamond: a multi-technique approach. *European Journal of Mineralogy*, **24**, 563–573.

Hutchison, M.T., Hursthouse, M.B. and Light, M.E. (2001) Mineral inclusions in diamonds: associations and chemical distinctions around the 670-km discontinuity. *Contributions to Mineralogy and Petrology*, **142**, 199–126.

Jochum, K.P., Willbold, M., Raczek, I., Stoll, B. and Herwig, K. (2005) Chemical characterisation of the USGS reference glasses GSA-1G, GSC-1G, GSD-1G, GSE-1G, BCR-2G, BHVO-2G and BIR-1G using EPMA, ID-TIMS, ID-ICP-MS and LA-ICP-MS. *Geostandards and Geoanalytical Research*, **29**, 285–302.

Jacobsen, S.D., Spetzler, H.A., Reichmann, H.J., Smyth, J.R., Mackwell, S.J., Angel, R.J. and Bassett, W.A. (2002) Gigahertz ultrasonic interferometry at high P and T: new tools for obtaining a thermodynamic equation of state. *Journal of Physics – Condensed Matter*, **14**, 11525–11530.

Kaminsky, F. (2012) Mineralogy of the lower mantle: a review of "super-deep" mineral inclusions in diamond. *Earth Science Reviews*, **110**, 127–147.

Kaminsky, F.V., Zakharchenko, O.D., Davies, R., Griffin, W.L., Khachatryan-Blinova, G.K. and Shiryaev, A.A. (2001) Superdeep diamonds from the Juina area, Mato Grosso State, Brazil. *Contributions to Mineralogy and Petrology*, **140**, 734–753.

Kolesov, B.A. and Geiger, C.A. (1998) Raman spectra of silicate garnets. *Physics and Chemistry of Minerals*, **25**, 142–151.

Lafuente, B., Downs, R.T., Yang, H. and Stone, N. (2015) The power of databases: the RRUFF project. Pp. 1–30 in: *Highlights in Mineralogical Crystallography* (T. Armbruster and R.M. Danisi, edtors). De Gruyter, Berlin, Germany.

Liou, J.G., Zhang, R.Y., Liu, F.L., Zhang, Z.M. and Ernst, W.G. (2012) Mineralogy, petrology, U-Pb geochronology, and geologic evolution of the Dabie-Sulu classic ultrahigh-pressure terrane, East-Central China. *American Mineralogist*, **97**, 1533–1543.

Mandarino, J.A. (1981) The Gladstone-Dale relationship: Part IV. The compatibility concept and its application. *The Canadian Mineralogist*, **19**, 441–450.

McCammon, C., Hutchison, M. and Harris, J. (1997) Ferric iron content of mineral inclusions in diamonds from São Luiz: a view into the lower mantle. *Science*, **278**, 434–436.

McCammon, C.A., Stachel, T. and Harris, J.W. (2004) Iron oxidation state in lower mantle mineral assemblages. II. Inclusions in diamonds from Kankan, Guinea. *Earth and Planetary Science Letters*, **222**, 423–434.

Milani, S., Nestola, F., Alvaro, M., Pasqual, D., Mazzucchelli, M.L., Domeneghetti, M.C. and Geiger, C.A. (2015) Diamond-garnet geobarometry: the role of garnet compressibility and expansivity. *Lithos*, **227**, 140–147.

Nestola, F. and Smyth, J.R. (2016) Diamonds and water in the deep Earth: a new scenario. *International Geology Review*, **58**, 263–276.

Nestola, F., Nimis, P., Angel, R.J., Milani, S., Bruno, M., Prencipe, M. and Harris, J.W. (2014*a*) Olivine with diamond-imposed morphology included in diamonds. Syngenesis or protogenesis? *International Geology Review*, **56**, 1658–1667.

Nestola, F., Periotto, B., Andreozzi, G.B., Bruschini, E. and Bosi, F. (2014*b*) Pressure-volume equation of state for chromite and magnesiochromite: a single-crystal X-ray diffraction investigation. *American Mineralogist*, **99**, 1248–1255.

Nestola, F., Boffa Ballaran, T., Koch-Mueller, M., Balic-Zunic, T., Taran, M., Olsen, L., Princivalle, F., Secco, L. and Lundegaard, L. (2010) New accurate compression data for gamma-Fe_2SiO_4. *Physics of the Earth and Planetary Interiors*, **183**, 421–425.

Parkinson, C.D. (2000) Coesite inclusions and prograde compositional zonation of garnet in whiteschist of the HP-UHPM Kokchetav massif, Kazakhstan: a record of progressive UHP metamorphism. *Lithos*, **52**, 215–233.

Sheldrick, G.M. (2008) A short history of SHELX. *Acta Crystallographica Section A*, **64**, 112–122.

Stachel, T. (2001) Diamonds from the asthenosphere and the transition zone. *European Journal of Mineralogy*, **13**, 883–892.

Thomson, A.R., Kohn, S.C., Bulanova, G.P., Smith, C.B., Araujo, D. and Walter, M.J. (2014) Origin of sub-lithospheric diamonds from the Juina-5 kimberlite (Brazil): constraints from carbon isotopes and inclusion compositions. *Contributions to Mineralogy and Petrology*, **168**, article 1081.

van Roermund, H.L.M. and Drury, M.R. (1998) Ultra-high pressure ($P > 6$ GPa) garnet peridotites in Western Norway: exhumation of mantle rocks from >185 km depth. *Terra Nova*, **10**, 295–301.

Vanpeteghem, C.B., Zhao, J., Angel, R.J., Ross, N.L. and Bolfan-Casanova, N. (2006) Crystal structure and equation of state of $MgSiO_3$ perovskite. *Geophysical Research Letters*, **33**, L03306.

Walter, M.J., Kohn, S.C., Araujo, D., Bulanova, G.P., Smith, C.B., Gaillou, E., Wang, J., Steele, A. and Shirey, S.B. (2011) Deep mantle cycling of oceanic crust: evidence from diamonds and their mineral inclusions. *Science*, **334**, 54–57.

Ye, Y., Smyth, J.R., Hushur, A., Manghnani, M.H., Lonappan, D., Dera, P. and Frost, D.J. (2010) Crystal structure of hydrous wadsleyite with 2.8% H_2O and compressibility to 60 GPa. *American Mineralogist*, **95**, 1765–1772.

Ye, Y., Brown, D.A., Smyth, J.R., Panero, W.R., Jacobsen, S.D., Chang, Y.Y., Townsend, J.P., Thomas, S.M., Hauri, E.H., Dera, P. and Frost, D.J. (2012) Compressibility and thermal expansion of hydrous ringwoodite with 2.5(3) wt% H_2O. *American Mineralogist*, **97**, 573–582.

Zedgenizov, D.A., Kagi, H., Shatsky, V.S. and Ragozin, A.L. (2014) Local variations of carbon isotope composition in diamonds from Sao-Luis (Brazil): Evidence for heterogenous carbon reservoir in sub-lithospheric mantle. *Chemical Geology*, **363**, 114–124.

Zhang, L.F., Ellis, D.J. and Jiang, W.B. (2002) Ultrahigh-pressure metamorphism in western Tianshan, China: Part I. Evidence from inclusions of coesite pseudomorphs in garnet and from quartz exsolution lamellae in omphacite in eclogites. *American Mineralogist*, **87**, 853–860.